

論文 / 著書情報
Article / Book Information

題目(和文)	軟岩中に埋設された大径片持ち式鋼管杭壁の各種荷重に対する安定性
Title(English)	Stability of large diameter cantilever type steel tubular pile wall embedded in soft rock subjected to various loadings
著者(和文)	SHAFIS M
Author(English)	S M Shafi
出典(和文)	学位:博士(学術), 学位授与機関:東京工業大学, 報告番号:甲第12791号, 授与年月日:2024年3月26日, 学位の種別:課程博士, 審査員:竹村 次郎,高橋 章浩,佐々木 栄一,田村 修次,丸山 泰蔵
Citation(English)	Degree:Doctor (Academic), Conferring organization: Tokyo Institute of Technology, Report number:甲第12791号, Conferred date:2024/3/26, Degree Type:Course doctor, Examiner:,,,,
学位種別(和文)	博士論文
Type(English)	Doctoral Thesis

Stability of large diameter cantilever type steel tubular pile wall embedded in soft rock subjected to various loadings

By
S M Shafi

A dissertation submitted in partial fulfilment of the requirements for the degree of
Doctor of Philosophy

Academic advisor
Dr. Jiro Takemura



Department of Civil and Environmental Engineering
Tokyo Institute of Technology
Tokyo, Japan
February 2024

Abstract

Stability of large diameter cantilever type steel tubular pile wall embedded in soft rock subjected to various loadings

By S M Shafi

*Doctor of Philosophy in Engineering, Department of Civil and Environmental Engineering
Tokyo Institute of Technology, Japan*

The application of Cantilever type Steel Tubular Pile (CSTP) walls as permanent or temporary retaining structures has increased in recent decades. Technological advancements like the rotary cutting press-in technique make constructing this wall in populated urban areas possible. Also, it becomes possible to construct this type of wall on comparatively stiff ground like soft or hard rock. Although technology has advanced, the current design guidelines are not well rationalized to consider the specific features of the wall, like a very large stiffness wall embedded in stiff ground. Several concerns were raised by the engineers and researchers, for example, the selection of minimum embedment depth, 3D behaviour of steel tubular pile wall, heterogeneity of embedment conditions in the stiff ground, and the applicability of the bi-linear p-y curve for dynamic conditions. Also, the stability of the CSTP wall against extreme loading like earthquakes, buildup of water pressure on the retain side or the combination of both should be checked from the serviceability limit to the ultimate conditions. Not enough research was done to investigate the concerns mentioned above by physical means, such as physical modelling. This research addresses these concerns by physical modelling using the Tokyo Tech Mark III centrifuge. At first, the complex CSTP walls model is simplified into simple pile loading and wall loading tests, with clear loading conditions, to avoid the complex soil wall interaction observed in actual CSTP walls with retained soil. Then, five centrifuge model tests were conducted using the actual CSTP wall with retained soil embedded into soft rock subjected to sequential loadings.

Using the Tokyo Tech centrifuge facility, a single pile loading test with different rock socketing depths (d_r) was conducted in 1g. The purpose of using the 1g model test was that it could provide helpful information about the lateral resistance of the pile due to less stress dependency of the soft rock material. Three stainless steel piles with outer diameter (Φ) of 40mm and thickness (t) of 0.5mm were used. The piles were socketed into artificially prepared soft rock with normalized rock socketing depths (d_r/Φ) of 1.0, 1.5, 2.0. By controlling the displacement, a one-way horizontal cyclic load was applied on each pile at a loading height (h_L) of 130mm from the rock surface. The 1g pile loading test results were compared with the previously conducted 50g pile loading test. The lateral resistance of the pile increases with the rock socketing depth in both the 1g and 50g pile loading tests. The 1g model could predict the lateral resistance of the centrifuge model test up to a small imposed displacement. However, at larger imposed displacement, the 1g model underestimates the lateral resistance compared to the 50g model due to early crack formation, proving the advantage of using the centrifuge model test. In addition, a detailed calibration of the model pile was conducted to investigate the mechanical behaviour of the pile. For a pile with a diameter-to-thickness ratio (Φ/t) of 80, nonlinearity in the bending moment and strain occurs at

approximately 65% of the theoretical yielding moment, which limits the applicability of the Euler-Bernoulli theorem up to this level.

The simplified CSTP wall loading test under 50g centrifugal acceleration with clear loading conditions was used to study the load resistance (p-y) curve concept, specifically to investigate the JARA-recommended design p-y curve. Also, Finite Element Method (FEM) analysis using Plaxis 2D was conducted to examine the potential impact of container boundaries on the lateral resistance of the centrifuge model. The analytical tool "Lpile" by Ensoft was utilized to study the p-y curve. Furthermore, using the centrifuge test condition, a stability analysis using the limit equilibrium method was carried out to discuss the effect of base shear on the lateral resistance of the wall. From the FEM analysis, no significant effect of the container side wall on the lateral resistance was seen, except a minor effect for $d_r/\Phi=2$. Based on the stability analysis, the factor of safety increases with the increase of embedment depth. Mobilization of the base shear resistance could provide additional stability to the wall. However, the contribution of base shear resistance depends on the d_r/Φ ratio, i.e., a smaller ratio would mobilize larger base shear resistance. The bi-linear P-y curve without base shear recommended by JARA (2017) could be more conservative for predicting the load-displacement relationship of large-diameter piles embedded in the stiff ground. Two springs model, where the lateral spring is defined by the JARA (2017) and a base shear spring with stiffness 1/3 of the lateral spring recommended for caisson type foundation by JARA (2017), could predict the load-displacement curve at small to large imposed displacement ($<10.0\%\Phi$) reasonably.

A large diameter ($\Phi=2\text{m}$) cantilever steel tubular piles (CSTP) walls embedded in a soft rock were modelled in a centrifuge with the wall height $H=12\text{m}$ and different embedment conditions and dry, dense sand as the retained soil under 50g centrifugal acceleration. Five centrifuge tests were conducted. Three tests included a single rock layer with embedment depth (d_r) of 2.5 ($\beta.d_r=1.0$) and 3.0m ($\beta.d_r=1.2$). Two tests included rock with overlaying sand layer (d_s) to discuss the effect of heterogeneity of the embedment condition. Among them, the first model had an embedment depth equal to 3m ($d_r=2.5\text{m};d_s=0.5\text{m}$), and the latter had an embedment depth of 3.5m ($d_r=2.5\text{m};d_s=1.0\text{m}$). Sequential loadings were applied to the wall to investigate the wall performance under extreme loading conditions. Dynamic loadings were first applied by sinusoidal input acceleration with a predominant frequency of 1Hz, followed by the water rise to the water height $h_w>2H/3$ in the retained sand as a static loading. Another series of dynamic loadings was applied in the wet condition. The water level was increased further, and dynamic loading was finally imposed on the wall. In one single rock layer model, static loading by water rise was applied first, followed by large dynamic loading. Stability against the catastrophic failure was confirmed for the single rock layer model with $d_r=2.5\text{m}$ ($\beta.d_r=1.0$) even at a wall displacement of more than $4\%H$. Further increasing the d_r by 0.5m could significantly improve the wall stability. The weathering of the shallow rock layer could reduce the factor of safety and increase the wall top displacement. For high-stiffness walls embedded into the stiff ground with good confinement conditions, the residual effective earth pressure increases with the wall displacement by dynamic loadings, defined as the "elastic resilience effect" in this study. The effective earth pressure ratio (σ'_h/σ'_v) observed after final loading was larger than the design active (K_a) or even at-rest (K_0) pressure coefficient due to the resilience effect. It suggests that commonly assumed K_a or K_0 earth pressure in the design might lead to underestimating the wall bending moment. The long-term

creep displacement could reduce the resilience effect for the less redundant CSTP wall used in this research. The long-term creep displacement of the wall will be less of a concern for the dynamic loading than the static loading due to the reduction of earth pressure developed by the resilience effect. For the large diameter thin wall tubular pile, a stress concentration or a propping action might cause the local deformation of the pile near the rock surface, which affects the bending moment measurement using strain gauges. 9. If the actual total earth pressure acting on the wall can be measured in the real site, using the two-spring model, where the lateral spring is defined by the JARA (2017) and a base shear spring with stiffness $1/3$ of the lateral spring recommended for caisson type foundation by JARA (2017) and actual total earth pressure as imposed load, could reasonably predict the residual wall displacement up to $\delta_r < 0.5\%H$. However, assuming the commonly used active or at-rest earth pressure as imposed external load might underestimate the residual wall displacement due to the resilience effect, which is unique for the high stiffness wall embedded into stiff ground. There are several limitations of using the bi-linear p-y curve to predict the residual wall displacement. Firstly, in actual conditions, as the residual wall displacement increases, the plastic deformation of the rock could reduce the k_H , which cannot be predicted by the bi-linear p-y curve with constant k_H . Therefore, a bi-linear p-y curve with variable k_H based on the plastic deformation could provide a more accurate residual wall top displacement prediction. Secondly, the bi-linear p-y curve cannot predict the resilience effect, which occurs during the dynamic loadings.

Acknowledgement

I want to express my deepest respect and appreciation to Associate Professor Jiro Takemura, my supervisor, for his exceptional guidance, unwavering motivation, significant suggestions, and understanding mentorship throughout the research project. His boundless enthusiasm and attentive support were indispensable in bringing this dissertation to completion.

I extend my heartfelt gratitude to the rest of my thesis committee members Prof. Akihiro Takahashi, Prof. Shuji Tamura, Prof. Eiichi Sasaki Ass. Prof. Taizo Maruyama for their kind advice and helpful comments.

I am indebted to the Ministry of Education, Culture, Sports, Science and Technology (MEXT), Japan, for granting me a Monbukagakusho scholarship. Without the financial aid from MEXT, this research would not have been possible.

I gratefully acknowledge the invaluable advice and guidance provided by the members and advisers of the IPA TC1 (Committee on Application of Cantilever-type Steel Tubular Pile Wall Embedded in Stiff Ground) in connection with this research.

I would like to express my heartfelt appreciation to the staff as well as colleagues at the Soil Lab for their warm and amiable demeanour, helpfulness, considerate encouragement, and positive outlook, all of which greatly enhanced my academic experience and life in Japan. I extend my sincere thanks to Mr. Sakae for his exceptional support and invaluable contributions to my research.

I am grateful to my family members, Mr. Faruque Ahmed, Ms. Ashfatunnesa, and Ms. Tanzima, for their continuous support and motivation. My deepest gratitude goes to my wife, Ms. Navila Tabassum, for her understanding, continuous support, and encouragement throughout my stay in Japan.

Table of contents

1	Introduction	1
1.1	General	1
1.2	Problem Statement	2
1.3	Goals and Objectives	3
1.4	Scope and Challenges	3
1.5	Organization of the dissertation	5
	References:	6
2	Literature review	8
2.1	Introduction:	8
2.2	Design and Stability of Cantilever retaining wall:	8
2.2.1	Design loads acting on the cantilever retaining wall:	8
2.2.2	Calculation of embedment depth	14
2.2.3	Stability analysis (Madabhushi and Chandrasekaran, 2005)	19
2.3	Catastrophic failure of Embedded retaining structure	23
2.3.1	Edinburgh tower basement construction Hong Kong (1981)	23
2.3.2	Failure of 20 ft Highway retaining wall (R.E. Olson, 1993)	23
2.3.3	Failure of cantilever retaining walls due to reduction of lateral support and earthquake (Day, 1997)	25
2.4	Centrifuge modeling of cantilever retaining wall embedded in various ground:	27
2.4.1	Dynamic loading:	27
2.4.2	Static loading:	31
2.5	Application of Steel Tubular Pile (STP) in Japan	33
2.6	Lateral response of pile/Wall	35
2.6.1	Elastic response	35
2.6.2	Load transfer curve of rock:	37
2.6.3	P-y curves for soft clay in presence of free water and stiff clay without free water under static or cyclic loading:	40
2.7	Properties of geomaterials:	43
2.7.1	Sand:	43
2.7.2	Rock:	46
2.7.3	Literature of artificial soft rock:	52
2.8	Centrifuge modeling:	54
2.8.1	Advantage of centrifuge modeling:	54
2.8.2	Principles of geotechnical centrifuge modelling:	54
2.8.3	Tokyo tech Mark III centrifuge and centrifuge scaling law:	56
	References:	58
3	Mechanical behaviour of laterally loaded single pile socketed in soft rock	62
3.1	Introduction:	62
3.2	Mechanical properties of model pile:	62
3.2.1	Model preparation and test conditions	62

3.2.2	Experimental measurement	65
3.2.3	Experimental results	66
3.2.4	Discussions	69
3.3	Preparation of soft rock ground layer	72
3.3.1	Material properties and the estimation of materials	72
3.4	1g rock socketed pile loading test	76
3.4.1	Model preparation and test conditions	76
3.4.2	Sensors and instrument used in 1g rock socketed pile loading test	82
3.4.3	Experimental result:	83
3.4.4	Discussions	85
3.5	Summary	90
	References	91
4	Lateral response of large diameter Cantilever type Steel Tubular Pile wall embedded in soft rock subjected to one-way cyclic loading	92
4.1	Introduction	92
4.2	Centrifuge test used to investigate the bilinear p-y curve	92
4.2.1	Model and test conditions	92
4.2.2	Observed results from the centrifuge test	95
4.2.1.1	Model and test conditions	92
4.2.1.2	Observed results from the centrifuge model	95
4.3	Investigation of the effect of container wall on the load-displacement behaviour by Numerical modelling	98
4.4	Investigation of effect of base shear to the lateral resistance of CSTP wall	103
4.5	Study of bi-linear p-y curves to predict the lateral resistance behaviour of CSTP wall	105
4.5.1	Model condition and the assumed p-y curves	105
4.5.2	Results and discussions	109
4.3	Summary	113
	References	114
5	Centrifuge modeling of large diameter Cantilever type Steel Tubular Pile wall embedded in soft rock subjected to sequential dynamic and static loadings	115
5.1	Introduction	115
5.2	Modeling concept	115
5.3	Model preparation and loading conditions	115
5.3.1	Model preparation	115
5.4	Centrifuge test conditions	123
5.4.1	Single rock layer model test conditions	123

5.4.2	Two layers model test conditions	131
5.5	Results and discussions	136
5.5.1	Typical acceleration and phase angle response	136
5.5.2	Observed typical behaviour of CSTP wall under dynamic loading	141
5.5.3	Typical dynamic soil wall interaction:	145
5.5.4	Lateral pressure acting on the CSTP wall	149
5.5.4.1	Qualitative discussion on total thrust force and the location of the total thrust force	154
5.5.4.2	Dynamic lateral pressure	157
5.5.5	Bending moment	157
5.5.5.1	Dynamic bending moment	161
5.5.6	Typical CSTP wall displacement behavior under dynamic loading	163
5.5.7	Effect of pre-shaking on the static loading behaviour of CSTP wall	165
5.5.8	Effect of embedment condition on the CSTP wall behaviour	166
5.5.9	Resilience effect	173
5.5.10	Use of active lateral pressure for the design of high stiffness CSTP wall embedded into stiff ground	174
5.5.11	Qualitative discussion on CSTP wall deflection behaviour	175
5.5.12	Effect of backfill soil on the stability and the failure mechanism of the CSTP wall	178
5.5.13	Long-term behaviour of CSTP wall	181
5.5.13.1	Long-term behaviour after dynamic loading	184
5.5.13.2	Long-term behaviour after static loading	186
5.5.14	Applicability of bi-linear p-y curve to predict the residual wall displacement after sequential loadings	187
5.6	Some appraisal against the concerns related to the design of CSTP walls embedded in the stiff ground	197
5.7	Summary	199
	References	201
6	Conclusions and recommendations	203
6.1	Conclusions	203
6.2	Further recommendation	205
	Appendix	207

List of Figures

Figure 1.1: Cantilever retaining walls.	1
Figure 1.2: Rotary cutting press-in technique (Gyro piler) (Kitamura and Kitamura, 2018).	2
Figure 1.3: Application of cantilever-type steel tubular pile walls (Miyanojara et al., 2018).	2
Figure 1.4: Orientation of the dissertation.	6
Figure 2.1: Flow performance verification of steel tubular earth retaining structure (IPA handbook, 2016).	9
Figure 2.2: States of the stress of active and passive conditions (a) Stress and pressure of soil element on wall (b) Mohr diagram.	10
Figure 2.3: Qualitative lateral pressure variation with wall movement (PYwall Technical Manual, 2022).	10
Figure 2.4: Measured point of applications of total dynamic active thrust force (Matsuzawa et al., 1985).	13
Figure 2.5: Simplified method (Elastic ground reaction force model).	17
Figure 2.6: Elasto-plastic ground reaction force model	19
Figure 2.7: Failure mechanism of cantilever retaining wall (a) flexural bending failure with the formation of a plastic hinge (b) body rotation about a pivotal point.	20
Figure 2.8: Pressure distribution for cohesionless soil.	21
Figure 2.9: Pressure distribution for cohesive soil.	21
Figure 2.10: Strains required for mobilization of active and passive earth pressures [after Clayton and Milititsky (1986)].	22
Figure 2.11: Sheet pile failure and Queen's Road collapse during Edinburgh Tower basement construction	23
Figure 2.12: Failed section of retaining wall.	24
Figure 2.13: Cantilever retaining wall in case study 1.	25
Figure 2.14: Wall deformation variation with time.	25
Figure 2.15: Cross section of the site for case study 2.	26
Figure 2.16: Centrifuge model configuration.	27

Figure 2.17: Back-calculated dynamic earth pressure coefficients at the time of maximum dynamic wall moments on the stiff and flexible walls as a function of peak ground acceleration measured at the top of the soil in the free field.	28
Figure 2.18: Geometry of the centrifuge model (a) cantilever retaining wall (b) propped retaining wall.	29
Figure 2.19: Centrifuge model configuration (a) Model A (height:5.4m) (b) Model B (height:10.8m).	30
Figure 2.20: Centrifuge model setup	32
Figure 2.21: Loading sequence followed in centrifuge tests.	32
Figure 2.22: influence of embedment depth: (a) normalized WT displacement and WT rotation plotted against the moment load; (b) photographs of wall and ground deformation taken in flight after excavation and loading processes.	33
Figure 2.23: Press-in or extraction mechanism and associated forces (Source: IPA handbook)	34
Figure 2.24: Some applications of steel tubular pile walls constructed by press-in method (Source: IPA handbook)	34
Figure 2.25: Lateral loading of rock socketed pile.	35
Figure 2.26: Elastic flexibility of free-headed piles in rock (Randolph, 2020)	37
Figure 2.27: Plot of results from simulated full-scale triaxial tests on a rock mass defined by a uniaxial compressive strength $\sigma_{ci} = 85$ MPa, a Hock-Brown constant $m_i = 10$ and Geological Strength Index $GSI = 45$ (Hoek-Brown, 1997).	38
Figure 2.28: Soil resistance variation with depth (a) predicted soil resistance by different researchers (b) effect of soil-pile adhesion on lateral resistance (Murff and Hamilton, 1993).	39
Figure 2.29: Chipping approach for the lateral response of rock socketed pile (Erbrich, 2004).	40
Figure 2.30: Stiffness - strain behaviour of soil and design strain levels for various structures and laboratory tests (after Atkinson and Sallfors, 1991; Mair, 1993; Ishihara, 1996; Sawangsuriya et al., 2005) (Sawangsuriya, 2012).	44
Figure 2.31: Dependency of stiffness on the void ratio of Toyoura sand at 98kPa confining pressure for different strain amplitudes (Iwasaki and Tatsuoka (1978)).	45

Figure 2.32: Relation between $G / (((2.17-e)^2)/(1+e))$ and confining pressure (p) for (a) air dried and (b) saturated Toyoura sand at different strain amplitudes (Iwasaki and Tatsuoka (1978)).	45
Figure 2.33: m_γ - γ relation for Toyoura sand (Iwasaki and Tatsuoka (1978)).	46
Figure 2.34: distribution of subsurface rock types in Japan (Geological Survey of Japan, 1995).	47
Figure 2.35: Classification of rock material strength (after Kulhawy and Phoon, 1993).	48
Figure 2.36: Hardness and unconfined compressive strength of rock materials in engineering classification (USDA-NRCS, 2012).	49
Figure 2.37: Classification of rock based on SPT value by Clayton (1995).	49
Figure 2.38: Engineering properties of some British mud rocks (after Cripps and Taylor, 1981).	50
Figure 2.39: influence of water content on measured uniaxial compressive strength of synthetic	51
Figure 2.40: RQD and its relationship to other rock mass measurements (after Farmer, 1983).	51
Figure 2.41: Mixing combination of artificial soft rock.	52
Figure 2.42: Relationship between E_{50} and UCS for artificial soft rock sample (Kunasegaram et al., 2015).	53
Figure 2.43: Comparison of experimental results with centrifuge model specimens (Kunasegaram et al., 2015).	53
Figure 2.44: Stress similarity between model and prototype (Shamy et al., 2013).	55
Figure 2.45: Variation of centrifugal acceleration with radius.	56
Figure 2.46: Tokyo Tech Mark III centrifuge.	57
Figure 3.1: 2D view of model pile calibration test setup.	63
Figure 3.2: (a) Pile cap used at top (b) Pile cap used at bottom (c) Pile holder used as fixed support (d) pile socketing condition inside the support.	63
Figure 3.3 Shear strain measurement technique (a) positioning of shear strain gauge on pile (b) levelling of strain gauge wire (c) Bridge box connection.	64
Figure 3.4: Test setup (a) model setup before conducting the test (b) top view of the model setup.	65

Figure 3.5: Time series of measurement (a) pile displacement by LTDs and dial gauge (b) applied load by the load cell.	66
Figure 3.6: Typical measurements by strain gauges (a) individual bending strain at $Z/\Phi=0.25$ (b) individual bending strain at $Z/\Phi=0.5$ (c) shear strain measurement at $Z/\Phi=0.5$ and 0.75 .	66
Figure 3.7: Typical loading (a) variation of applied lateral load (P_L) with pile top displacement (δ_t) (b) variation of applied moment load M_{La} to the measured bending strain (ϵ)	67
Figure 3.8: Variation of applied bending strain with measured bending strain at different locations from the support.	68
Figure 3.9: the variation of measured shear strain with the applied load.	69
Figure 3.10: (a) Variation of extension and compression strain with applied moment load; (b) Variation of measured bending strain with applied moment load.	70
Figure 3.11: Variation of residual bending strain with applied pre-max moment load.	71
Figure 3.12: Variation of measured shear force with applied load.	72
Figure 3.13: Grain size distribution and physical properties of Toyoura sand (Dong et al. 2015).	73
Figure 3.14: Material used for the modelling of the artificial soft rock.	73
Figure 3.15: Sand and clay used in this research.	73
Figure 3.16: Screener to screen cement.	75
Figure 3.17: (a) mixing container attached to the mixing machine (b) cleaning of the periphery of the container and blade by spatula.	75
Figure 3.18: 2D view of 1g rock socketed pile loading test (a) Model 3 (b) Model 9.	76
Figure 3.19: pile cap used in (a) Model 3 (b) Model 9	77
Figure 3.20: simple model pile calibration test.	77
Figure 3.21: (a) side view of the model container with acrylic plate (b) top view of the model container with acrylic plate (c) preparation of model ground by compaction (d) preparation of mould sample for unconfined compression test.	79
Figure 3.22: Mechanical properties of model soft rock (a) Consolidated undrained triaxial test result under different confining stress (b) Relationship between secant stiffness (E_{50}) with unconfined compressive strength (UCS).	80

Figure 3.23: Pile installation process in the unconsolidated ground (a) installation of the pile with the help of a guide (b) front view of the pile (c) checking of verticality (d) installed pile in with safety plate to restrict the settlement of the pile in unconsolidated ground.	81
Figure 3.24: (a) short-range Laser Displacement Transducers (LDTs) (b) Long-range LDTs (c) strain gauge used to affix on rock surface (d) Load cell used to apply the horizontal loading.	82
Figure 3.25: (a) acrylic compaction guide (b) mechanical vibrator	83
Figure 3.26: Variation of lateral load with pile top displacement (a) Model 3 (b) Model 9.	84
Figure 3.27: observe state of rock ground after 1g model test (a) SP_SR_80 [#] (b) SP_SR_60 [#] (c) SP_SR_60 (d) SP_SR_40 [#] .	84
Figure 3.28: Variation of rock surface strain and lateral loading with normalized pile top displacement.	85
Figure 3.29: Effect of loading height and filling condition.	86
Figure 3.30: Comparison between 1g model with Kunasegaram and Takemura, 2022 50g model (a) backbone curve (b) summary of lateral load variation with rock socketing depth.	87
Figure 3.31: Comparison of accumulation of residual displacement with imposed displacement between the 1g model and 50g model.	89
Figure 3.32: Comparison of system stiffness between 1g model and 50g model.	89
Figure 4.1: 2D view of the model conditions.	93
Figure 4.2: Model CSTP wall (a) two model CSTP wall before strain gauge attachment (b) CSTP wall model with strain gauge attachment (c) arrangement of the strain gauges on the wall.	94
Figure 4.3: Variation of lateral load with the wall top displacement.	96
Figure 4.4: Variation of tensile strain, compressive strain at wall toe and lateral load at wall top with normalized wall top displacement.	97
Figure 4.5: Observed failure mechanism in the centrifuge model test.	97
Figure 4.6: Plaxis model conditions.	98
Figure 4.7: Principal total stress variation with imposed displacement.	101

Figure 4.8: Comparison of variation of lateral load with wall top displacement from FEM analysis.	102
Figure 4.9: Comparison of variation of lateral load with wall top displacement between FEM analysis and centrifuge model test.	102
Figure 4.10: Pressure distribution diagram assumed for stability analysis of CSTP wall.	103
Figure 4.11: Variation of the factor of safety with the lateral load.	104
Figure 4.12: Variation of the factor of safety with embedment depth for imposed lateral load of 200 kN/m and 600 kN/m.	104
Figure 4.13: Lpile model condition	105
Figure 4.14: (a) effect of translation and rotation on the lateral response of large diameter pile (b) assumed condition in Lpile stimulation.	106
Figure 4.15: Model 1 p-y curve.	107
Figure 4.16: Model 2 p-y curve (a) lateral (b) base shear.	107
Figure 4.17: Model 3 p-y curve (a) lateral (b) base shear.	108
Figure 4.18: Model 4 p-y curve (a) lateral (b) base shear.	108
Figure 4.19: Observed results from p-y analysis at $\delta t=1\% \Phi$ (a) bending moment (b) shear force (c) wall deflection (d) soil reaction	110
Figure 4.20: Variation of lateral load with wall top displacement from centrifuge test and p-y analysis.	111
Figure 4.21: Variation of β and $3/\beta$ value with pile diameter.	111
Figure 4.22: Effect of base shear stiffness on the lateral resistance of the wall.	112
Figure 4.23: Variation of base shear and base displacement with lateral load (a,b) base shear (c,d) base displacement.	112
Figure 5.1: 2D view of the model setup (a) Case 1 (b) Case 3 (c) Case 6 (d) Case 4 (e) Case 5.	116
Figure 5.2: Model container used (a) front view (b) top view (c) acrylic plate attached to the container back wall to reduce the container width.	117
Figure 5.3: (a) Pile holder (b) pile cap used to attach at the top (c) location of L-angle and acrylic bar.	118
Figure 5.4: Strain gauges location in single rock layer model.	119
Figure 5.5: Strain gauges location in rock with overlaying sand layer model.	119

Figure 5.6: (a) 5x5 mm mesh drawn on rock surface for image analysis (b) Model CSTP wall in rigid container and socketed into the artificial soft rock (c) Gap between the piles filled with silicon rubber.	121
Figure 5.7 (a) rubber bag without bottom rough surface (b) carbon fibre used at the bottom of the rubber bag (c) adhesive used to prepare the rubber bag (d) rubber bag with sand attached at the bottom.	122
Figure 5.8: Model container mounted on the centrifuge platform just before the test.	123
Figure 5.9 Mechanical properties of model soft rock (a) stress-strain relationship form UCT test (b) variation of E_{50} with the q_u .	124
Figure 5.10: Assumed pressure distribution diagram for stability analysis.	125
Figure 5.11: Variation of the factor of safety with the water level.	125
Figure 5.12: Loading sequence and histories followed in Cases 1, 3 and 6.	128
Figure 5.13: Typical shape of input motion in (a) Case 1 (shake 4), (b) Case 3 (shake 1) and (c) case 6 (shake 1).	129
Figure 5.14: Applied static loading by water rise (a) WR1 (b) WR2 (c) photo showing the evidence of water level during Case 1 WR1.	131
Figure 5.15: Variation of stress-strain obtained from the unconfined compression test for cases 4 and 5.	133
Figure 5.16: Variation of the factor of safety with water level for Cases 4 and 5.	133
Figure 5.17: loading sequence followed in Cases 4 and 5.	134
Figure 5.18: Typical shape of input motion in Cases 4 and case 5.	135
Figure 5.19: Measured water level during WR1 and WR2 for Cases 4 and case 5.	135
Figure 5.20: Typical example of acceleration time history measurement.	137
Figure 5.21: Variations of (a,b) amplification ratio; (c,d) phase angle; by cycles at the wall ($Z=0m$) and backfill ($Z=1.25m$): Shake 4 and Shake 11.	138
Figure 5.22: (a,b) Average amplification ratio; (c,d) average phase angle in early and late loading cycles at the wall ($Z=0m$) and backfill ($Z=1.25m$) plotted against input acceleration.	139
Figure 5.23: Amplification ratio observed at different depths of Case 1 and 3.	140

Figure 5.24: Example of measured (a,e) wall top displacement; (b,f) bending moment at $Z=10.75\text{m}$; (c,g) lateral pressures at $Z=11.25\text{m}$; (d,f) lateral pressure at $Z=2\text{m}$; with the kinematic components during shaking and the long-term variation after shake 4 Case 1.	141
Figure 5.25: Example of measured (a,e) wall top displacement; (b,f) bending moment at $Z=10.75\text{m}$; (c,g) lateral pressures at $Z=11.25\text{m}$; (d,f) lateral pressure at $Z=2\text{m}$; with the kinematic components during shaking and the long-term variation after shake 1 Case 3.	142
Figure 5.26: Example of measured (a,e) wall top displacement; (b,f) bending moment at $Z=11.25\text{m}$; (c,g) lateral pressures at $Z=11.75\text{m}$; (d,f) lateral pressure at $Z=1.75\text{m}$; with the kinematic components during shaking and the long-term variation after shake 1 Case 4.	143
Figure 5.27: Example of measured (a,e) wall top displacement; (b,f) bending moment at $Z=9.0\text{m}$; (c,g) lateral pressures at $Z=9.75\text{m}$; (d,f) lateral pressure at $Z=2.25\text{m}$; with the kinematic components during shaking and the long-term variation after shake 1 Case 5.	145
Figure 5.28: Time history of wall displacement measured by LDT and back calculated from acceleration of Case 1 (a,b) Shake 4 (c,d) Shake 11.	146
Figure 5.29: Comparison between dynamic wall displacement obtained from LDT and back calculated from acceleration (a) Shake 4 (b) Shake 11.	147
Figure 5.30: Relationships between the wall top displacement (a,b) total earth pressure at $Z=11.25\text{m}$; (c,d) total earth pressure at $Z=2.0\text{m}$; (e,f) bending moment at $Z=10.75\text{m}$ (g,h) dynamic component of earth pressure: Shake 4 and Shake 11.	148
Figure 5.31: Total lateral pressure distribution with depths (a) Case 1 shake 4 (b) Case 3 shake 1 (c) Case 6 shake 1.	149
Figure 5.32: Lateral pressure distribution with depths (a) Case 4 (b) Case 5.	150
Figure 5.33: Variation of measured Lateral pressure and calculated effective earth pressures with the wall top displacements in the entire loading history from Case 1.	150
Figure 5.34: Variation of measured Lateral pressure and calculated effective earth pressures with the wall top displacements in the entire loading history from Case 3.	151
Figure 5.35: Effective earth pressure ratio of Case 1 (a) variation of effective earth pressures with wall displacements measured for the entire loading history of Case 1 (b-c) effective earth pressure ratios distribution with depth.	152

Figure 5.36: Effective earth pressure ratio of Case 3 (a) variation of effective earth pressures with wall displacements measured for the entire loading history of Case 3 (b) effective earth pressure ratios distribution with depth.	153
Figure 5.37: Comparison of lateral pressure and effective earth pressure at $Z=2\text{m}$ and 11.25m of Case 1 ($d_r=3.0\text{m}$) and Case 3 ($d_r=2.5\text{m}$).	154
Figure 5.38: (a) method to calculate resultant thrust force and location of resultant thrust force; (b) Variation of normalized resultant thrust force with the wall top displacement.	155
Figure 5.39: Variation of location of total and effective resultant thrust force with the wall top displacement.	156
Figure 5.40: The variation of maximum lateral pressure with input acceleration.	157
Figure 5.41: Bending moment distribution with depths (a) Case 1 shake 4 (b) Case 3 shake 1 (c) Case 6 shake 1.	158
Figure 5.42: Variations of measured bending moment at different depths with the wall top displacement from Case 1.	159
Figure 5.43: Variations of measured bending moment at different depths with the wall top displacement from Case 3.	160
Figure 5.44: Variation of moment with wall top displacement from Case 1 and 3 (a) bending moment at $Z=10.75\text{m}$ (b) moment load.	161
Figure 5.45: Variation of moment loads with series of loadings (a,b) Case 1 (c) Case 1&3 comparison.	162
Figure 5.46: Variation of kinematic component of wall top displacement with arias intensity.	163
Figure 5.47: (a) Variation of wall displacement with input acceleration; (b) variation of wall displacement with cumulative arias intensity	164
Figure 5.48: Variation of wall top displacement with water level.	165
Figure 5.49: (a) variation of wall top displacement with cumulative arias intensity (b) wall and ground condition after tests.	167
Figure 5.50: Variation of wall top displacement with the cumulative arias intensity.	167
Figure 5.51: Variation of wall top displacement increment with the arias intensity during dynamic loading.	168
Figure 5.52: Variation of amplification ratio of Cases 1, 3 and 4.	169

Figure 5.53: Variation of wall top displacement with water level of Cases 1, 3 and 4.	169
Figure 5.54: Variation of effective earth pressure ratio of Case 1, 3 and 4.	171
Figure 5.55: Variation of effective earth pressure with wall displacement of Case 1, 3 and 4.	172
Figure 5.56: Variation of normalized effective thrust force with normalized wall top displacement.	172
Figure 5.57. Schematic diagram to explain the mechanism of resilience effect.	173
Figure 5.58: Wall deflection variation (a) Case 1 ($d_r=3.0\text{m}$) (b) Case 3 ($d_r=2.5\text{m}$).	174
Figure 5.59: Different components contributing to the wall deflection.	175
Figure 5.60: An example of qualitative bending moment distribution with depths (a) Case 1 ($d_r=3.0\text{m}$) and (b) Case 3 ($d_r=2.5\text{m}$).	176
Figure 5.61: Wall deflection profile (a) Case 1 ($d_r=3.0\text{m}$) (b) Case 3 ($d_r=2.5\text{m}$).	177
Figure 5.62: (a) Variation of different displacement components with wall top displacement (b) contribution of different components to the wall top displacement.	177
Figure 5.63: Variation of the principal total stress (a,b) without backfill (c,d) with backfill.	180
Figure 5.64: Variation of the shear strain (a,b) without backfill (c,d) with backfill.	181
Figure 5.65: Variation of long-term residual component of wall top displacement, lateral pressures and bending moment with time for Case 1 (a) Shake 4; (b) Shake 11; (c) First water rise; (d) Second water rise.	182
Figure 5.66: Variation of long-term residual component of wall top displacement, lateral pressures and bending moment with time for Case 3 (a) Shake 1; (b) Shake 4; (c) First water rise; (d) Second water rise.	183
Figure 5.67: Schematic diagram for the mechanism behind the creep.	183
Figure 5.68: Increment during loading and long-term during dynamic loading from case 1 (Case 1) (a) wall top displacement (b) bending moment at $Z=10.75\text{m}$ (c) lateral pressure at $Z=11.25\text{m}$ (d) lateral pressure at $Z=2.0\text{m}$	184
Figure 5.69: Increment during loading and long-term during dynamic loading from case 3 (Case 3) (a) wall top displacement (b) bending moment at $Z=10.75\text{m}$ (c) lateral pressure at $Z=11.25\text{m}$ (d) lateral pressure at $Z=2.0\text{m}$	185

Figure 5.70: Ratio of long-term increment to the increment during shaking (a) wall top displacement (b) bending moment at $Z=10.75\text{m}$ (c) lateral pressure at $Z=11.25\text{m}$ (d) lateral pressure at $Z=2.0\text{m}$.	186
Figure 5.71: Long-term increment in wall top displacement after static loading.	187
Figure 5.72: Wall deflection obtained from p-y analysis (a,b) Case 1:dr=3.0m (c,d) Case 3:dr=2.5m	189
Figure 5.73: Wall bending moment distribution obtained from p-y analysis (a,b) Case 1:dr=3.0m (c,d) Case 3:dr=2.5m	190
Figure 5.74: Wall shear force distribution obtained from p-y analysis (a,b) Case 1:dr=3.0m (c,d) Case 3:dr=2.5m	191
Figure 5.75: Soil reaction profile obtained from p-y analysis (a,b) Case 1:dr=3.0m (c,d) Case 3:dr=2.5m.	192
Figure 5.76: Predictability of residual wall displacement after dynamic loading by bi-linear p-y curve.	193
Figure 5.77: Predictability of dynamic wall displacement by bi-linear p-y curve.	194
Figure 5.78: Variation of plastic deformation or yielding of rock with moment load.	195
Figure 5.79: Variation of normalised base shear stress with moment load.	196
Figure 5.80: Applicability of using design active and at-rest pressure to predict wall displacement after dynamic loading.	197

List of Tables

Table 2.1: Deformation modulus (E_0) and (α)	15
Table 2.2: Allowable displacement based on performance	15
Table 2.3: Constant ‘m’ and ‘n’ used by different researchers	17
Table 2.4: List of some common types of soft rock	47
Table 2.5: Scaling law followed in geotechnical centrifuge modelling.	55
Table 2.6: Key specification of Tokyo Tech Mark III centrifuge	57
Table 3.1. Test conditions and the properties of 1g model pile	78
Table 4.1: Model and test conditions	95
Table 4.2: Properties of 2D plate used in the numerical model	99
Table 4.3: Properties of soil used in the numerical model	99
Table 4.4: Parameters used to calculate horizontal subgrade modulus	106
Table 4.5: List of spring stiffness (k_H), ultimate resistance (p_{ult}) and critical deflection (y_c) of model 1, 2, 3 and 4	109
Table 5.1: Physical properties of model soft rock	120
Table 5.2. Test conditions and material properties of single rock layer cases	126
Table 5.3. Observed frequency of wall and backfill top by white noise from Case 1	130
Table 5.4: Observed frequency of wall and backfill top by white noise from Case 3	130
Table 5.5. Test conditions and material properties of rock with overlaying sand layer cases	132
Table 5.6 Variation of the factor of safety with and without backfill condition	178
Table 5.7: Parameters used to define sand layers	179
Table 5.8: Parameters used to calculate horizontal subgrade modulus of Model-1	188

Chapter 1

Introduction

1.1 General:

The application of Cantilever type Steel Tubular Pile (CSTP) walls (Figure 1.1) as permanent or temporary retaining structures has increased in recent decades (Gaba et al., 2017). Typically, the application of cantilever-type sheet pile walls is limited to moderate retained heights in relatively soft foundation conditions due to various limitations associated with the soil, structure, and soil-structure interaction (JARA 1999; AIJ, 2001; Madabhushi and Chandrasekaran, 2005). rapid urbanization and infrastructure development near mountainous sites often require taller cantilever-type retaining walls due to space constraints or anchoring complexities. The recent advancements in technology, like the rotary cutting press-in technique (as shown in Figure 1.2), have made it possible to install large-diameter steel tubular piles even in hard ground conditions such as rock, gravel, and even concrete, as shown in. (Kitamura and Kitamura, 2018; Miyanochara et al., 2018; Matsuzawa et al., 2021). Although technology has advanced, the current design guidelines are not well rationalized to consider the specific features of the wall, like a very large stiffness wall embedded in stiff ground. Therefore, the engineers and researchers raise several concerns about applying the CSTP wall into stiff ground.

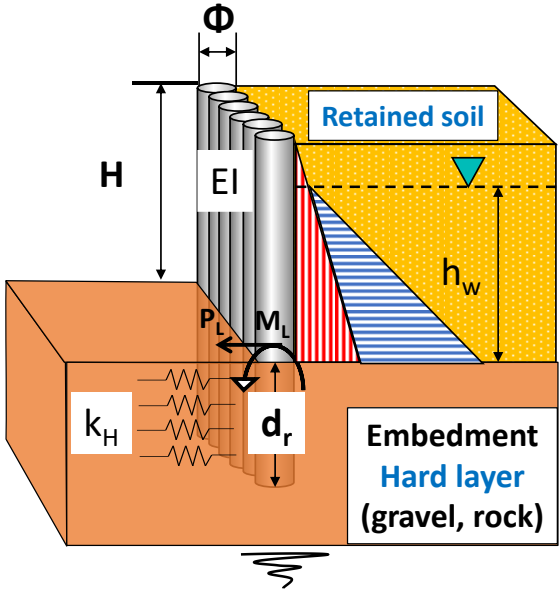


Figure 1.1: Cantilever retaining walls.

1.2 Problem Statement:

There are two main concerns when using large-height cantilever walls as permanent structures. First, significant displacements are caused by wall bending and deflection (translation and rotation) in the embedded soil, which exponentially increases with the retaining height. Second, the lack of structural supports such as tie-back plates or ground anchors reduces the redundancy of the structure. While high-stiffness walls can reduce bending deformation, they require a large embedment depth to control wall deflection within allowable limits in soft ground (Powrie, 1996). Conversely, wall deflection can be significantly reduced in relatively hard mediums such as soft to hard rocks.

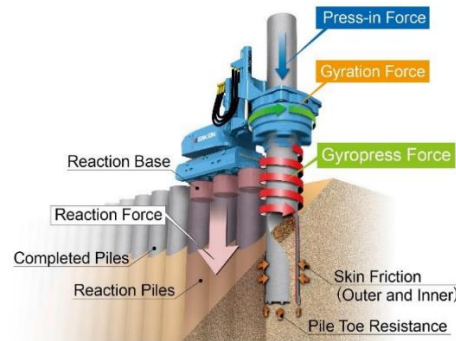


Figure 1.2: Rotary cutting press-in technique (Gyro piler) (Kitamura and Kitamura, 2018).



Figure 1.3: Application of cantilever-type steel tubular pile walls (Miyanojara et al., 2018).

However, the design of Cantilever type Steel Tubular Pile (CSTP) walls in relatively hard mediums still lacks specific guidelines (Takemura, 2021). The current design methods rely on the theory of

beams on elastic foundation, where the required minimum embedment depth increases with the flexural rigidity of the wall, regardless of types of lateral loads (simple earth pressure in normal conditions or in extreme conditions like buildup of water pressure due to poor drainage, earthquake or the combination of both) and retained height (JTASPP-ACTC, 2007). Another concern is the local and 3D behaviour of the steel tubular pile wall compared to conventional 2D walls. Also, the heterogeneity of the embedment condition needs to be considered when constructing a CSTP wall in stiff ground like soft rock, as the shallow rock layer may deteriorate by the construction process, providing no to small lateral resistance to the wall. Furthermore, using a simple bi-linear p-y curve to predict the wall behaviour, especially after seismic loading, needs to be thoroughly investigated for CSTP walls embedded in stiff ground. In addition, the long-term behaviour of the large retain height CSTP wall should be studied. Although the current design technique covers all the concerns related to design, this can significantly overestimate the embedment depth and overall cost of applying CSTP wall in the hard medium.

1.3 Goals and Objectives:

The main goal of this research is to investigate the stability of CSTP walls embedded in soft rock subjected to various loads and provide some appraisal of the rationalization of the design method.

To achieve this goal, several detailed objectives have been defined as follows:

1. To develop a centrifuge model for the CSTP wall embedded in soft rock or soft rock with overlaying sand subjected to various loadings.
2. To investigate the deformation and failure behaviour of CSTP wall embedded in soft rock or rock with overlaying sand subjected to sequential dynamic and static loading.
3. To select a suitable lateral resistance (p-y) curve to stimulate the behaviour of the CSTP wall embedded in soft rock subjected to various loadings.
4. Through objectives 1 to 3, provide some prediction to rationalize the current design method of CSTP wall embedded in stiff ground like soft rock subjected to various loadings.

1.4 Scope and Challenges:

This research focuses specifically on applying cantilever-type steel tubular pile (CSTP) walls in soft rock. Although various alternative methods and materials can be used to construct cantilever walls, this study narrows down the investigation to large-diameter CSTP walls in soft rock. Also, the actual construction process includes several construction stages. The wall behaviour depends on those construction stages. However, in this study, the investigation of the wall behaviour is limited to the construction stage of the CSTP wall after excavation.

Different modelling and testing approaches can be utilized to investigate the behaviour of the CSTP walls. The three most common approaches are real field tests, numerical, and physical modelling. In the actual field, conditions pose challenges due to their diverse and complex nature, influenced by factors like discontinuities, fissures, and cavities. Conducting load tests to study the behaviour of CSTP walls under different deformations is not feasible in the actual field, and the associated costs are high. Furthermore, the mechanical properties of the embedment medium vary between locations, making it challenging to develop generalized design guidelines. On the other hand, numerical simulation offers advantages over experiments, allowing for a wide range of analyses by adjusting the strength and stiffness of the embedded medium to account for discontinuities, fissures, and degradation of soft rock materials. However, numerical models have limitations in capturing the actual behaviour of rock-wall interactions, nonlinear deformations of embedded mediums, local deformations, failure modes of both the structure (tubular pile walls) and rock, and time-dependent characteristics like creep.

Considering the limitations of real field tests and numerical modelling, this study uses physical modelling by using a geotechnical centrifuge. The geotechnical centrifuge modelling provides several advantages. Centrifuge modelling offers the possibility of achieving stress similarity between a model and a prototype, allowing for the modelling of rock-wall interaction under similar confining pressures. This approach enables the study of time-dependent deformation characteristics, such as creep, at a scale of the model-to-prototype ratio of 1:1. Additionally, the long-term consolidation behaviour, with a model-to-prototype ratio of $1:N^2$, can be simulated in a shorter period by utilizing centrifugal acceleration. Several challenges are associated with the geotechnical centrifuge modelling of soft rock. Commonly, synthetic soft rock models are used for experimental investigations, proving their ability to replicate the stress-strain behaviour of natural

soft rocks. These models allow for parametric studies and provide uniform conditions for advanced experimental investigations and the characterization of embedded medium. However, they cannot capture non-uniformities and discontinuities present in actual field conditions. Therefore, a combination of field investigations, numerical analysis, and physical modeling is recommended to change the design guidelines.

1.5 Organization of the Dissertation

Figure 1.4 shows the orientation of the dissertation. The dissertation is organised into six chapters. A summary of each chapter is given below:

Chapter 1 (Introduction): This chapter discusses the motivation, problem statement, scope and challenges related to this research.

Chapter 2 (Literature review): This chapter includes the necessary literature review related to cantilever-type retaining walls, the current design method, the failure history of the cantilever retaining wall, the lateral resistance of the pile in different ground conditions, and centrifuge modelling of the cantilever retaining wall.

Chapter 3 (Mechanical behaviour of laterally loaded single pile socketed in soft rock): This chapter includes the method of preparation of artificial soft rock and pre-study related to critical parameters like mechanical properties of the model pile, soft rock and the lateral response of the pile socketed in the rock layer.

Chapter 4 (Lateral response of large diameter Cantilever type Steel Tubular Pile wall (CSTP) wall embedded in soft rock subjected to one-way cyclic loading): This chapter includes the investigation of lateral resistance of the CSTP wall by utilizing analytical tools like Lpile software. Finally, from this chapter, the lateral resistance (p-y) curve, which is used to investigate the complex CSTP wall model discussed in Chapter 5, is studied.

Chapter 5 (Centrifuge modeling of large diameter Cantilever type Steel Tubular Pile wall (CSTP) wall embedded in soft rock subjected to sequential dynamic and static loadings): This chapter includes the modelling technique of the CSTP wall embedded into soft rock subjected to sequential

dynamic and static loadings. Discuss the limitations and challenges of the modelling technique and the observed typical behaviour of the CSTP wall based on the test conditions.

Chapter 6 (Conclusions and recommendations): This chapter includes the conclusions from this research and provides some future recommendations.

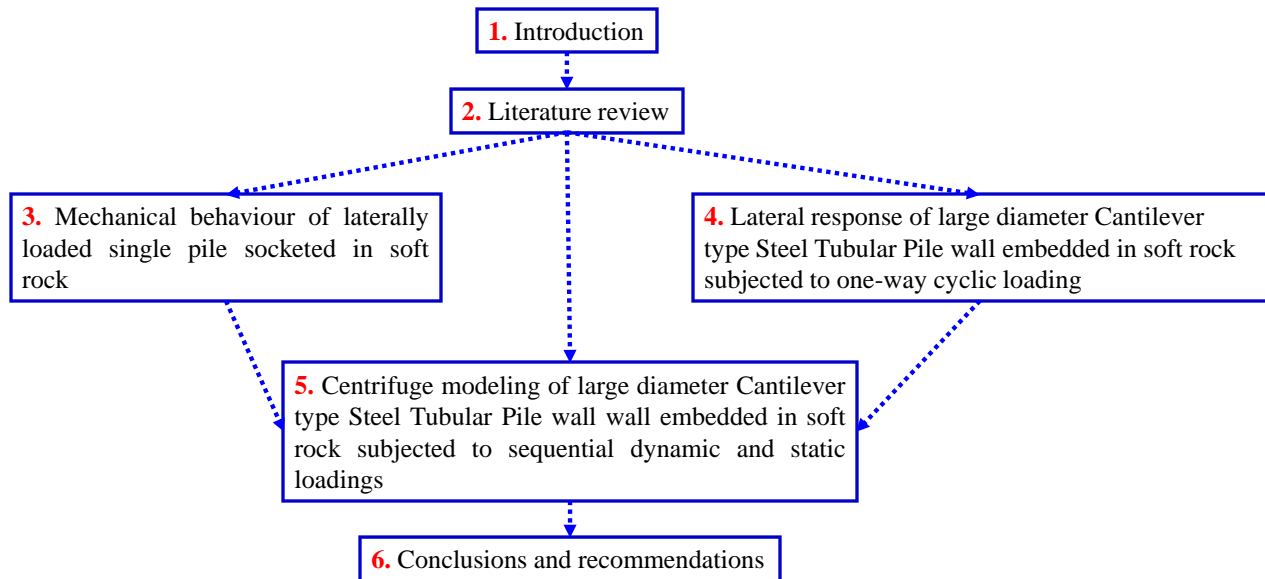


Figure 1.4 : Orientation of the dissertation.

References:

1. Architectural Institute of Japan (AIJ). 2001. Design Recommendations for Architectural Foundation.
2. Gaba, A., Hardy, S., Doughty, L., Powrie, W. and Selemetas, D., 2017. *Guidance on embedded retaining wall design*. London, UK: Ciria.
3. Gopal Madabhushi, S.P. and Chandrasekaran, V.S., 2005. Rotation of cantilever sheet pile walls. *Journal of geotechnical and geoenvironmental engineering*, 131(2), pp.202-212.
4. Japan Road Association (JARA). 1999. Guideline of road works and temporary structures.

5. Japanese Technical Association for Steel Pipe Piles and Advanced Construction Technology Center (JTASPP-ACTC) 2007. *Cantilever Steel Piles Retaining Wall-Design Manual*: 138p. (in Japanese).
6. Kitamura, M. and Kitamura, S., 2018. Cantilevered Road Retaining Wall Constructed of 2,000 mm Diameter Steel Tubular Piles Installed by the Gyro Press Method with the GRB System. In *First International Conference on Press-in Engineering* (pp. 437-444).
7. Matsuzawa, K., Hayashi, T. and Shirasaki, K., 2021, June. Construction of retaining wall for river disaster restoration by Gyropress Method. In *Proceedings of the Second International Conference on Press-in Engineering 2021, Kochi, Japan* (pp. 474-481). CRC Press.
8. Miyanohara, T., Kurosawa, T., Harata, N., Kitamura, K., Suzuki, N. And Kajino, K., 2018. Overview of the self-standing and high stiffness tubular pile walls in Japan. In *Proceedings of the International Conference on Press-in Engineering First International Conference* (pp. 167-174). International Press-in Association.
9. Powrie, W., 1996. Limit equilibrium analysis of embedded retaining walls. *Geotechnique*, 46(4), pp.709-723.
10. Takemura, J., 2021, June. State of the art report on application of cantilever type steel tubular pile wall embedded to stiff grounds. In *Proceedings of the Second International Conference on Press-in Engineering 2021, Kochi, Japan* (pp. 27-41). CRC Press.

Chapter 2

Literature review

2.1 Introduction:

To gain a comprehensive understanding of the complex behavior of CSTP walls, it is crucial to explore the design principles behind cantilever retaining walls, the various modelling techniques to investigate the behaviour of cantilever retaining walls, and the anticipated lateral response of the wall under various loading conditions. Extensive literature exists on the subject, and this chapter provides a summary of the relevant literature related to this research.

2.2 Design and Stability of Cantilever retaining wall:

A typical design chart followed by IPA to construct a steel tubular earth retaining structure is shown in Figure 2.1. The first step in the design process includes the selection of design loads. So, a proper estimation of the design loads is one of the crucial conditions for the proper design of the wall. Once the design loads are determined, adequate stability analysis should be conducted to determine the embedment depth. This article discusses the different design loads acting on the wall and the stability analysis that can be carried out to design the cantilever earth retaining structure.

2.2.1 Design loads acting on the cantilever retaining wall:

Under static loading:

A Mohr diagram, as shown in Figure 2.2 (b), is used to represent the states of stress at a specific underground point. The initial vertical and horizontal stresses are denoted as σ_v and σ_h , respectively, as shown in Figure 2.2 (a). The active failure state occurs when the horizontal effective stress decreases until it becomes tangent to the failure envelope. This state is represented by σ_a . The passive failure state occurs when the horizontal effective stress increases until failure occurs, represented by σ_p .

The earth pressures exerted against a wall are directly related to the movements of the wall. The relationship between wall movements and earth pressures is depicted in Figure 2.3. Initially, when a wall is placed into a sand deposit without causing any disturbance, it experiences the in-situ stresses of the soil. The soil pressure against a unit area of the wall at a depth Z below the groundline can be calculated using Equation 2.1. The lateral earth pressure, P_o , corresponds to zero deflection of the wall and is represented by a point on the vertical axis in Figure 2.3. As the wall is deflected in the backward direction, the pressure on the left face of the wall increases until it reaches the limiting value, which can be represented by Equation 2.2. Conversely, the pressure on the wall decreases while moving forward until it reaches the limiting value, which can be represented by Equation 2.3.

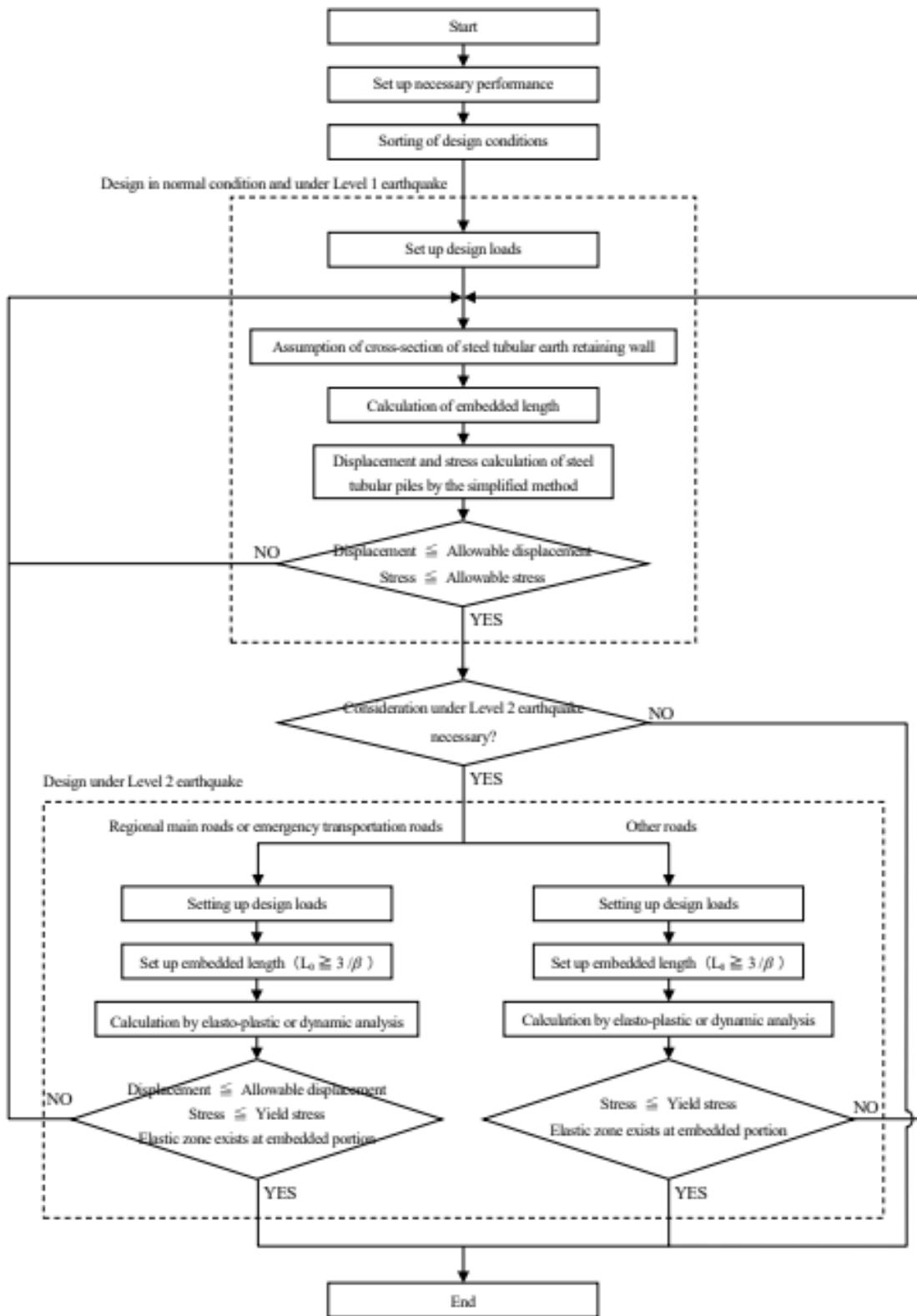


Figure 2.1: Flow performance verification of steel tubular earth retaining structure (IPA handbook, 2016).

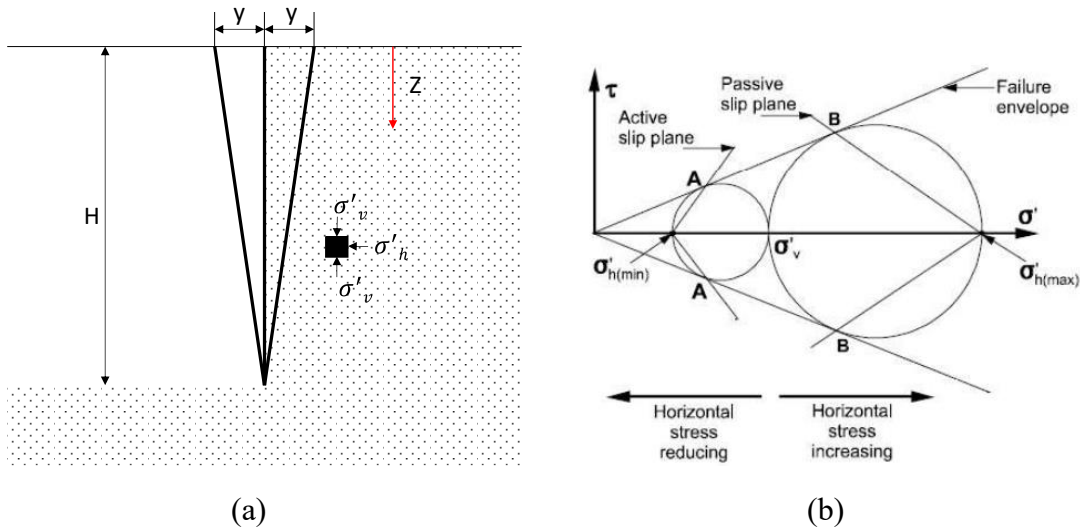


Figure 2.2: States of the stress of active and passive conditions (a) Stress and pressure of soil element on wall (b) Mohr diagram (PYwall Technical Manual, 2022).

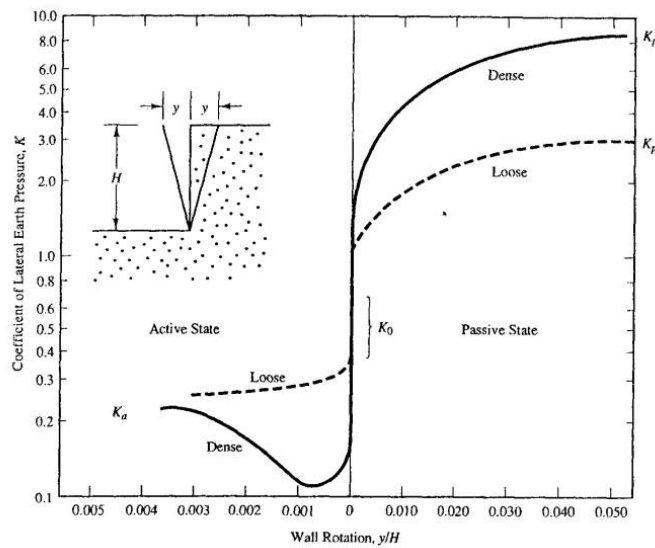


Figure 2.3: Qualitative lateral pressure variation with wall movement (PYwall Technical Manual, 2022).

$$\sigma_o = K_0 \gamma Z \dots \dots \dots \text{Equation 2.1}$$

$$\sigma_p = K_p \gamma Z \dots \dots \dots \text{Equation 2.2}$$

$$\sigma_a = K_a \gamma Z \dots \dots \dots \text{Equation 2.3}$$

Where,

σ_o : 'at rest' lateral pressure

σ_p : passive lateral pressure

σ_a : active lateral pressure

K_o : coefficient of 'at rest' pressure

K_p : coefficient of 'passive' pressure

K_a : coefficient of 'active' pressure

γ : unit weight of soil

Z : distance below ground surface

The total active and passive thrust force can be calculated following Coulomb's theory by Equations 2.4 and 2.5.

$$P_a = \left(\frac{1}{2}\right)K_a\gamma H^2 - 2c\sqrt{K_a}H \dots \dots \dots \text{Equation 2.4}$$

$$P_p = \left(\frac{1}{2}\right)K_p\gamma H^2 + 2c\sqrt{K_p}H \dots \dots \dots \text{Equation 2.5}$$

The coefficient of lateral earth pressure can be calculated by Coulomb's theory (Equation 2.6-2.7) or by Jack's Equation (Equation 2.8-2.9)

$$K_a = \tan^2\left(45^\circ - \frac{\phi}{2}\right) \dots \dots \dots \text{Equation 2.6}$$

$$K_p = \tan^2\left(45^\circ + \frac{\phi}{2}\right) \dots \dots \dots \text{Equation 2.7}$$

$$K_a = \frac{1-\sin\phi}{1+\sin\phi} \dots \dots \dots \text{Equation 2.8}$$

$$K_p = \frac{1+\sin\phi}{1-\sin\phi} \dots \dots \dots \text{Equation 2.9}$$

Under Dynamic loading:

In the case of dynamic loading, for sandy soil, the coefficient of active seismic earth pressure K_{EA} can be calculated based on the pseudo-static approach given by the Mononobe-Okabe method, as shown in Equation 2.10. The coefficient of active seismic earth pressure K_{EA} is calculated, assuming $\sin(\phi - \theta) = 0$ for $(\phi - \theta) < 0$.

$$K_{EA} = \frac{\cos^2(\phi-\theta)}{\cos\theta \cos(\delta+\theta) \left(1 + \sqrt{\frac{\sin(\phi+\delta) \sin(\phi-\theta)}{\cos(\delta+\theta)}}\right)^2} \dots \dots \dots \text{Equation 2.10}$$

The total dynamic active thrust force (P_{EA}) can be calculated by using the equation 2.11

$$P_{EA} = \frac{1}{2} \cdot \gamma_d \cdot H^2 \cdot (1 - k_v) \cdot K_{EA} \dots \dots \dots \text{Equation 2.11}$$

Where,

K_{EA} : coefficient of active earth pressure by Coulomb's earth pressure

θ : the synthesized angle at the time of the earthquake,

$$\theta = \tan^{-1}(k_h) \text{ or } \theta = \tan^{-1}(k_h')$$

k_h : design horizontal seismic intensity

k_h' : apparent seismic intensity

$$k_h' = \frac{\gamma_{sat}}{\gamma_{sat} - \gamma_w} k_h \dots \dots \dots \text{Equation 2.12}$$

ϕ : angle of shear resistance of soil ($^\circ$)

δ : friction angle between the wall surface and soil ($^\circ$) [Typically recommended 15° (IPA Handbook, 2016) if not determined or assumed as $2/3$ of ϕ Ichihara (1983)]

Seed and Whitman (1970) proposed placing P_{EA} at a height of $0.6H$ above the base of the wall. However, recent experiments show that P_{EA} is applied slightly lower, and its location depends on the wall movement mode. Figure 2.4 displays measured values of the application point of the total P_{EA} for different wall movement modes. The data suggests that P_{EA} is typically applied between $0.45H$ and $0.55H$ from the base of the wall depending on the wall movement, as indicated in Figure 2.4.

Soil and water pressure of submerged soil Matsuzawa et al., (1985):

For highly permeable backfill soil, it is assumed that pore water can move freely within the soil without any hindrance from the soil particles. The calculations involve determining the vertical body force (F_V) and horizontal inertial body force (F_H) acting on the soil during an earthquake. Equation 2.13 allows the calculation of the apparent seismic intensity, denoted as θ' , for highly permeable backfill soil.

$$\tan\theta' = \frac{F_H}{F_V} = \frac{G_s k_h}{(G_s - 1)(1 \pm k_v)} \dots \dots \dots \text{Equation 2.13}$$

A different definition of the apparent seismic coefficient is used in the case of backfill soil with low permeability, which is denoted by Equation 2.14

$$\tan\theta'' = \frac{F_H}{F_V} = \frac{\gamma_{sat} k_h}{(\gamma_{sat} - \gamma_w)(1 \pm k_v)} \dots \dots \dots \text{Equation 2.14}$$

Equation 2.11 should be modified based on Equations 2.13 and 2.14 in case of submerged soil.

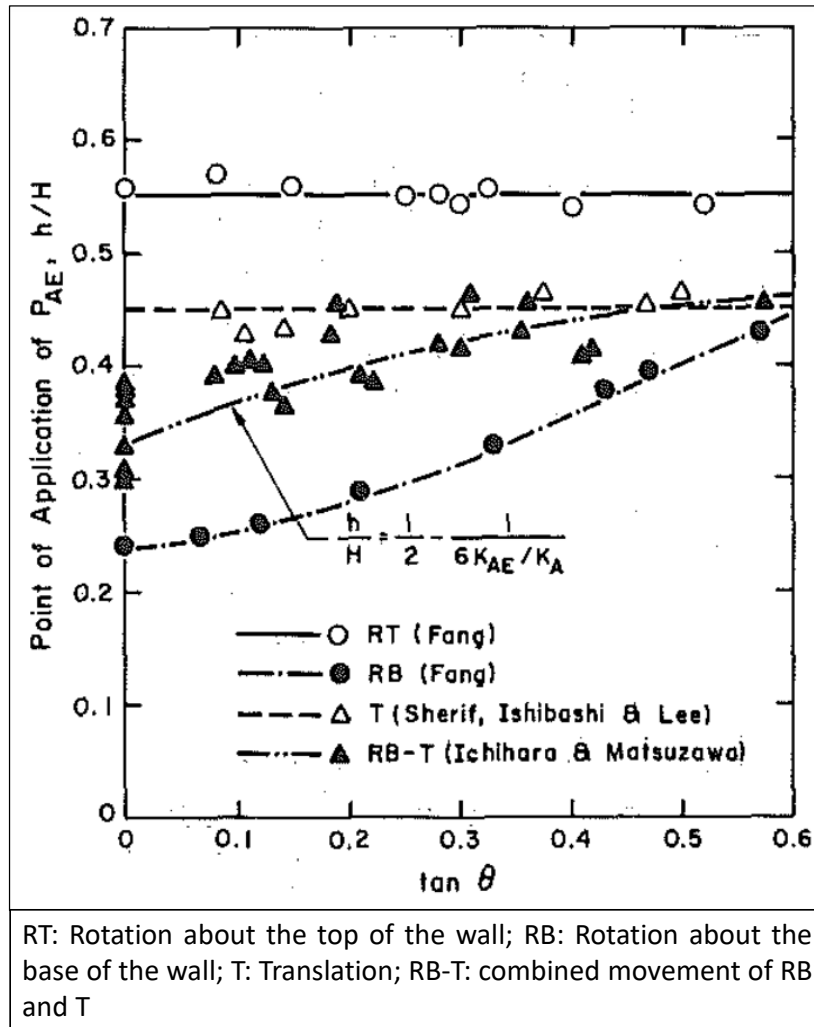


Figure 2.4: Measured point of applications of total dynamic active thrust force (Matsuzawa et al., 1985).

Westergaard developed a solution for calculating hydrodynamic water pressure on vertical walls during horizontal earthquake ground motions. The solution considers parameters such as the horizontal seismic coefficient (k_h), water depth (x), total water depth (H_w), ground vibration period (T), and water compressibility (E_w). Westergaard provided approximate formulas for estimating the distribution of dynamic water pressure (p_{wd}) along the wall and the resultant dynamic water pressure (P_{wd}), as shown in Equations 2.15 and 2.16, respectively.

$$p_{wd} = \frac{7}{8} k_h \gamma_w \sqrt{H_w x} \dots \dots \dots \text{Equation 2.15}$$

$$P_{wd} = \frac{7}{12} k_h \gamma_w H_w^2 \dots \dots \dots \text{Equation 2.16}$$

In the approximate solution, the location of the resultant water pressure is at $0.4H$ above the base of the reservoir.

2.2.2 Calculation of embedment depth

When constructing cantilever-type embedded retaining structures, it is crucial to ensure that the stress and deformation occurring in the wall structures remain within acceptable limits. Moreover, it is essential to maintain the overall stability of the surrounding ground. Additionally, if required, it is important to assess any potential impacts on neighbouring structures.

The determination of the horizontal coefficient of subgrade reaction (k_H) should be based on a thorough evaluation of ground investigations and soil tests. This value is essential in performing structural calculations, including simplified and elasto-plastic methods. It is important to note that the calculation of k_H may vary depending on the specific standards or specifications applied. Therefore, it is crucial to calculate k_H in accordance with the relevant standards or specifications that pertain to the specific structure under consideration.

$$k_H = k_{H0} \left(\frac{B_H}{B_{ref}} \right)^{-3/4} \dots \dots \dots \text{Equation 2.17}$$

$$k_{H0} = \frac{1}{B_{ref}} \alpha E_0 \dots \dots \dots \text{Equation 2.18}$$

Where,

k_H : lateral coefficient of ground reaction force (kN/m³)

B_H : equivalent loading width (m)

k_{H0} : lateral coefficient of ground reaction force corresponding to the value of plate loading test using a stiff circular disc with a diameter of B_{ref} (kN/m³)

B_{ref} : reference loading width (= 0.3m)

E_0 : deformation modulus of ground(kN/m²)

α : coefficient used to estimate the coefficient of ground reaction force

The recommended testing method to determine the deformation modulus (E_0) of the ground and the corresponding value of α are shown in Table 2.1

When dealing with structures that have extensive spans, such as steel tubular earth retaining walls, the equivalent loading width B_H was established as 10 m, as specified in the "Highway Earthworks, Temporary Structure Works Guideline). It is important to note that if the actual loading width is less than 10 m, that value is used instead. Furthermore, in the event of liquefaction caused by seismic activity, the calculation of the horizontal coefficient of subgrade reaction force should follow an appropriate standard or guideline, considering the reduction in the coefficient that must be taken into account.

It is necessary to establish an appropriate allowable displacement that ensures the fulfilment of the performance requirements for a steel tubular retaining wall. This is crucial for maintaining the stability of the steel tubular earth retaining wall and effectively managing the deformation of the ground located behind it. The allowable displacement based on the performance is given in Table 2.2

Table 2.1: Deformation modulus (E_0) and (α)

Deformation modulus (E_0) by the following testing methods (kN/m^2)	Value of α	
	Normal condition	At earthquake
1. Half of the deformation modulus obtained from the hysteresis curves of the plate loading test using a stiff disc with a diameter of 0.3 m	1	2
2. Deformation modulus measured in the borehole	4	8
3. Deformation modulus obtained from uniaxial or triaxial compression tests on specimens	4	8
4. Deformation modulus obtained as $2,800 \times N$ (kN/m^2) where N is the SPT N-value	1	2

Table 2.2: Allowable displacement based on performance

Performance 1	Normal load	Lateral displacement of steel tubular pile on the design ground surface < 15 mm, and lateral displacement at the steel tubular pile top < 1.0 % of wall height.
	Level 1 earthquake	Lateral displacement of steel tubular pile on the design ground surface < 15 mm, and lateral displacement at the steel tubular pile top < 1.5 % of wall height.
Performance 2	Level 2 earthquake	Lateral displacement of the steel tubular earth retaining wall top < 300 mm.
Performance 3	Level 3 earthquake	

Where the performances are categorized as:

Performance 1: Soundness as the retaining wall, including surrounding facilities by the assumed loads, is not harmed, and its function is not hindered.

Performance 2: Damage on the surrounding facilities due to assumed loads is limited, and the repair to restore function as the retaining wall can be carried out relatively easily.

Performance 3: Damage due to assumed loads does not become as fatal as the retaining wall.

The calculation of the embedment depth can be determined by two methods. Method 1: which is based on Chang's equation (Simplified method); Method 2: which is based on elasto-plastic method.

Method 1: Simplified method

In Chang's method (1937), an embedded length larger than $3/\beta$ is considered semi-infinite, and it is thought that the effect of the non-fixed tip of a steel tubular pile appears when the embedded length is shorter than $3/\beta$.

$$L_o \geq 3/\beta \dots \dots \dots \text{Equation 2.19}$$

Where,

L_o : embedded length (m)

β : characteristic value of pile (m^{-1})

$$\beta = \sqrt[4]{\frac{k_H \cdot B}{4EI}} \dots \dots \dots \text{Equation 2.20}$$

k_H : lateral coefficient of ground reaction force (kN/m^3). Usually, the average value of those in each layer within a range of $1/\beta$, given by Equation 2.20

B : width of steel tubular earth retaining wall. Unit width of 1m

E : Young's modulus of steel tubular earth retaining wall (kN/m^2)

I : second moment of area of steel tubular earth retaining wall per unit width (m^4)

As shown in Figure 2.5, in the simplified method, the soil below the excavation level is replaced by spring (based on the so-called 'Winkler' foundation) with a spring constant of k_H determined by Equation 2.17.

The elastic horizontal reaction force, p , at different depths can be determined by Equation 2.21.

$$p = k_H \cdot x^m y^n \dots \dots \dots \text{Equation 2.21}$$

Where,

p : elastic horizontal reaction force (kN/m)

k_H : lateral coefficient of ground reaction force (kN/m^3).

x : depth below the excavation level (m)

y : Lateral deflection of the retaining wall (m)

The constant ‘m’ and ‘n’ represent the subgrade condition. For example, $m > 0$ indicates the depth effect, and $1 > n > 0$ provides the stress strain characteristics of the soil. As shown in Table 2.3, different researchers used different ‘m’ and ‘n’ constants to investigate the subgrade reaction.

Table 2.3: Constant ‘m’ and ‘n’ used by different researchers

Researchers	m	n
Chan (1937)	0	1
Row (1956)	1	1
Terzaghi (1955)	1	1
Reese-Matlock (1960)	1	1
Rifaat (1935)	1	$n \neq 0$
Kubo (1964)	1	0.5

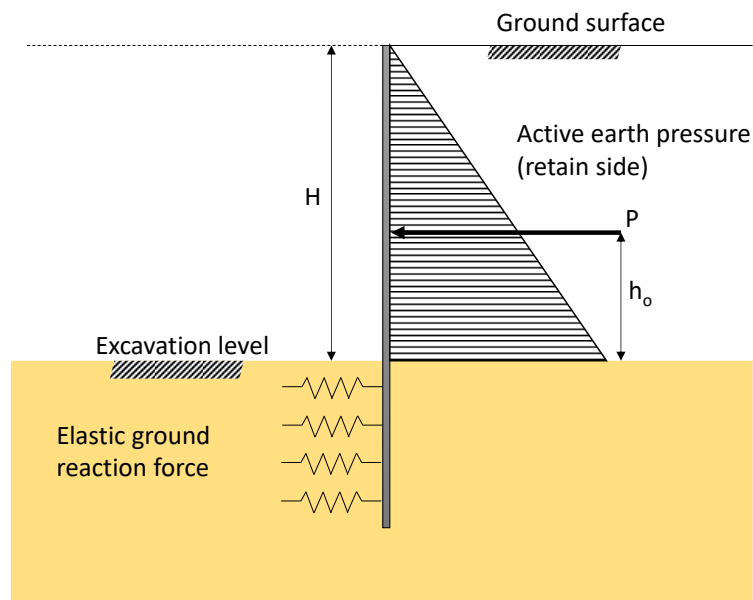


Figure 2.5: Simplified method (Elastic ground reaction force model).

The simplified method involves the calculation of displacement and bending moment distributions for the steel tubular earth retaining wall using techniques like frame analysis. It takes into account the corrosion margin to ensure the accuracy of the results. Furthermore, for the steel tubular pile, the lateral displacement and induced bending moment are computed based on the assumption that

it is a semi-infinitely long pile. This assumption is valid since the simplified method guarantees an embedded length greater than $3/\beta$. Based on Figure 2.5, the total wall top displacement can be calculated as

$$\delta = \delta_1 + \delta_2 + \delta_3 \dots \dots \dots \text{Equation 2.22}$$

δ_1 : displacement on the design ground surface (m)

$$\delta_1 = \frac{(1+\beta \cdot h_o)}{2 \cdot EI \cdot \beta^3} P \dots \dots \dots \text{Equation 2.23}$$

δ_2 : displacement due to deflection angle on the design ground surface (m)

$$\delta_2 = \frac{(1+2\beta \cdot h_o)}{2 \cdot EI \cdot \beta^2} PH \dots \dots \dots \text{Equation 2.24}$$

δ_3 : displacement of the cantilever above the design ground surface (m)

$$\delta_3 = \frac{H^3}{6EI} (3 - \alpha)\alpha^2 P \dots \dots \dots \text{Equation 2.25}$$

Where,

β : characteristic value of pile (m^{-1})

h_o : height from the design ground surface to the location where the resultant force is acting (m)

P : resultant force of lateral pressure per unit width (kN)

E : Young's modulus of steel tubular earth retaining wall (kN/m^2)

I : second moment of area of steel tubular earth retaining wall (m^4)

H : height of steel tubular earth retaining wall (m)

α : ratio of acting height to the wall height (h_o/H)

Method 2: Elasto-plastic method and the dynamic analysis method

When calculating a steel tubular earth retaining wall, the elasto-plastic method or dynamic analysis method is utilized if the simplified method is deemed unsuitable. In the elasto-plastic method, the horizontal ground reaction force model is represented as a bi-linear model, as shown in Figure 2.6, where the upper limit is determined by the passive earth pressure. This method involves the progression of plasticity in the ground on the passive side, extending from the designed ground surface towards the pile tip. To ensure an adequate embedded length, it is necessary to have an

elastic zone present at the tip of the embedded portion of the steel tubular earth retaining wall. On the other hand, in the dynamic analysis method, the steel tubular earth retaining wall structures are modelled alongside the surrounding ground to comprehend the behaviour of the ground surrounding the steel tubular. This is accomplished through a non-linear dynamic analysis that accurately captures the non-linear characteristics of the ground. Different analytical tools like ‘Lpile’ or ‘PYwall’ can be used to conduct the elasto-plastic analysis. Also, FEM analysis can be used to conduct the dynamic analysis.

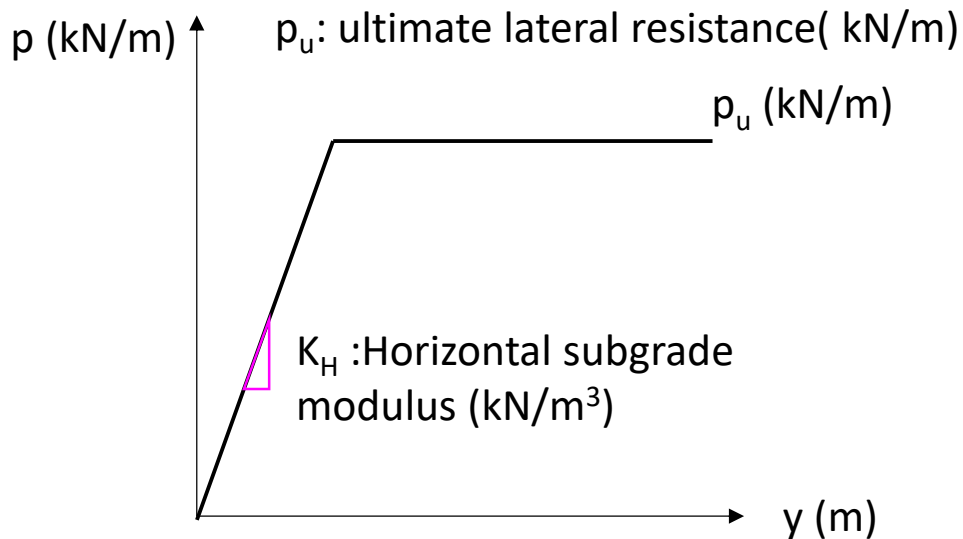


Figure 2.6: Elasto-plastic ground reaction force model

2.2.3 Stability analysis (Madabhushi and Chandrasekaran, 2005)

Broms (1995) identified two possible failure mechanisms for cantilever sheet pile walls: (1) flexural bending leading to the formation of a plastic hinge and (2) the body rotation of the sheet pile wall. In the case of a comparatively stiff sheer pile, the wall suffers rigid body rotation about a pivot point. From a stability perspective, the design parameter of interest is the depth of penetration (D) of the sheet pile wall needed to retain a specific height (H) of the backfill material. This paper focuses on the rotational failure mechanism of cantilever retaining walls with different types of backfill material. The goal is to determine the location of the pivot point for the wall to rotate by minimizing the ratio of moments, as shown in Equations 2.26 and 2.27, generated by active (disturbing moment M_a) and passive (resisting moment M_r) forces for cohesionless and cohesive soil respectively. Also, the force equilibrium can be obtained in this method. The pressure diagram used for cohesionless and cohesive soil is shown in Figures 2.8 and 2.9, respectively. By considering the moment ratio and assuming a full generation of active earth pressures, the required shear strength for the wall to remain in equilibrium can be calculated. This approach offers advantages in establishing wall stability compared to Bolton and Powrie's (1987) method. The effectiveness of the procedure is demonstrated using centrifuge test data and small-scale model

tests conducted by various researchers (Bolton and Powrie, 1987; Bransby and Milligan, 1975), including the writers of this paper.

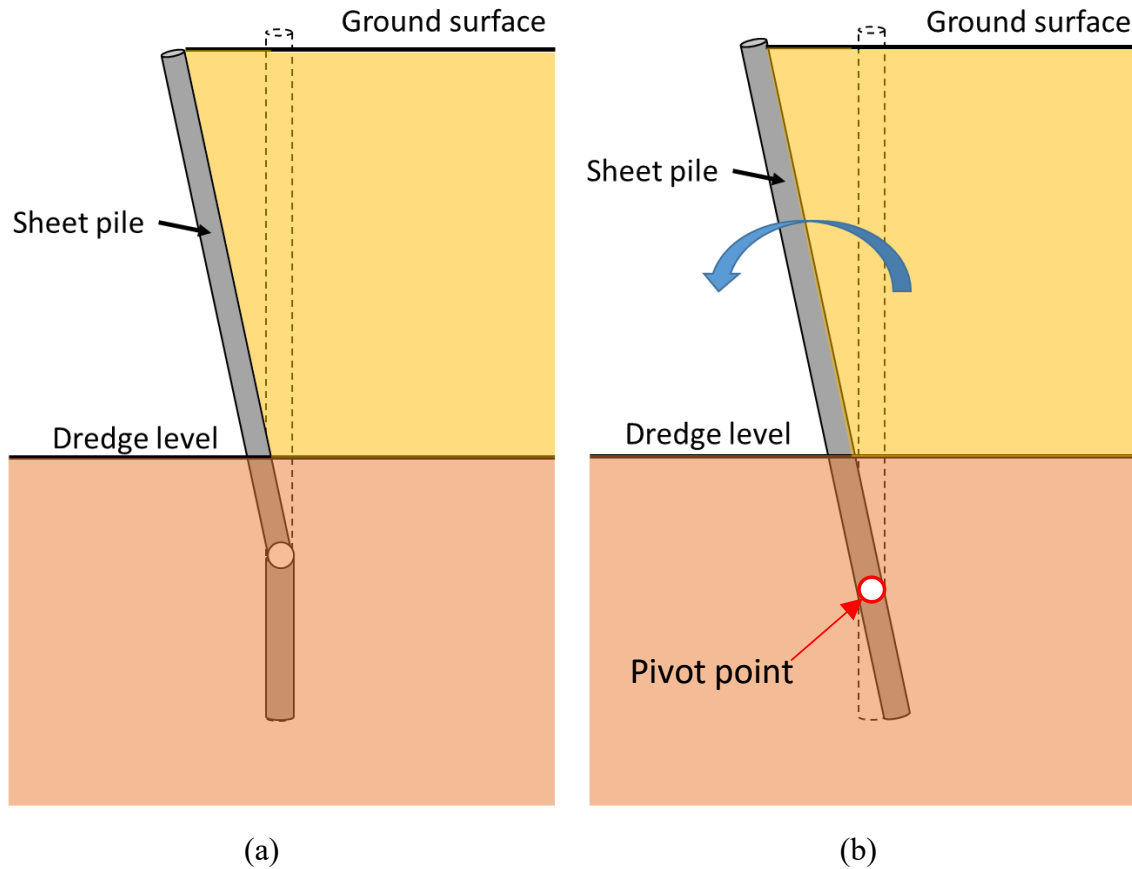


Figure 2.7: Failure mechanism of cantilever retaining wall (a) flexural bending failure with the formation of the plastic hinge (b) body rotation about a pivotal point.

$$\frac{M_a}{M_r} = \frac{K_p \left[\frac{(H+z)(D-z)^2}{2} + \frac{(D-z)^3}{3} + \frac{z^3}{6} \right]}{K_a \left[\frac{(H+z)^3}{6} + \frac{z(D-z)^2}{2} + \frac{(D-z)^3}{3} \right]} \dots \dots \dots \text{Equation 2.26}$$

$$\frac{M_r}{M_a} = \frac{\frac{1}{2}(\gamma(H+Z)+2c_u)(D-z)^2 + \frac{1}{3}\gamma(D-z)^3 + c_u z^2 + \frac{1}{6}\gamma z^3}{\frac{1}{6}(\gamma(H+Z)-2c_u)\left(H+z-\frac{2c_u}{\gamma}\right)^2 + \frac{1}{2}(\gamma z - 2c_u)(D-z)^2 + \frac{1}{3}\gamma(D-z)^3} \dots \dots \dots \text{Equation 2.27}$$

Using the moment minimization technique, the smallest ratio of (M_r/M_a) will provide the minimum embedment depth that will be required to maintain stability against rotational failure.

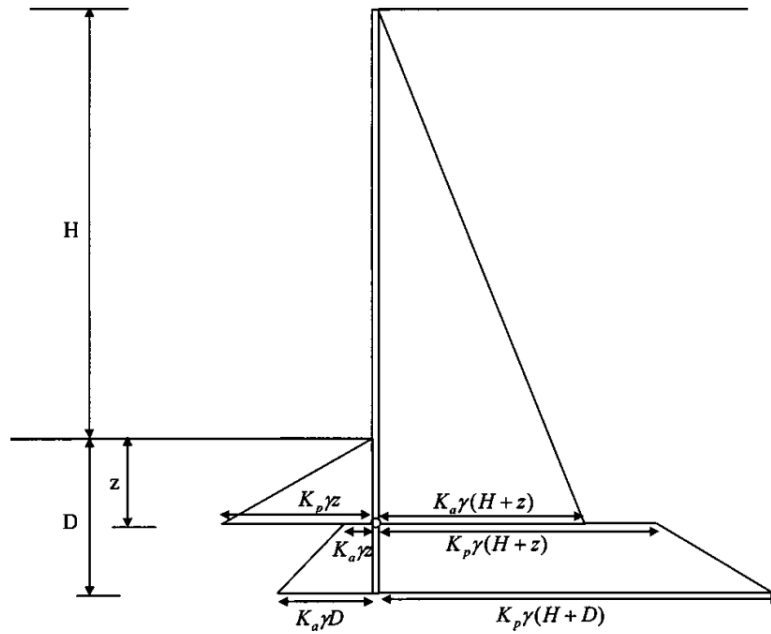


Figure 2.8: Pressure distribution for cohesionless soil.

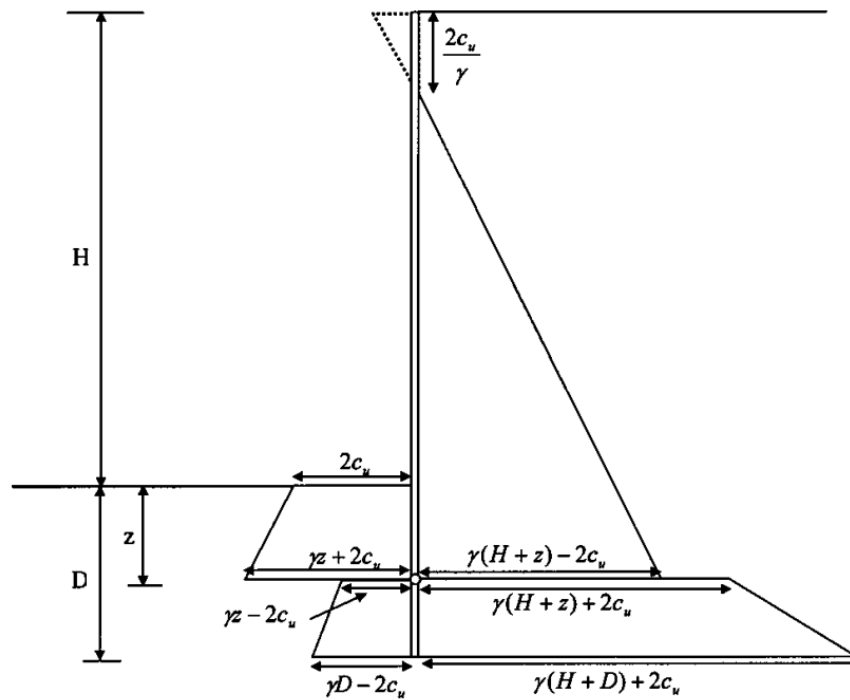


Figure 2.9: Pressure distribution for cohesive soil.

Shear strength demand:

A cantilever sheet pile wall is typically constructed by driving the sheet pile to a certain depth (D) and then adding backfill or by excavation in front of the wall. The wall is expected to experience deformation and move outward. In normally consolidated soils, this leads to the activation of full active earth pressure but not necessarily full passive earth pressure. Experimental studies by Terzaghi (1934 a,b) and based on Clayton and Milititsky (1986) have shown that smaller strains are required to mobilize the active earth pressure compared to the passive earth pressure, as shown in Figure 2.10. For small angles of dilatancy, the average shear strain can be represented as (δ/H) , as shown in Figure 2.10. Bolton suggests using the active earth pressure when there is no significant support at the base of the sheet pile wall or when existing support may be lost. In this paper, it is assumed that the active earth pressures are fully mobilized while the passive earth pressure is mobilized only to maintain the wall in equilibrium. The shape of the earth pressure distribution remains unchanged, with only the magnitudes adjusting based on the extent of mobilized passive earth pressure. This concept is defined as shear strength demand. Equations 2.28 and 2.29 define the shear strength demand of cohesionless and cohesive soil, respectively. Based on the concept, the disturbing moment M_a will remain the same, but the resisting moment will change based on the shear strength demand.

$$K_{p-demand} = \frac{M_a}{\gamma \left(\frac{(H+z)(D-z)^2}{2} + \frac{(D-z)^3}{3} + \frac{z^3}{6} \right)} \dots \dots \dots \text{Equation 2.28}$$

$$c_{u-demand} = \frac{M_a - \frac{1}{6}\gamma z^3 - \frac{1}{3}\gamma(D-z)^3 - \frac{1}{2}\gamma(H+z)(D-z)^2}{D^2 + 2z^2 - 2Dz} \dots \dots \dots \text{Equation 2.29}$$

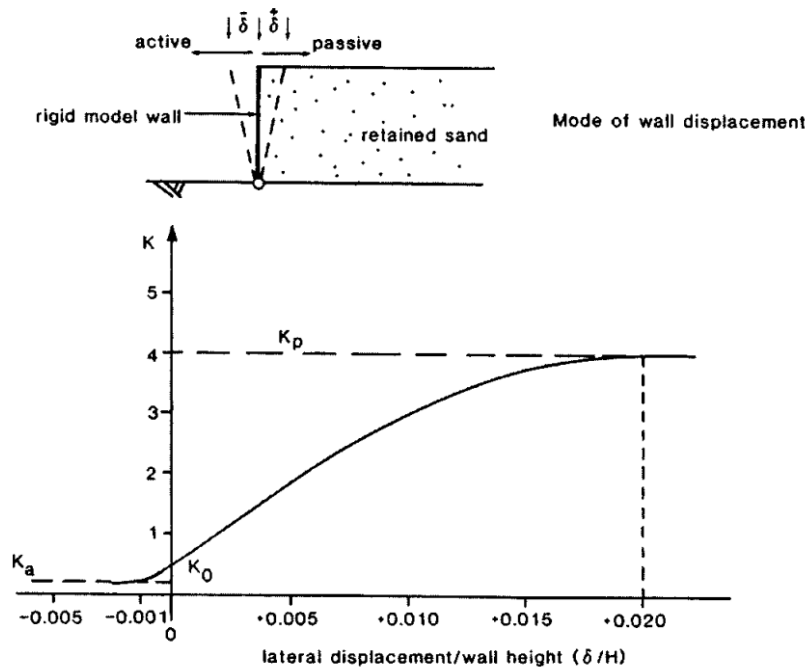


Figure 2.10: Strains required for mobilization of active and passive earth pressures [after Clayton and Milititsky (1986)].

2.3 Catastrophic failure of Embedded retaining structure

2.3.1 *Edinburgh Tower Basement Construction Hong Kong (1981)*

The failure incident was attributed to insufficient lateral support or bracing during the construction's final stages. While constructing a two-level basement for the Edinburgh Tower in Hong Kong, it was discovered that the underlying rock layer was situated at a higher elevation than initially anticipated. Consequently, the sheet pile's toe was driven into the rock strata, and excavation work adjacent to Queens Road was carried out with two levels of propping at the top and bottom. However, when constructing the base slab, the construction team made the decision to remove the lower level of propping and rely solely on the resistance provided by the rock socket at the sheet pile's toe. Regrettably, inadequate lateral resistance led to lateral sliding within the socketed section, resulting in the sheet pile rotating around the top-level propping. This ultimately caused the collapse of half of the Queens Road span at the construction site, as depicted in Figure 2.11.



Figure 2.11: Sheet pile failure and Queen's Road collapse during Edinburgh Tower basement construction

2.3.2 *Failure of 20 ft Highway retaining wall (R.E. Olson, 1993)*

In late July, after a period of heavy rain, a sudden horizontal displacement occurred in a section of the lower rear wall measuring about 135 feet (41 m). The initial site observation took place approximately seven hours after the onset of the failure, revealing a horizontal displacement of approximately 15 feet (5 m) in the lower wall (see Figure 2.12). As a consequence of this displacement, a significant vertical scarp formed in the fill, resulting from the upper wall descending into the void created by the lower wall's displacement. The lower wall continued to slowly displace horizontally over time. Eventually, several months later, when the damaged section of the wall approached the property line, it was removed.



Figure 2.12: Failed section of retaining wall.

During the discovery phase preceding the trial, the calculations made by the designer were carefully examined. It was determined that the primary cause of the problem stemmed from the designer relying on a standard engineering handbook without fully comprehending its limitations. More specifically, the following technical issues were identified:

1. The designer followed a common yet illogical practice of limiting the apparent tip stress instead of accurately estimating the bearing capacity of the base slab. While bearing capacity equations for cases involving inclined and eccentric loads or footings on a slope introduce some level of uncertainty, they still offer a rational approach to analysis.
2. The designer appeared to lack an understanding of the disparities in strength between soil under drained and undrained conditions.
3. Without providing any explanation, the designer disregarded the impact of the upper wall on the loads exerted on the lower wall.

This case study serves as a reminder of valuable lessons often taught in college but frequently forgotten in practical engineering applications. These lessons include:

- Engineers should stay within the bounds of their training and experience, avoiding venturing into unfamiliar territories.
- Engineers must resist client pressure for immediate design turnaround driven by economic considerations. Rushing through a design without due diligence can result in severe consequences for the engineer.
- Design recommendations found in standard civil engineering handbooks often oversimplify geotechnical problems and fail to provide the necessary technical guidance required for successful designs.
- Designers should consider both short-term (undrained) and long-term (drained) conditions unless a comprehensive understanding of the problem clearly indicates that one condition is more critical than the other.
- Implementing effective measures to control water pressures on walls is crucial for successful design outcomes.

2.3.3 Failure of cantilever retaining walls due to reduction of lateral support and earthquake (Day, 1997)

In this case study, a retaining wall failure occurred in San Diego, California. Originally constructed as a basement wall for a building, the wall became a cantilevered structure after the building was demolished in 1984. With no lateral support except from the footing, the wall experienced movement, resulting in damage to the adjacent property and cracks in the concrete flatwork behind the wall, as shown in Figure 2.13. The movement was intermittent, as shown in Figure 2.14, with the wall moving forward, cracks opening up, and then lateral movement pausing as the soil readjusted. Settlement and voids also developed beneath the flatwork due to the wall's lateral movement.



Figure 2.13: Cantilever retaining wall in case study 1.

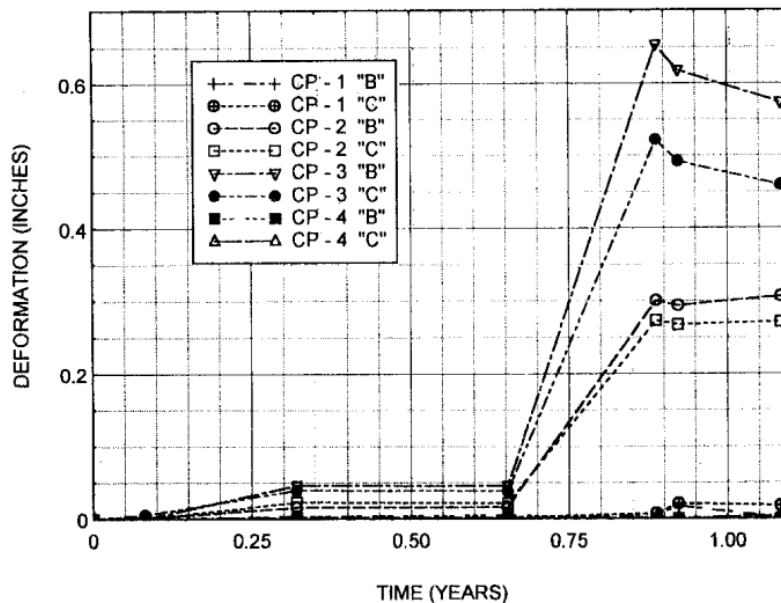


Figure 2.14: Wall deformation variation with time.

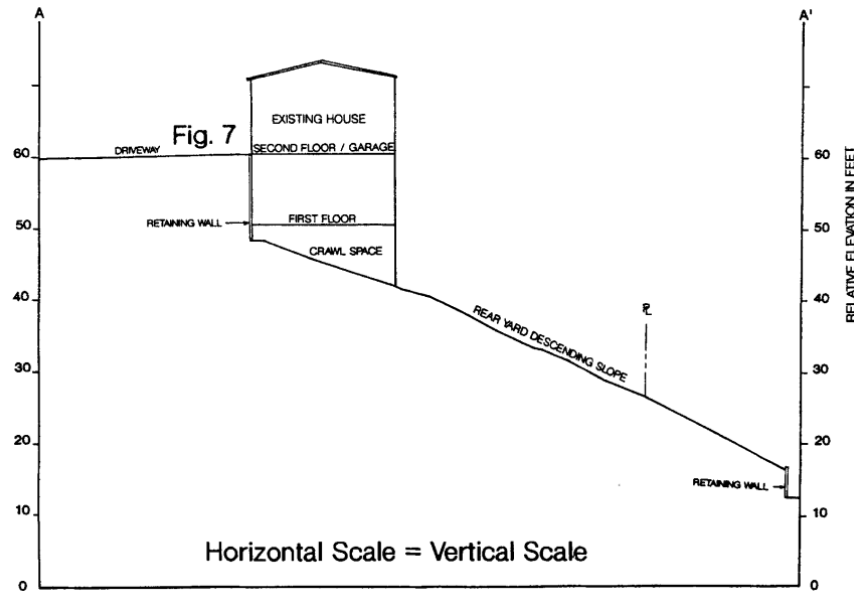


Figure 2.15: Cross section of the site for case study 2.

In the first case study, it is noted that most retaining wall failures occur gradually, with the wall tilting or moving laterally intermittently. However, sudden failures can happen when there is a slope-type failure or inadequate foundation-bearing capacity, especially if the wall is supported by clay. Earthquakes can also cause sudden wall failures, but accurately predicting the additional lateral forces generated during earthquakes is challenging. Many retaining walls are designed only for active earth pressure and fail when subjected to earthquake forces. Methods for incorporating earthquake forces in retaining wall design are outlined in NAVFAC DM 7.2 (1982).

The second case study involves retaining wall damage caused by the Northridge earthquake in California. A retaining wall was constructed near the top of a slope, with a house built in front of a portion of the wall providing lateral support, as shown in Figure 2.15. However, the portion of the retaining wall without house support experienced cracking, tilting, and settlement during the earthquake. The backfill behind the wall densified and increased lateral pressure, leading to damage in the unsupported section.

Finally, this paper describes the design and construction of cantilevered retaining walls. These walls experience three different pressures: active earth pressure, passive pressure, and footing bearing pressure. The key considerations for designing these walls are ensuring an adequate factor of safety against sliding and overturning and keeping the footing bearing pressure below the allowable limit. Retaining wall failures are often gradual, with intermittent tilting or lateral movement. Common causes include reduced wall support and additional loads from events like earthquakes. One common reason for failure is the use of on-site soil instead of granular import backfill, which may lack the required shear strength and permeability. Additionally, excessive pressures during backfill compaction can damage the walls, emphasizing the need for proper compaction techniques using appropriate equipment.

2.4 Centrifuge modelling of cantilever retaining wall embedded in various ground:

2.4.1 Dynamic loading:

Al Atik and N. Sitar (2010)

Designers of retaining structures in seismic regions have found that traditional methods, such as the Mononobe-Okabe (MO) method modified by Seed and Whitman, result in excessively large seismic forces, making the structures economically impractical. An experimental and analytical program was conducted to assess the lateral earth pressures on cantilever retaining structures with dry medium dense sand backfill under seismic conditions. The study involved dynamic centrifuge experiments (as shown in Figure 2.16) under 36g centrifugal acceleration and two-dimensional nonlinear finite-element analyses. Based on the findings from the centrifuge experiment and FEM analysis, recommendations for changes in the design approach for seismic loads in cantilever retaining structures are proposed.

Two sets of dynamic centrifuge experiments were performed on cantilever walls connected to stiff floor slab open channel structures, representing prototype structures for the Bay Area Rapid Transit System (BART) and Valley Transportation Authority (VTA). The experiments were conducted at the Center for Geotechnical Modeling at the University of California, Davis, using the dynamic centrifuge. Technical specifications for the centrifuge and shaking table are reported by Kutter et al. (1994).

Multiple shaking events were conducted on the LAA01 and LAA02 models to assess their response under various ground motion conditions. The shaking was applied parallel to the long sides of the model container and perpendicular to the model structures. Ground motion recordings from different earthquakes, including Loma Prieta 1989, Kobe 1995, and Kocaeli 1999, were used to generate the input motions. The peak ground acceleration of the input motions ranged from 0.1 to 0.87 g, while the predominant period varied from 0.2 to 0.62 seconds.

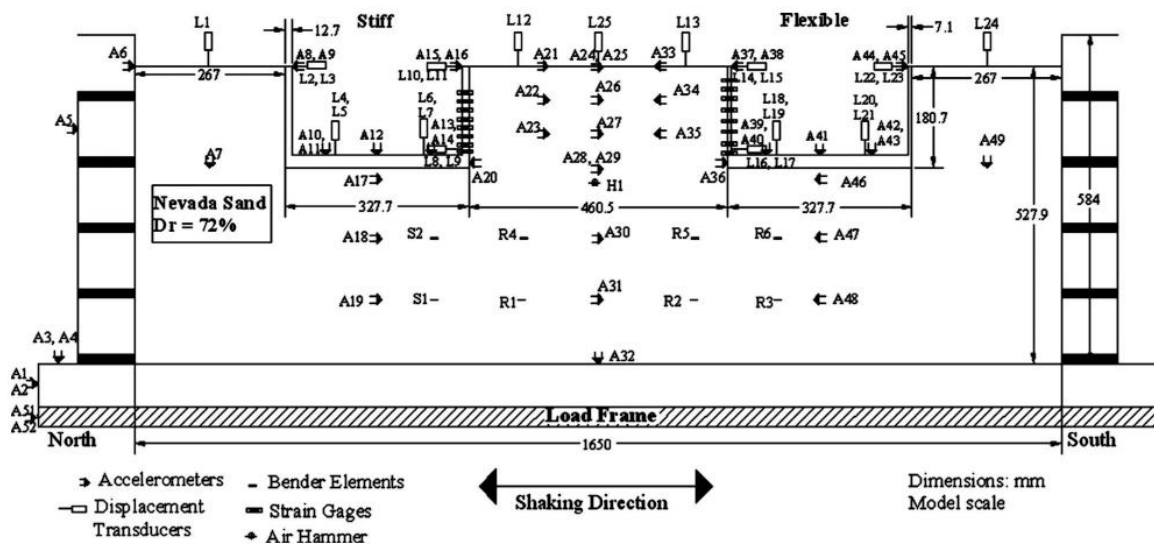


Figure 2.16: Centrifuge model configuration.

The results indicated that maximum dynamic earth pressures increase with depth and can be approximated by a triangular distribution. It was also observed that dynamic earth pressures and inertia forces do not act simultaneously on the retaining walls. Consequently, the current practice of designing for maximum dynamic earth pressure increment and maximum wall inertia is overly conservative and does not reflect the true seismic response of the wall-backfill system.

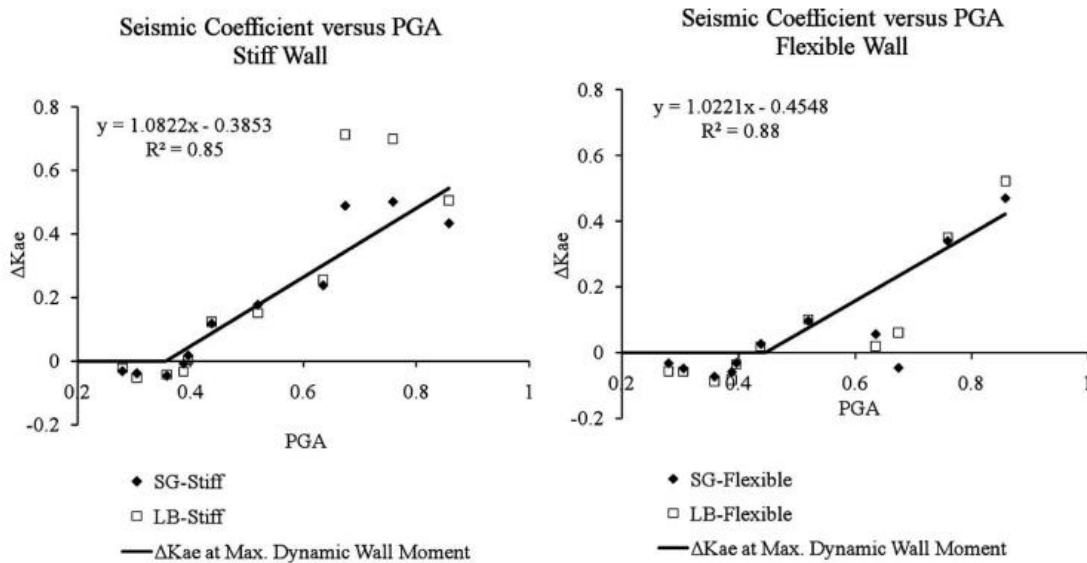


Figure 2.17: Back-calculated dynamic earth pressure coefficients at the time of maximum dynamic wall moments on the stiff and flexible walls as a function of peak ground acceleration measured at the top of the soil in the free field.

Also, as shown in Figure 2.17, based on the relationship between the seismic earth pressure increment coefficient at the time of maximum wall moment and peak ground acceleration, it was suggested that seismic earth pressures can be disregarded at accelerations below 0.4 g. This finding aligns with the observed satisfactory seismic performance of conventionally designed cantilever retaining structures.

Conti et al. (2012)

An experimental investigation of embedded retaining walls subjected to seismic forces was carried out using nine centrifuge tests considering reduced-scale models of retaining walls in dry sand. The geometry of the model is shown in Figure 2.18. The experimental program was conducted using the 10 m diameter Turner beam centrifuge at the University of Cambridge. The program consisted of nine tests on models of paired retaining walls in dry sand with varying relative densities. Six of the models were cantilevered walls, while three were propped against each other. The tests were performed at centrifugal accelerations of 80g and 40g, respectively. The models were prepared within two equivalent-shear-beam containers.

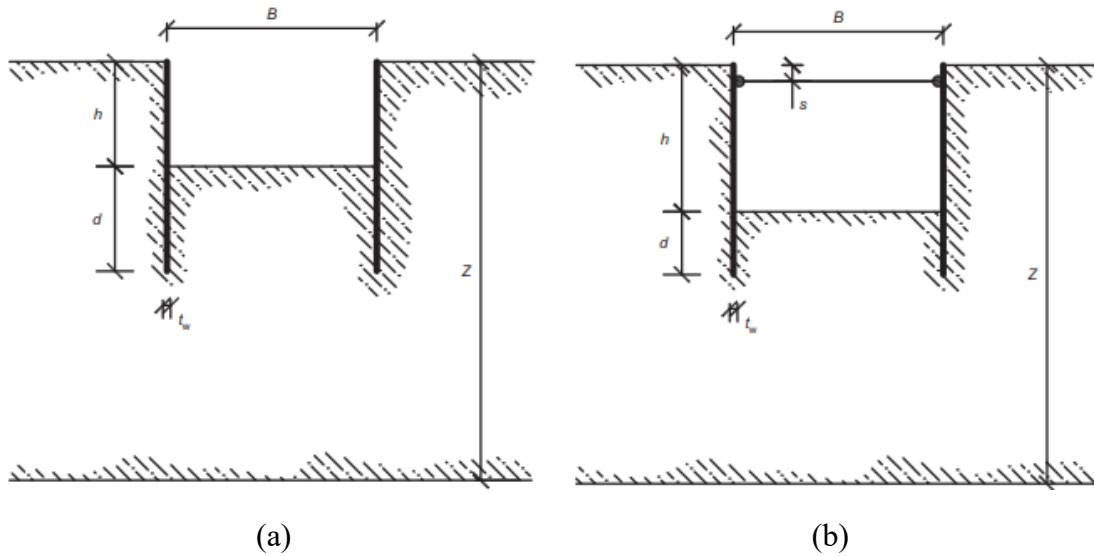


Figure 2.18: Geometry of the centrifuge model (a) cantilever retaining wall (b) propped retaining wall.

Dynamic input for the tests was provided by a stored angular momentum (SAM) actuator. The model experienced a series of sinusoidal wave trains with varying frequencies and amplitudes. The duration of the wave trains differed for cantilevered and propped walls. The applied signals were not perfectly harmonic, exhibiting variations in amplitude and containing energy at secondary frequencies.

The results show that when the maximum acceleration is below a critical limit equilibrium value, the walls experience significant permanent displacements under increasing structural loads. However, for larger accelerations, the walls rotate under constant internal forces. The critical acceleration at which rotation occurs increases with higher maximum acceleration. Negligible displacements are observed if the current earthquake is less severe than previous events experienced by the wall. The increase in critical acceleration is attributed to earth pressure redistribution and progressive mobilization of passive strength in front of the wall. For cantilevered retaining walls, the permanent displacements can be reasonably predicted using a Newmark-type calculation with a critical acceleration that is a fraction of the limit equilibrium value.

Jo et al. (2014)

To reevaluate conventional pseudo-static method and understand the seismic lateral earth pressure on a flexible retaining wall with a dry sand backfill, two dynamic centrifuge tests were conducted at KOCED Geo-Centrifuge Test Center at KAIST using inverted T-shape flexible retaining wall models. The centrifugal acceleration used in the experiments was 50g. The KAIST centrifuge has a maximum capacity of 2,400 kg and can achieve up to 100 g of centrifugal acceleration. The earthquake loading was simulated using an in-flight earthquake simulator equipped with an electro-hydraulic system, capable of generating random earthquake excitations with a modal

frequency range of 30 to 300 Hz and durations of up to 1 s. Detailed technical specifications for the centrifuge and earthquake simulator can be found in the literature (Kim et al., 2013a,b).

Figure 2.19 depicts the models that were constructed in an Equivalent Shear Beam model container, which consisted of stacked aluminium alloy frames with internal dimensions of 490 mm × 490 mm × 630 mm and external dimensions of 650 mm × 650 mm × 650 mm. Rubber layers and ball bearings were placed between each frame to match the dynamic stiffness of the container walls to the soil column.

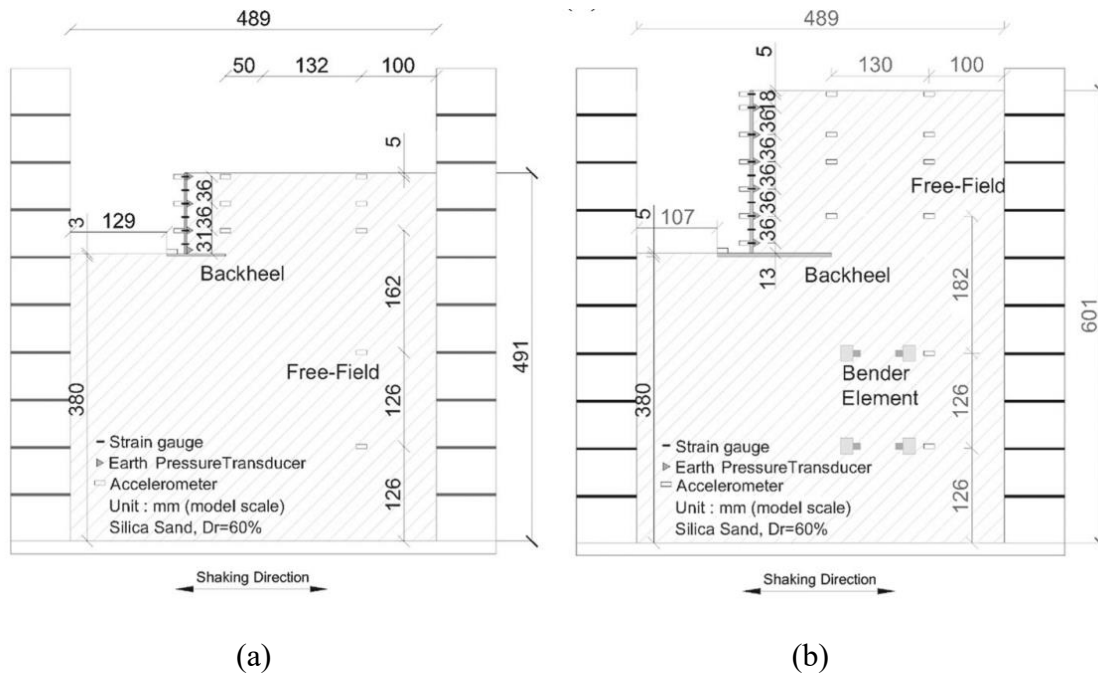


Figure 2.19: Centrifuge model configuration (a) Model A (height: 5.4m) (b) Model B (height: 10.8m).

Two types of earthquake motions were utilized as input for the experiments: the Ofunato earthquake recorded at Miyagi-Ken Oki, Japan (Date: 1978/06/12, Magnitude = 7.4) and the Hachinohe earthquake recorded at Tokachi Oki, Japan (Date: 1968/05/16, Magnitude = 7.9). The Ofunato record represents a short-period-dominated earthquake, which is relevant for Korea. On the other hand, the Hachinohe record represented a long-period-dominant earthquake and was used for comparison with the behaviour observed during the Ofunato record. The peak acceleration was determined as the maximum value observed throughout the acceleration response. The peak accelerations of the bedrock motions ranged from 0.04 to 0.35 g.

The results indicate that the seismic behaviour of the flexible retaining wall is significantly influenced by inertial forces. Additionally, it was observed that the dynamic earth pressure at the moment of maximum earthquake-induced moment was not synchronized and had minimal impact. Also, the study found that seismic earth pressure on flexible cantilever retaining walls can be disregarded when the peak ground acceleration is below 0.4 g, consistent with previous research.

Therefore, further experimental and numerical analysis is required to establish a comprehensive relationship for flexible retaining walls.

2.4.2 Static loading:

Vijay and Takemura (2021)

Vijay and Takemura (2021) developed a centrifuge modelling system to simulate the loading process and failure conditions of an embedded wall in soft rock at a constant centrifugal acceleration. To develop an effective design method for optimizing embedment depth in cantilever-type retaining walls, it is crucial to examine both the serviceability and ultimate limit states. This involves ensuring acceptable displacements through a reasonable evaluation method under design conditions and confirming an extra safety margin to prevent catastrophic failure. The study investigated the stability of cantilever-type retaining walls with large stiffness, equivalent to 2.5 m diameter steel tubular pile walls with a retained height of 12m, embedded in soft rock.

Two centrifuge model tests were conducted to examine the effect of reduced embedment depth over the design embedment depth, as mentioned in article 2.2.2, on the stability of large-stiffness cantilever walls. The experiments were conducted using a TIT Mark III geotechnical centrifuge with a centrifugal acceleration of 50g. The centrifuge model set-up is shown in Figure 2.20. The model container had internal dimensions of 700 mm in length, 150 mm in width, and 500 mm in depth. It consisted of a removable rear-side steel wall and a front-side transparent acrylic wall, which were bolted together with the main container body to create a rigid box and ensure plane strain conditions. The front of the retaining wall was filled with plain water. This plain water is drained out to stimulate the excavation process and supplied at the back side of the wall to stimulate the loading sequence. The Full loading sequence is shown in Figure 2.21.

Although the simple modelling technique employed in this study offers the advantage of capturing the behaviour of walls embedded in harder mediums across different limit states, it is important to acknowledge that uncertainties in the initial conditions of the model can arise due to differences between the at-rest pressure in the sand behind the wall and the water pressure acting on the wall front. To minimize backward wall movements, plain water was used instead of a heavy fluid, and the initial stiffness of the soft rock provided substantial lateral confinement, ensuring wall equilibrium with minimal deformation of the embedded rock in the elastic range at a centrifugal acceleration of 50g. Failure mechanisms observed included compression failure at the shallow wall front and shear wedge failure at the wall back.

As shown in Figure 2.22, it was found that a relatively shallow embedment depth could secure the stability of the walls, even for a significant retaining wall height of 12 m under design conditions. Incrementally increasing the embedment depth by a small amount, such as 0.5 m or 20% from the initial depth of 2.5 m, proved effective in reducing deformation under ordinary design loads and significantly increasing the ultimate failure load. This adjustment also enhanced the redundancy of the walls, leading to a shift in failure behaviour from brittle to ductile. Also, the deflection

behaviour of the walls involved a combination of translation, rotation, and bending, with rigid-body rotation becoming dominant as the load from the retained soil increased.

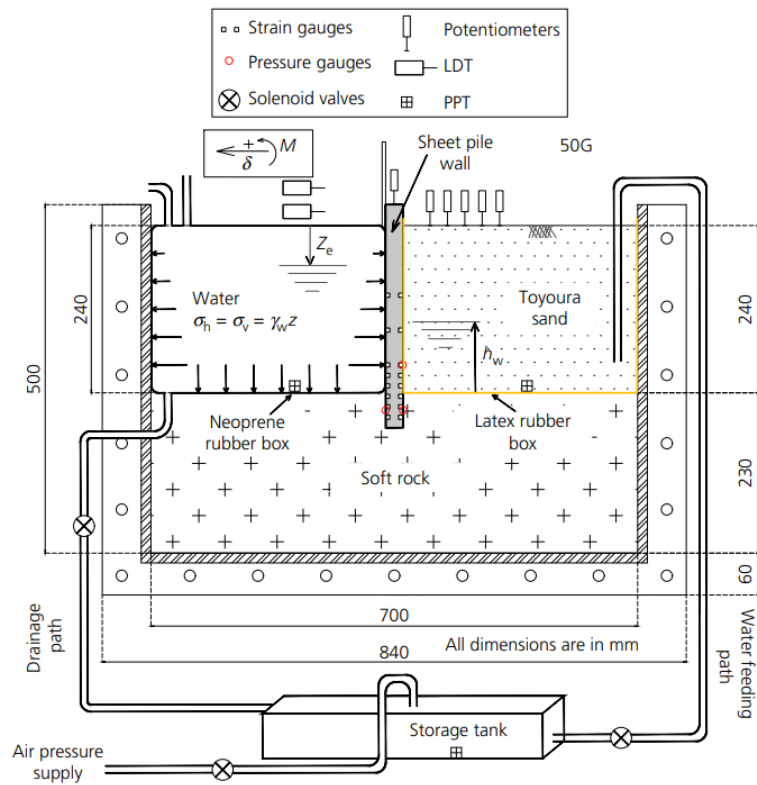


Figure 2.20: Centrifuge model setup

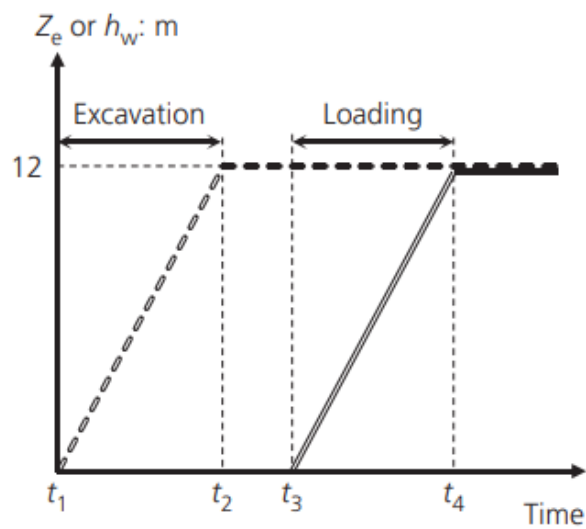


Figure 2.21: Loading sequence followed in centrifuge tests.

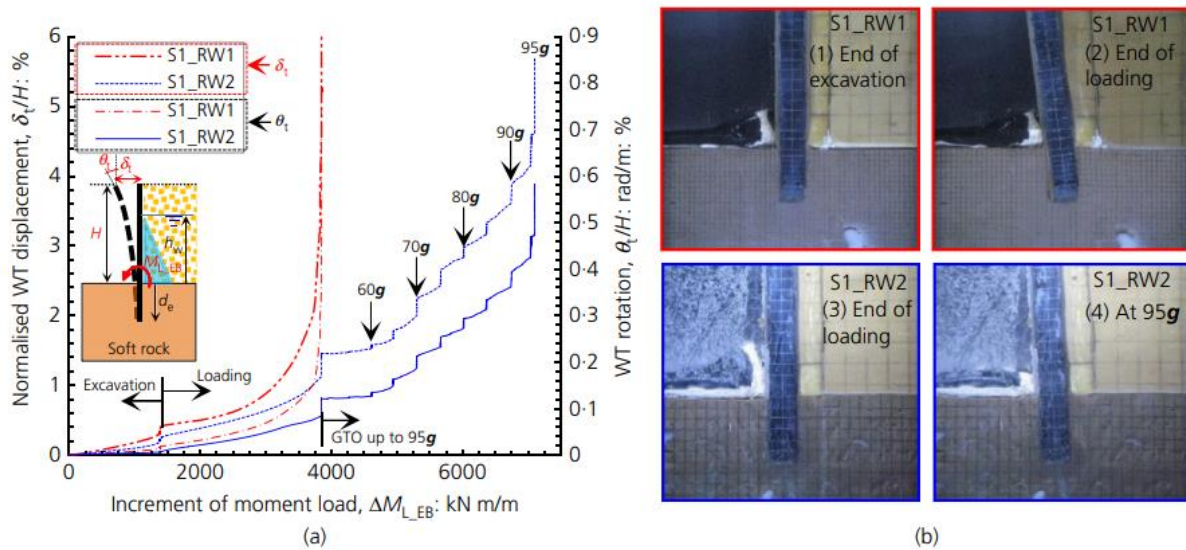


Figure 2.22: influence of embedment depth: (a) normalized WT displacement and WT rotation plotted against the moment load; (b) photographs of wall and ground deformation taken in flight after excavation and loading processes.

2.5 Application of Steel Tubular Pile (STP) in Japan

The application of cantilever-type retaining structures, particularly those constructed using the press-in method, has been increasing in Japan and other countries. This method uses advanced penetration techniques like gyro-press or rotary drilling, as shown in Figure 2.23, which is beneficial in sites with limited space, time, and technology constraints. The press-in technique, particularly with vibration-free installation using silent pilers, relies on the extraction resistance provided by previously installed piles to penetrate the current pile. The hydraulic pressure helps install the pile, while the extraction resistance serves as a counterbalance for the piler. The efficiency of the piler depends on the hardness of the embedment medium, with harder mediums requiring driving assistance techniques like rotary cutting or gyro-press to reduce resistance and deformation.

As shown in Figure 2.24, Steel tubular pile walls have diverse applications, including coffer dams, cantilevered retaining walls, and basement walls. However, limited research exists on the behaviour of these walls in hard mediums like soft to hard rocks. Although demand for steel tubular piles is increasing due to their stiffness, applicability in hard mediums, and constructability in limited space and time, there is a need for a specific design method considering the mechanical behaviour of the walls. This method should address stability against ground failure, structural yielding, and displacement limitations. Physical model studies, simulating prototype behaviour from serviceability limits to ultimate loading conditions, can provide insights into deformation and failure mechanisms. However, conducting extensive centrifuge model studies for all influential factors is costly and time-consuming. Therefore, a combination of critical experimental

investigations, numerical modelling, and parametric studies can lead to the development of a generalized design method.

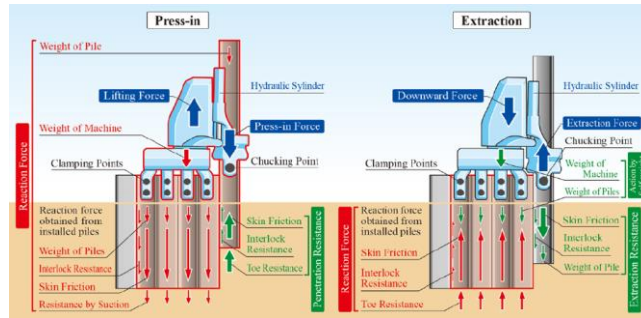
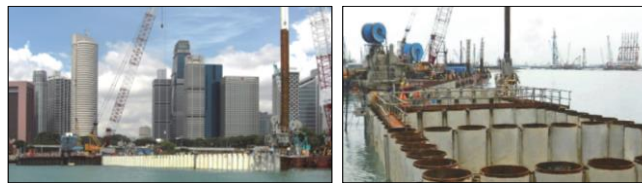


Figure 2.23: Press-in or extraction mechanism and associated forces (Source: IPA handbook)



River revetment and highway protection wall (Singapore)
Conservation of surrounding environment with no noise or vibration

Cofferdam for revetment with 1200 mm diameter tubular piles installed in soft and hard marine clay (Singapore)

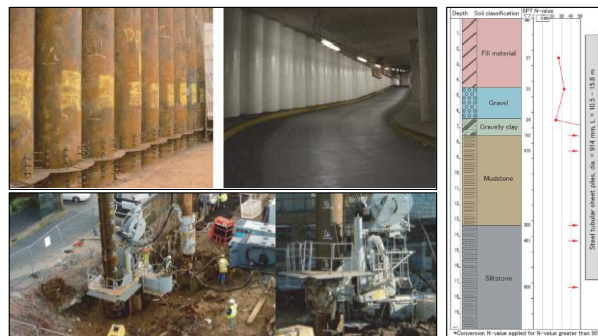
(a)



Construction of cantilever type embedded retaining wall in a narrow space adjacent to the highway with operation (Yokohama, Japan)

Pressing of steel tubular piles with 900 mm diameter in to mudstone (N-value of 166) to widen the existing highway (Yokohama, Japan)

(b)



Construction of dual purpose underground wall and a retaining structure for a new shopping mall in Cardiff, UK using steel tubular piles with diameter of 914 mm

(c)

Figure 2.24: Some applications of steel tubular pile walls constructed by press-in method (Source: IPA handbook)

2.6 Lateral response of pile/Wall

To understand the mechanical behaviour of the CSTP wall embedded in rock, it is important to know the lateral response of the pile socketed into rock. Piled foundations in rock, specifically rock-socketed piles, are commonly used to provide significant axial capacity. These piles can be cast in situ or driven into soft rock, and when the rock surface is near the ground level, they benefit from both axial and lateral resistance along the shaft in addition to end bearing and base shear resistance. It is crucial to accurately quantify the limits of shaft and base resistance in different types of soft rock and understand how construction methods can affect these values. Different models have been proposed to analyze the lateral response of piles in rock, primarily using load transfer curves (P-y curves), which can be categorized into two groups: ductile (non-softening) models and brittle (softening) models.

2.6.1 Elastic response

In the case of rock-socketed piles, it is often observed that they respond elastically to operational lateral loads. The deflection (y_0) and rotation (θ_0) of the pile head under combined lateral force (H) and moment (M) can be approximated using simple closed-form expressions, as shown in Figure 2.25. To assess the flexibility of a rock-socketed pile relative to its embedment length (L) and the stiffness ratio (E_{pile}/E_m) (where E_{pile} is the equivalent solid pile modulus $((EI)_{pile}/(\pi D^4/64))$ and E_m is Young's modulus of the rock mass), the Equation 2.30 and 2.31 can be used to characterize the behaviour of the pile.

$$L/D \geq 1.2 \left(\frac{E_{pile}}{E_m} \right)^{0.3} \dots \dots \dots \text{Equation 2.30}$$

$$L/D \leq 0.07 \left(\frac{E_{pile}}{E_m} \right)^{0.3} \dots \dots \dots \text{Equation 2.31}$$

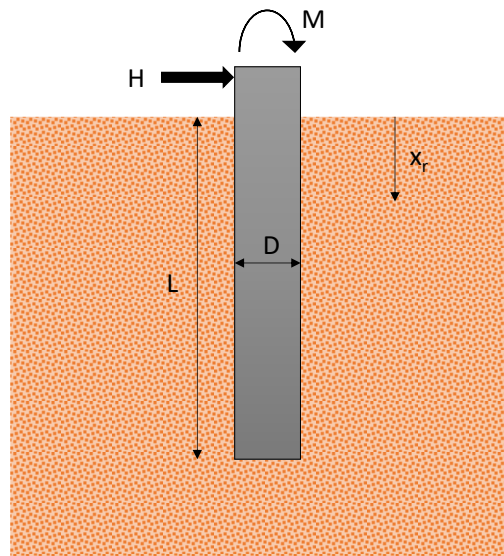


Figure 2.25: Lateral loading of rock socketed pile.

In order to use these equations, accurate estimation of the rock mass modulus (E_m) is crucial and can be done using various methods. Hoek et al. (2002) provide recommendations to calculate E_m based on parameters such as σ_{ci} (uniaxial compressive strength), damage factor (D), and Geological Strength Index (GSI). Alternatively, Liang et al. (2009) propose a correlation for E_m , which requires estimating the intact rock modulus (E_i). ‘ E_i ’ can be determined from initial stiffness values obtained from unconfined compression strength (UCS) tests or through correlations with q_u (uniaxial compressive strength).

The flexibility coefficients for pile head deflection have been proposed by Randolph (1981) and Carter and Kulhawy (1992) for the extremes of flexible and rigid piles, respectively. These coefficients are expressed in terms of an equivalent shear modulus. By substituting the rock mass modulus (E_m) in place of the shear modulus, the relationships can be applied as shown in Equation 2.32-2.37, where Equation 2.32-2.34 represents flexible pile and Equation 2.35-2.37 represents rigid pile.

For Flexible pile:

$$f_{yH} = \frac{y_o D E_m}{H} \sim \left(\frac{E_{pile}}{E_m}\right)^{-0.14} \dots \dots \dots \text{Equation 2.32}$$

$$f_{\theta H} = \frac{\theta_o D^2 E_m}{H} = \frac{y_o D^2 E_m}{M} \sim 1.7 \left(\frac{E_{pile}}{E_m}\right)^{-0.43} \dots \dots \dots \text{Equation 2.33}$$

$$f_{\theta M} = \frac{\theta_o D^3 E_m}{M} \sim 8 \left(\frac{E_{pile}}{E_m}\right)^{-0.71} \dots \dots \dots \text{Equation 2.34}$$

For rigid pile:

$$f_{yH} = \frac{y_o D E_m}{H} \sim 0.7 \left(\frac{L}{D}\right)^{-0.33} \dots \dots \dots \text{Equation 2.35}$$

$$f_{\theta H} = f_{yM} = \frac{\theta_o D^2 E_m}{H} = \frac{y_o D^2 E_m}{M} \sim 0.36 \left(\frac{L}{D}\right)^{-0.88} \dots \dots \dots \text{Equation 2.36}$$

$$f_{\theta M} = \frac{\theta_o D^3 E_m}{M} \sim 0.55 \left(\frac{L}{D}\right)^{-1.67} \dots \dots \dots \text{Equation 2.37}$$

In the design of rock-socketed piles, it is common to encounter combinations of stiffness ratio (E_{pile}/E_m) and slenderness ratio (L/D) that fall within the intermediate zone between fully flexible and rigid pile responses. In such cases, the pile head response can be interpolated to determine its behaviour, as illustrated in Figure 2.26.

Alternatively, according to the suggestion made by Carter and Kulhawy (1992), a slightly conservative approach can be adopted. In this approach, the given flexibility coefficient is estimated as 1.25 times the larger value obtained by considering two scenarios:

1. Estimating the flexibility coefficient assuming a flexible pile with the given E_{pile}/E_m .
2. Estimating the flexibility coefficient assuming a rigid pile with the given L/D .

By taking the larger value from these two estimates and applying the 1.25 multiplication factor, a slightly conservative assessment of the pile head response can be achieved.

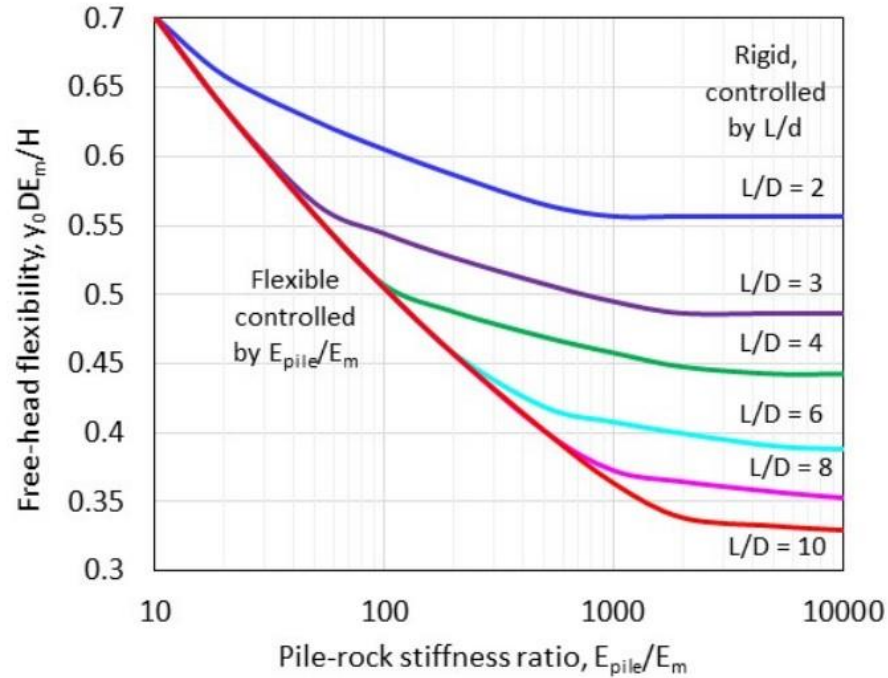


Figure 2.26: Elastic flexibility of free-headed piles in rock (Randolph, 2020)

2.6.2 Load transfer curve of rock:

In the design of rock-socketed piles, the load transfer curves, represented as P-y curves (where P is the lateral force per unit depth and y is the lateral displacement), can vary in terms of whether potential brittle failure of the rock near the rock surface is considered. Figure 18 provides a visual representation of this.

The overall P-y response is typically described by mathematical functions such as power law, and hyperbolic or hyperbolic tangent functions. These functions approach an ultimate force per unit length (P_u) or a nominal pressure ($p_u = P_u/D$) asymptotically. The value of p_u is then correlated either directly to the unconfined compressive strength (UCS), as proposed by Reese (1997) and Erbrich (2004), or to the strength envelope based on the Hoek-Brown criterion (as shown in Figure 2.27), as suggested by Liang et al. (2009).

One of the critical conditions in the determination of the p-y curves is the effect of depth. The ultimate resistance of the pile depends on the failure envelope along the depths, as shown in Figure 2.28. At the shallow depths ($\leq 3D$), the effect of the depth can be confirmed in the ultimate lateral resistance of the pile, as shown in Equation 2.38. However, in deeper depth ($\geq 3D$), in the case of the smooth pile, Reese et al. (1975) recommended an ultimate value of $11.0s_uD \sim 5.2q_u$. and Equation 2.39 can be used for the ultimate resistance. The adjustment parameter α is used to account for strength loss in rock. Reese proposed that α increases from 0.33 for a rock quality designation (RQD) of 100, indicating the possibility of maximum strength loss, to unity for an RQD of zero, where no further strength loss is expected. In the case of intermediate-quality rock

with RQD around 60-70, the limiting nominal pressure p_u is approximately 3 times the unconfined compressive strength (q_u), which corresponds to about 6 times the shear strength of the rock at low confining stresses.

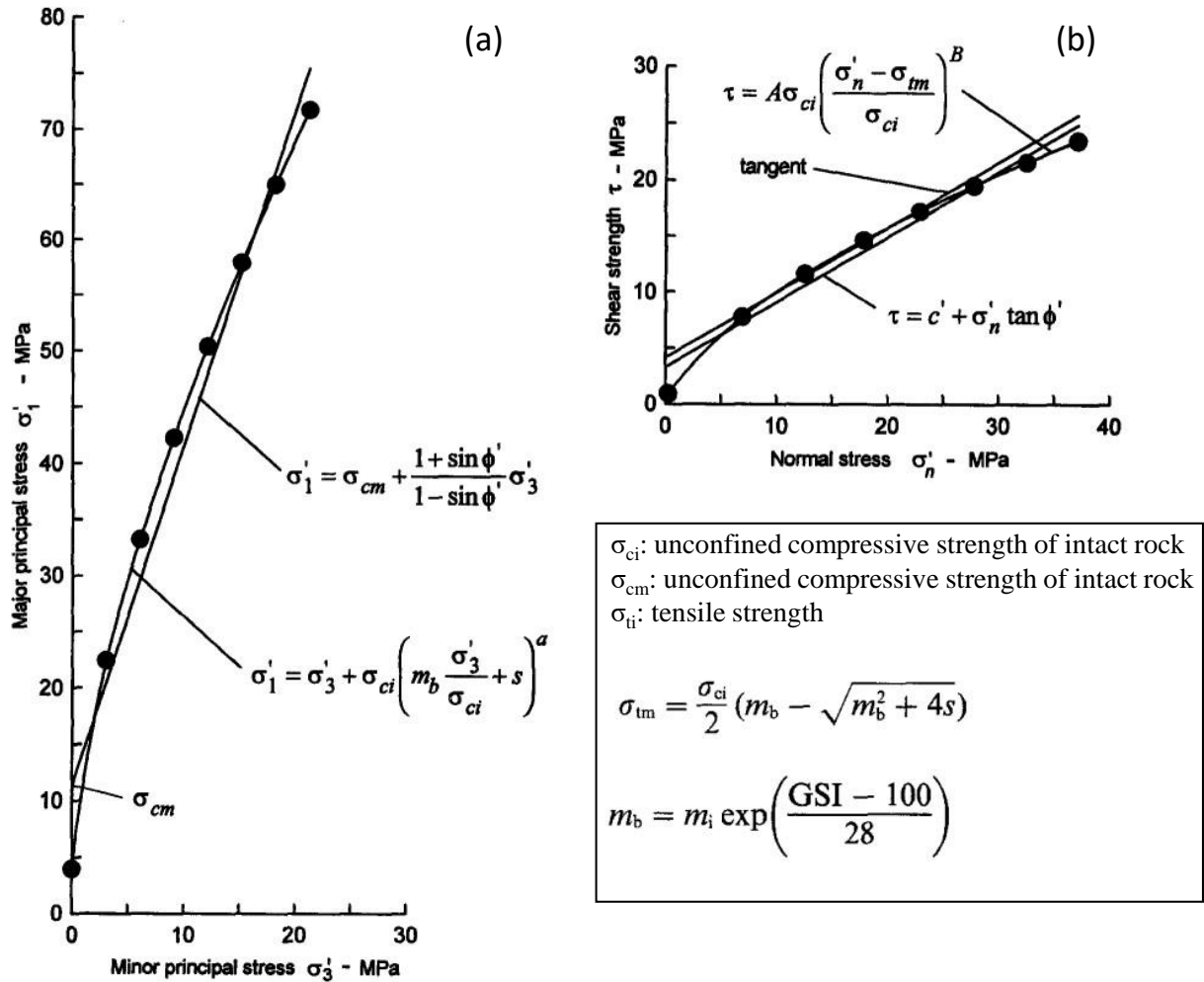


Figure 2.27: Plot of results from simulated full-scale triaxial tests on a rock mass defined by a uniaxial compressive strength $\sigma_{ci} = 85$ MPa, a Hock-Brown constant $m_i = 10$ and Geological Strength Index $GSI = 45$ (Hoek-Brown, 1997).

$$p_{ur} = \alpha_r q_{ur} b \left(1 + 1.4 \frac{x_r}{D} \right) \text{ for } 0 \leq x_r \leq 3D \dots \dots \dots \text{Equation 2.38}$$

$$p_{ur} = 5.2 \alpha_r q_{ur} b \text{ for } x_r \geq 3D \dots \dots \dots \text{Equation 2.39}$$

In the Reese model of the p-y curve for rock, the estimation of initial modulus (K_{ir}) ($K_{ir} \cong k_{ir} * E_{ir}$, where K_{ir} : initial modulus; E_{ir} : initial modulus of rock; k_{ir} : dimensionless constant) is sometimes overestimated due to the unrealistic proposed value of k_{ir} which varies from 100-500 based on the depth Cho et al. (2005). Therefore, the ultimate resistance is achieved at very small displacements. Similarly, the Liang et al. (2009) hyperbolic curve exhibits a comparable behaviour, with the lateral

resistance reaching approximately 90% of P_u (ultimate force per unit length) at a displacement of approximately 0.02 times the pile diameter (0.02D). In the elastic part of the p-y curve, the relationship between p and y can be expressed as equation 2.40. In the nonlinear part of the p-y curve, the relationship can be expressed as Equation 2.41. The deflection of the elastic range can be expressed by Equation 2.42, which is almost zero. Therefore, the p-y curve is mostly composed of nonlinear and plastic parts.

$$p = K_{ir}y \text{ for } y \leq y_A \dots \dots \dots \text{Equation 2.40}$$

$$p = \frac{P_u}{2} \left(\frac{y}{y_{rm}}\right)^{0.25} \text{ for } y_A < y \leq 16y_{rm}, p \leq p_{ur} \dots \dots \dots \text{Equation 2.41}$$

$$y_{rm} = \epsilon_{rm}D, \text{ where } \epsilon_{rm} \text{ is the strain measured at } 50\%q_u \text{ or from } 0.0005 - 0.00005$$

$$y_A = \left(\frac{P_u}{2(y_{rm})^{0.25} M_{ir}}\right)^{1.333} \dots \dots \dots \text{Equation 2.42}$$

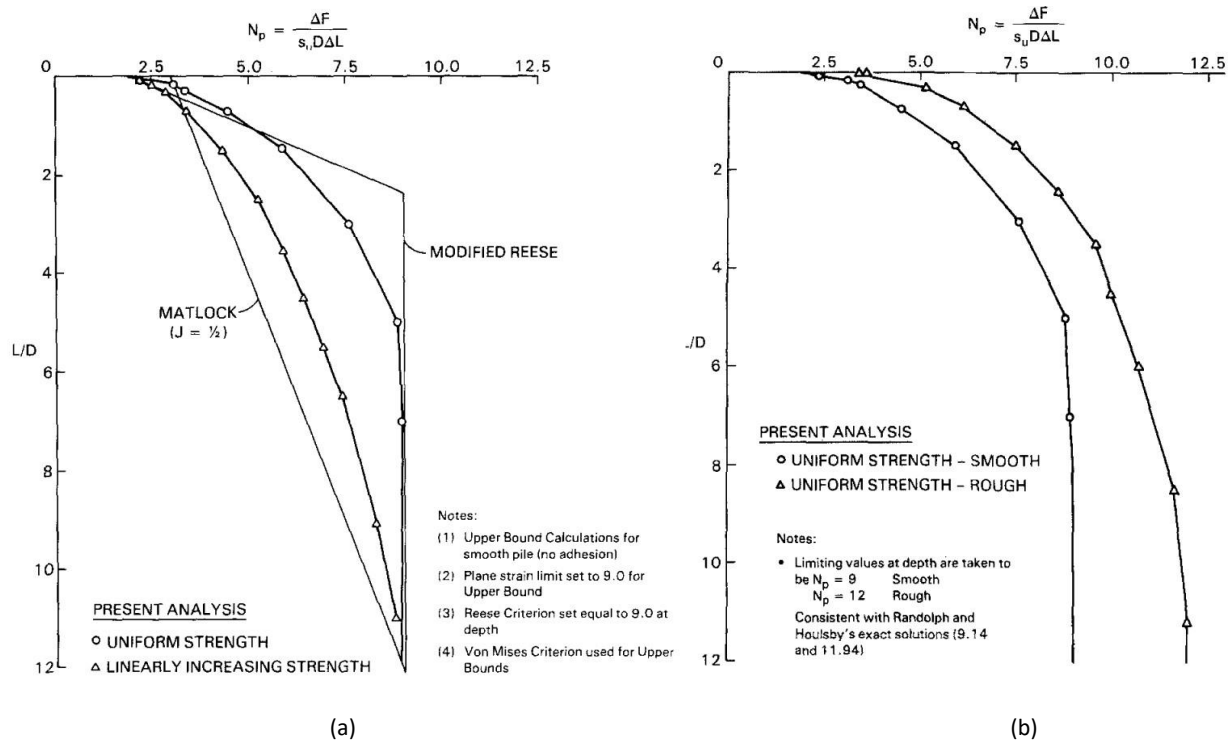


Figure 2.28: Soil resistance variation with depth (a) predicted soil resistance by different researchers (b) effect of soil-pile adhesion on lateral resistance (Murff and Hamilton, 1993).

On the other hand, Liang et al. (2009) assumed a wedge failure mechanism near the surface and derived a $c'-\phi'$ strength model from the Hoek-Brown strength envelope. They considered the ultimate resistance as a combination of side friction and a limiting normal pressure (p_L), with the dominant contribution usually coming from side friction. However, Liang et al. (2009) suggest that even the side friction term will be relatively small, limited to the maximum compressive stress

the rock can sustain within the Hoek-Brown strength envelope, taking the overburden stress as the minor principal stress. Erbrich (2004) introduced a different approach for estimating the ultimate lateral resistance, suggesting that it can be represented by $P_u = N_p(q_u/2)$, where N_p is the bearing factor obtained from the Murff-Hamilton (1993) solution. This formulation provides a simplified expression for the ultimate lateral resistance of the rock mass. Erbrich (2004) proposed the use of different values for the bearing factor N_p based on the depth of the rock. For surface conditions, $N_{p(\text{surf})}$ was suggested to be approximately 2, while for deeper regions, $N_{p(\text{deep})}$ was recommended as around 10. Additionally, the option of applying a maximum cutoff value, $N_p \leq N_{p(\text{max})}$, was also considered. Erbrich's approach accounted for brittle failure on angled conical wedges, gradually progressing from the rock surface to a depth corresponding to "deep" failure. The significant innovation of the proposed P-y curves was the inclusion of progressive brittle failure, as depicted in Figure 2.29. Beyond this point, the lateral resistance decreased to a low value based on the P-y response of uncemented sand, similar to the assumption in Abbs (1983). The onset of chipping was set just below the true ultimate resistance for that depth, with a reduction factor of approximately 0.85. An automated algorithm was used to determine the maximum chipping depth by introducing an additional model parameter.

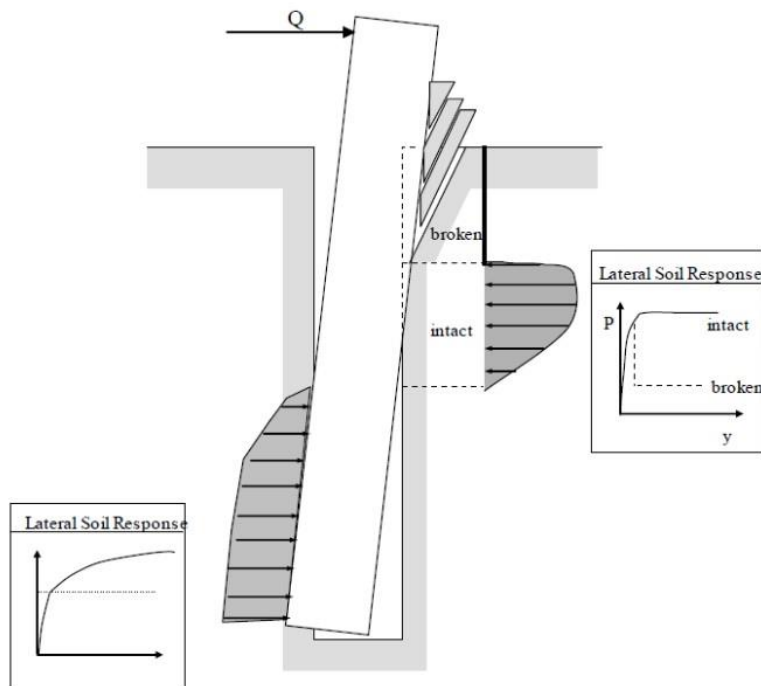


Figure 2.29: Chipping approach for the lateral response of rock socketed pile (Erbrich, 2004).

2.6.3 P-y curves for soft clay in the presence of free water and stiff clay without free water under static or cyclic loading:

Soft clay in the presence of free water:

In a study conducted by Matlock (1970), a lateral load test was performed on a steel pipe pile with a diameter of 324 mm (13 in.) and a length of 12.8 m (42 ft). The pile was driven into clays near Lake Austin, Texas, which had an average shear strength of approximately 38 kPa (800 lb/ft²). Subsequently, the pile was recovered and transported to Sabine Pass, Texas, where it was driven into clay with an average shear strength of approximately 14.4 kPa (300 lb/ft²) in the significant upper zone.

The ultimate resistance of the pile can be computed based on the minimum value obtained from Equations 2.43 and 2.44. Here, γ'_{avg} = average effective unit weight from the ground surface to the p-y curve, x = depth from the ground surface to the p-y curve, c = shear strength at depth x , and D = pile width.

$$p_u = \left[3 + \frac{\gamma'_{avg}}{c} x + \frac{j}{D} x \right] cD \dots \dots \dots \text{Equation 2.43}$$

$$p_u = 9cD \dots \dots \dots \text{Equation 2.44}$$

In the study by Matlock (1970), it was found through experimentation that the value of the coefficient ‘j’ was approximately 0.5 for soft clay and about 0.25 for medium clay. Although a value of 0.5 is commonly used for ‘j’, it may vary depending on the specific soil conditions.

The deflection at one-half of the ultimate soil resistance can be expressed by Equation 2.45.

$$y_{50} = 2.5\varepsilon_{50}D \dots \dots \dots \text{Equation 2.45}$$

Finally, the p-y curve can be computed using the Equation 2.46

$$\frac{p}{p_u} = 0.5\left(\frac{y}{y_{50}}\right)^{1/3} \text{ for } y \leq 8y_{50} \dots \dots \dots \text{Equation 2.46}$$

In the case of cyclic loading, the critical depth x' should be calculated by solving the Equation 2.14 and 2.15, which becomes Equation 2.47:

$$x' = \frac{6cD}{\gamma'D + jc} \dots \dots \dots \text{Equation 2.47}$$

It was assumed that the γ'_{avg} and c remain constant at the upper region ($\leq x'$). For $x \geq x'$, select p as $0.72p_u$ for all values of $y > 3y_{50}$. For $x \leq x'$, select p as $0.72p_u$ at $y = 3y_{50}$ and to the value given by Equation 2.48 at $y=15y_{50}$.

$$p = 0.72p_u \left(\frac{x}{x'}\right); \text{ beyond } y = 15y_{50} \quad p = p_u \quad \dots \dots \dots \text{ Equation 2.48}$$

Stiff clay without free water:

At a site in Houston, a lateral load test was conducted on a bored pile with a diameter of 915 mm (36 in.). Prior to the placement of concrete, a 254-mm (10 in.) diameter pipe was positioned along the pile's axis and equipped with electrical-resistance-strain gauges at intervals along its length. The embedded length of the pile was 12.8 m (42 ft). The clay in the upper 6 m (20 ft) of the soil had an average undrained shear strength of approximately 105 kPa (2,200 lb/ft²). The experiments and their interpretation are extensively discussed by Welch and Reese (1972) and Reese and Welch (1975). The experiment in Houston was utilized to derive both the static and cyclic p-y curves. Additionally, in contrast to the other experiments, the load was applied unidirectionally in this case.

The minimum value from Equations 2.43 and 2.44 should be used for the ultimate resistance of the pile p_u . Similarly, the y_{50} can be calculated using Equation 2.45. Finally, the p-y curves can be drawn by the Equation 2.49.

$$\frac{p}{p_u} = 0.5\left(\frac{y}{y_{50}}\right)^{0.25} \text{ for } y \leq 16y_{50} \quad \dots \dots \dots \text{ Equation 2.49}$$

In the case of cyclic loading, determine the constant value C, which can be found from the relationship developed by laboratory tests conducted by Welch and Reese, 1972 as given in Equation 2.50.

$$C = 9.6\left(\frac{p}{p_u}\right)^4 \quad \dots \dots \dots \text{ Equation 2.50}$$

At the value of p corresponding to the values of p/p_u from Equation 2.49, compute new values of y for cyclic loading by Equation 2.51

$$y_c = y_s + y_{50} C \log|N| \quad \dots \dots \dots \text{ Equation 2.51}$$

Where, y_c = deflection under N-cycles of load, y_s = deflection under short-term static load, y_{50} = deflection under short-term static load at one-half the ultimate resistance, and N = number of cycles of load application.

2.7 Properties of geomaterials:

2.7.1 Sand:

Figure 2.30 illustrates the strain ranges and allowable strain levels for different geotechnical structures, showing the reduction in shear moduli with increasing strain. The stiffness degradation can be categorized into elastic, elastic-plastic, and failure zones, with the shear moduli being independent of strain in the elastic zone, highly influenced by shear strain in the intermediate zone, and dictated by shear flow in the failure zone. Considering the strain-dependent stiffness is crucial for economical and safe design under different displacement and loading conditions. Researchers have described the stress and strain dependency of Toyoura sand stiffness, emphasizing its importance in the numerical modelling of soil structure interaction (Iwasaki et al., 1978; Jamiolkowski et al., 1994; Lo Presti et al., 1993; Fukushima et al., 1984). Functions proposed by Iwasaki and Tatsuoka (1977) estimate shear strain moduli for clean sand based on resonant column test, which can be expressed by Equations 2.52 to 2.53. The functions were proposed from the strain level of 10^{-6} to 10^{-4} , attributing to the non-linear response and large damping of soil beyond the strain level of 10^{-4} ; the resonant-column method could not be accurate. Based on the equations, it can be said that the exponent of mean effective stress increases with the increasing strain level. Extended strain measurements were conducted by Iwasaki and Tatsuoka (1978) using resonant-column and torsional shear devices up to the level of 10^{-2} , providing generalized equations and design charts for shear strain and confining stress-dependent shear moduli.

$$G = \frac{900(2.17-e)^2 p^{0.4}}{1+e} \text{ at shear strain } (\gamma) = 10^{-6} \dots \dots \dots \text{ Equation 2.52}$$

$$G = \frac{850(2.17-e)^2 p^{0.44}}{1+e} \text{ at shear strain } (\gamma) = 10^{-5} \dots \dots \dots \text{ Equation 2.53}$$

$$G = \frac{700(2.17-e)^2 p^{0.5}}{1+e} \text{ at shear strain } (\gamma) = 10^{-4} \dots \dots \dots \text{ Equation 2.54}$$

Where,

e : Void ratio

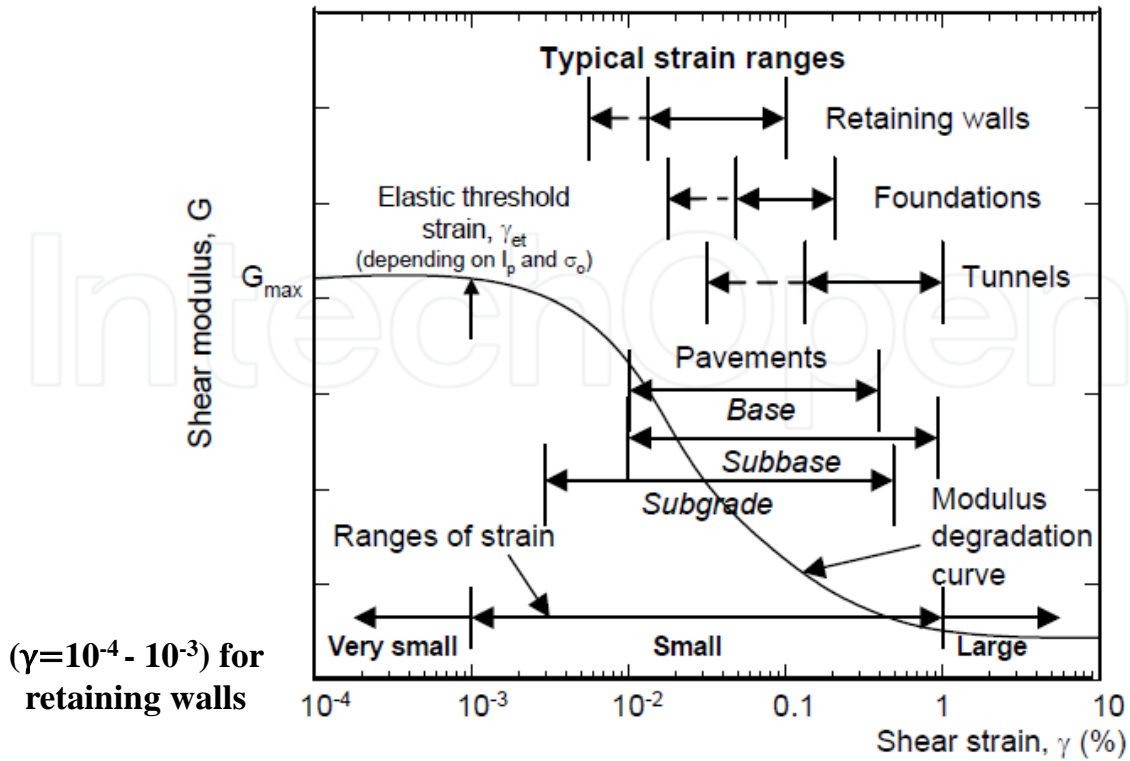
γ : Shear strain

p : Mean effective stress or confining pressure

G : Shear modulus of soil

Furthermore, Iwasaki and Tatsuoka (1978) conducted experiments to examine the influence of the void ratio on the shear modulus of Toyoura sand. They investigated a wide range of strain amplitudes (10^{-6} to 3×10^{-3}) while keeping the confining pressure constant at 100kPa, as shown in Figure 2.31. Based on their extensive experimental data, they determined that the slope of the G - e relation, which represents the relationship between shear modulus and void ratio, remained consistent regardless of the strain amplitude. This observation was captured in equation 2.56. The findings from Figure 2.32 supported the conclusion that the slope of the G - e relation was not affected by the strain amplitude.

slope of $G - e$ relation (S_{Ge}) = $\frac{(2.17-e)^2}{1+e}$ Equation 2.55



Phenomena		Wave propagation, vibration	Crack, differential settlement	Slide, compaction, liquefaction
Soil behavior		Elastic	Elastic-plastic	Failure
Soil properties		Shear modulus, Poisson's ratio, damping		Angle of internal friction, cohesion
Effect of load repetition		←————→		
Effect of loading frequency		←————→		
In situ measurement	Seismic wave method	←————→		
	In situ vibration test	←————→		
	Repeated loading test	←————→		
Laboratory measurement	Wave propagation test	←————→		
	Resonant column test	←————→		
	Repeated loading test	←————→		

Figure 2.30: Stiffness - strain behaviour of soil and design strain levels for various structures and laboratory tests (after Atkinson and Salfors, 1991; Mair, 1993; Ishihara, 1996; Sawangsuriya et al., 2005) (Sawangsuriya ,2012).

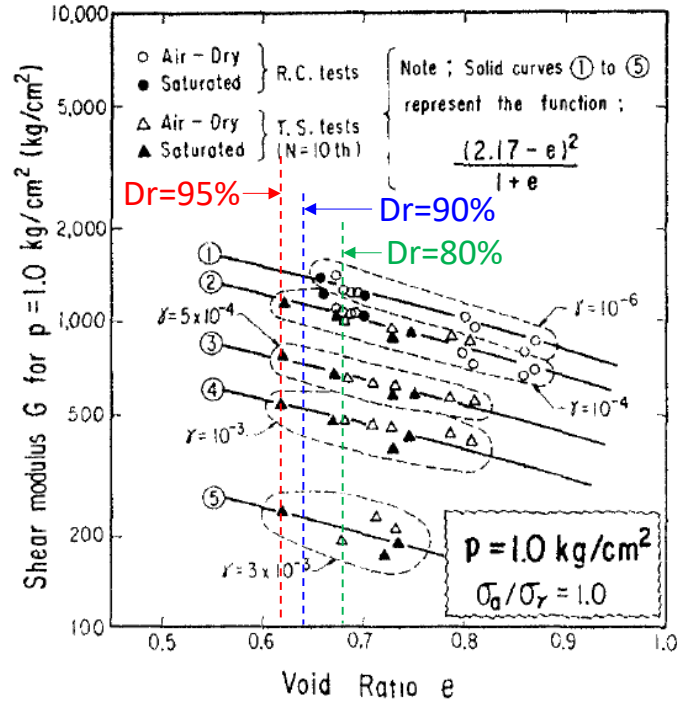


Figure 2.31: Dependency of stiffness on the void ratio of Toyoura sand at 98kPa confining pressure for different strain amplitudes (Iwasaki and Tatsuoka (1978)).

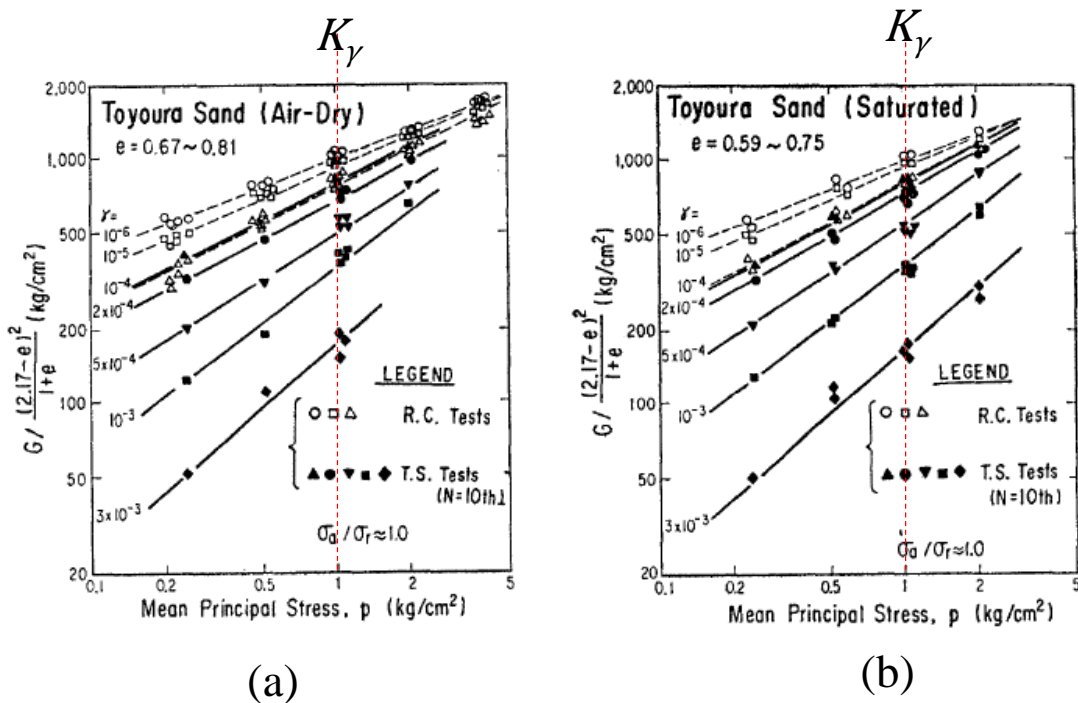


Figure 2.32: Relation between $G / \left(\frac{(2.17 - e)^2}{1 + e} \right)$ and confining pressure (p) for (a) air-dried and (b) saturated Toyoura sand at different strain amplitudes (Iwasaki and Tatsuoka (1978)).

Iwasaki and Tatsuoka (1978) conducted experiments to investigate the influence of confining pressure on the shear modulus of Toyoura sand. They eliminated the influence of the void ratio by dividing the shear modulus by the slope of the G-e relation. The relationship between G/S_{Ge} (where S_{Ge} is the slope of the G-e relation) and confining pressure for air-dried and saturated Toyoura sand was found to be linear on a logarithmic scale.

$$(G)_{\gamma,p} = K_{\gamma} \frac{(2.17-e)^2 p^{m_{\gamma}}}{1+e} \dots \dots \dots \text{equation 2.56}$$

They presented a generalized equation to estimate shear moduli at different strain levels and confining pressures as given by Equation 2.56. The relationship between $m_{\gamma}-\gamma$ is given in Figure 2.33. Based on their observations, an exponent of $m_{\gamma}=0.5$ provided more realistic and conservative stress and strain-dependent stiffness values. The stress dependency on the stiffness of Toyoura sand at high relative densities can be estimated using the shear modulus and void ratio relation. Klinkvort et al. (2013) investigated the stress dependency on the stiffness of high-density sand and described it using triaxial tests. The properties of Fontainebleau sand, including its higher mean particle size compared to Toyoura sand and its stress dependency at 90% relative density, were also examined.

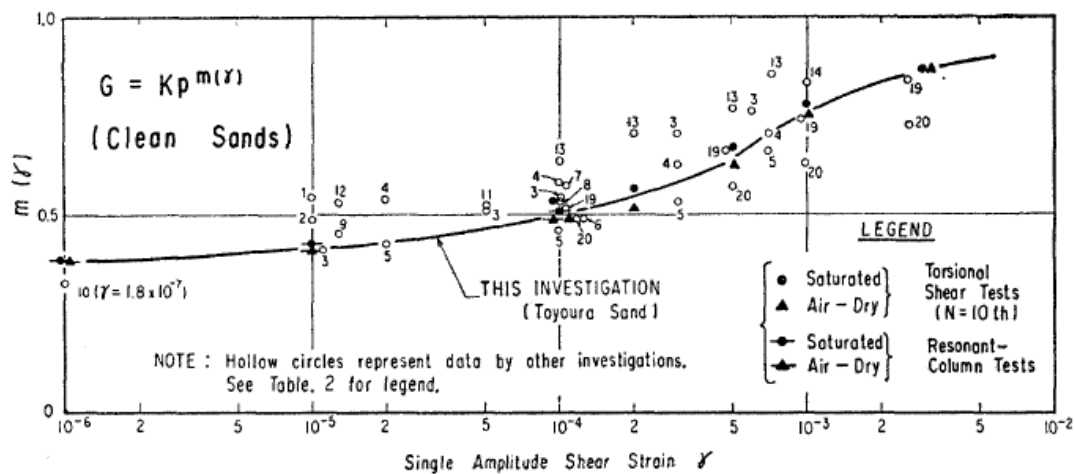


Figure 2.33: $m_{\gamma}-\gamma$ relation for Toyoura sand (Iwasaki and Tatsuoka (1978)).

2.7.2 Rock:

Different terms are used to describe weak rock, such as weathered and broken rock, indurated soil, soft rock, and intermediate geomaterial. Weak rock falls within a spectrum between rock and soil, being harder and more brittle than soil but softer and less brittle than other rocks. Weak rocks are also more compressible and susceptible to changes in effective stress. Soft rocks present various challenges, such as low strength, crumbling, and fast weathering, making them unsuitable for engineering projects Kanji (2014). Additionally, their intermediate strength level makes it difficult to accurately determine their properties through testing. Soft rock sampling and site investigation are complex, and existing classification systems are unsuitable for continuous soft rock masses. Some common types of soft rock are listed in Table 2.4.

Table 2.4: List of some common types of soft rock

Basic types	Subclasses
Sedimentary rocks	Clastic: mudstones, shales, siltstones, sandstones, conglomerates and beccias, and marl; Evaporites: salt rock, carnallite, etc.; Soluble: limestone, dolomite, and gypsum; and Coal
Igneous rocks	Volcanic conglomerates, breccias, and lahar; Basaltic breccia; Piroclastic deposits, volcanic ash, tuff and ignimbrite; and Weathering products of crystalline rocks
Metamorphic rocks	Slate, phyllite, schists, quartzite little cemented, Metavolcanic deposits

Soft rocks present numerous challenges due to their undesirable properties, including low strength, disaggregation, crumbling, high plasticity, slaking, and rapid weathering, among others. As a result, they are typically avoided in the construction of structures like dams, hydroelectric facilities, and tunnels for highways or railways. However, in certain regions of the world, soft rock dominates the geology, leaving no alternative to better-quality rock. As shown in Figure 2.34, Japan, for instance, is composed of soft rock formations and has adapted to working with these materials in its construction projects.

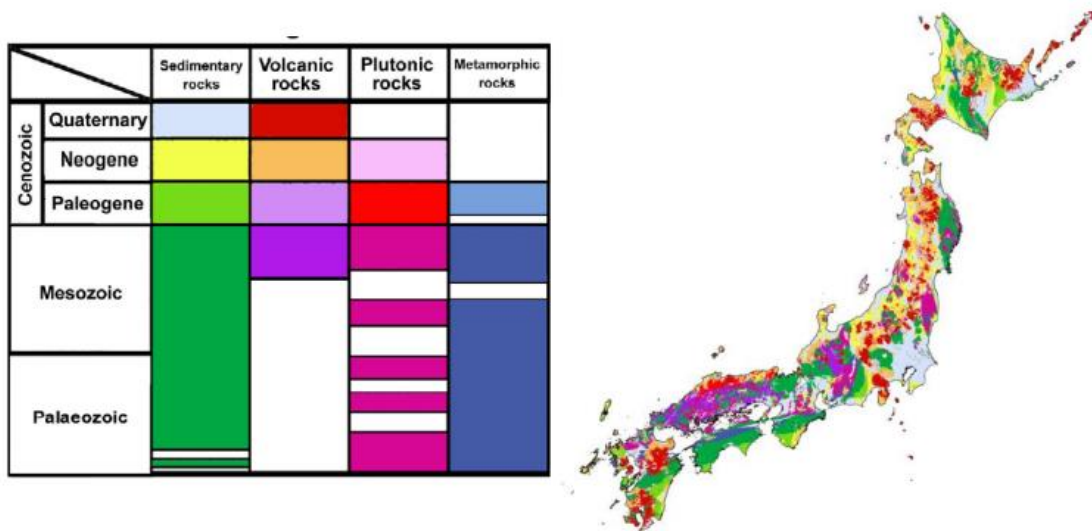


Figure 2.34: distribution of subsurface rock types in Japan (Geological Survey of Japan, 1995).

Rock is weak either because the rock material is itself weak or because the mass is fractured. Thus, the definition of weak rock has to account for material strength and mass structure. Figure 2.35

describe the different range of unconfined compressive strength of different rock adopted from Kylhawy and Phoon (1993).

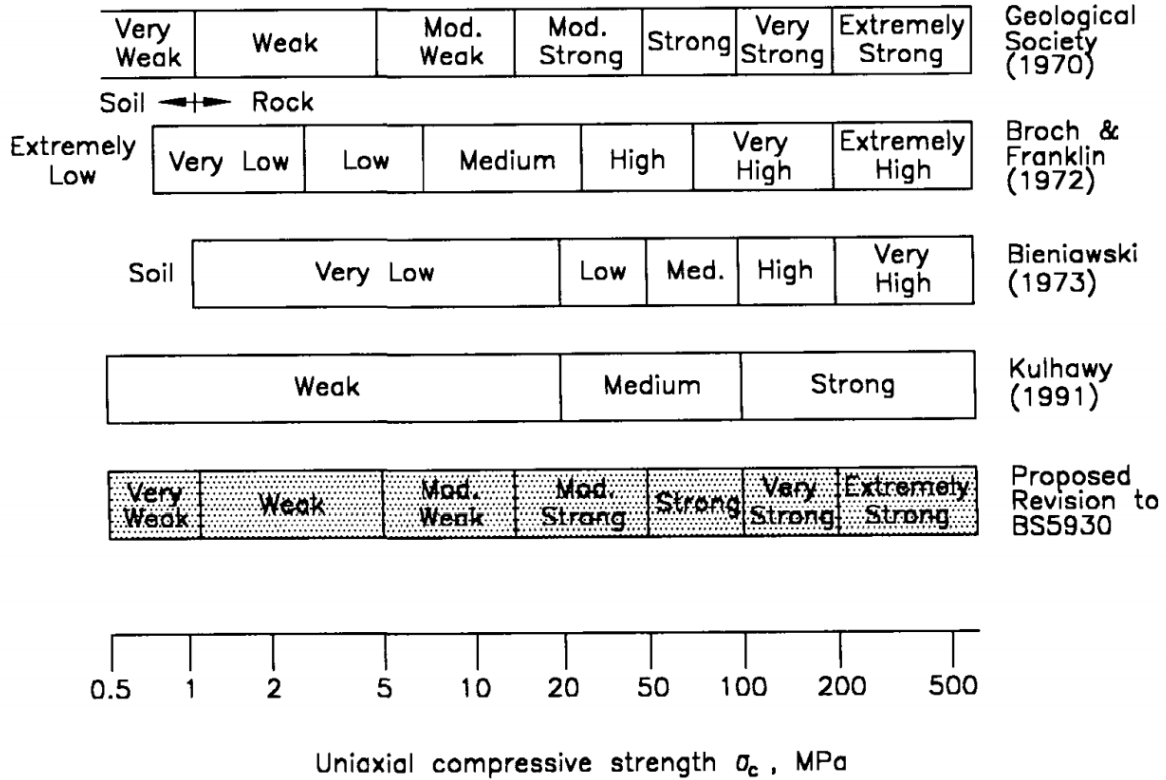


Figure 2.35: Classification of rock material strength (after Kulhawy and Phoon, 1993).

However, USDA-NRCS, 2012 also classified the rock material based on the unconfined compressive strength. Figure 2.36 shows the Hardness and unconfined compressive strength of rock materials in engineering classification.

After Kulhawy and Phoon (1993), in practice, weak rocks will commonly display unconfined compressive strength in the range of 0.6-12.5 MPa and mass stiffness values of 100-1000 MPa. According to the engineering classification, 0.6MPa - 1.25MPa is defined as very soft rock material and 1.25MPa-5.0MPa given as soft rock.

In addition, it provides the upper limit of the soft rock as 12.5MPa, but there is a practical coincidence where the upper limit considered 25MPa as unconfined compressive strength (Kanji, 2014). Establishing the lower limit for the strength of soft rock is more complicated since some hard soils also exhibit higher unconfined compressive strength. However, Terzaghi and Peck (1967) defined based on an SPT value above 50 and UCS greater than 0.4 MPa as the lower limit of soft rocks, whereas Dobereiner (1982) considered a UCS value of 0.5 MPa.

Hardness category	Typical range in unconfined compressive strength (MPa)	Field test on sample
Soil	< 0.60	
Very soft rock or hard soil	0.60–1.25	Scratched with fingernail. Slight indentation by light blow of point of geologic pick. Requires power tools for excavation. Peels with pocketknife.
Soft rock	1.25–5.0	Permits denting by moderate pressure of the fingers. Handheld specimen crumbles under firm blows with point of geologic pick.
Moderately soft rock	5.0–12.5	Shallow indentations (1–3 mm) by firm blows with point of geologic pick. Peels with difficulty with pocketknife. Resists denting by the fingers, but can be abraded and pierced to a shallow depth by a pencil point. Crumbles by rubbing with fingers.
Moderately hard rock	12.5–50	Cannot be scraped or peeled with pocketknife. Intact handheld specimen breaks with single blow of geologic hammer. Can be distinctly scratched with 20d common steel nail. Resists a pencil point, but can be scratched and cut with a knife blade.
Hard rock	50–100	Handheld specimen requires more than one hammer blow to break it. Can be faintly scratched with 20d common steel nail. Resistant to abrasion or cutting by a knife blade, but can be easily dented or broken by light blows of a hammer.
Very hard rock	100–250	Specimen breaks only by repeated, heavy blows with geologic hammer. Cannot be scratched with 20d common steel nail.
Extremely hard rock	> 250	Specimen can only be chipped, not broken by repeated, heavy blows of geologic hammer.

Figure 2.36: Hardness and unconfined compressive strength of rock materials in engineering classification (USDA-NRCS, 2012).

Classification of rock based on SPT test:

Clayton (1995) also classified the weak rock based on SPT value. According to Figure 2.37, the weak rock should have N_{60} value form 80-200 with the correction of $\pm 15\%$ change of N value.

$0 < N_{60} < 80$	Very weak
$80 < N_{60} < 200$	Weak
$N_{60} \geq 200$	Moderately weak and stronger

Figure 2.37: Classification of rock based on SPT value by Clayton (1995).

Factors influencing the properties of soft rock:

The properties of weak rock provided quantitative support to engineering geologist descriptions of rock cores and exposures. They may be used as indices of behaviour or inputs to a classification system and provide a link to key engineering parameters required for the design of pile sockets. Index properties of rock are one of the key properties to define rock type. Depending on the rock type, the following properties are used to characterize the physical attributes of the rock material:

1. Whether it disaggregates in water
2. Clay fraction
3. Moisture content
4. Density
5. Atterberg limits

The other characteristics that may be relevant are swelling index, durability, soundness, abrasivity and solubility. Some engineering properties of British mud rocks by Cripps and Taylor (1981) are shown in Figure 2.38.

Uniaxial compressive strength is the main index property by which weak rocks are classified, from which design values of ultimate shaft friction and ultimate end resistance for pile socket design are obtained. The influence of specimen size, moisture content and specimen orientation relative to rock fabric on observed test results is important. Figure 2.39 shows the relationship between the uniaxial compressive strength and the moisture content. Uniaxial compressive strength reduces with the increase of the moisture content.

Formation	Water content		Liquid limit		Plasticity index I_p (%)	Clay fraction < 2μ (%)	Porosity n (%)	Undrained shear strength	
	W (%)		w_l (%)					S_u (kPa)	
	W	U	W	U				W	U
<i>Cretaceous</i>									
Gault Clay	32–34	18–30	70–82	50–120	27–80	38–62	31–48	17–26	56–1280
<i>Jurassic</i>									
Lower Oxford Clay	20–33	15–25	–	45–75	28–50	30–70	30–54	52–93	96–1300
<i>Triassic</i>									
Mercia Mudstone	12–40	5–15	25–60	25–35	10–35*	10–50	10–50	70–200	130–800
<i>Carboniferous</i>									
Etruria Marl	17–24	9–22	43–79	35–52	8–32	12–25	21–35	40–240	120–620
Coal Measures Mudstone	6–8	8	39–49	42	9–19	24–53	2–25	15–335	9–103 MPa
Shale	9–14	8	42–45	44–51	12–19	37–87	3–30	15–335	29 MPa
Shale	11	9	33–34	30–35	13–41	33–77	3–28	15–335	

Notes: * may be non-plastic
W = weathered, U = unweathered

Figure 2.38: Engineering properties of some British mud rocks (after Cripps and Taylor, 1981).

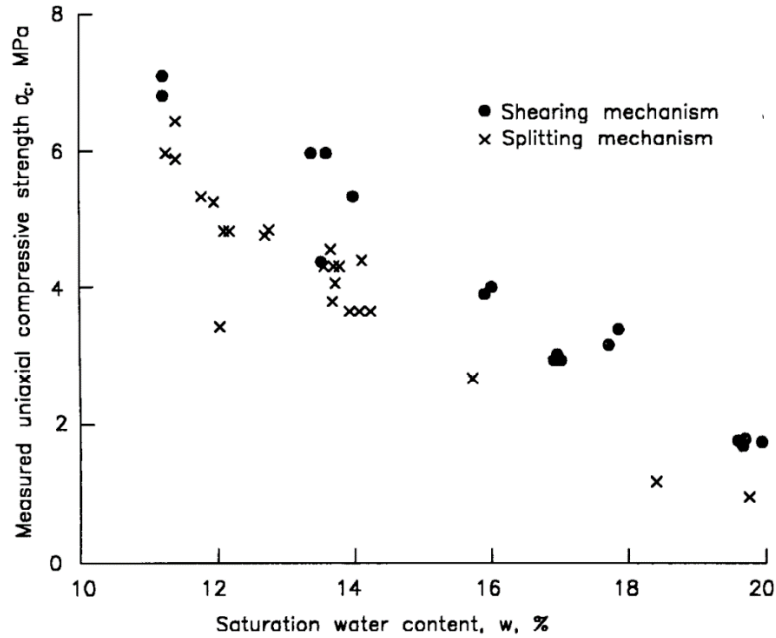


Figure 2.39: influence of water content on measured uniaxial compressive strength of synthetic rock specimens (after Johnston, 1995)

At a site where piling is expected to be required, rock will generally not be exposed. Thus, considerable reliance may have to be placed on the assessment of the fracture state from the borehole core only, using the values of solid core recovery (SCR), fracture index, and rock quality designation (RQD). Figure 2.40 demonstrates the quality of the rock mass based on RQD.

Relation between RQD and j				
Quality classification	RQD (%)	Fracture frequency (per metre)	Velocity index v_F^2/v_L^2	Mass factor j
Very poor	0–25	> 15	0–0.2	0.2
Poor	25–50	15–8	0.2–0.4	0.2
Fair	50–75	8–5	0.4–0.6	0.2–0.5
Good	75–90	5–1	0.6–0.8	0.5–0.8
Excellent	90–100	1	0.8–1.0	0.8–1.0

Note: fracture frequency is the number of natural discontinuities per metre length of rock core/rock mass

Figure 2.40: RQD and its relationship to other rock mass measurements (after Farmer, 1983).

2.7.3 Literature of artificial soft rock:

Artificially prepared soft rock can be created through different mixture compositions. One approach commonly employed is the combination of cement-treated soil, clay, and water. Kunasegaram et al. (2015) conducted a study involving the preparation of samples using different ratios of cement, sand, and clay, as shown in Figure 2.41. They also investigated the impact of variations in the water-cement ratio, clay-sand content, and moisture content of the mixture on the unconfined compressive strength of the resulting soft rock samples.

Mix number	Water-Cement ratio (%)	Clay-Sand content	Water content (%)	Bulk density(g/cm ³)
1	300	20:80	20	2.10-2.11
2	330	20:80	20	2.06-2.09
3	250	30:70	17	2.11-2.15
4	330	30:70	20	2.03-2.10
5	370	30:70	20	2.09-2.10
6	440	30:70	20	2.08-2.10
7	330	40:60	20	2.06-2.09

Figure 2.41: Mixing combination of artificial soft rock.

Cylindrical specimens with a diameter of 50mm and height of 100mm were prepared for conducting unconfined compression tests. The specimens were composed of cement-treated soils mixed with Sumiclay (with a specific gravity of 2.67, liquid limit of 34%, and plastic limit of 19%) and Toyoura sand (with a specific gravity of 2.65, median particle diameter of 0.18mm, and uniformity coefficient of 1.4). Different samples were created by varying the mixing ratios, including the water-cement ratio (ranging from 250% to 440%), clay content (20%, 30%, and 40%), and moisture content (17% and 20%), all measured by weight. The specimens were prepared using early-strength Portland cement (with a specific gravity of 3.14) obtained from Taiheiyo Cement. The moulded specimens were subjected to curing periods of 3, 7, 14, and 28 days in preparation for the unconfined compression tests. Further details regarding the specific mixing ratios can be found in Figure 2.41, as reported by the researcher. The researcher investigated the variation in unconfined compressive strength (UCS) and secant modulus (E_{50}) for different mixing conditions. The results of this study are presented in Figures 2.42 and 2.43. They observed that both E_{50} and UCS increase with longer curing times. Also, they used two types of methods to measure the strain: (1) using a dial gauge and (2) using bending strain. Based on the test result, it was found that the strength and stiffness measured by using strain gauge is about 2-3 times larger than the dial gauge measurement.

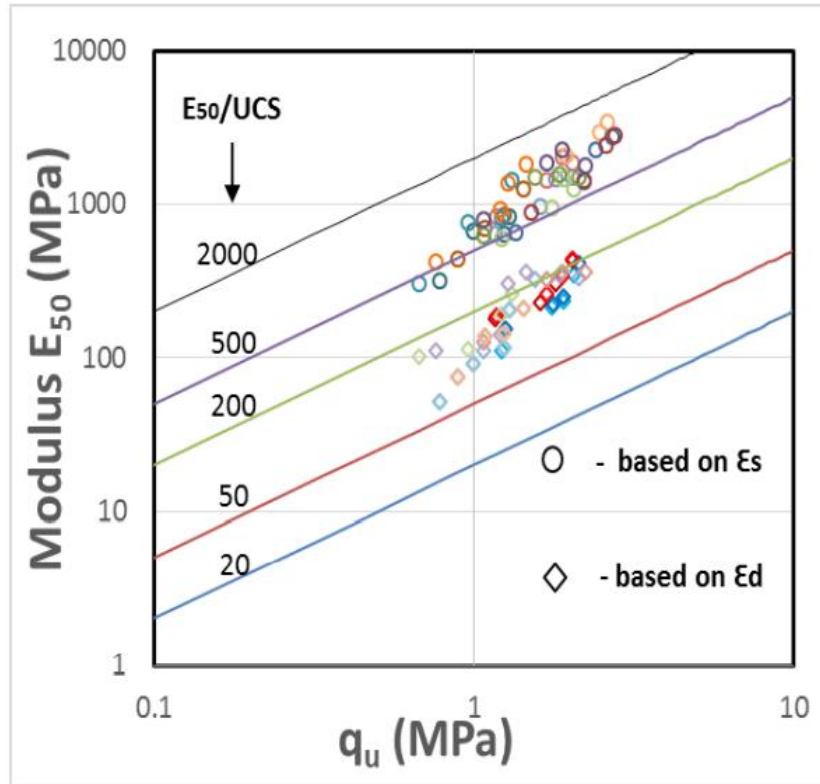


Figure 2.42: relationship between E_{50} and UCS for artificial soft rock samples (Kunasegaram et al., 2015).

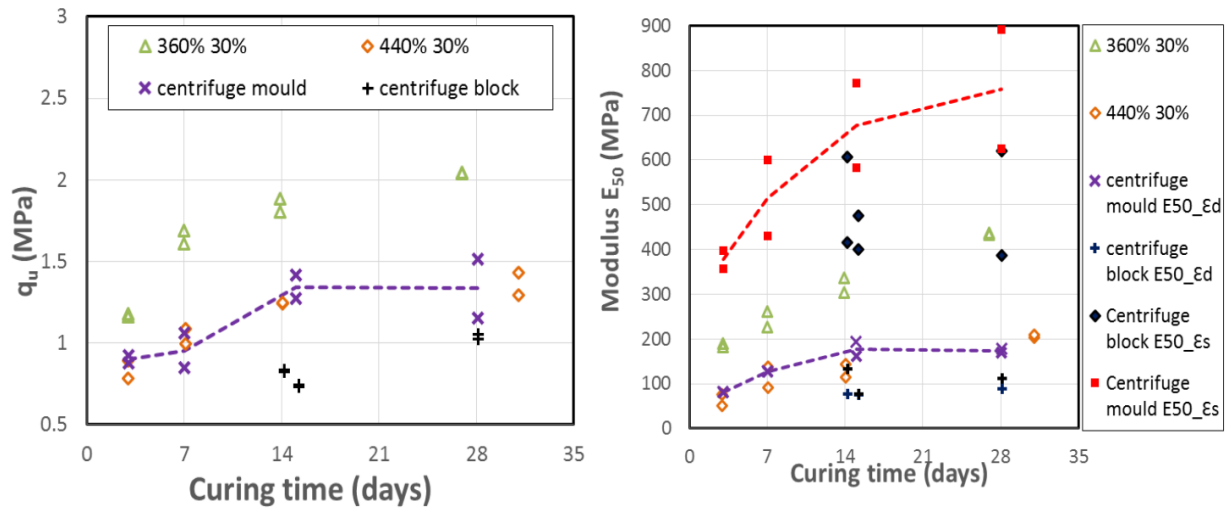


Figure 2.43: Comparison of experimental results with centrifuge model specimens (Kunasegaram et al., 2015).

2.8 Centrifuge modeling:

2.8.1 Advantage of centrifuge modelling:

Centrifuge modelling offers several advantages for geotechnical research and investigations:

1. **Realistic Simulation:** Confining stresses and stiffness of the ground can be accurately modelled in a small container using higher centrifugal accelerations. This allows for precise replication of shear strain mobilization, closely resembling real field conditions.
2. **Time Efficiency:** Geotechnical problems that involve long durations, such as consolidation or diffusion, can be studied within shorter time frames under high "g" environments. This accelerates the research process and enables quicker analysis of time-dependent phenomena.
3. **Soil-Structure Interactions:** Centrifuge modelling enables the study of deformation mechanisms and failure modes of geotechnical structures, including investigations into soil-structure interactions. This provides valuable insights into the behaviour and performance of structures under realistic conditions.
4. **Cost-Effectiveness:** Centrifuge modelling offers a cost-effective solution compared to conducting investigations in the real field, especially for complex phenomena. It allows for in-depth analysis and understanding of geotechnical problems without the need for large-scale field experiments.
5. **3D Analysis:** Centrifuge modelling helps unravel the three-dimensional behaviour of intricate soil-structure interaction problems. This allows researchers to explore complex scenarios and evaluate the performance of structures more comprehensively.
6. **Dynamic Studies:** Centrifuge modelling allows for the study of the dynamic behaviour of structures under specific ground excitations. This is particularly useful for investigating seismic effects, which are challenging to replicate accurately in the real field, except on large-scale shake tables.

Overall, centrifuge modeling provides a powerful and versatile tool for geotechnical research, offering realistic simulations, time efficiency, cost-effectiveness, and the ability to study complex phenomena and dynamic behavior.

2.8.2 Principles of geotechnical centrifuge modelling:

In dynamic centrifuge modelling, the scaling laws described by Schofield (1980) are utilized. Table 2.5 summarize some scaling law followed in geotechnical centrifuge modelling. The main principle is that a model scaled down by a factor of N , placed at the end of a centrifuge arm, and subjected to a centrifugal acceleration of $N g$ will experience the same stresses as the prototype, as shown in Figure 2.44. For example, if a 50 m depth of ground surface needs to be modelled, a 1 m deep model container is filled with soil, placed on the centrifuge arm, and subjected to a centrifugal acceleration of 50 g. This increases the pressures and stresses by a factor of 50, effectively representing the vertical stress at a depth of 50 m below the ground surface on Earth. Thus, the 1 m deep model represents 50 m of prototype soil.

Table 2.5: Scaling law followed in geotechnical centrifuge modelling.

Parameter	Units	Ratio of model to prototype
Length	m	1/N
Area	m ²	1/N ²
Density	kg/m ³	1
Velocity	m/s	1
Acceleration	m/s ²	N
Stress	N/m ²	1
Strain	-	1
Force	N	1/N ²
Bending moment	Nm	1/N ³
Time(dynamic)	s	1/N
Time(consolidation)	s	1/N ²

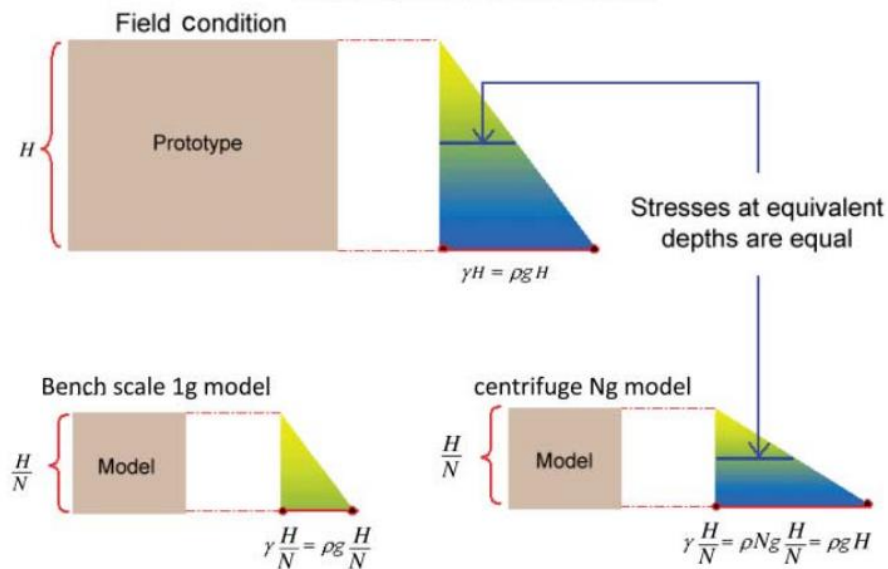


Figure 2.44: Stress similarity between model and prototype (Shamy et al., 2013).

The purpose of the centrifuge is to enable small-scale models to experience the same stresses as the full-scale prototype. However, the accuracy of the model study depends on the size of the

model and the spinning radius of the centrifuge. Unlike the Earth's gravity field, where the acceleration remains constant, the centrifugal acceleration in the centrifuge increases with the radius, as shown in Figure 2.45. Therefore, maintaining a constant centrifugal acceleration throughout the model is not possible. To minimize the effects on model studies, the centre of gravity of the model is kept at the intersection radius of both the constant g environment and the parabolic distribution of the centrifugal acceleration, as illustrated in Figure 2.45.

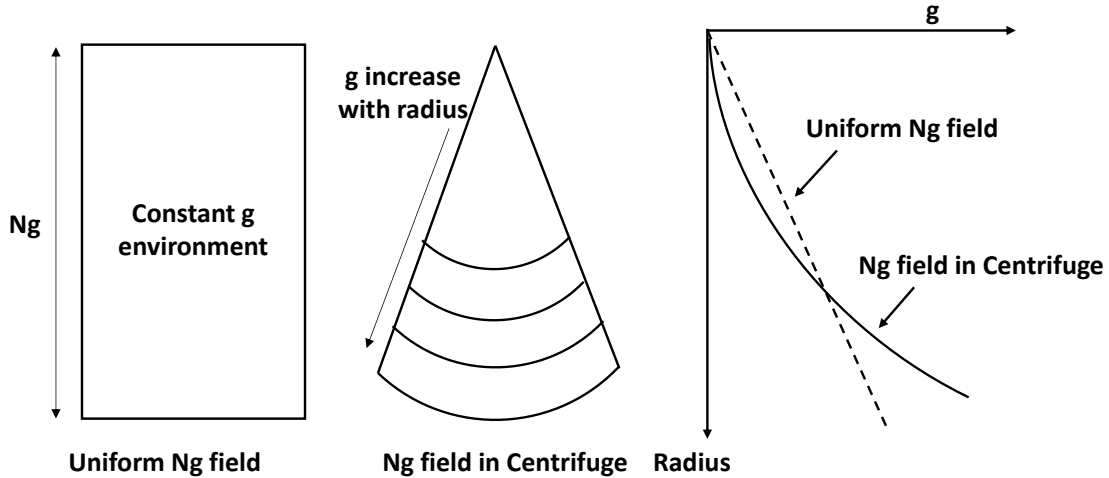


Figure 2.45: Variation of centrifugal acceleration with radius.

In summary, dynamic centrifuge modelling utilizes scaling laws to replicate the stresses of the prototype in scaled-down models. Although the model studies are beneficial for understanding prototype behaviour, the accuracy depends on the model size and the centrifuge's spinning radius. Efforts are made to minimize the differences between the constant g environment and the centrifugal acceleration distribution to enhance the reliability of the model studies.

2.8.3 Tokyo tech Mark III centrifuge and centrifuge scaling law:

The Tokyo Tech Mark III centrifuge, as shown in Figure 2.46, a beam-type centrifuge with parallel arms, was installed at the soil mechanics laboratory of the Tokyo Institute of Technology in 1995. It features a 2.45 m radius of rotation and platforms for holding the model container and counterbalancing weight. Data acquisition is accomplished through electrical slip rings and an optical rotary joint, allowing the signal transmission to amplifiers and a PC. A hydraulic rotary joint facilitates oil charging and discharging, while a hydraulic accumulator ensures an adequate flow rate for the high-performance 1D shaker. Full details and specifications can be found in Takemura et al. (1999), and some key specifications are mentioned in Table 2.6.

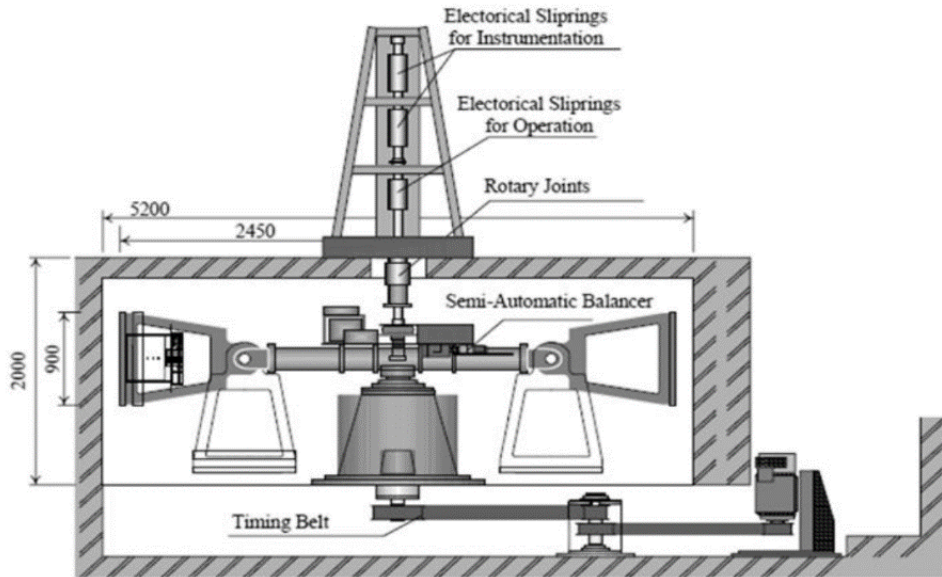


Figure 2.46: Tokyo Tech Mark III centrifuge.

Table 2.6: Key specification of Tokyo Tech Mark III centrifuge

Radius	Platform radius	2.45m
	Effective radius	2.0 - 2.2m
Platform dimensions	Width	0.90m
	Depth	0.90m
	Maximum height	0.97m
Capacity	Maximum payload	50g.ton
	Maximum number of rotations	300rpm
	Maximum payload at 80-g	600kg
Electrical slip rings	For operation	18 chs
Rotary joints	Number of ports for air and water	2
	Working pressure for air and water	1MPa
	Number of ports for oil	2
	Working pressure for oil	21MPa
Optical rotary joints	Number of ports	4

References:

1. Abbs, A.F., 1983. Lateral pile analysis in weak carbonate rocks. In Geotechnical practice in offshore engineering (pp. 546-556). ASCE.
2. Al Atik, L., Sitar, N., 2010. Seismic Earth Pressures on Cantilever Retaining Structures. *J. Geotech. Geoenviron. Eng.* 136, 1324–1333. [https://doi.org/10.1061/\(ASCE\)GT.1943-5606.0000351](https://doi.org/10.1061/(ASCE)GT.1943-5606.0000351)
3. Atkinson, J.H., 1991. Experimental determination of stress-strain-time characteristics in laboratory and-in-situ tests. General report. In Proc. 10th Eur. Conf. Soil Mech. and Fnd Engng (Vol. 3, pp. 915-956).
4. Bolton, M.D., Powrie, W., 1987. The collapse of diaphragm walls retaining clay. *Géotechnique* 37, 335–353. <https://doi.org/10.1680/geot.1987.37.3.335>
5. Bransby, P.L., Milligan, G.W.E., 1975. Soil deformations near cantilever sheet pile walls. *Géotechnique* 25, 175–195. <https://doi.org/10.1680/geot.1975.25.2.175>
6. Broms, B. B. (1995). “Design of sheet pile walls.” *Foundation engineering, Geotexts & Publicatio*
7. Carter, J.P., Kulhawy, F.H., 1992. Analysis of Laterally Loaded Shafts in Rock. *J. Geotech. Engrg.* 118, 839–855. [https://doi.org/10.1061/\(ASCE\)0733-9410\(1992\)118:6\(839\)](https://doi.org/10.1061/(ASCE)0733-9410(1992)118:6(839))
8. Chang, Y.L., 1937. Lateral pile loading tests. *Transaction of ASCE*, 102, pp. 273-276.
9. Cho, K.H., Gabr, M.A., Clark, S., Borden, R.H., 2007. Field $P - y$ curves in weathered rock. *Can. Geotech. J.* 44, 753–764. <https://doi.org/10.1139/t07-026>
10. Clayton, C. R. I., and Milititsky, J. (1986). *Earth pressure and earth retaining structures*, Surrey University Press, London.
11. Clayton, C.R., 1995. The standard penetration test (SPT): methods and use. *Construction Industry Research and Information Association*.
12. Conti, R., Madabhushi, G.S.P., Viggiani, G.M.B., 2012. On the behaviour of flexible retaining walls under seismic actions. *Géotechnique* 62, 1081–1094. <https://doi.org/10.1680/geot.11.P.029>
13. Cripps, J.C., Taylor, R.K., 1981. The engineering properties of mudrocks. *QJEGH* 14, 325–346. <https://doi.org/10.1144/GSL.QJEG.1981.014.04.10>
14. Day, R.W., 1997. Design and Construction of Cantilevered Retaining Walls. *Pract. Period. Struct. Des. Constr.* 2, 16–21. [https://doi.org/10.1061/\(ASCE\)1084-0680\(1997\)2:1\(16\)](https://doi.org/10.1061/(ASCE)1084-0680(1997)2:1(16))
15. Dobereiner, L., Freitas, M.H.D., 1986. Geotechnical properties of weak sandstones. *Géotechnique* 36, 79–94. <https://doi.org/10.1680/geot.1986.36.1.79>
16. Erbrich, C.T., 2004. A New Method for the Design of Laterally Loaded Anchor Piles in Soft Rock, in: *All Days*. Presented at the Offshore Technology Conference, OTC, Houston, Texas, p. OTC-16441-MS. <https://doi.org/10.4043/16441-MS>
17. Farmer, I.W., Farmer, I.W., 1983. *Engineering behaviour of rocks*, 2nd ed. ed. Chapman and Hall, London ; New York.
18. Fukushima, S., Tatsuoka, F., 1984. Strength and Deformation Characteristics of Saturated Sand at Extremely Low Pressures. *Soils and Foundations* 24, 30–48. https://doi.org/10.3208/sandf1972.24.4_30
19. GEOCEDHG (Geotechnical Engineering Office, Civil Engineering Department, Hong Kong, 1993. *Geoguide1 “ Guide to Retaining Wall Design”*.
20. Gopal Madabhushi, S.P., Chandrasekaran, V.S., 2005. Rotation of Cantilever Sheet Pile Walls. *J. Geotech. Geoenviron. Eng.* 131, 202–212. [https://doi.org/10.1061/\(ASCE\)1090-0241\(2005\)131:2\(202\)](https://doi.org/10.1061/(ASCE)1090-0241(2005)131:2(202))

21. Hoek, E., Carranza-Torres, C. and Corkum, B., 2002. Hoek-Brown failure criterion-2002 edition. *Proceedings of NARMS-Tac*, 1(1), pp.267-273.
22. Hoek, E., Brown, E.T., 1997. Practical estimates of rock mass strength. *International Journal of Rock Mechanics and Mining Sciences* 34, 1165–1186. [https://doi.org/10.1016/S1365-1609\(97\)80069-X](https://doi.org/10.1016/S1365-1609(97)80069-X)
23. Ichihara, M., 1983. Remarks on Mononobe's Earth Pressure Theory. *Tsuchi-to-kiso*, Japanese Society of Soil Mechanics and Foundation Engineering, 31(11).
24. International Press-in Association (IPA), 2016. *Press-in retaining structure: a handbook*, 1st ed.
25. Ishihara, K., 1996. *Soil behaviour in earthquake geotechnics*, Oxford engineering science series. Clarendon Press ; Oxford University Press, Oxford : New York.
26. Iwasaki, T., Tatsuoka, F., 1977. Effects of Grain Size and Grading on Dynamic Shear Moduli of Sands. *Soils and Foundations* 17, 19–35. https://doi.org/10.3208/sandf1972.17.3_19
27. Iwasaki, T., Tatsuoka, F., Takagi, Y., 1978. Shear Moduli of Sands under Cyclic Torsional Shear Loading. *Soils and Foundations* 18, 39–56. <https://doi.org/10.3208/sandf1972.18.39>
28. Johnston, IW, 1995. Rational determination of the engineering properties of weak rocks, *Proc. ICE, Geotechnical Engineering*, 177.86-92
29. Jo, S.-B., Ha, J.-G., Yoo, M., Choo, Y.W., Kim, D.-S., 2014. Seismic behavior of an inverted T-shape flexible retaining wall via dynamic centrifuge tests. *Bull Earthquake Eng* 12, 961–980. <https://doi.org/10.1007/s10518-013-9558-9>
30. Kanji, M.A., 2014. Critical issues in soft rocks. *Journal of Rock Mechanics and Geotechnical Engineering* 6, 186–195. <https://doi.org/10.1016/j.jrmge.2014.04.002>
31. Kim, D.-S., Kim, N.-R., Choo, Y.W., Cho, G.-C., 2013a. A newly developed state-of-the-art geotechnical centrifuge in Korea. *KSCE J Civ Eng* 17, 77–84. <https://doi.org/10.1007/s12205-013-1350-5>
32. Kim, D.-S., Lee, S.-H., Choo, Y.W., Perdriat, J., 2013b. Self-balanced earthquake simulator on centrifuge and dynamic performance verification. *KSCE J Civ Eng* 17, 651–661. <https://doi.org/10.1007/s12205-013-1591-3>
33. Kubo, K., 1964. A new method for the estimation of lateral resistance of piles. *Report of the port and harbour research institute*, 2(3), pp.1-37.
34. Kulhawy, F.H. and Phoon, K.K., 1993, October. Drilled shaft side resistance in clay soil to rock. In *Design and performance of deep foundations: Piles and piers in soil and soft rock* (pp. 172-183). ASCE.
35. Kunasegaram, V., Akazawa, S., Takemura, J., Seki, S., Fujiwara, K., Ishihama, Y. and Fujii, Y., 2015. Modeling of soft rock for a centrifuge study. *Proc. 12th GeoKanto*, pp.15-19.
36. Kunasegaram, V., Takemura, J., 2021. Deflection and failure of high-stiffness cantilever retaining wall embedded in soft rock. *International Journal of Physical Modelling in Geotechnics* 21, 114–134. <https://doi.org/10.1680/jphmg.19.00008>
37. Kutter, B., 1994. Design of a large earthquake simulator at UC Davis. In *Proceedings of The International Conference Centrifuge 94*, Singapore (pp. 169-175).
38. Liang, R., Yang, K., Nusairat, J., 2009. p-y Criterion for Rock Mass. *J. Geotech. Geoenviron. Eng.* 135, 26–36. [https://doi.org/10.1061/\(ASCE\)1090-0241\(2009\)135:1\(26\)](https://doi.org/10.1061/(ASCE)1090-0241(2009)135:1(26))
39. LoPresti, D.C.F., Pallara, O., Lancellota, R., Armandi, M., Maniscalco, R. 1993. *Wave Propagation Methods for Determining Stiffness of Geomaterials*. *Geotechnical Testing Journal*, ASTM, 164409424
40. Mair, R.J., UNWIN, 1993. UNWIN MEMORIAL LECTURE 1992. DEVELOPMENTS IN

- GEOTECHNICAL ENGINEERING RESEARCH: APPLICATION TO TUNNELS AND DEEP EXCAVATIONS. DELIVERED AT THE ICE ON 17 MARCH 1992. (ABRIDGED). (WINNER OF 1994 GEOTECHNICAL RESEARCH MEDAL). Proceedings of the Institution of Civil Engineers - Civil Engineering 97, 27–41. <https://doi.org/10.1680/icien.1993.22378>
41. Matlock, H., 1970. Correlation for Design of Laterally Loaded Piles in Soft Clay, in: All Days. Presented at the Offshore Technology Conference, OTC, Houston, Texas, p. OTC-1204-MS. <https://doi.org/10.4043/1204-MS>
 42. Matlock, H., Reese, L.C., 1960. Generalized Solutions for Laterally Loaded Piles. J. Soil Mech. and Found. Div. 86, 63–92. <https://doi.org/10.1061/JSFEAQ.0000303>
 43. Matsuzawa, H., Ishibashi, I., Kawamura, M., 1985. Dynamic Soil and Water Pressures of Submerged Soils. J. Geotech. Engrg. 111, 1161–1176. [https://doi.org/10.1061/\(ASCE\)0733-9410\(1985\)111:10\(1161\)](https://doi.org/10.1061/(ASCE)0733-9410(1985)111:10(1161))
 44. Murff, J.D., Hamilton, J.M., 1993. *P* -Ultimate for Undrained Analysis of Laterally Loaded Piles. J. Geotech. Engrg. 119, 91–107. [https://doi.org/10.1061/\(ASCE\)0733-9410\(1993\)119:1\(91\)](https://doi.org/10.1061/(ASCE)0733-9410(1993)119:1(91))
 45. Olson, R.E., 1993. Failure of a twenty-foot high retaining wall. Proceedings of 3rd international conference on case histories in geotechnical engineering, St. Louis, Missouri, June 1-4,1992, Paper No. 5.31
 46. Randolph, M., 2020. Keynote Lecture: Considerations in the Design of Piles in Soft Rock, in: Duc Long, P., Dung, N.T. (Eds.), Geotechnics for Sustainable Infrastructure Development, Lecture Notes in Civil Engineering. Springer Singapore, Singapore, pp. 1297–1312. https://doi.org/10.1007/978-981-15-2184-3_171
 47. Randolph, M.F., 1981. The response of flexible piles to lateral loading. Géotechnique 31, 247–259. <https://doi.org/10.1680/geot.1981.31.2.247>
 48. Reese, L.C., 1997. Analysis of Laterally Loaded Piles in Weak Rock. J. Geotech. Geoenviron. Eng. 123, 1010–1017. [https://doi.org/10.1061/\(ASCE\)1090-0241\(1997\)123:11\(1010\)](https://doi.org/10.1061/(ASCE)1090-0241(1997)123:11(1010))
 49. Reese, L.C., Cox, W.R., Koop, F.D., 1975. Field Testing and Analysis of Laterally Loaded Piles on Stiff Clay, in: All Days. Presented at the Offshore Technology Conference, OTC, Houston, Texas, p. OTC-2312-MS. <https://doi.org/10.4043/2312-MS>
 50. Reese, L.C., Welch, R.C., 1975. Lateral Loading of Deep Foundations in Stiff Clay. J. Geotech. Engrg. Div. 101, 633–649. <https://doi.org/10.1061/AJGEB6.0000177>
 51. Rifaat, I., 1935. Die Spundwand als Erddruckproblem: das Spundwandproblem mit Berücksichtigung der Erddeformation und der Wandelastizität. ETH Zurich. <https://doi.org/10.3929/ETHZ-A-000112729>
 52. Rowe, P.W., 1956. The Single Pile Subject to Horizontal Force. Géotechnique 6, 70–85. <https://doi.org/10.1680/geot.1956.6.2.70>
 53. Sawangsuriya, A., 2012. Wave Propagation Methods for Determining Stiffness of Geomaterials, in: Giovine, P. (Ed.), Wave Processes in Classical and New Solids. InTech. <https://doi.org/10.5772/48562>
 54. Sawangsuriya, A., Bosscher, P.J., Edil, T.B., 2005. Alternative Testing Techniques for Modulus of Pavement Bases and Subgrades, in: Geotechnical Applications for Transportation Infrastructure. Presented at the 13th Great Lakes Geotechnical and Geoenvironmental Conference, American Society of Civil Engineers, Milwaukee, Wisconsin, United States, pp. 108–121. [https://doi.org/10.1061/40821\(181\)9](https://doi.org/10.1061/40821(181)9)
 55. Schofield, A.N., 1980. Cambridge Geotechnical Centrifuge Operations. Géotechnique 30,

- 227–268. <https://doi.org/10.1680/geot.1980.30.3.227>
56. Takemura, J., Kondoh, M., Esaki, T., Kouda, M., Kusakabe, O., 1999. Centrifuge Model Tests on Double Propped Wall Excavation in Soft Clay. *Soils and Foundations* 39, 75–87. https://doi.org/10.3208/sandf.39.3_75
 57. Terzaghi, K., 1934. Large retaining-wall tests. I. Pressure of dry sand. *Engineering News-Record*, 102(20).
 58. Terzaghi, K. (1934b). “Large retaining wall tests. II. Pressure of dry sand.” *Eng. News-Rec.*, 259–262
 59. Terzaghi, K., 1955. Evaluation of Coefficients of Subgrade Reaction. *Géotechnique* 5, 297–326. <https://doi.org/10.1680/geot.1955.5.4.297>
 60. Terzaghi, K. and Peck, R.B., 1967. *Soil mechanics in engineering practice* (No. 624.151 T47 1967).
 61. USDA-NRCS, United State Department of Agriculture, Natural Resource Conservation Service, 2012. *National Engineering Handbook. Engineering Classification of Rock Materials. Part 631.Ch- 4. (210–VI–NEH, Amend. 55, January 2012).*
 62. Welch, R.C., 1972. *Lateral load behavior of drilled shafts.* The University of Texas at Austin.

Chapter 3

Mechanical behaviour of laterally loaded single pile socketed in soft rock

3.1 Introduction:

Before conducting a complex centrifuge model, it is necessary to know about the critical parameters that can affect the complex centrifuge model results. This chapter studies the critical conditions that could affect the behaviour to model the CSTP wall embedded in soft rock subjected to dynamic loading. The primary purpose of this chapter is to:

1. To investigate the mechanical properties of the model steel tubular pile used in the CSTP wall model preparation.
2. To explain the preparation of the model soft rock ground and the mechanical properties of the model soft rock ground.
3. To conduct a simple 1g pile loading test to investigate the effect of rock socketing depth, loading height, and in-fill condition on the lateral response of the pile.
4. To understand the applicability of the 1g model by comparing it with the actual centrifuge test model.

3.2 Mechanical properties of model pile:

3.2.1 Model preparation and test conditions:

In this research, a 1g lateral loading test was performed on model steel tubular piles with a diameter of $\Phi=40\text{mm}$ and thickness of $t=0.5\text{mm}$ with $(\Phi/t=80)$. The application of large-diameter piles ($\Phi>1.5\text{m}$) has increased in the past decades to construct retaining structures (Takemura, 2022). In this research, a pile diameter of 40mm was used considering the container width so that plane strain conditions could be maintained. The thickness of the pile was determined using API (2014) guideline ($t=0.00635+\Phi/100$). The objectives of the pile calibration test were to investigate the nonlinear stress-strain behaviour, the symmetric response of tensile and compressive strains, and the point of bifurcation and failure mode under combined lateral and moment loads. Figure 3.1 illustrates the 2D view of the model setup. A stainless steel (SUS304) pile with Young's modulus (E) of 193 GPa and yield stress (σ_y) of 255 MPa was used to conduct the calibration. Two aluminium pile caps (see Figure 3.2 (a) and (b)) were firmly fixed at the top and bottom of the pile. The upper pile cap had a socketing depth of 15mm, while the bottom pile cap had a socketing depth of 45mm. The top pile cap provided a solid loading head, and the bottom pile cap created an unplugged ground condition, as shown in Figure 3.2 (d). The pile was securely fixed inside a pile holder (as shown in Figure 3.2 (c)) with a dimension of 160mm x 60mm x 60mm, which was bolted to the container bottom (Figure 3.1).

To measure strains, the model pile was instrumented with individual axial tension (ϵ_t) and compression (ϵ_c) strain gauges, as well as bending strain and shear strain gauges, at various locations along the pile from the fixed end (Figure 3.1). Strain measurements were made using a

Whitestone bridge circuit. Figure 3.3 depicts the bridge connections made for strain measurement from the shear strain gauges. By making a 45° angle, the strain gauges were pasted on the two sides of the pile parallel to the loading direction.

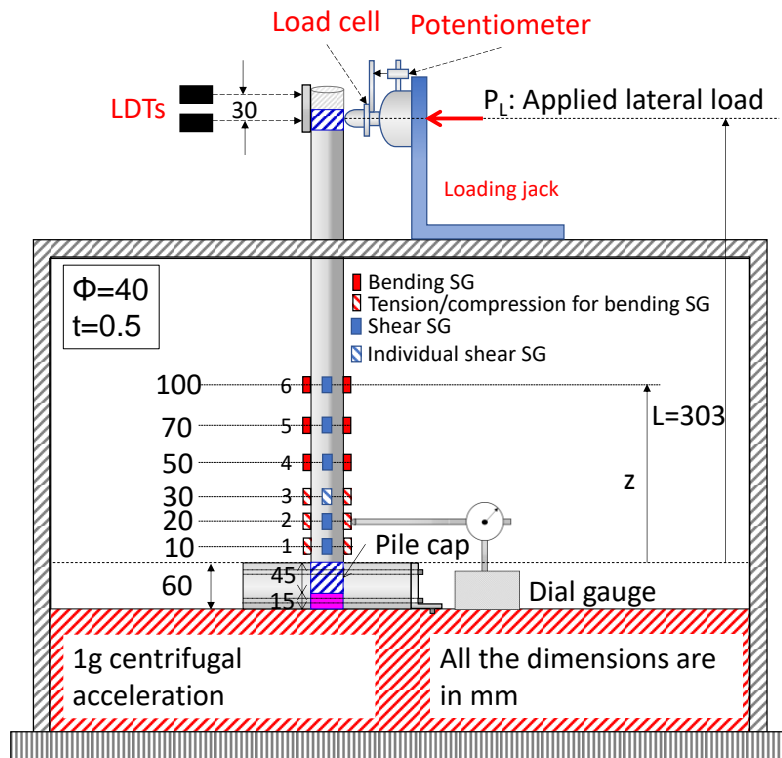


Figure 3.1: 2D view of model pile calibration test setup.

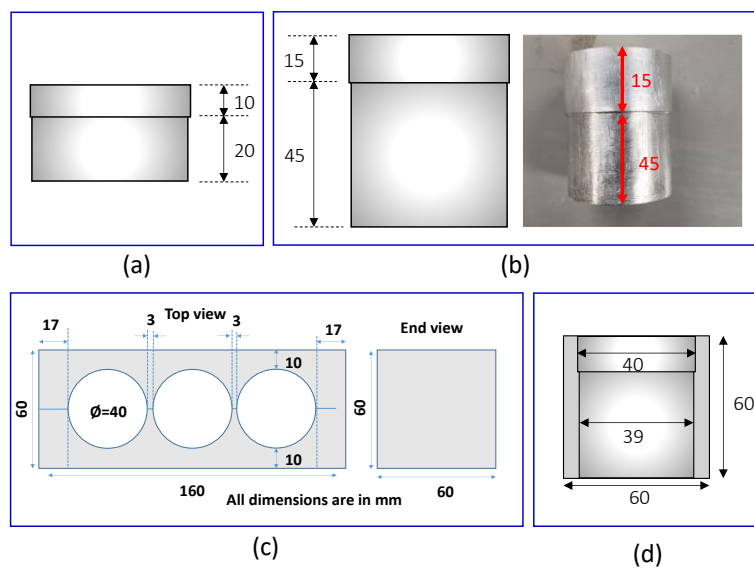


Figure 3.2: a) Pile cap used at top (b) Pile cap used at bottom (c) Pile holder used as fixed support (d) Pile socketing condition inside the support.

The process used to level the strain gauge wires is shown in Figure 3.3 (b). Figure 3.3 (c) shows the bridge box connection made to measure the strain. During the conversion of the strain to shear strain by using Equation 3.1, it should be multiplied by 2. Bending strain and shear strain were measured using a full-bridge Wheatstone circuit, while axial strain was measured using a half-bridge Wheatstone circuit.

$\gamma = 2 \times \epsilon$ at 45° angle strain gauge Equation 3.1

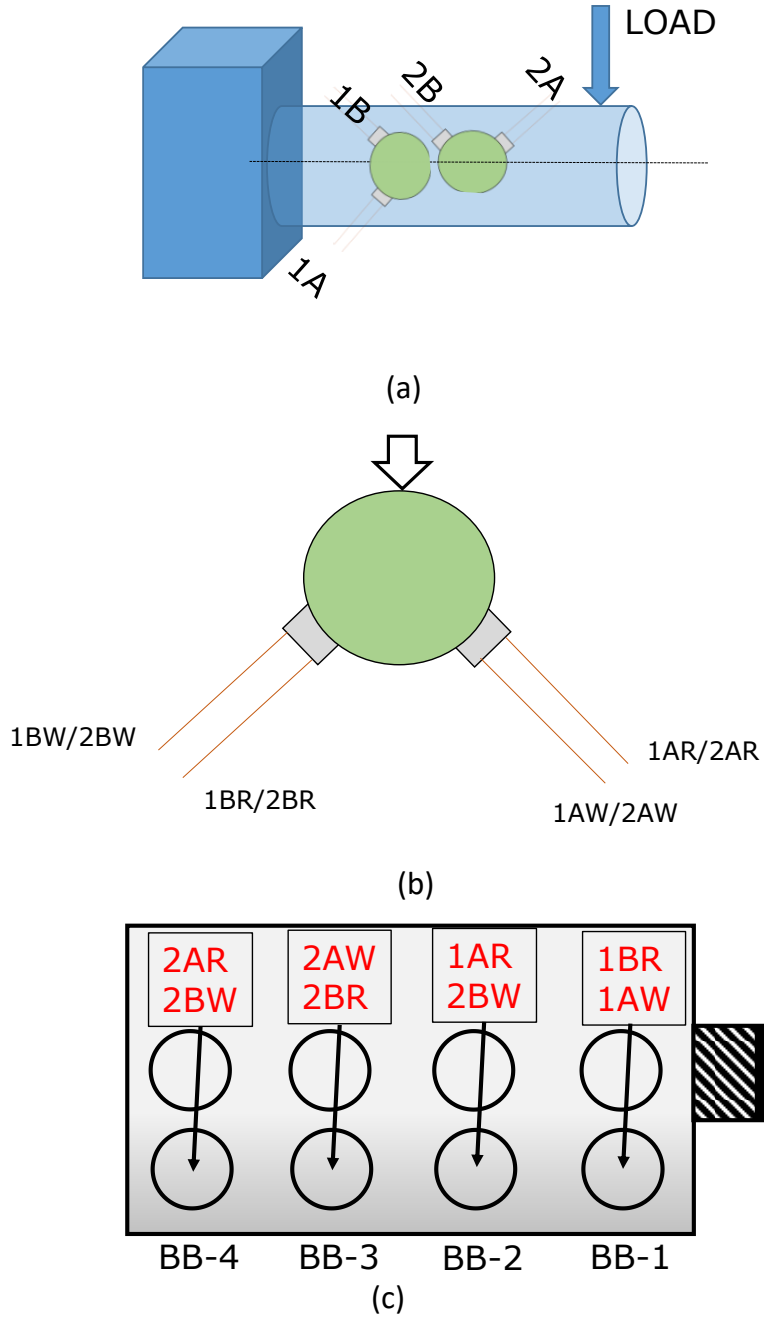


Figure 3.3: Shear strain measurement technique (a) positioning of shear strain gauge on pile (b) leveling of strain gauge wire (c) Bridge box connection.

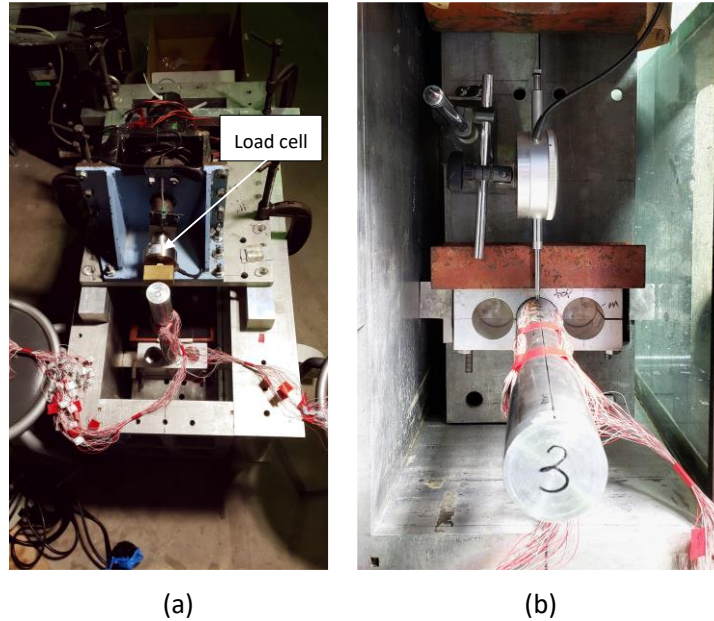


Figure 3.4: Test setup (a) model setup before conducting the test (b) top view of the model setup.

The load was applied at the pile top by using a load cell (Figure 3.4 (a)) which has a capacity of 5kN. The pile was calibrated under one-way cyclic loading with increasing cyclic displacement amplitudes at the pile head until structural buckling near the fixed end was observed. Two Laser Displacement Transduce (LDTs) were placed at the top to measure the pile top displacement and the pile top rotation at the loading point. Also, a dial gauge was used to measure the displacement near the support (about 10mm from the support).

3.2.2 Experimental measurement:

Figure 3.5 depicts the time series of measured pile top displacement by two LDTs, dial gauge (D.G.) and load cell. As shown in Figure 3.5, a total of 9 cycles of loading were applied by increasing the amplitude of loading. After 9 cycles, monotonic loading was applied until the ultimate failure occurred.

Figure 3.6 depicts the typical measurement by the strain gauge. Figure 3.6 (a) and (b) show the individual tensile and compressive strain measurements by strain gauge located at $Z/\Phi=0.25$ and 0.5, respectively. The bending strain was measured by converting the millivolt (mV) measurements from the data logger using the Wheatstone bridge principle. Figure 3.6 (c) shows the shear strain measurement by two shear gauges at $Z/\Phi=0.5$ and 0.75, respectively. Similarly, the shear strain was measured by converting the millivolt (mV) measurements from the data logger using the Wheatstone bridge principle.

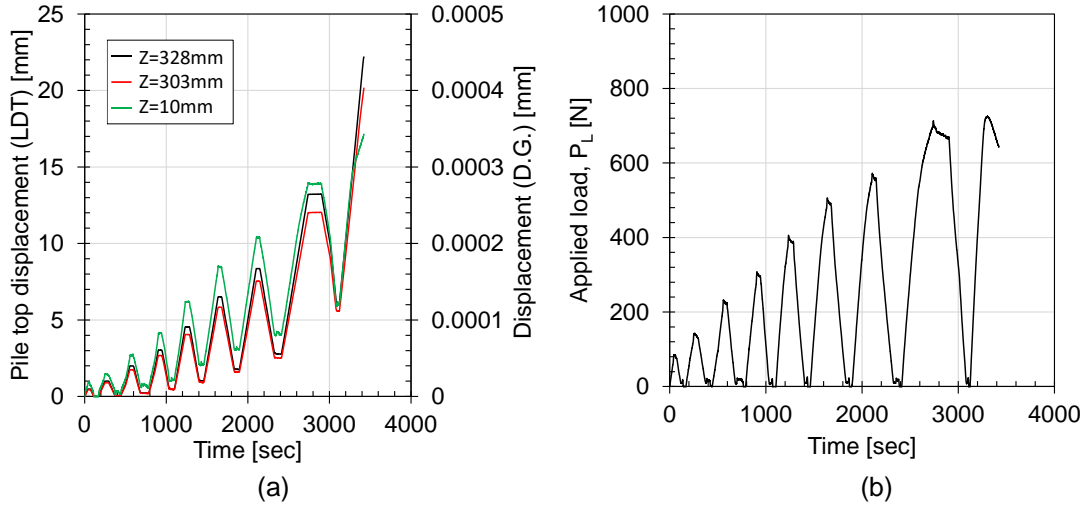


Figure 3.5: Time series of measurement (a) pile displacement by LTDs and dial gauge (b) applied load by the load cell.

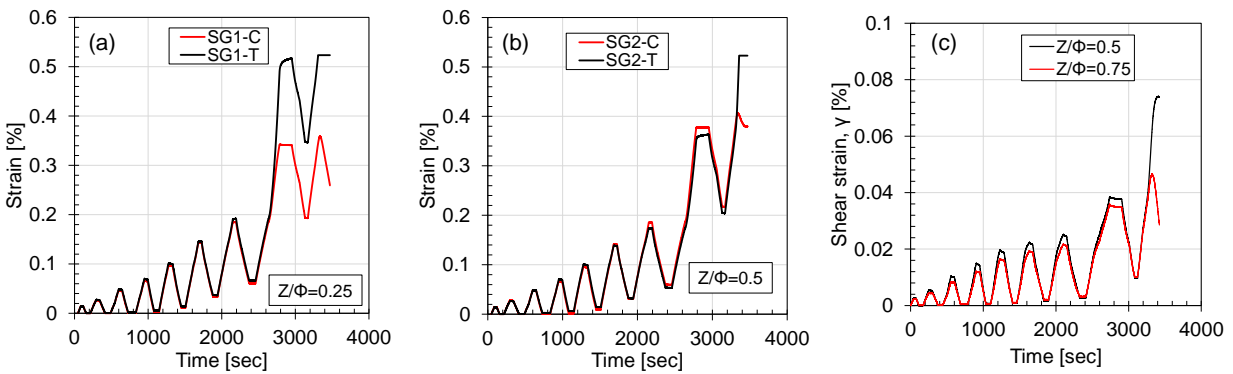


Figure 3.6: Typical measurements by strain gauges (a) individual bending strain at $Z/\Phi=0.25$ (b) individual bending strain at $Z/\Phi=0.5$ (c) shear strain measurement at $Z/\Phi=0.5$ and 0.75 .

Good measurement accuracy was achieved in the bending strain measurements. However, in the case of shear strain measurement, unintentional errors like pasting the strain gauge in perfect alignment and the adhesion between the pile and strain gauge might affect the measurement quality. Based on the measurement, this kind of effect might not significantly affect the bending strain measurement.

3.2.3 Experimental results:

Figure 3.7 shows the variation of applied lateral load (P_L) with pile top displacement (δ_i) at the loading point and the variation of applied moment load M_{La} to the measured bending strain (ϵ). As shown in Figure 3.7 (a), the reloading curve takes a unique shape, which can be considered as the

envelope of the cyclic loading. This unique curve is termed the ‘backbone’ curve in this research. With the increase of applied lateral load and moment load per cycle, the accumulation of residual displacement and residual strain takes place. As the main purpose of the calibration test was to understand the stress-strain behaviour measured by the strain gauge, different definitions used to discuss the behaviour are shown in Figure 3.7 (b).

Figure 3.8 depicts the variation of the applied bending strain with the measured bending strain. With the applied strain, the measured strain was increased with the increase of distance from the support. The accumulation of residual strain with the increase in the number of cycles was confirmed at all the locations. This accumulation of residual strain was significant for strain gauges located near the support rather than far from the support. The effect of buckling formation on the strain measurement was confirmed by large residual strain during the final cycle at $Z/\Phi=0.25$ and 0.5 . Also, before the final cycle, no change in the slope of the loading and reloading cycle was confirmed at $Z/\Phi=0.25$ and 0.5 . After the final cycle, the slope of the unloading curve was decreased than the slope of loading.

The variation of applied load to the measured shear strain at different locations from the support is depicted in Figure 3.9. Using Equation 3.1, the shear strain was calculated from the measured strain by the shear gauge. It was observed that the applied load and the variation of the measured shear strain follow almost linear trends before the final cycle. After the buckling formation, the accumulation of residual shear stain was confirmed at different depths after the final loading. Good agreement in the measurement at $Z/\Phi=0.75$ and 1.75 was confirmed. However, at $Z/\Phi=0.5$ and 1.25 , the measurement might be affected by the previously mentioned unintentional error.

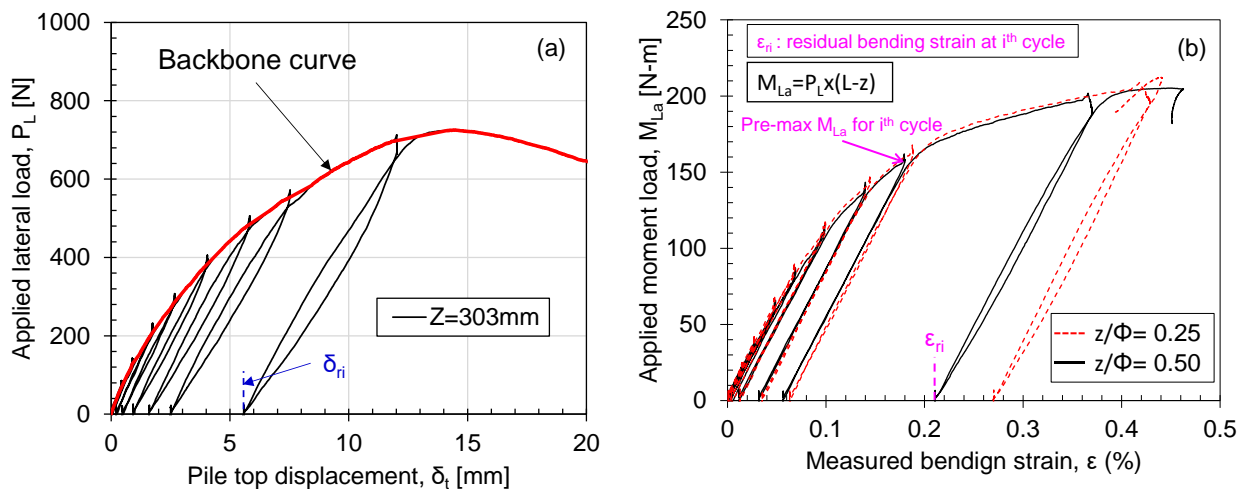


Figure 3.7: Typical loading (a) variation of applied lateral load (P_L) with pile top displacement (δ_t) (b) variation of applied moment load M_{La} to the measured bending strain (ϵ).

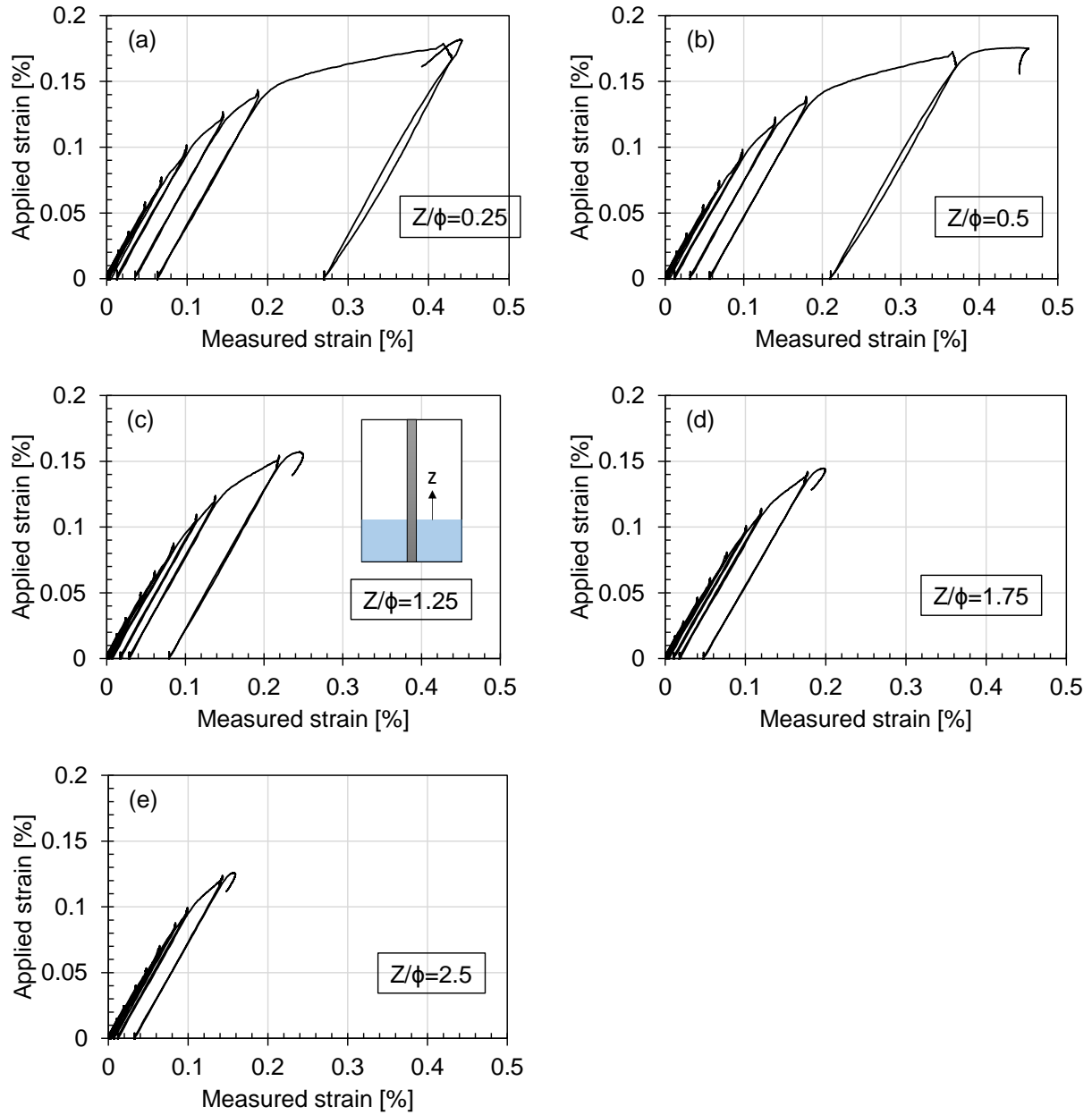


Figure 3.8: Variation of applied bending strain with measured bending strain at different locations from the support.

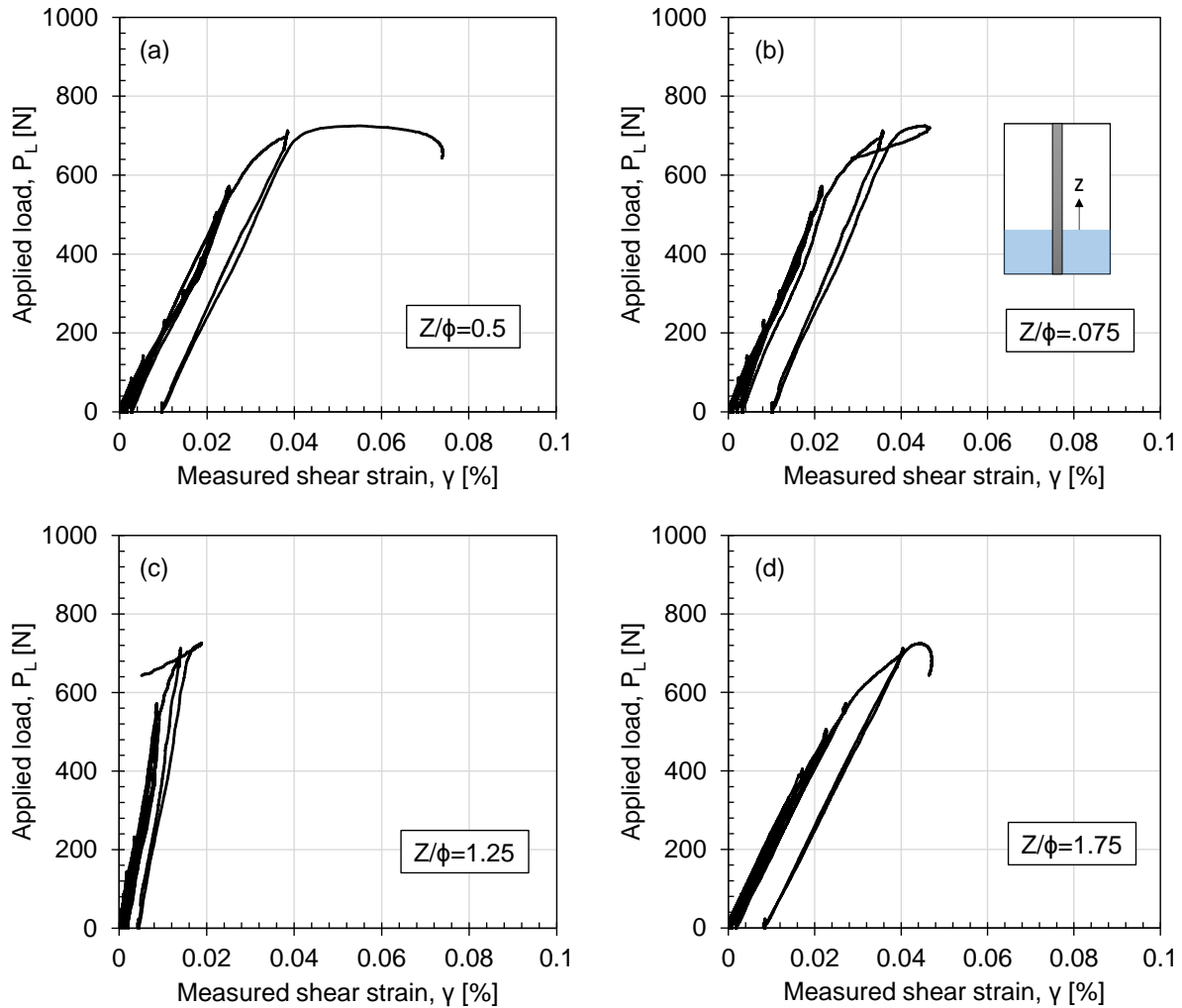


Figure 3.9: The variation of measured shear strain with the applied load.

3.2.4 Discussions:

Effect of nonlinearity on the bending strain measurements:

Figure 3.10 describes the variation of individual strain measured at the extension and compression side against the applied moment load with the physical evidence of pile buckling. A theoretical linear relationship is also shown in this figure to discuss the nonlinearity. From Figure 3.10 (a), a linear elastic relationship could be expected up to 65% of the theoretical yielding moment (M_y). Therefore, the application of Euler-Bernoulli's theorem could be reasonably adopted up to this limit. Although, some differences in the tension and compression strain could be observed earlier than 65% M_y . However, this discrepancy could be due to the unintentional difference in the relative position of the gauges. Figure 3.10 (a) also confirms that the compressive strain initiates the local buckling of the tubular piles in ultimate condition. In the ultimate condition, an elephant foot-type buckling was physically confirmed, similar to the observation done by Kunasegaram and

Takemura (2022). In the case of compressive strain at $z/\Phi=0.25$, a decreasing trend after the ultimate condition is observed, which agrees with the outward bucking of the piles.

The backbone curve obtained from the measured bending strain relationship with applied moment load at different depths is shown in Figure 3.10 (b). The bending strains dependency on the strain gauges location can be confirmed from this figure. As the location moves away from the fixed end, the deviation from the linear elastic trend decreases.

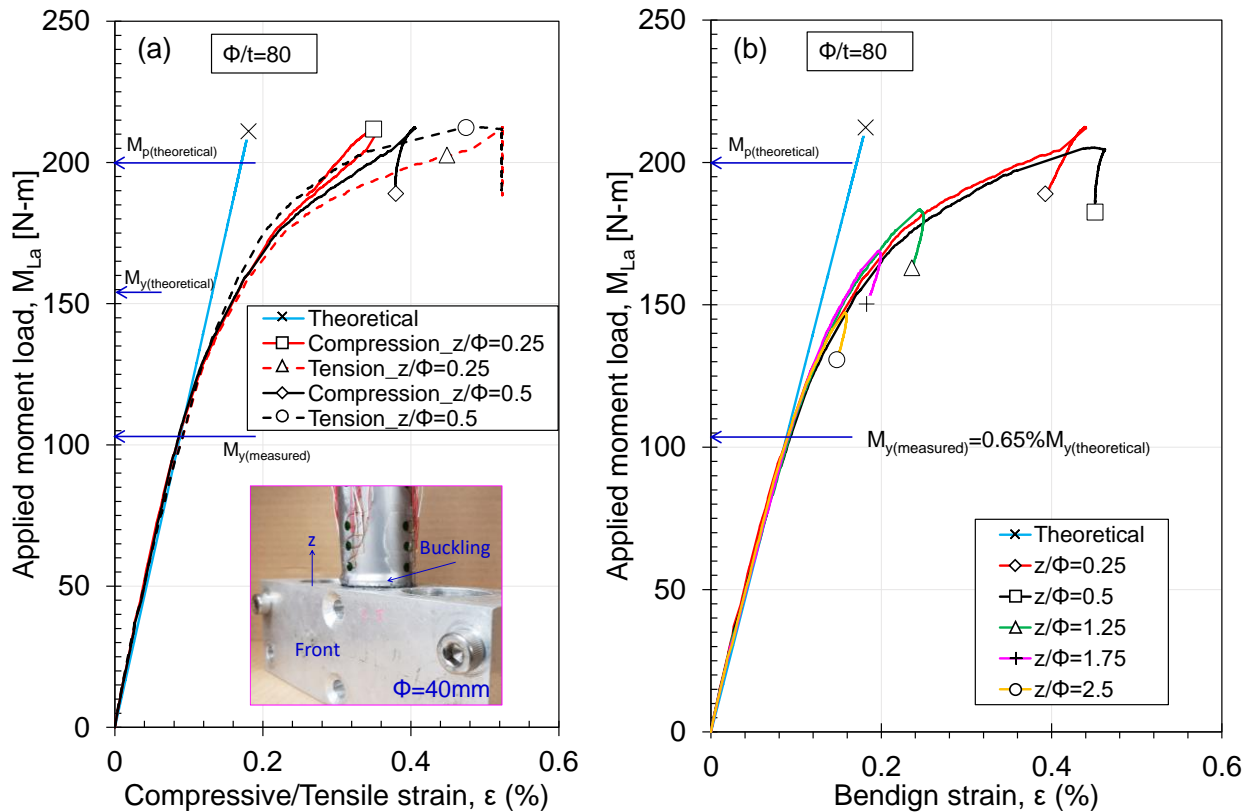


Figure 3.10: (a) Variation of extension and compression strain with applied moment load; (b) Variation of measured bending strain with applied moment load.

Figure 3.11 depicts the residual bending strain accumulation with the applied pre-max moment load. Before $65\%M_{y(theoretical)}$, no effect of the location could be confirmed. After the final cycle, large residual strain can be confirmed at $z/\Phi=0.25$ and 0.5 due to bucking. Although no effect of the location on the accumulation of residual strain can be confirmed before $65\%M_{y(theoretical)}$, however some residual strain (about 0.01%) can be confirmed before that limit. Therefore, some plastic deformation can be expected to occur even before reaching the actual yielding moment, but considering the magnitude, it can be ignored.

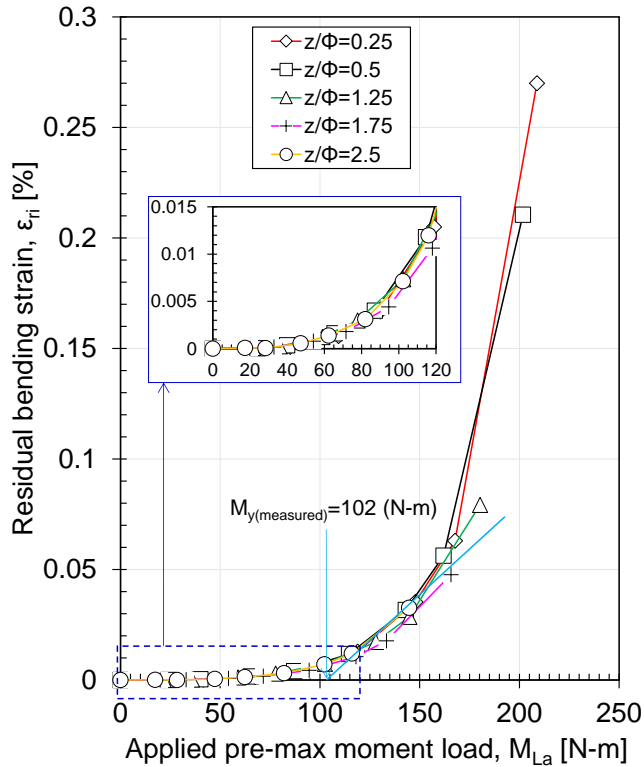


Figure 3.11: Variation of residual bending strain with applied pre-max moment load.

Applicability of shear force measurement:

Figure 3.12 shows the backbone curve of the variation of measured shear force with applied load. The measured shear force is calculated from the measured shear strain by using Equation 3.1

$$F_v = \frac{G \cdot \gamma \cdot t \cdot I}{Q} \dots \dots \dots \text{Equation 3.2}$$

Where,

$$G = \text{modulus of shear strain} = \frac{E}{2(1+\mu)}$$

γ = shear strain calculated by Equation 3.1

t = thickness of the pile

I = moment of inertia

Q = moment of area

E = Young's modulus of pile

μ = poisson's ratio of pile

A reference line is drawn to compare the accuracy of the measurement. As mentioned earlier, the shear force measurement is very much susceptible to measurement conditions. The shear force at $Z/\Phi=0.5$ shows significant variation from the beginning from the reference line due to the large plastic deformation at that location. From the other three locations, no significant deviation from the reference line can be confirmed up to an applied load of 400N (equivalent to 1MN, in prototype scale under 50g). By avoiding human error, this shear force measurement technique can be reasonably applied up to the limit of 1MN on a prototype scale.

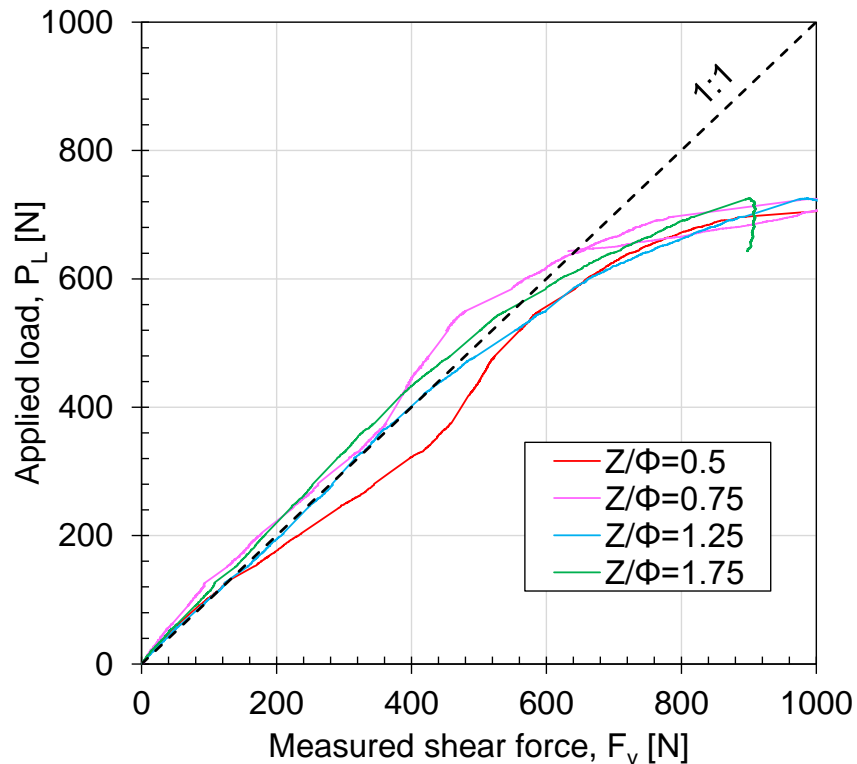


Figure 3.12: Variation of measured shear force with applied load.

3.3 Preparation of soft rock ground layer:

3.3.1 Material properties and the estimation of materials:

Portland cement [$G_s=3.14$] manufactured by Taiheiyo Cement has been mixed with the Sumi-clay and Toyoura sand to prepare the soft rock mixture. Sumi clay used in this study was processed by Sumitomo Osaka Cement Co., Ltd., having a specific gravity (G_s) of 2.67, liquid limit (LL) of 34% and plastic limit (PL) of 19%. The plasticity index of the sumi clay was estimated as 15% based on the difference between liquid limit and plastic limit. From this, it can be confirmed that the swelling potential of this clay is low, and it can be considered as a normal clay. The property of the Toyoura sand can be learned from Figure 3.13. Figure 3.14 and Figure 3.15 shows the material used to prepare the artificial soft rock.

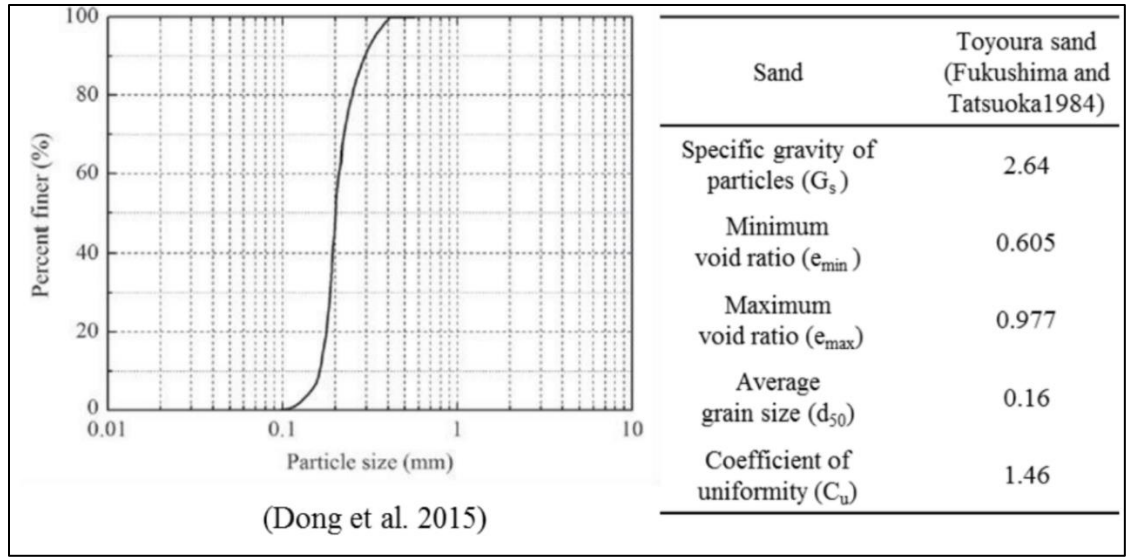


Figure 3.13: Grain size distribution and physical properties of Toyoura sand (Dong et al. 2015).



Figure 3.14: Material used for the modelling of the artificial soft rock.



Figure 3.15: Sand and clay used in this research.

A similar ground condition was ensured for all models, and the mixing conditions followed in all models are as follows:

$$\frac{\text{water}}{\text{cement}} = 395\% \text{ by weight}$$

$$\frac{\text{Clay}}{\text{Sand}} = 30:70 \text{ by weight}$$

Moisture content = 21.5%.

The required volume mixed was considered based on the container dimension and layer height. However, 20% of the extra volume was considered to avoid any lack of material in case of an accident. A sample calculation for the required volume mix of 28 litres, including 20% extra, is described below:

$$\text{Water} = 3.95 \text{ Cement} \dots \dots \text{Equation 3.3}$$

$$\text{Clay} = \frac{3}{7} \text{ Sand} \dots \dots \text{Equation 3.4}$$

$$\frac{\text{Water}}{\text{Clay} + \text{Sand} + \text{Cement}} = 0.215 \dots \dots \text{Equation 3.5}$$

$$\frac{28}{1000} = \frac{\text{Water}}{1000} + \frac{\text{Cement}}{3140} + \frac{\text{Clay}}{2670} + \frac{\text{Sand}}{2600} \dots \dots \text{Equation 3.6}$$

The calculated dry unit weights of cement, sand, clay, and water are 2.569 kg, 31.245 kg, 13.391 kg, and 10.149 kg. In reality, it is impossible to get the dry condition of these materials since they absorb a certain amount of moisture from the environment. Therefore prior to the mixing, it is important to estimate the existing moisture content of clay sand. From the experience of the writer, the measured moisture content of Toyoura sand used in this study was negligible as its purchased state. However, Semi clay poses about 1.4% - 2% moisture content, depending on the weather and preserved conditions. In order to model the mix exactly or closer to the target water-cement ratio, it is important to do the correction for existing moisture.

It was assumed that the existing moisture content of clay is 1.7%; then,

$$\frac{100}{101.7} \times \text{Bulk weight of clay} = 13.391 \text{ kg}$$

$$\text{Bulk weight of clay} = 13.618 \text{ kg}$$

$$\text{Moisture contribution from clay} = \frac{100}{101.7} \times 13.618 \text{ kg}$$

$$\text{Corrected amount of water to be added} = (10.149 - 0.227) = 9.922 \text{ kg.}$$

The above-mentioned calculation is subject to change based on the change of the required rock layer in the model and the dimension of the container.

Preparation of rock mixture:

Prior to the addition of water in to the mixture the dry sand –clay –cement was mixed well for 15 minutes to achieve uniformly distributed dry mix using the mixing machine as shown in Figure 3.17 (a). The cement before mixing with sand and clay was screed though the screener with sieve

opening of 425 μ shown in Figure 3.16. Upon completion of the dry state mixing, the required amount of water to maintain the moisture content was added to the mixing container and the slurry state mixing was continued by the mixing machine. Initial mixing under wet conditions was conducted for about 10 minutes; after that, the machine was stopped, and the wet slurry layer attached to the periphery of the mixing container was detached by a spatula, shown in Figure 3.17 (b) and mixed with the main mix. Subsequently, the mixing was continued for a further 30 minutes to achieve a well-saturated and uniform mix.



Figure 3.16: Screener to screen cement.

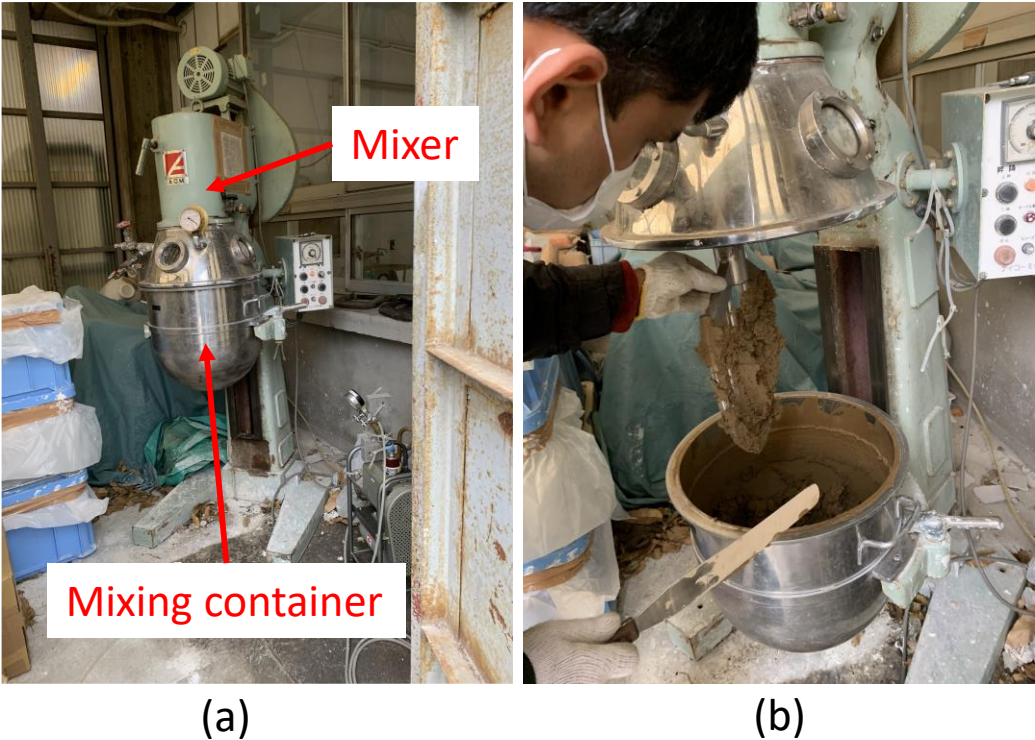


Figure 3.17: (a) mixing container attached with the mixing machine (b) cleaning of the periphery of the container and blade by spatula.

3.4 1g rock socketed pile loading test

3.4.1 Model preparation and test conditions:

Figure 3.18 depicts the 2D view of the two 1g model setups, which were conducted at the Tokyo Tech Mark III centrifuge facility Takemura et al. (1999). A rigid container measuring 700mm in length, 500mm in depth, and 150mm in width was used for both 1g model tests. Identical stainless steel (SUS304) piles with Young's modulus (E) of 193 GPa and yield stress (σ_y) of 255 MPa were used in both models. As shown in Figure 3.19, a solid circular pile cap with a 30mm and 45mm socketing depth was firmly fixed to form a solid loading head at the pile top for models 3 and 9, respectively. After fixing the pile cap, strain gauges were attached throughout the pile length to calculate the bending strain. After attaching the strain gauges to the pile, epoxy resin was used to coat the strain gauges so that the strain gauge didn't get damaged while installed inside the rock ground and the surrounding environment. After a minimum of one day of coating, a simple calibration, as shown in Figure 3.20 was performed to ensure the performance of the strain gauges. The mechanical properties and the notation of the piles used in the two 1g model tests are presented in Table 3.1.

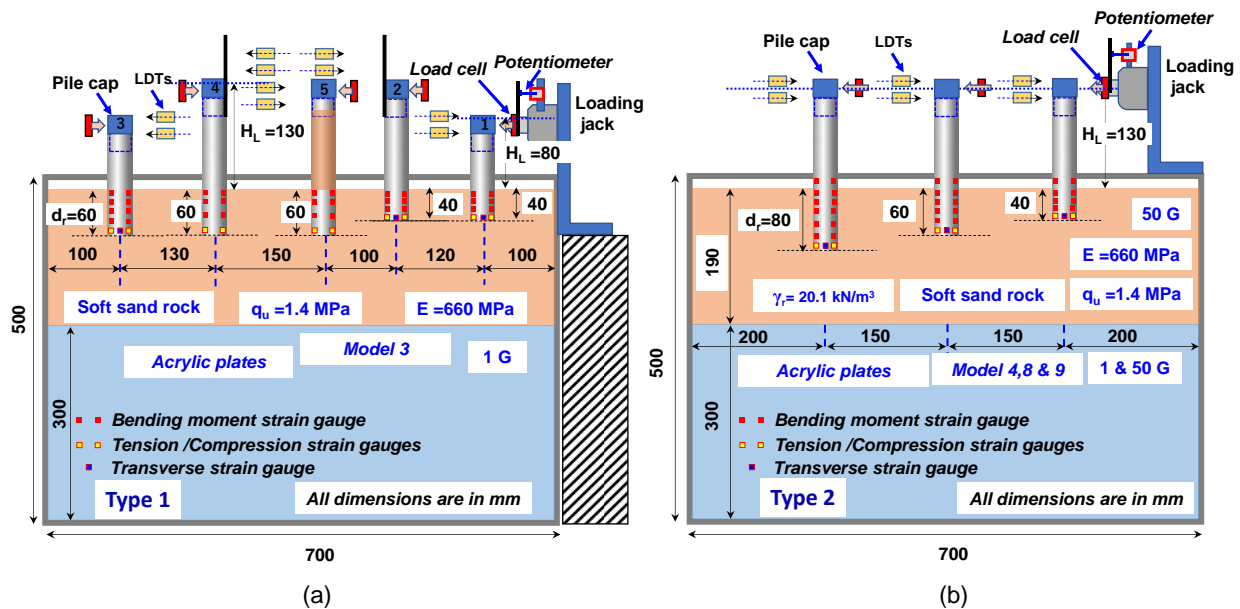


Figure 3.18: 2D view of 1g rock socketed pile loading test (a) Model 3 (b) Model 9.

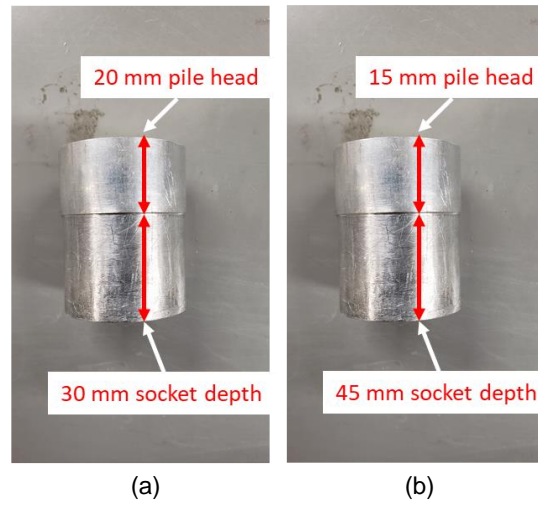


Figure 3.19: pile cap used in (a) Model 3 and (b) Model 9.



Figure 3.20: Simple model pile calibration test.

Table 3.1: Test conditions and the properties of 1g model pile

Model no. (g level)	Pile notation (Pile no.)	Rock socketing depth: d_r [d_r/Φ]	Loading height: H_L [H_L/Φ]	Pile properties
Model 3 1g	SP-SR-40	40mm [1.0]	130mm [3.25]	$\Phi = 40$ mm (2 m) $t = 0.5$ mm (25mm) $EI = 2.34 \times 10^{-6}$ GNm ² (14.6 GNm ²) $M_y = 1.54 \times 10^{-4}$ MNm (19.3 MNm) $M_p = 1.99 \times 10^{-4}$ MNm (24.9 MNm)
	SP-SR-60	60mm [1.5]		
	SP-SR-60-Fill	60mm [1.5]		
	SP-SR-40-1	40mm [1.0]	80mm [2.0]	
SP-SR-60-L	60mm [1.5]			
Model 9 1g	SP_SR_40 [#]	40mm [1.0]	130mm [3.25]	
	SP_SR_60 [#]	60mm [1.5]		
	SP_SR_80 [#]	80mm [2.0]		

EI: Pile flexural rigidity, M_y : Bend moment causing pile yielding, M_p : bending moment causing pile plastic failure, *Preloaded prior to the test without instrumentation before centrifugation, [§]: prototype scales under 50g are given in parentheses

The model soft rock mixture was made by following the procedure mentioned in article 3.2. Figure 3.21 Figure 3.1 shows the common way to model ground preparation for the 1g model test. Before preparing the model ground, 0.5 mm thick Poly Tetra Fluoro Ethylene (PTFE) sheets were attached to both sides of the container to prevent the container wall from being affected by the cement-treated rock soil, as shown in Figure 3.21 (a). After attaching the PTFE sheets, a thick acrylic plate stack was tightly placed at the bottom of the container, reducing the depth to 200mm (see Figure Figure 3.21 (a)). The gap between the container wall and the acrylic plate was sealed with silicon rubber to prevent moisture loss during ground preparation, as shown in Figure 3.21 (b). As shown in Figure 3.21 (c), the rock ground was then made by compacting the mixture using a mechanical vibrator (See Figure 3.25 (b)) layer by layer every 30mm thickness, securing the target density up to the depth of 190mm. In the case of model 3, an acrylic compaction plate (see Figure 3.25) was used during layer-by-layer compaction. However, in the case of model 9 compaction, the initial three layers were done without using the acrylic compaction plate as the old plate was damaged and new plates took time to make. After making the ground, 10 mould samples were prepared for the conduction of the unconfined compression test, as shown in Figure 3.21 (d). The whole compaction process was tried to be finished within 1.5 hours before the solidification of cement.

An unconfined compression strength (UCS) test was conducted on the 14th-day mould sample. Also, a consolidated undrained (CU) triaxial test was conducted by the external company on the 14th day cured mould sample. Figure 3.22 (a) illustrates the variation of deviatoric stress (q) with axial strain (ϵ_a) (measured using a dial gauge) for three confining pressures (σ_3) of 50kPa, 100kPa, and 200kPa. Figure 3.22(a) confirms that there was a large increase in strength with increasing

confining pressure. Moreover, no effect of confinement was confirmed at a small strain level. Figure 3.22 (b) shows the variation of the secant stiffness with the unconfined compressive strength reported by Vijay and Takemura (2021) for two types of strain measurement methods, using a dial gauge and strain gauges. Additionally, the variation of E_{50} and UCS for the test shown in Figure 3.22 (a) is also shown in Figure 3.22 (b). The results indicate that the strength and stiffness measured by the dial gauge highly underestimate the strength and stiffness measured by the strain gauges. As proposed by Vijay and Takemura (2021), an unconfined compressive strength of 1.4 MPa and secant stiffness of 660 MPa were considered as representative strength and stiffness of the artificial model soft rock.

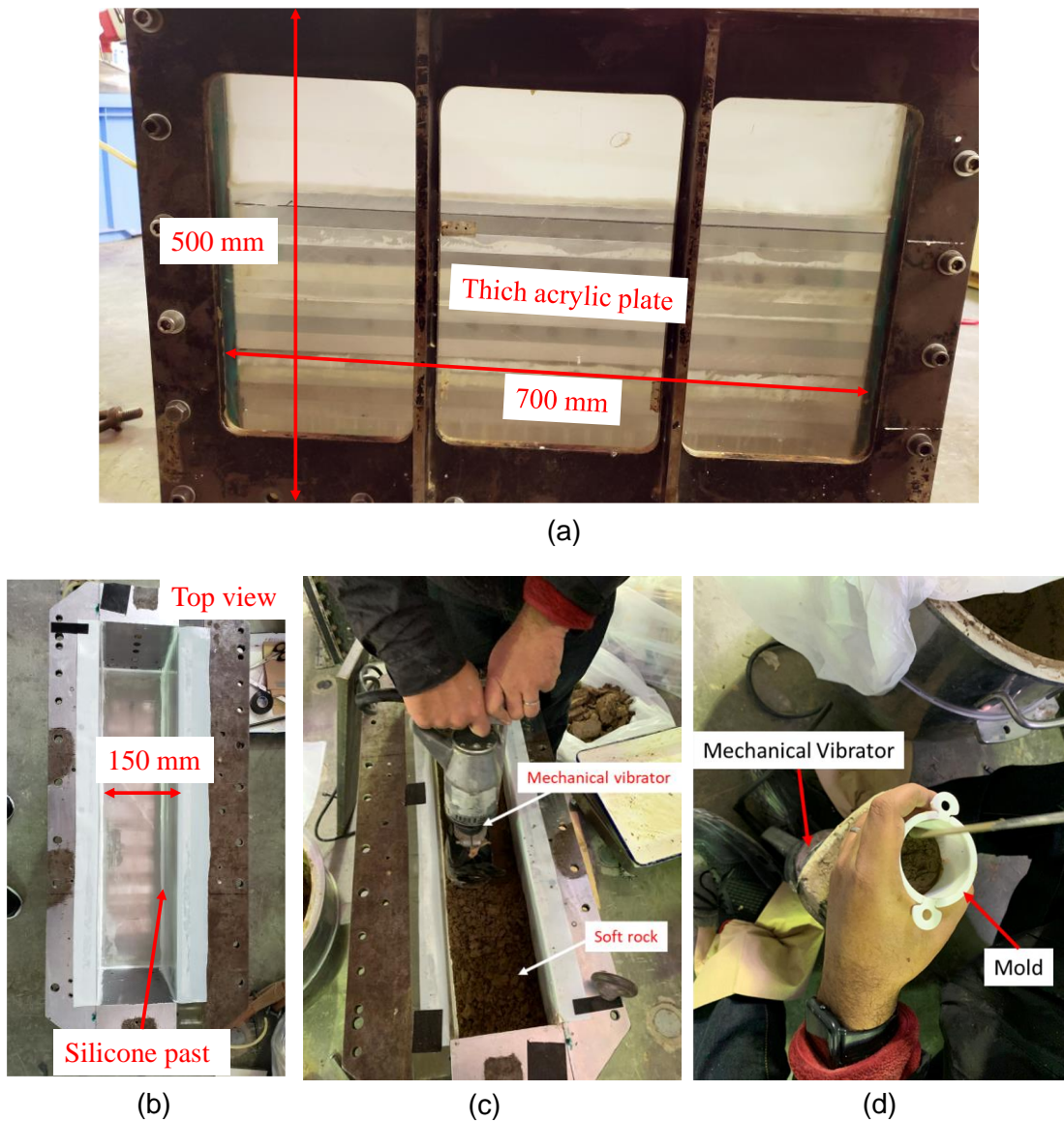


Figure 3.21: (a) side view of the model container with acrylic plate (b) top view of the model container with acrylic plate (c) preparation of model ground by compaction (d) preparation of mold sample for unconfined compression test.

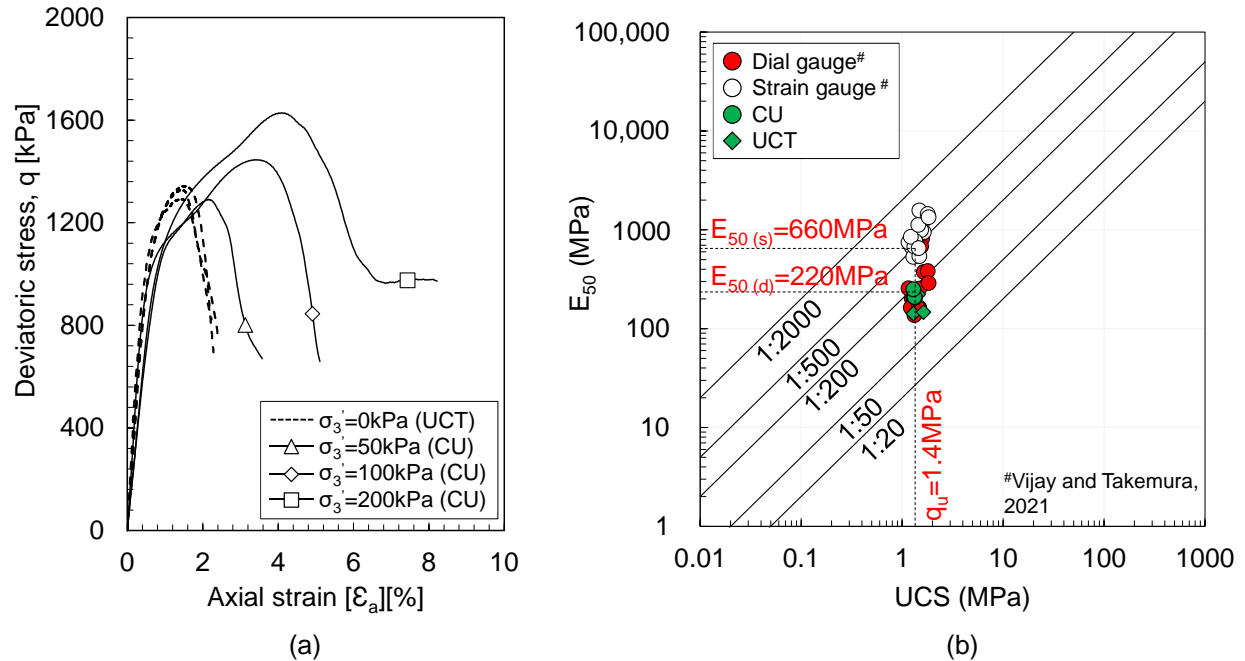


Figure 3.22: Mechanical properties of model soft rock (a) Consolidated undrained triaxial test result under different confining stress (b) Relationship between secant stiffness (E_{50}) with unconfined compressive strength (UCS).

The pile installation process into the unsolidified rock ground is depicted in Figure 3.23. As shown in Figure 3.23 (a), a guide was used to place the pile in the desired location. Figure 3.23 (b) shows the front view of the pile with a strain gauge passed on the pile and covered with epoxy resin. After installing each pile, the verticality and the tilting of the pile were checked by placing the balance on top of the pile. Finally, safety plates, as shown in Figure 3.23 (d), were placed to prevent horizontal or vertical movement of the pile. After that, wet towels were placed on the ground to facilitate the curing process. In the first 1g model test (Figure 3.18 (a)), the rock socketing depths (d_r) were 40mm and 60mm, and the loading heights (H_L) were 80mm and 130mm in model scale, respectively. The second 1g model test (Figure 3.18 (b)) employed three rock socketing depths of 40mm, 60mm, and 80mm with a loading height of 130mm in the model scale. In model 3, pile-5 (SP-SR-60-fill) was filled with rock up to the file top, as shown in Figure 3.18 (a). In all the tests conducted, the piles were socketed into a single layer of soft rock. Before conducting the test on the 14th day of curing time, strain gauges were affixed on the solidified rock surface at the front and back of the pile to measure the rock surface strain.

The wall top displacement has been measured by the LDT placed at the top of each pile. One-way horizontal cyclic load was applied by an electric loading jack to the pile top at 130mm and 80mm above the ground surface by controlling the displacement with a loading rate of 0.5 mm/min in the centrifuge. Bending, axial strain and rock surface strain were measured by strain gauge.

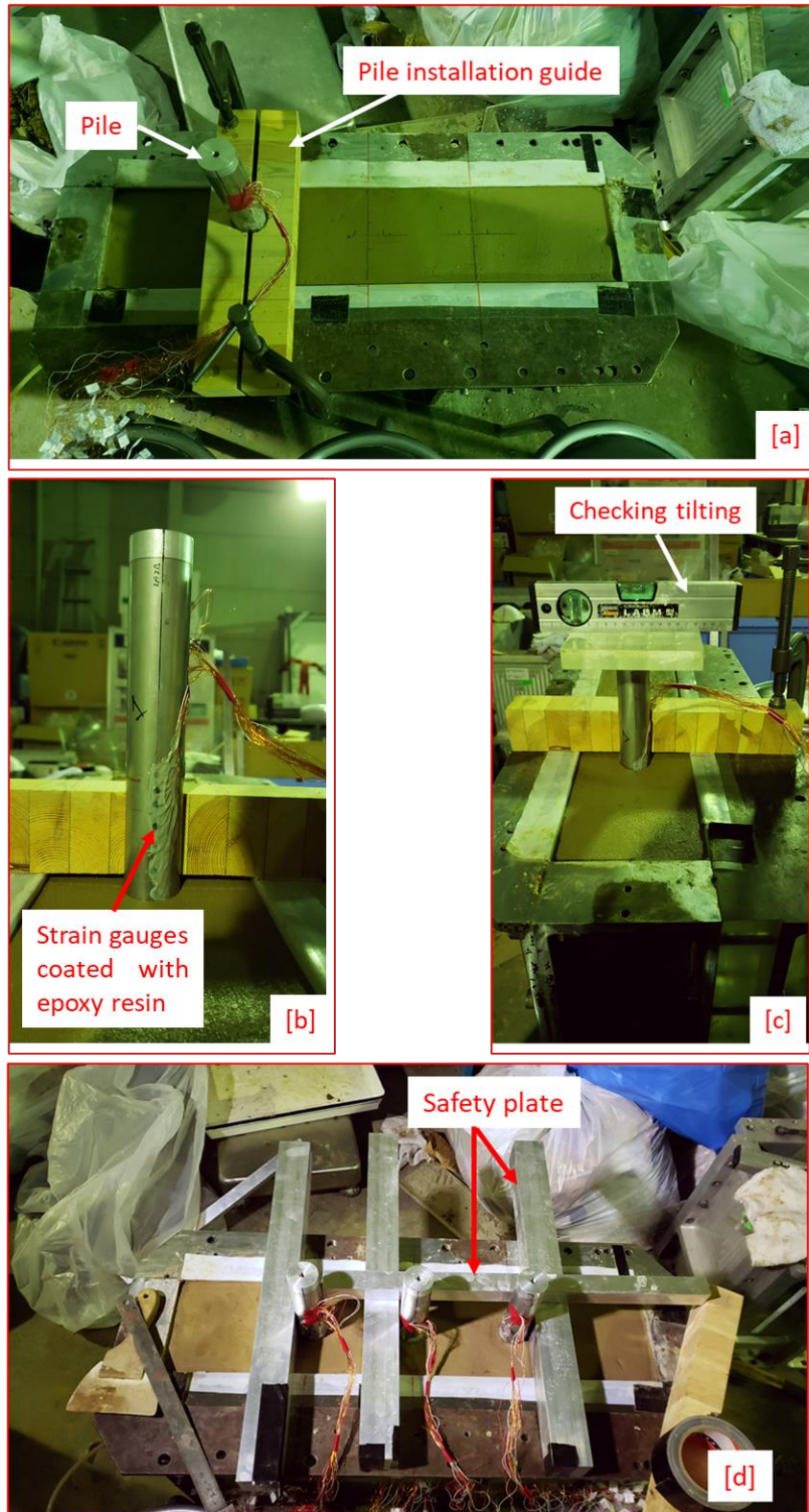


Figure 3.23: Pile installation process in the unsolidified ground (a) installation of the pile with the help of a guide (b) front view of the pile (c) checking of verticality (d) installed pile in with safety plate to restrict the settlement of the pile in unsolidified ground.

3.4.2 Sensors and instrument used in 1g rock socketed pile loading test:

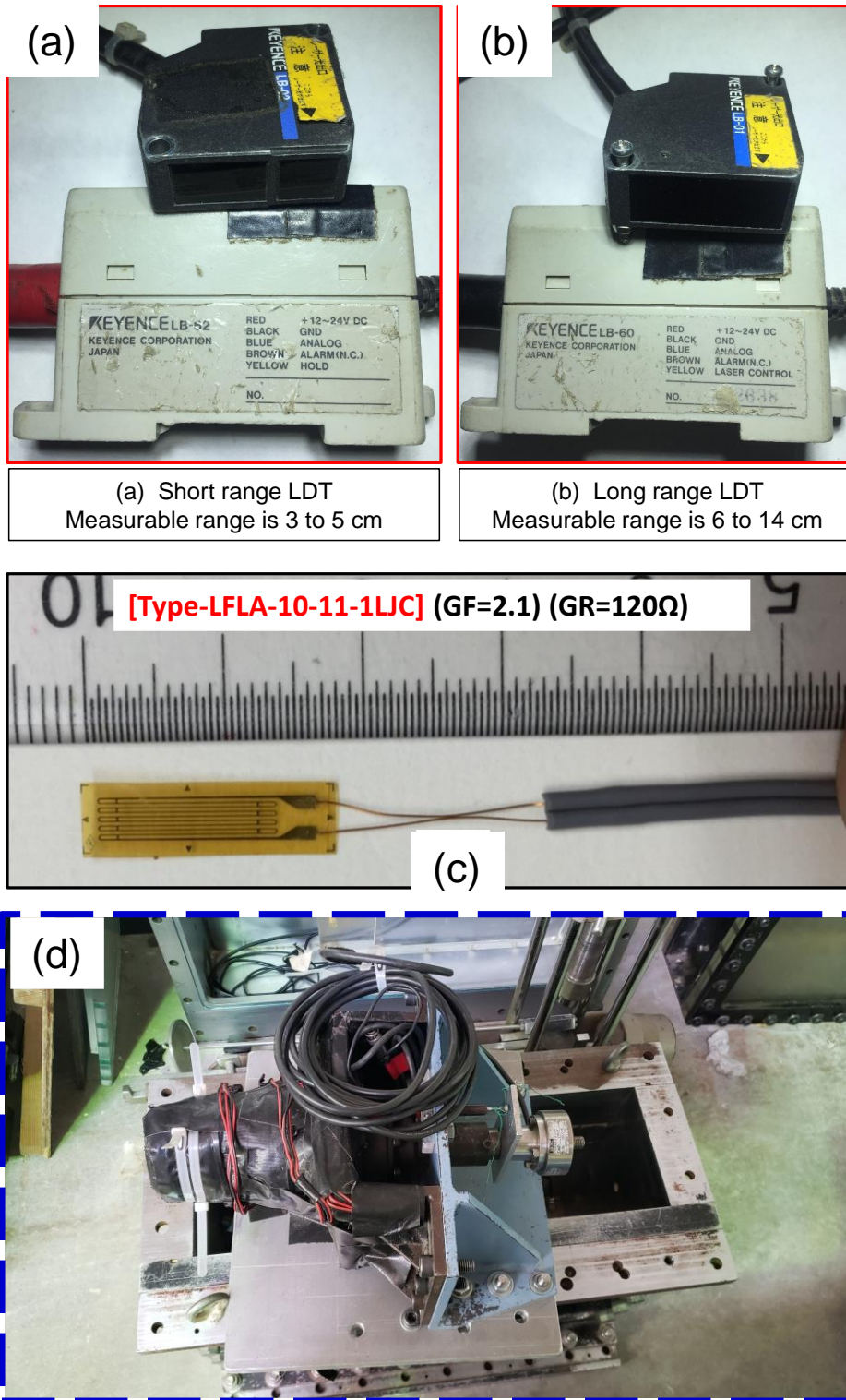


Figure 3.24: (a) Short-range Laser Displacement Transducers (LDTs) (b) Long-range LDTs (c) strain gauge used to affix on rock surface (d) Load cell used to apply the horizontal loading.

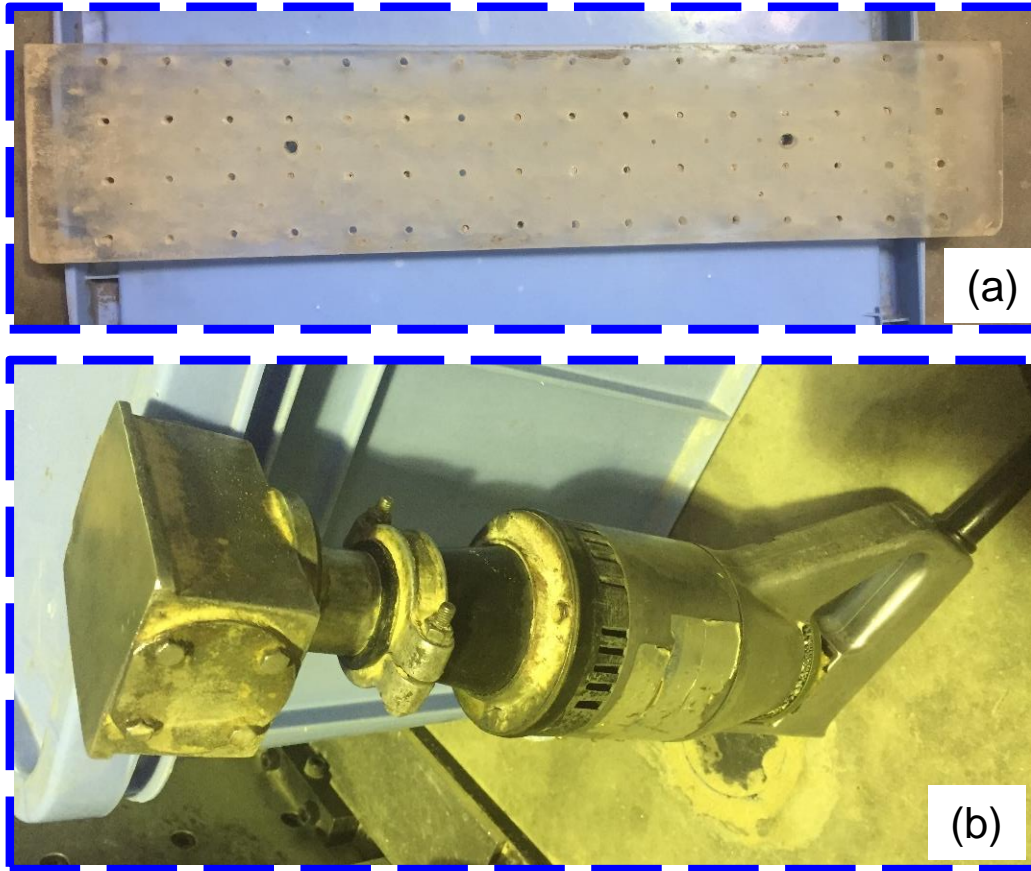


Figure 3.25: (a) acrylic compaction guide (b) mechanical vibrator.

3.4.3 Experimental result:

Load displacement behaviour:

Figure 3.26 illustrates the relationship between lateral load and pile top displacement for models 3 and 9, with similar loading cycles maintained for each pile. Residual displacement accumulates with each reloading cycle, and the slope of the reloading cycle changes as the number of cycles increases. The effect of rock socketing depth on lateral resistance is evident in the 1g model test, showing that deeper socketing depths result in increased resistance. When comparing SP-SR-40 and SP-SR-40-L, despite different loading heights, no significant difference in lateral resistance is observed. Furthermore, no significant difference in the load-displacement behaviour can be observed when comparing SP-SR-40[#] to SP-SR-40 and SP-SR-40-L. However, the impact of loading height becomes apparent when comparing SP-SR-60-L to SP-SR-60. Additionally, no significant difference in lateral resistance is observed when comparing SP-SR-60 and SP-SR-60-Fill, despite the latter being filled with soft rock. In the case of SP-SR-80[#], a sudden reduction in lateral load is observed at $\delta_t=2.5\text{mm}$, and it exhibits a distinct peak followed by displacement softening behaviour.

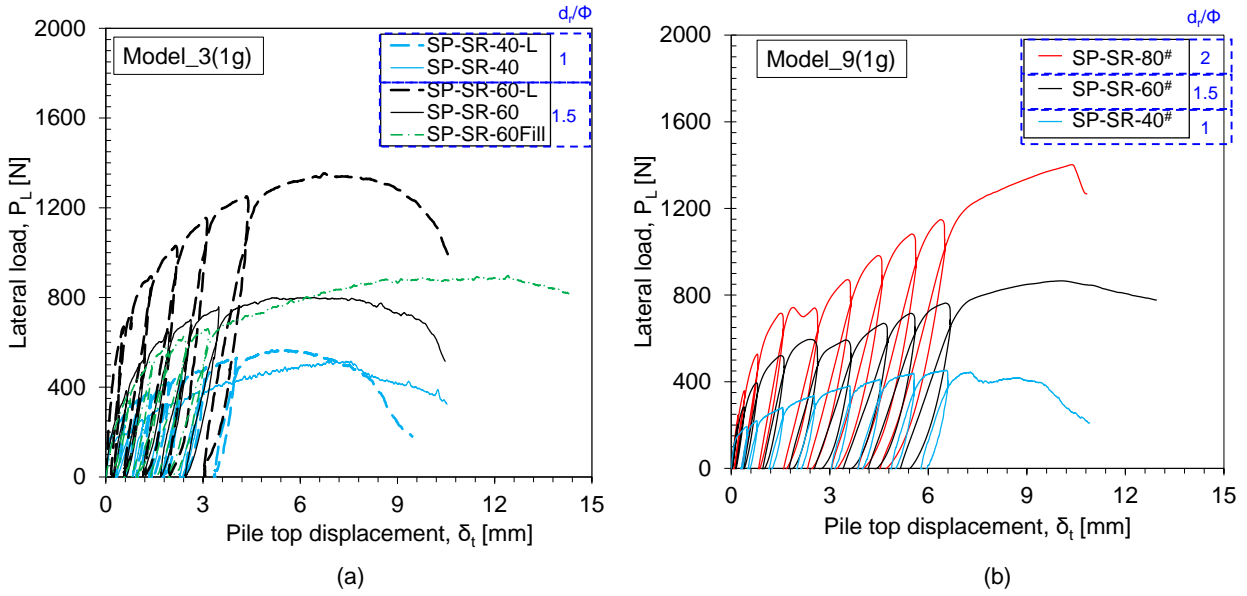


Figure 3.26: Variation of lateral load with pile top displacement (a) Model 3 (b) model 9.

Rock ground conditions after test:

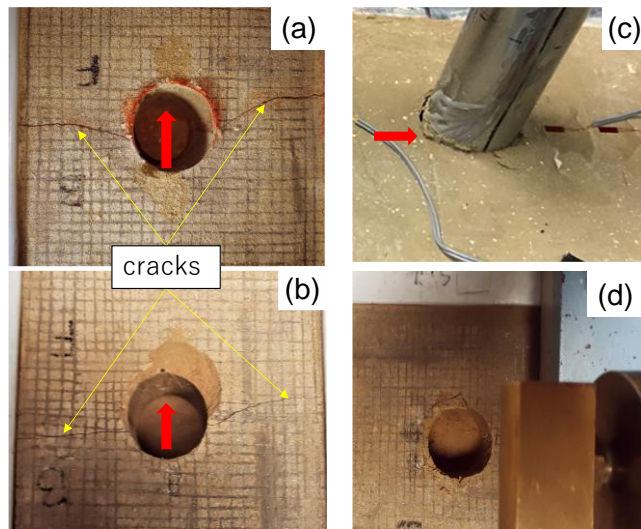


Figure 3.27: Observe state of rock ground after 1g model test (a) SP_SR_80# (b) SP_SR_60# (c) SP_SR_60 (d) SP_SR_40#.

Figure 3.27 presents the post-test condition of the rock ground following the 1g model test. In the ultimate condition of the test, ground failure consistently occurs. Comparing SP_SR_60# with SP-SR-60, a tension crack was observed in SP_SR_60#, while compressive failure was observed at the front of the pile in SP-SR-60. No significant crack or appearance of a compressive failure block

was noticed for SP-SR-40[#]. However, a distinct tension crack extending to the side of the container was observed in SP-SR-80[#].

Response of rock surface to lateral loading:

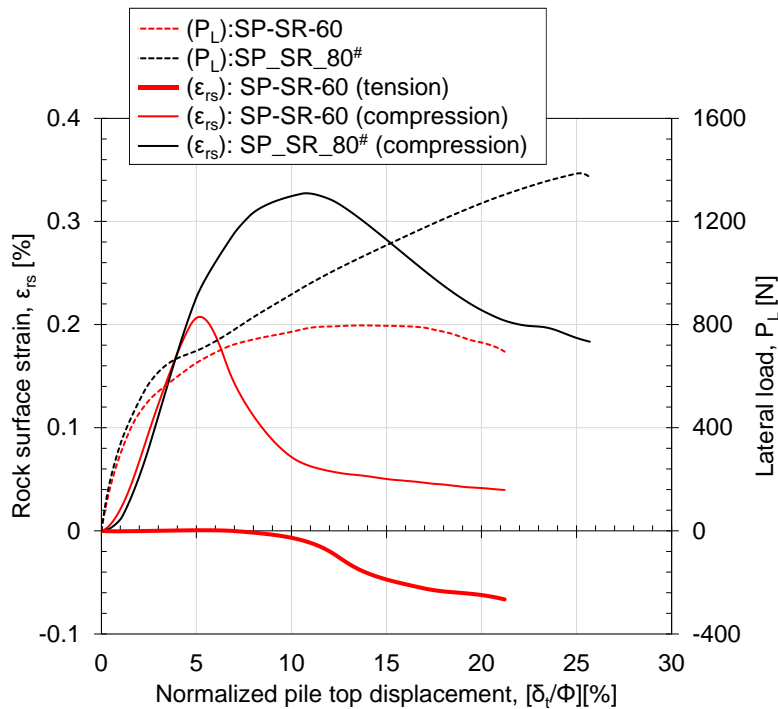


Figure 3.28: Variation of rock surface strain and lateral loading with normalized pile top displacement.

Figure 3.28 presents the results of the 1g model tests, showing the variation of rock surface strain and lateral load against the normalized pile top displacement for the SP-SR-60 and SP-SR-80[#] piles. The front (compression) and back (tension) rock surface strains are displayed for SP-SR-60, while only the front strain is shown for SP-SR-80[#]. The peak rock surface strain occurs at a pile top displacement of approximately 6-10% Φ , indicating the point at which the rock surface begins to deteriorate. In the case of SP-SR-60, no visible tensile strain was measured up to $\delta_t=5\% \Phi$, while the compressive strain decreased significantly from $\delta_t=5-10\% \Phi$, with the tensile strain remaining relatively constant. However, after $\delta_t>10\% \Phi$, the tensile strain increased significantly while the compressive strain remained relatively constant.

3.4.4 Discussions:

Effect of loading height and infill condition:

Figure 3.29 shows the variation of load-displacement and moment load-rotation relationship for $d_r/\Phi=1.5$. Comparing SP-SR-60 with SP-SR-60-Fill, no significant differences in lateral resistance

were observed. However, the SP-SR-60-Fill pile was filled with soft rock up to the pile cap due to a small variation (about 3% increase) of the relative stiffness ratio (E_p/G^* , where E_p is the equivalent stiffness of the pile and G^* is the equivalent shear modulus Carter and Kulhawy, 1992), no significant difference in the lateral resistance was observed. However, in the ultimate condition, the formation of cracks and failure mechanisms could cause differences in load-displacement behaviour.

As shown in Figure 3.26, no effect of loading height can be confirmed for $d_r/\Phi=1$ due to the rigid nature of the pile. However, as shown in Figure 3.29, for $d_r/\Phi=1.5$, the small moment load produced by a small loading height (SP-SR-60-L) provides larger lateral resistance than the large moment load produced by a large loading height (SP-SR-60). This observation confirms the significance of the loading height and the corresponding moment load on the lateral resistance of the pile. Furthermore, comparing the moment load-rotation relationship between SP-SR-60 and SP-SR-60-L, an almost identical relationship can be observed throughout the loading process. This observation confirms that the SP-SR-60-L behave as a rigid pile compared to SP-SR-60.

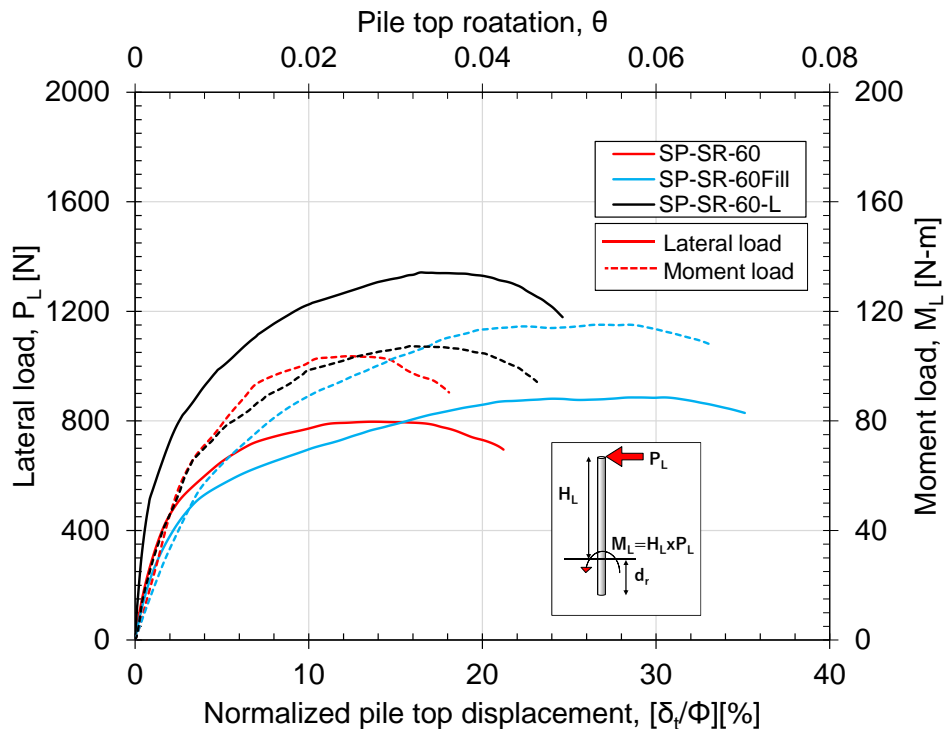


Figure 3.29: Effect of loading height and filling condition.

Comparison of 1g test result with 50 test results reported by Kunasegaram and Takemura (2022)

The findings from the 1g model test are compared with the 50g model tests reported by Kunasegaram and Takemura (2022). The pile notations used by the authors for their 50g test results

are used to compare with the 1g model test results. However, for easy comparison between the 1g and 50 model tests, all the results from the 50g test are shown in the model scale.

Load-displacement behavior:

Figure 3.30 (a) illustrates the lateral load-displacement backbone curve observed in the 1g and 50g model tests. The effect of rock socketing depth is evident in both tests. However, the 1g model underestimates the lateral resistance, particularly at large displacements for $d_r/\Phi=1.5$ and 2. For $d_r/\Phi=1$, no effect of the g level or the material stiffness is observed on the load-displacement behaviour due to the rigid nature of the pile.

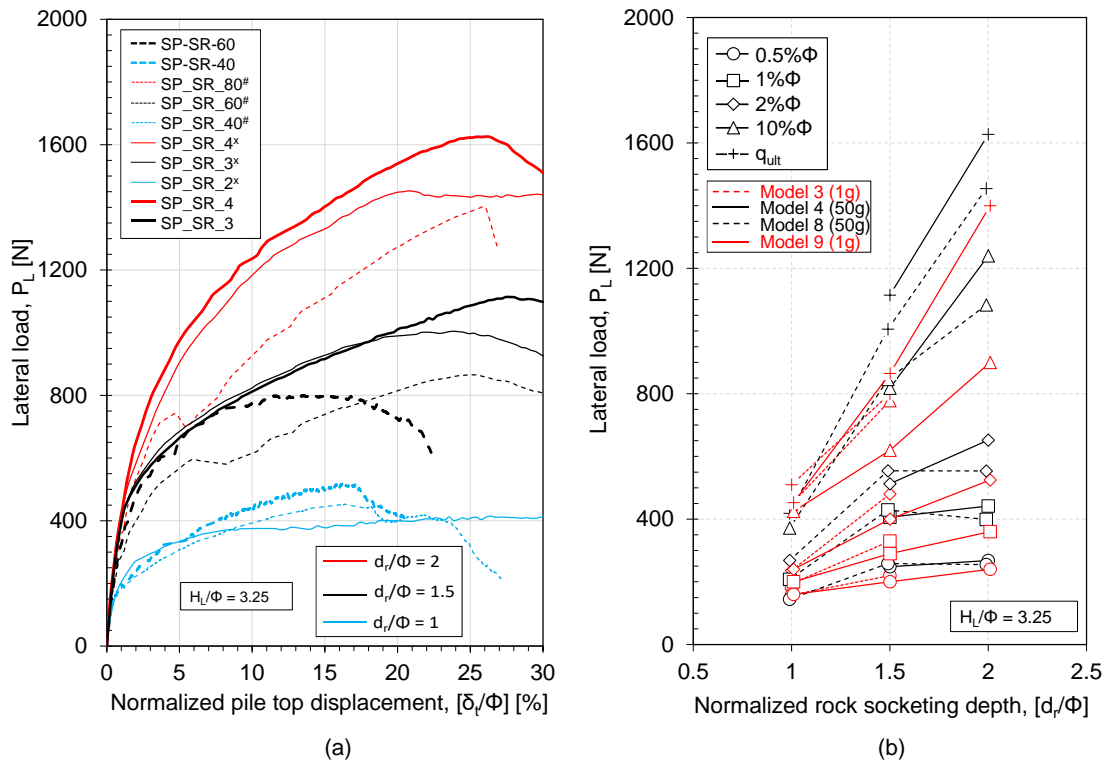


Figure 3.30: Comparison between 1g model with Kunasegaram and Takemura, 2022 50g model (a) backbone curve (b) summary of lateral load variation with rock socketing depth.

Comparing SP_SR_4 and SP_SR_3 reveals no effect of rock socketing depth up to $\delta_t=1\%\Phi$, consistent with the results of the CU triaxial test presented in Figure 3.22 (a). These results indicate negligible confinement effects at small strain levels due to the large cohesion ($c_u=q_u/2$) and low stress dependency of the rock material. This behaviour can also be confirmed by comparing SP_SR_4x and SP_SR_3x. However, the backbone curve for SP_SR_2x deviates from those of SP_SR_3x and SP_SR_4x from the beginning. This deviation is attributed to the rigid nature and large rotation of the pile, as explained by Kunasegaram and Takemura (2022).

To compare the load-displacement behavior of the 1g and 50g models under small pile top displacement, the lateral load at different imposed displacements ($0.5\%Φ$, $1\%Φ$, $2\%Φ$, $10\%Φ$, and q_{ult}) is plotted against the normalized rock socketing depth in Figure 3.30 (b). The results show that, for the 50g model, there is no significant effect of rock socketing depth up to $δ_t=2\%Φ$. In the load-displacement behaviour, the confinement effect becomes visible as the imposed displacement increases beyond $2\%Φ$. In contrast, the 1g model can predict this behaviour up to $δ_t=0.5\%Φ$. As the imposed displacement increases, the effect of rock socketing depth becomes more pronounced in both the 1g and 50g models. These results suggest that the 1g model may not accurately predict the load-displacement behaviour of piles at large displacements, especially for high rock socketing depths. However, for $d_r/Φ=1$, there is no significant difference between the 1g and 50g models, likely due to the rigid nature of the pile.

The load-displacement behaviour of the pile is dictated by the failure mechanism. Kunasegaram and Takemura (2022) reported that for SP_SR_4 and SP_SR_4^x, two types of failure mechanisms were observed: structural failure for the former and ground failure for the latter. The two types of failure could be due to the difference in the number of loading cycles applied before the monotonic loading. For SP_SR_4^x, due to a larger number of loading cycles than SP_SR_4, the rock pile confinement deteriorates, leading to ground failure. Due to the structural failure, clear post-peak displacement softening behaviour is observed in the backbone curve, as shown in Figure 3.30 (a).

Accumulation of residual displacement and change in system stiffness:

With the increase of the cyclic loading, the accumulation of rotation occurs (Leblanc et al., 2010). Figure 3.31 shows the variation of accumulated residual displacement with the imposed displacement observed in the 1g model and calculated from the cyclic load-displacement curve of the 50g model reported by Kunasegaram and Takemura (2022). With an increase in the imposed displacement, the residual displacement also increases. In the case of the 50g model, good agreement between the two models can be confirmed regarding the accumulation of the residual displacement. However, in the case of the 1g model, the difference in the residual displacement can be confirmed due to the difference in the failure mechanism and crack formation. Comparing the accumulation of residual displacement of SP-SR-60 with SP-SR-60-fill, SP-SR-60-fill shows a significant accumulation of residual displacement than SP-SR-60. Overall, the observed residual

displacement for the 1g model was overestimated compared to the 50g model, especially for $d_r/\Phi=1$, where the overestimation occurred even at small, imposed displacements.

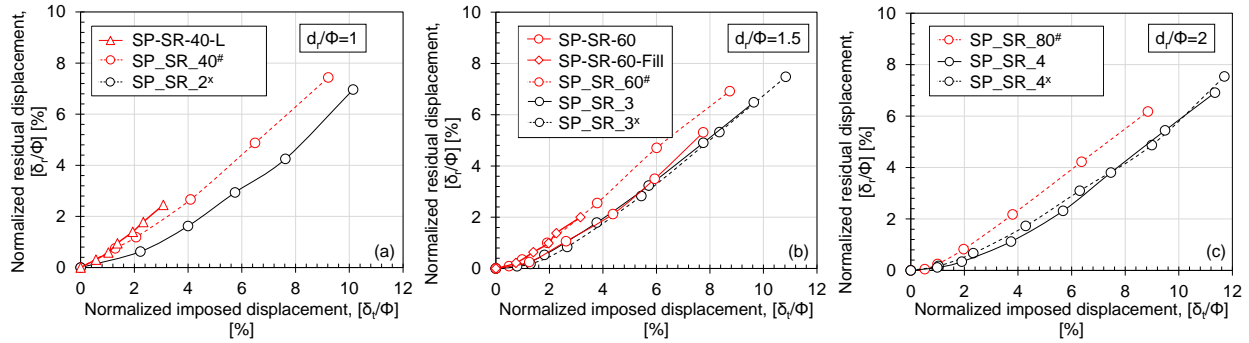


Figure 3.31: Comparison of accumulation of residual displacement with imposed displacement between the 1g model and 50g model.

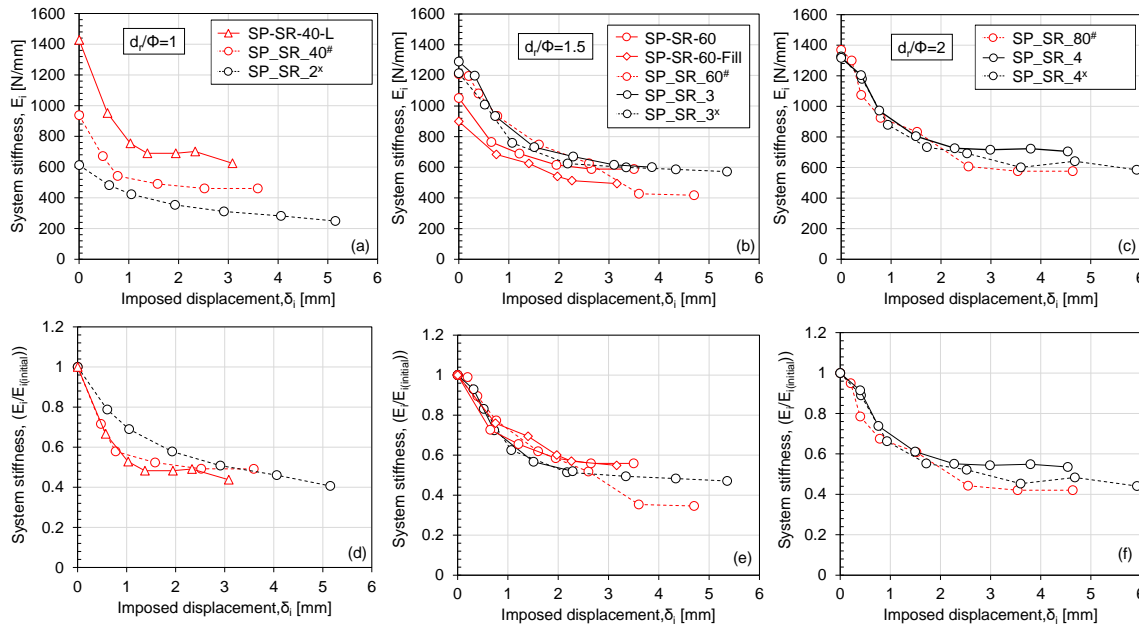


Figure 3.32: Comparison of system stiffness between 1g model and 50g model.

Figure 3.32 depicts the variation of system stiffness (defined as the slope of the reloading curve) with imposed displacement. For stiff monopiles used in offshore wind turbines, the stiffness of the ground changes due to long-term cyclic loading (Leblanc et al., 2010). The system stiffness for soft rock exhibits a different trend than sand. In sand, system stiffness increases with an increase in cyclic loading, whereas for rock, the system stiffness changes with an increase in the number of cycles Kunasegaram et al. (2020) Kunasegaram and Takemura (2022). This difference in behaviour between sand and rock can be attributed to the fact that in the sand, the surrounding soil densifies with an increase in the number of cycles, while in rock, residual displacement occurs at

the rock surface, creating a gap (accumulation of residual displacement) between the pile and rock, leading to the deterioration of confinement. For the 50g model, identical initial system stiffness was confirmed for $d_r/\Phi=1.5$ and 2, which decreased with an increase in the number of cycles. The system stiffness for $d_r/\Phi=1$ was less than that for $d_r/\Phi=1.5$ and 2. In the 1g model, a difference in the initial system stiffness was observed for different d_r/Φ ratios. Therefore, the system stiffness was normalized by the initial stiffness to compare it with the 50g model test data. The trend of reduction in the system stiffness for $d_r/\Phi=1.5$ and 2 of the 1g model captured the 50g model test trend. For $d_r/\Phi=1$, the reduction in system stiffness was larger for the 1g model than for the 50g model. Comparing SP-SR-40-L with SP_SR_40#, the observed system stiffness was larger for a short loading height than for a large loading height. For SP-SR-40-L, due to the small loading height, the corresponding moment load became smaller, leading to small rotation at the pile top, causing small displacement and, thus, a larger stiffness ratio than for the large loading height SP_SR_40#. Comparing SP-SR-60 with SP-SR-60-fill, as the accumulation of residual displacement is larger for SP-SR-60-fill than SP-SR-60, the change in system stiffness is larger for SP-SR-60-fill than SP-SR-60.

3.5 Summary:

Based on the test conditions, observation, results and discussions presented in this chapter, the following conclusion can be drawn:

1. Based on the steel tubular pile with diameter $\Phi=40\text{mm}$ and thickness $t=0.5\text{mm}$ ($\Phi/t=80$), the actual yielding of the pile occurs around 65% of the theoretical yielding moment. In ultimate condition, failure occurs by creating elephant-footed buckling near the support. This failure mechanism is mostly affected by the socketing condition (solid or hollow).
2. As nonlinear strain occurs around 65% of the theoretical yielding moment, the application of Euler-Bernoulli theorem can be reasonably applied up to this limit. Beyond that, the application of the Euler-Bernoulli theorem can overestimate the bending moment.
3. The application of shear strain measurement can be reasonably applied up to an applied load of 400N in the model scale. However, extra care should be taken to accurately put the strain gauge on the pile.
4. The lateral resistance of the pile increases with the increase of rock socketing depth, which can be effectively captured by both the 50g and 1g model tests. Both models show the effect of $\Delta d_r/\Phi=0.5$. However, the 1g model underestimates the lateral resistance of the pile compared to the 50g model, especially after the formation of tension cracks near the rock surface. This kind of tension crack formation in the 1g model test can be considered a limitation.
5. The failure mechanism affects the load-displacement behaviour, especially the post-peak behaviour for both the 50g and 1g models. Both ground and structural failure were observed in the 50g model test for $d_r/\Phi=2$, but the 1g model always showed ground failure.

6. No effect of confining pressure or rock socketing depth can be confirmed up to $\delta_t=1\%\Phi$ for $d_r/\Phi=1.5$ and 2 in the 50g model test. However, in the 1g model test, this behaviour is limited to $\delta_t=0.5\% \Phi$. For $d_r/\Phi=1$, due to the rigid nature of the pile, no effect of material weight or gravity can be expected.
7. With an increase in loading cycles, residual displacement occurs with a reduction in system stiffness. This observation is confirmed in both the 1g and 50g model tests. The 1g model overestimates the accumulation of residual displacement and underestimates the system stiffness, particularly for $d_r/\Phi=1$.
8. The effect of loading height and moment load on the load-displacement behaviour can be confirmed. The lateral resistance of the pile increases with a decrease in the loading height or the corresponding moment load. However, the rigid nature of the pile can affect the moment load-rotation relationship.
9. No significant effect of the filling conditions on the lateral resistance of the pile can be confirmed unless the relative stiffness changes significantly.

References:

1. API, 2014. Recommended Practice Planning, Designing, and Constructing Fixed Offshore Platforms-Working Stress Design. API 2A-WSD, twenty-second ed. (Washington, DC).
2. Carter, J.P., Kulhawy, F.H., 1992. Analysis of Laterally Loaded Shafts in Rock. *J. Geotech. Engrg.* 118, 839–855. [https://doi.org/10.1061/\(ASCE\)0733-9410\(1992\)118:6\(839\)](https://doi.org/10.1061/(ASCE)0733-9410(1992)118:6(839))
3. Dong, Q., Xu, C., Cai, Y., Juang, H., Wang, J., Yang, Z., Gu, C., 2016. Drained Instability in Loose Granular Material. *Int. J. Geomech.* 16, 04015043. [https://doi.org/10.1061/\(ASCE\)GM.1943-5622.0000524](https://doi.org/10.1061/(ASCE)GM.1943-5622.0000524)
4. Kunasegaram, V., Takemura, J., 2022. Mechanical Behaviour of Laterally Loaded Large-Diameter Steel Tubular Piles Embedded in Soft Rock. *Geotech Geol Eng* 40, 2967–3005. <https://doi.org/10.1007/s10706-022-02075-z>
5. Kunasegaram, V., Takemura, J., 2021. Deflection and failure of high-stiffness cantilever retaining wall embedded in soft rock. *International Journal of Physical Modelling in Geotechnics* 21, 114–134. <https://doi.org/10.1680/jphmg.19.00008>
6. Leblanc, C., Houlsby, G.T., Byrne, B.W., 2010. Response of stiff piles in sand to long-term cyclic lateral loading. *Géotechnique* 60, 79–90. <https://doi.org/10.1680/geot.7.00196>
7. Takemura, J., Kondoh, M., Esaki, T., Kouda, M., Kusakabe, O., 1999. Centrifuge Model Tests on Double Propped Wall Excavation in Soft Clay. *Soils and Foundations* 39, 75–87. https://doi.org/10.3208/sandf.39.3_75
8. Takemura, J., 2021, June. State of the art report on application of cantilever type steel tubular pile wall embedded to stiff grounds. In *Proceedings of the Second International Conference on Press-in Engineering 2021, Kochi, Japan* (pp. 27-41). CRC Press.

Chapter 4

Lateral response of large diameter Cantilever type Steel Tubular Pile wall embedded in soft rock subjected to one-way cyclic loading

4.1 Introduction:

The analysis of piles under lateral loading is a complex problem in foundation engineering due to the soil-structure interaction involved. Analyzing a single pile under lateral loading is challenging because the pile's deflection influences the soil reaction or resistance along the pile. Conversely, the pile's deflection depends on the soil resistance, creating a soil-structure interaction problem. For various loading conditions on complicated structures like CSTP walls, the soil-wall interaction problem becomes more complex. Therefore, a straightforward approach is needed to simplify this intricate situation.

This chapter aims to study the load resistance curve concept to understand the retaining wall's soil-structure interaction behaviour. A design p-y curve recommended by JARA (2017) is studied in this chapter. Centrifuge model test with clear loading condition is used to study this p-y curve. FEM analysis is also carried out to discuss the possible effect of the container boundary on the lateral resistance of the centrifuge model test by Plaxis 2D analysis. Finally, the analytical tool named "Lpile (version 2022.12.06)" by Ensoft is used to conduct the p-y analysis.

4.2 Centrifuge test used to investigate the bilinear p-y curve:

Chapter 5 examined the CSTP wall model with complicated loading (sequential dynamic and static loading) conditions. However, due to the challenges involved with such complicated loading and the associated time and cost of conducting sophisticated investigations, a simplified lateral loading approach was adopted for studying the CSTP wall behaviour using a centrifuge. One major advantage of this approach is the simplicity of the loading mechanism, allowing for accurate estimation of lateral and moment loads, unlike the more complex estimation methods related to the CSTP wall model in Chapter 5. Additionally, one-way horizontal cyclic loading was employed, which represents a typical loading condition for actual retaining walls. However, it is important to note that this modelling concept does not account for the contribution of confining pressures from the backfill of the retaining wall. Nonetheless, the purpose of using this centrifuge model is to establish a suitable p-y curve to represent the soft rock ground in the model, which can be used in the CSTP wall model explained in Chapter 5.

4.2.1 Model and test conditions

Figure 4.1 shows the 2D view of the centrifuge model. The test was conducted under 50g centrifugal acceleration. A model container with inner dimensions of 700 mm in width, 150 mm in breadth, and 500 mm in depth was utilized for the modelling process. A thick acrylic plate stack was tightly inserted into the container to achieve the desired depth, reducing the depth to 200 mm

for the single rock layer model. Additionally, a 20 mm acrylic plate was added to the inner rear face of the container to decrease the breadth to 130 mm. This adjustment aimed to simulate the plane strain conditions experienced by the steel tubular pile walls.

The wall model used steel pipes (SUS304) with an outer diameter of $\Phi=40\text{mm}$ and a thickness of $t=0.5\text{mm}$. The steel tubular pipe wall models consisted of three steel pipes securely fixed at the top by an aluminium block, as depicted in Figure 4.2. Two wall models, with embedment depths of 6cm (3m in the prototype) and 8cm (4m in the prototype), were prepared, as shown in Figure 4.2 (a), prior to the installation of strain gauges. A rigid aluminium cap was attached at the top of each pile to represent the socketing solid portion, extending 40mm (in the model) below the loading point. In the model wall, a 3mm gap was maintained between the piles to simulate real-life conditions, where an unavoidable gap of 0.18m exists between the piles due to limitations in pile installation machines. In the centrifuge model, this gap represents 0.15m in the prototype, corresponding to the 50g model, due to the constraints of the model container. The model piles were fixed to the top loading frame, as shown in Figure 4.2 (b), using six bolts, with two bolts passing through the solid cap of the middle pile. After securing all three piles to the top loading frame, additional stability between the piles and the loading frame was achieved by applying Scotch glue. Subsequently, strain gauges were installed to measure bending strains in the embedded zone and axial strains at the bottom tip of the walls, as depicted in Figure 4.2 (c).

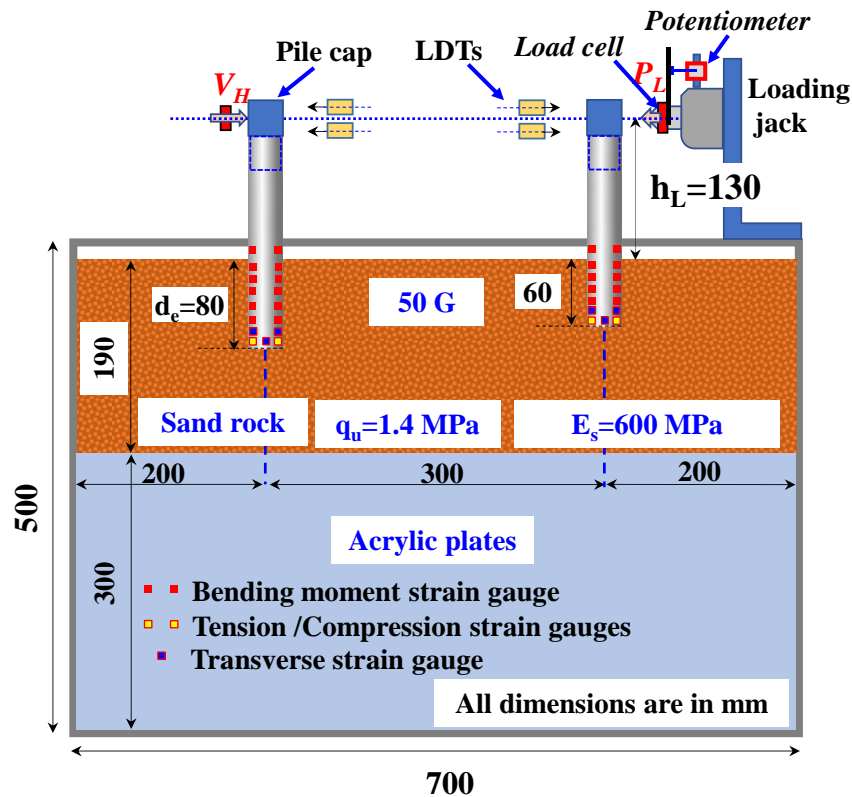


Figure 4.1: 2D view of the model conditions.

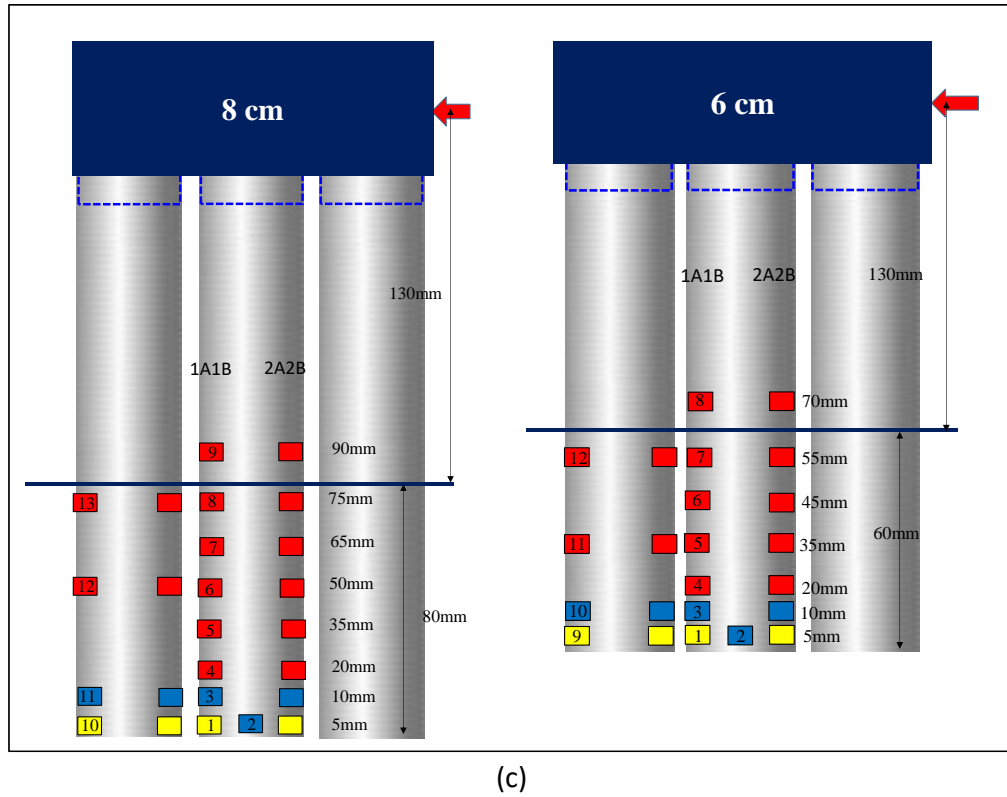
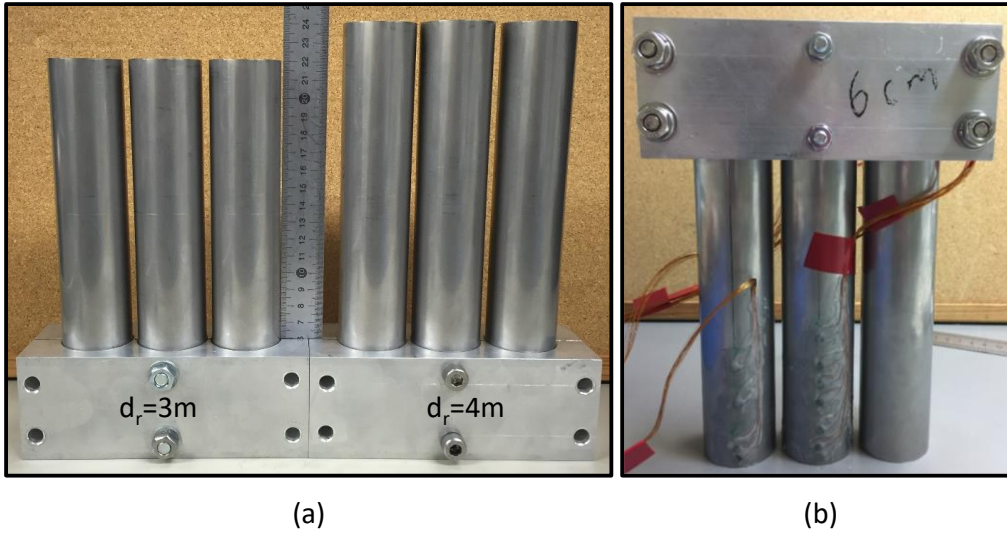


Figure 4.2: Model CSTP wall (a) two model CSTP wall before strain gauge attachment (b) CSTP wall model with strain gauge attachment (c) arrangement of the strain gauges on the wall.

The soft rock was made by following a similar process as described in article 3.3. Before pouring the unsolidified rock mixture into the container, 0.5mm thick Teflon sheets were placed on the inner faces of the container. The soft sand rock was created by compacting the mixture layers by layers, each with a thickness of 30mm. Once the mixture was poured, the model walls were

vertically inserted into the unsolidified mixture using a pile guide, reaching the desired embedment depth. The mixture was then left to cure for 14 days. Table 4.1 summarizes the test conditions.

Two LDTs and a load cell were used to measure the wall displacement and the load. A one-way horizontal cyclic loading was applied to each model until the ultimate condition (structural or ground failure) occurred. More details about the centrifuge test condition and model preparation were reported by Kunasegaram et al. (2020).

Table 4.1: Model and test conditions

Structure and embedment medium	Properties of soft rock and sand	Wall embedment depth into S.R.: d_R [normalized depth: βd_R]*	STP Wall spec. [model scale]
<u>Model-6</u> RPW_SR_3m	$\gamma_t=20.1\text{kN/m}^3$ $q_u=1.4\text{MPa}$ $E_s=660\text{MPa}$	3m (60 mm) [1.2]	$\Phi=2$ m (40 mm), $t = 25$ mm (0.5mm) C.C. Spacing: 2.15m (43mm) $EI= 6.8$ GNm ² /m (5.4×10^{-5} GNm ² /m) $M_y= 9.0$ MNm/m (3.6×10^{-3} MNm/m) $M_p=11.6$ MNm/m (4.6×10^{-3} MNm/m)
<u>Model-6</u> RPW_SR_4m		4m (80 mm) [1.6]	
E.I.: Pile flexural rigidity, M_y : Bend moment causing pile yielding, M_p : bending moment causing pile plastic failure, β was evaluated $E_s=660\text{MPa}$, $k_h=4E_s (B/0.3)^{-3/4}$ ($B=\Phi$ for pile, $B=10\text{m}$ for wall)			

4.2.2 Observed results from the centrifuge test

In order to define the p-y curve, two important information are required. First, the load-displacement behaviour at specific locations and the failure mechanism. The direct measurement of the load displacement can be used to validate the selected p-y curve. The failure condition can provide an idea about selecting the ultimate lateral resistance.

Figure 4.3 displays the relationship between observed lateral load and wall top displacement ($P_L - \delta_t$). Additionally, the figure presents the backbone curve derived from the $P_L - \delta_t$ relationship. It was observed that an increase in embedment depth resulted in higher lateral resistance of the wall. Moreover, as the number of cycles increased, residual displacement occurred. No significant effect of embedment depth was observed until δ_t reached $1\% \Phi$ (0.02mm). This observation can be attributed to the similar stress-strain relationship at small strain levels, regardless of the different confining pressures, as illustrated in Figure 3.22.

At wall top displacement around 0.3m, a sudden reduction in the lateral resistance was observed for both embedment depth conditions. To investigate this sudden drop in lateral resistance, the tensile and compressive strain measured at the pile toe is plotted against the normalized wall top displacement in Figure 4.4. The tensile strain was measured in the loading direction, and the compressive strain was measured in the opposite direction. At the wall top displacement of around $15\% \Phi$, the tensile strain decreased, indicating the possible progressive failure initiation. Although

the tensile strain decreased, the compressive strain showed increasing trends until the ultimate condition was reached, especially for $d_r=4\text{m}$, which could explain the increase in the further lateral resistance.

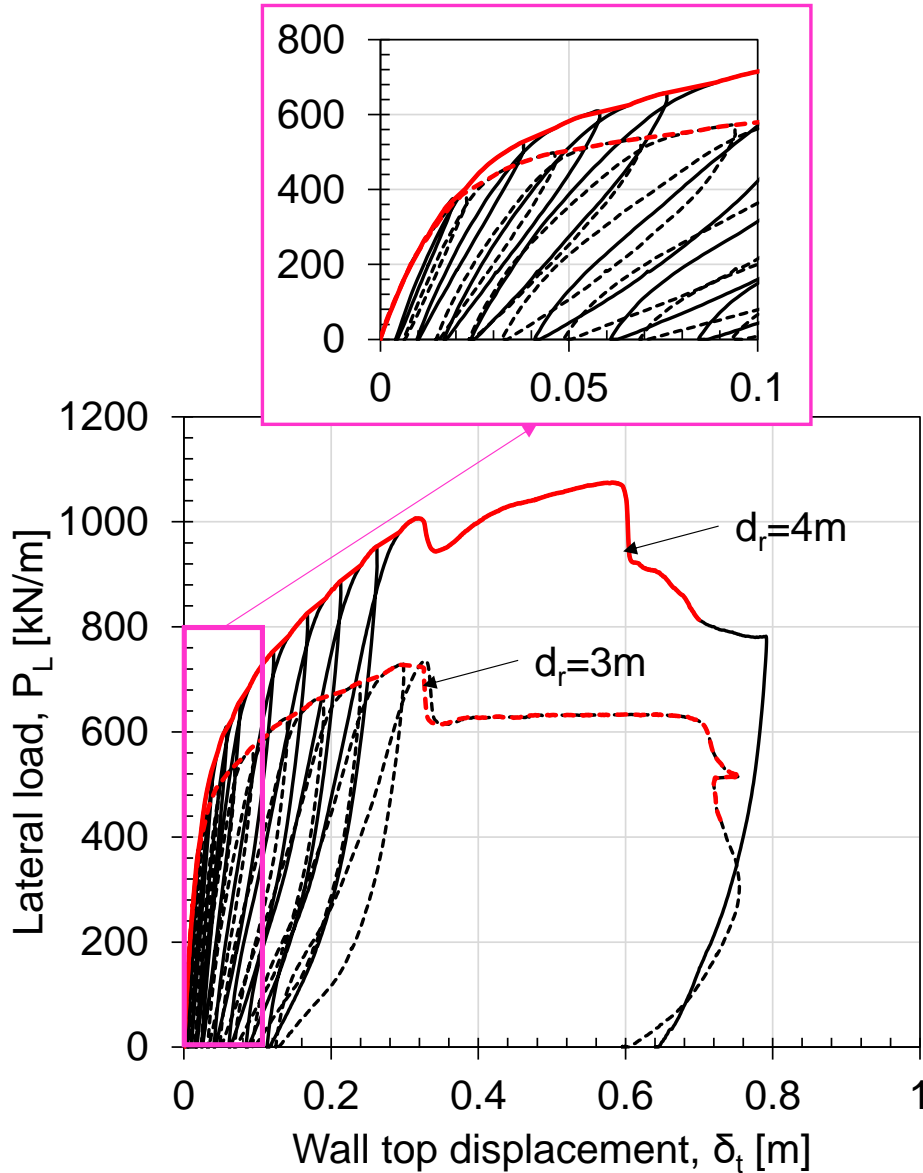


Figure 4.3: Variation of lateral load with the wall top displacement.

Figure 4.5 shows the wall and ground condition after the test. Two types of failure were observed for both 3m and 4m embedment depth. In both cases, apparent wedge-type failure was observed at the back and compressive failure at the wall front. In the case of wedge-type failure, the failure path reached almost close to the back of the rigid container.

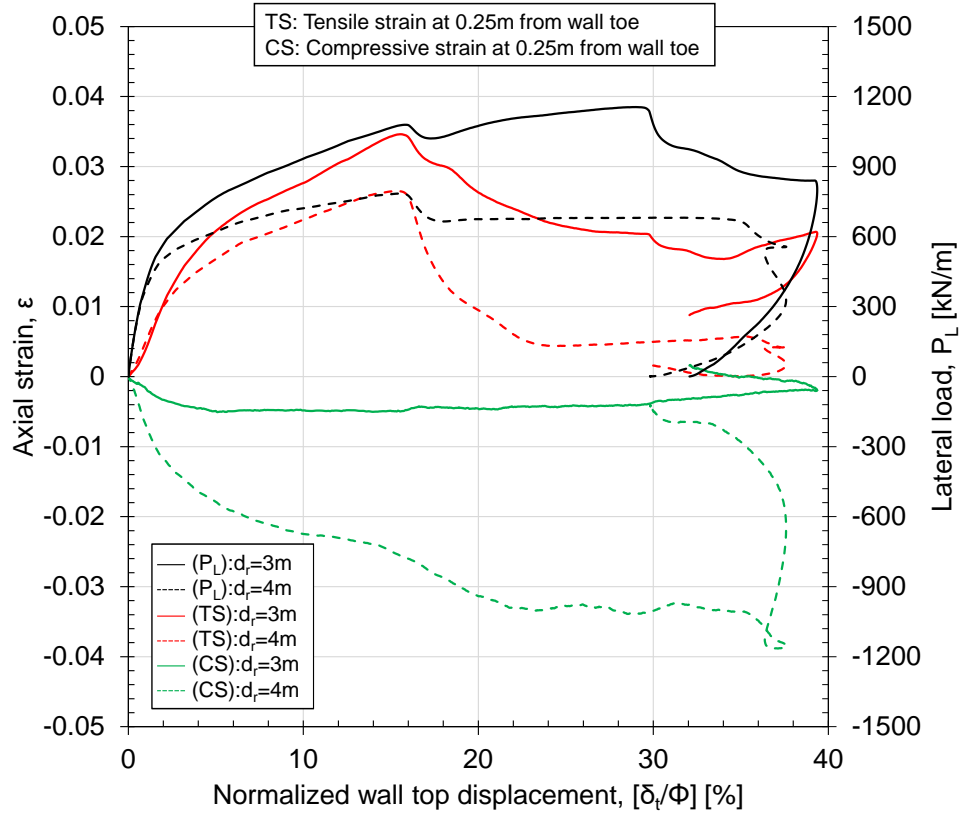


Figure 4.4: Variation of tensile strain, compressive strain at wall toe and lateral load at wall top with normalized wall top displacement.

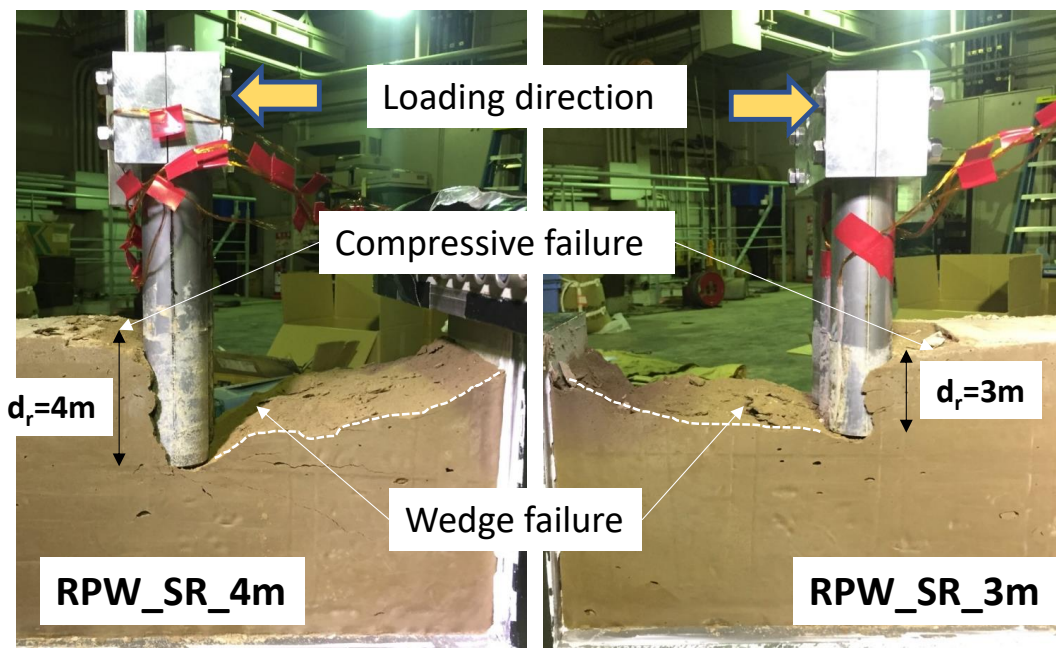


Figure 4.5: Observed failure mechanism.

Therefore, to use the load-displacement measurement to validate the selected p-y curve, the effect of the container wall on the load-displacement should be checked. A simple numerical analysis by Plaxis 2D was conducted and reported in the following section to investigate the effect of the container wall on the load-displacement behaviour.

4.3 Investigation of the effect of container wall on the load-displacement behaviour by Numerical modelling

The modeling concept used in Plaxis 2D is depicted in Figure 4.6. Based on Figure 4.1, the distance from the wall to the container back was denoted by x_1 . At the front, half the distance between two walls was considered and denoted by x_2 . Two boundary conditions were assumed and denoted by B1 and B2. The horizontal movement was fixed, and the vertical movement was allowed for the boundary (B1). On the other hand, in the case of the bottom boundary, both horizontal and vertical movements were considered fixed. Two models were made by changing the x_1 and x_2 , as mentioned in Figure 4.6.

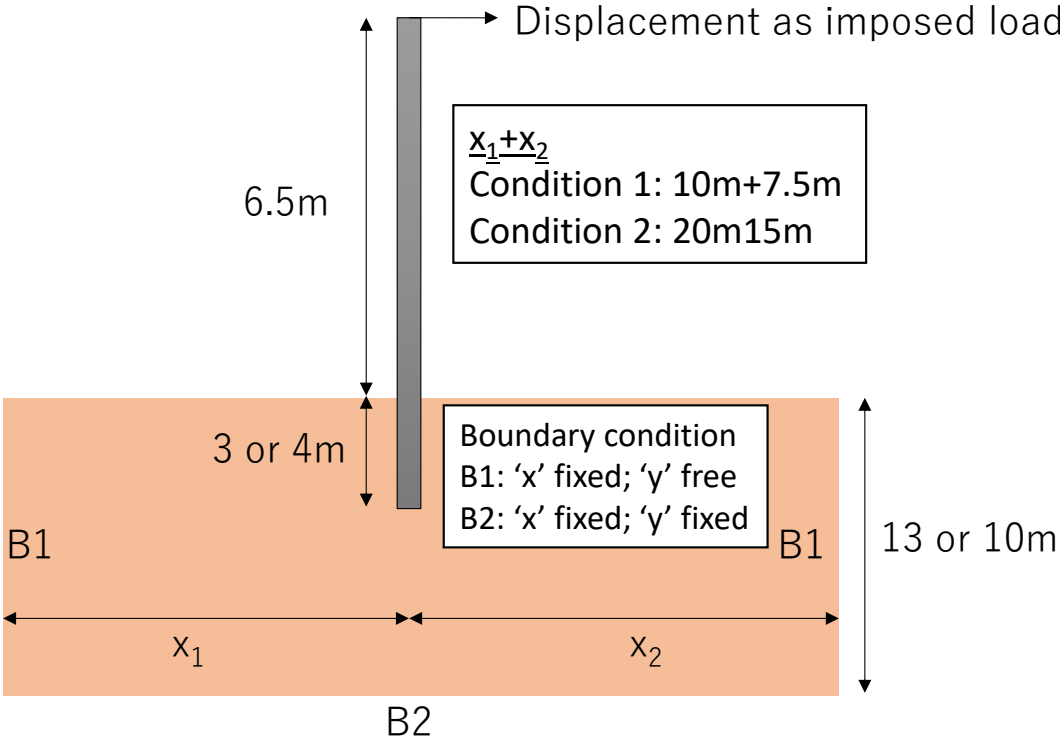


Figure 4.6: Plaxis model conditions.

In this Plaxis model, the wall was designed as a plate. The mechanical properties of the plate are shown in **Table 4.2**.

Table 4.2: Properties of 2D plate used in the numerical model

Properties	Unit	Value
Axial stiffness, EA_1	kN/m	200×10^6
Bending stiffness, E.I.	kN/m	6.8×10^6
Poisson's ratio, ν	-	0.3
Plate thickness, d	m	0.6387
Unit weight, γ	kN/m^3	78.4
$w = \gamma \times d$	kN/m/m	50.1

The plate material was assumed 'elastic'. Also, the punching was prevented in the model.

Table 4.3: Properties of soil used in the numerical model

Properties	Unit	Value
Unsaturated unit weight, γ_{unsat}	kN/m^3	16.8
Saturated unit weight γ_{sat}	kN/m^3	20.1
Elastic modulus, E	kN/m^2	2000 MPa
Poisson's ratio, ν	-	0.2
Cohesion, C	kN/m^2	330
Angle of internal friction, ϕ	$^\circ$	31
Interface strength, R_{inter}	-	Rigid:1 Manual:0.3

The ground was modelled as the Mohr-coulomb model, where perfectly elastic and plastic spring conditions were considered. The mechanical properties of the model ground are shown in **Table 4.3**. The mechanical properties were determined based on Figure 3.22. The initial stiffness of the rock mass was assumed to be 2000MPa. Two soil-plate interphase conditions were assumed to investigate the soil-plate interaction on the lateral resistance. At first, it was assumed to be full mobilization of soil wall friction by assuming $R_{inter}=1$ (Rigid). Next, the R_{inter} was reduced by 70% to check the effect of reduced interface strength on lateral resistance. Also, the gapping between the wall and soil was considered by activating the "Tension cut-off". However, program-generated values were used in that case.

Point load was applied at the wall top as loading. The range of displacement was from 0-150mm, with 10mm increments up to 150mm (7.5% Φ).

Figure 4.7 illustrates the distribution of principal total stress (σ_1) in the ground for imposed wall top displacement of $\delta_t=7.5\%Φ$. At imposed displacement ($\delta_t=7.5\%Φ$), stress concentration occurs in the shallow rock layer in front of the wall, which can be confirmed in both R_{inter} conditions. Also, as the displacement increases, the wall begins to rotate about a pivotal point, increasing σ_1 at the front and back (near the wall toe). This stress profile supports the failure mechanism observed in Figure 4.5, where the high-stress concentration at the front causes compressive failure, and the large backward stress concentration at the wall toe causes wedge-type failure in the ultimate condition.

Overall, all the stress profiles indicated that the stress profile did not reach the back of the container for different model dimensions (except Figure 4.7 (c)). Also, comparing the stress plane observed at the back side from 3m and 4m embedment depth, the zone of influence is larger for the 4m embedment depth than the 3m embedment depth. Therefore, the effect of the container back wall on the lateral resistance could be more significant for the 4m embedment depth than for a 3m embedment depth. This could be the reason behind the increase in the lateral resistance after a sudden drop of lateral resistance at δ_t about $15\%Φ$, as observed in Figures 4.3 and 4.4.

Figure 4.8 displays the load-displacement curve obtained from two models for different R_{inter} conditions. It was observed that a larger R_{inter} value provided larger lateral resistance. Also, the difference between the load-displacement curve for two container dimensions becomes smaller for larger R_{inter} values. Overall, increasing the model dimension by twice the centrifuge model condition resulted in about a 4-5% difference in the lateral resistance. Therefore, based on the results shown in Figures 4.7 and 4.8, the effect of the side wall of the container could be ignored.

Before comparing the numerical model with the centrifuge test result, two points are needed to be considered. First, the Mohr-Coulomb (MC) model was assumed in the numerical model. Due to this, the MC model will overestimate the strength at a stress level of less than 50% of ultimate strength and underestimate the strength beyond that. Also, the centrifuge test result was obtained from one-way horizontal loading. On the other hand, in numerical modelling, monotonic loading was applied.

The load-displacement curve obtained from the numerical modelling is compared with the centrifuge model test in Figure 4.9. The load-displacement curve observed at small imposed displacement is shown in Figure 4.9 (b). It was observed that small interface strength underestimates the initial stiffness more than larger interface strength.

In the centrifuge test result, no visible effect of embedment depth was observed at an imposed displacement of $\delta_t=1\%Φ$. This observation could be interpreted as the stiffness of the soft rock from the centrifuge model being much larger, which caused the reduction of the required d_r obtained from Equation 2.19 to less than 3m. Therefore, 3m and 4m embedded walls behave as long piles, and the displacement becomes proportional to the load. From Figure 4.9, it can also be said that small interface strength in the ultimate condition provides better agreement, which indicates a small effect of skin friction on the ultimate lateral resistance of the pile.

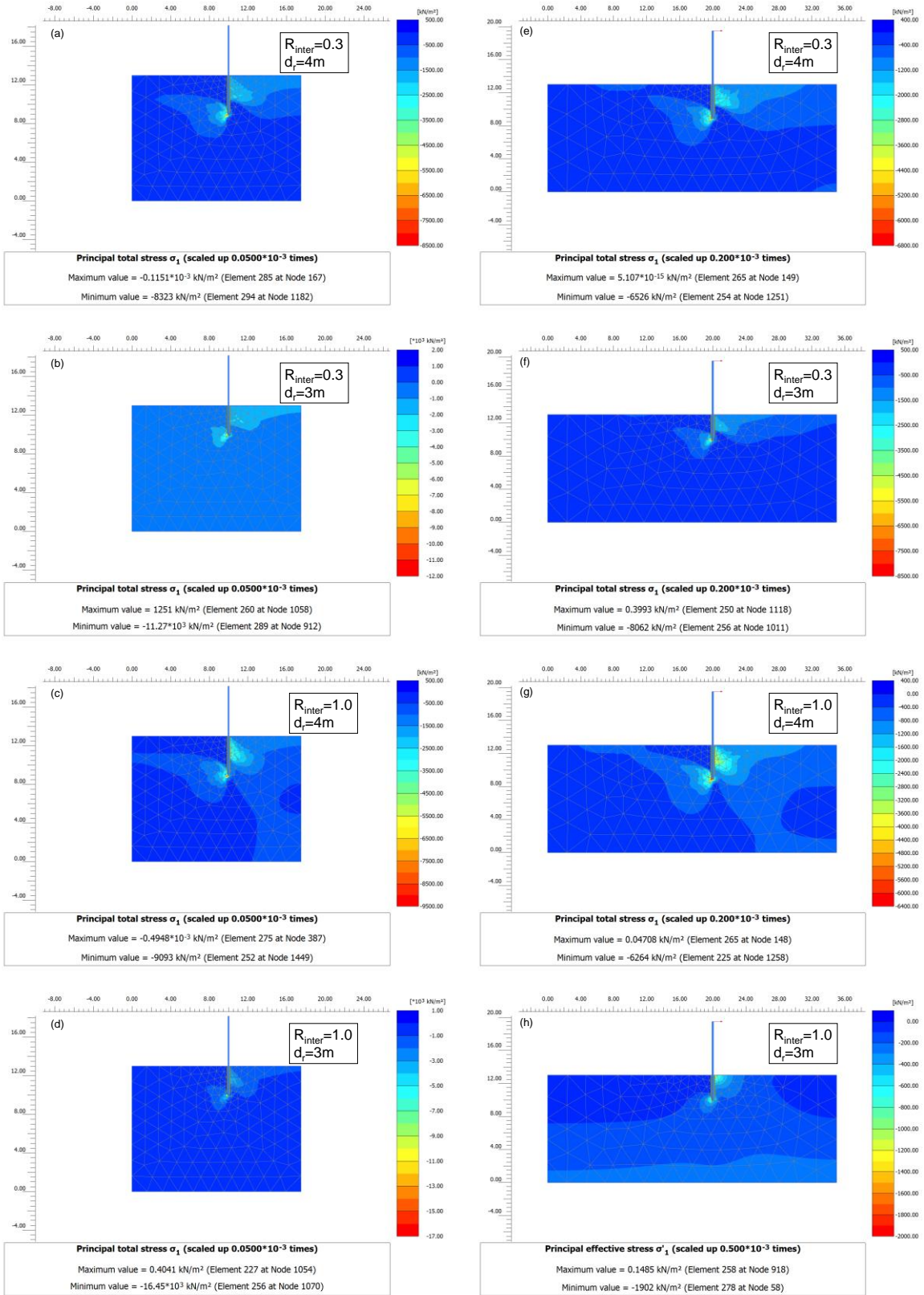


Figure 4.7: Principal total stress variation with imposed displacement.

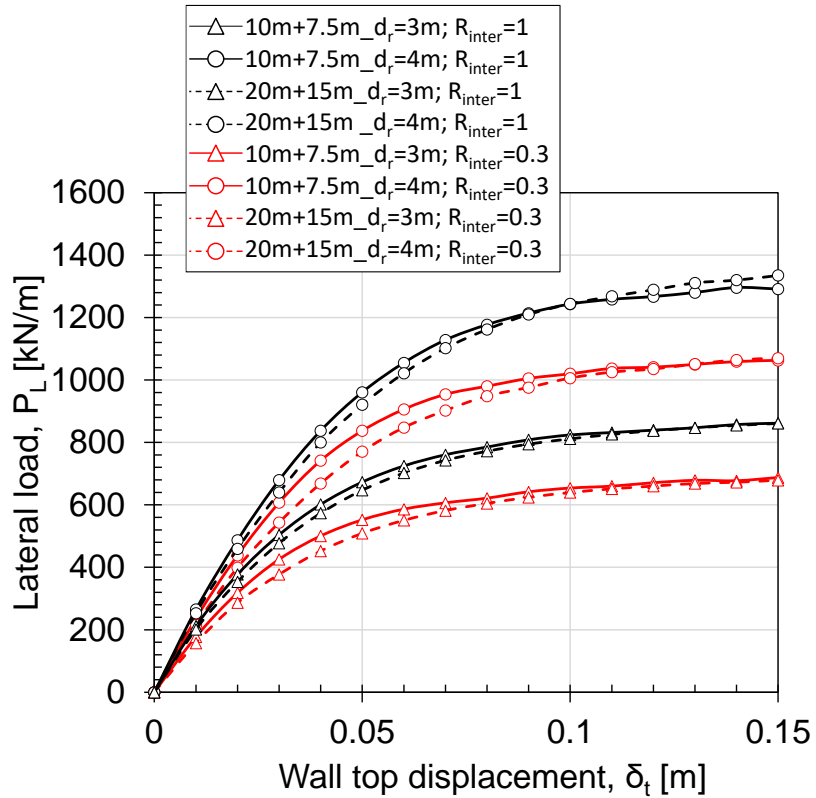


Figure 4.8: Comparison of variation of lateral load with wall top displacement from FEM analysis.

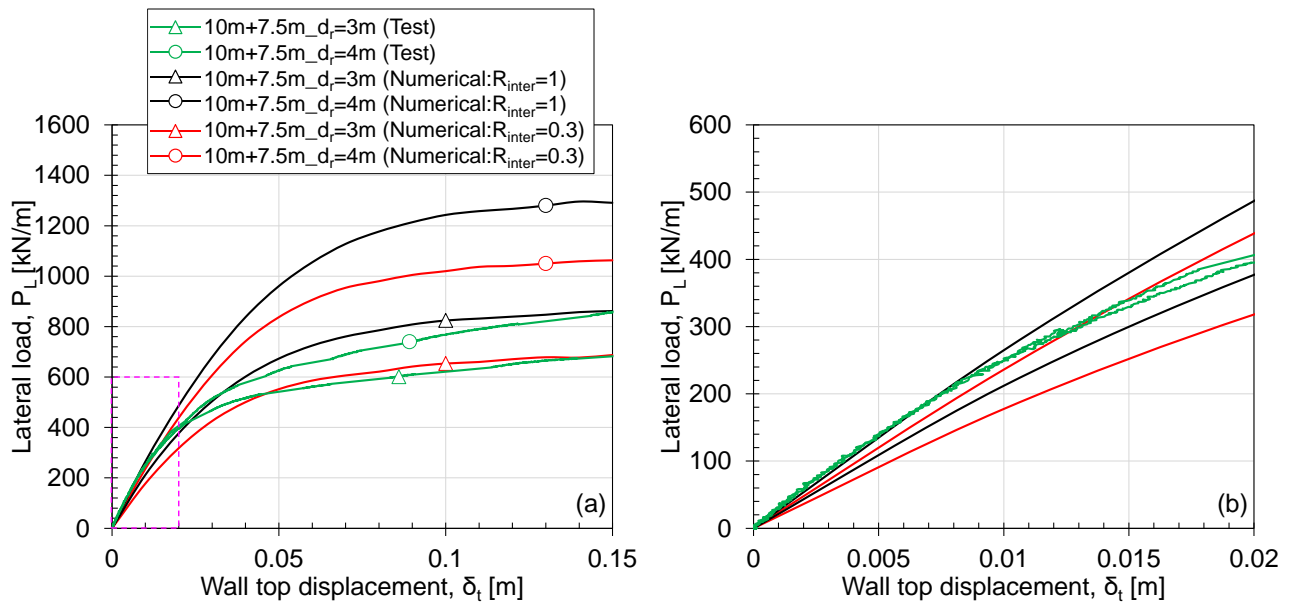


Figure 4.9: Comparison of variation of lateral load with wall top displacement between FEM analysis and centrifuge model test.

4.4 Investigation of the effect of base shear on the lateral resistance of CSTP wall

The pressure distribution diagram used to conduct the stability analysis for this retaining structure is shown in Figure 4.10. The factor of safety was calculated by the moment minimization technique, i.e., minimum ratio of M_r/M_a , where M_a is the acting moment due to pint load and the M_r is the resisting moment due to passive resistance about the pivotal point. The moment minimization was achieved by changing the location of the pivotal point. This stability analysis was done by considering 'with' and 'without' the effect of base shear.

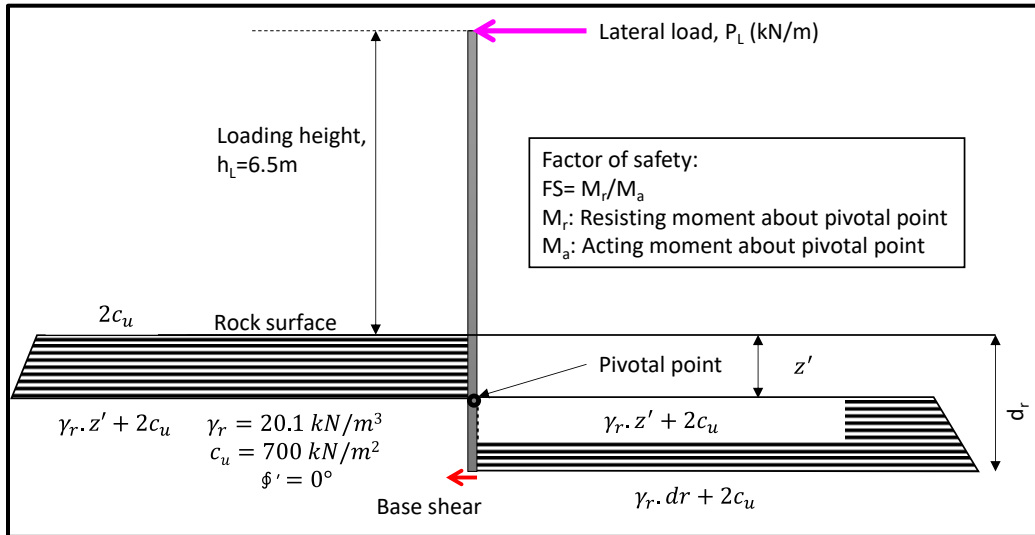


Figure 4.10: Pressure distribution diagram assumed for stability analysis of CSTP wall.

Figure 4.11 illustrates the variation of the factor of safety with increasing lateral load for $d_r=3\text{m}$ and 4m under 'with' and 'without' base shear conditions. Also, the ultimate lateral resistance from the centrifuge test result (defined at $15\%\Phi$) for $d_r=3\text{m}$ and 4m are indicated in this figure. The factor of safety decreased with the increase of the lateral load. A larger factor of safety can be observed for $d_r=4\text{m}$ than $d_r=3\text{m}$. The factor of safety calculated at the ultimate lateral load from the centrifuge test is smaller than unity, which could cause catastrophic failure for both embedment depths, as shown in Figure 4.5. The base shear positively affects the factor of safety, i.e., a larger factor of safety if the base shear is mobilized.

To further investigate the effect of embedment depth on the base shear, the variation of the factor of safety for $P_L=200$ and 600 kN/m was calculated for $d_r=3\text{m}$ and 4m and presented in Figure 4.12. The sub-axis displays the ratio between the factor of safety 'with' and 'without' base shear. It is observed that increasing the embedment depth led to higher factors of safety. but the ratio between the factor of safety 'with' and 'without' base shear decreased with increasing embedment depth. This observation can be interpreted as; increasing the embedment depth causes the wall to behave more like a flexible wall with less translation and rotation, resulting in less effect of base shear.

However, as the embedment depth decreases, the effect of base shear increases; for example, decreasing the embedment depth from 4m to 3m caused the increase of the F.S. from 1.46 to 1.6.

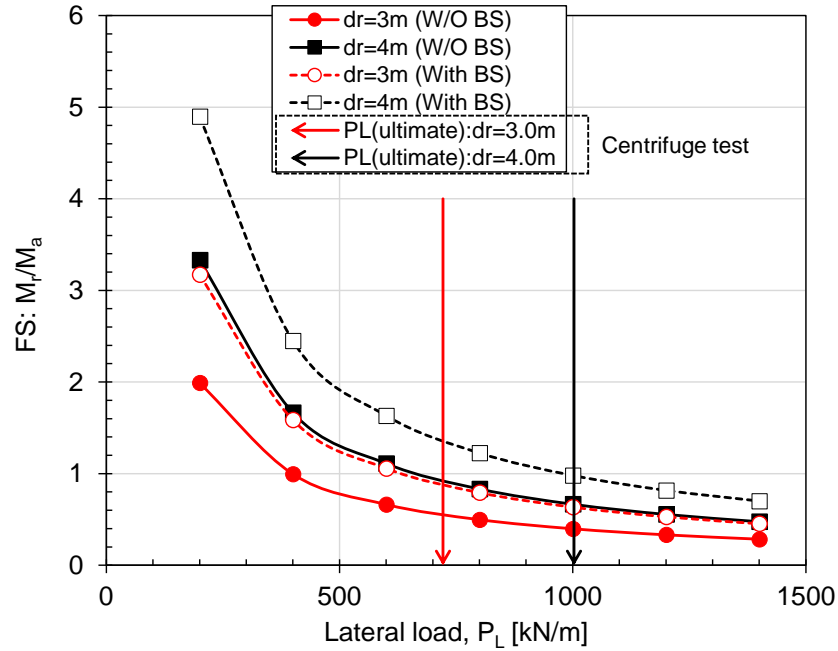


Figure 4.11: Variation of the factor of safety with the lateral load.

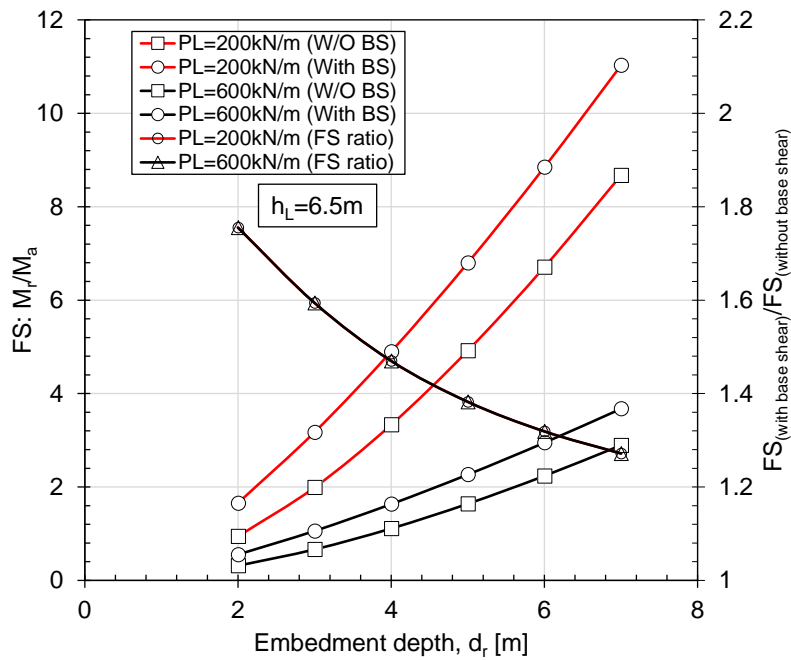


Figure 4.12: Variation of the factor of safety with embedment depth for imposed lateral load of 200 kN/m and 600 kN/m.

4.5 Study of bi-linear p-y curves to predict the lateral resistance behaviour of CSTP wall:

4.5.1 Model condition and the assumed p-y curves

Typically, the calculation of a steel tubular earth retaining wall involves the utilization of either the elastoplastic method or the dynamic analysis method, depending on the appropriateness of the simplified method. When employing the elastoplastic method, the horizontal ground reaction force model follows a bi-linear pattern, with the upper limit of the horizontal ground reaction force determined by the passive earth pressure. Within the elastoplastic method, plasticity progresses in the ground on the passive side, extending from the designed ground surface towards the pile tip. Consequently, the embedded length is determined to ensure the presence of at least an elastic zone in the ground at the tip of the embedded portion of the steel tubular earth retaining wall. In total, four models were developed to conduct the p-y analysis. Lpile software was used to conduct the analysis.

Figure 4.13 shows the Lpile model conditions where a pile was socketed into a single ground layer. In this model, displacement was used as the input loading condition at a height of 6.5m from the ground surface. Mechanical properties of the pile and ground mentioned in Table 4.1 were used in the Lpile model simulation.

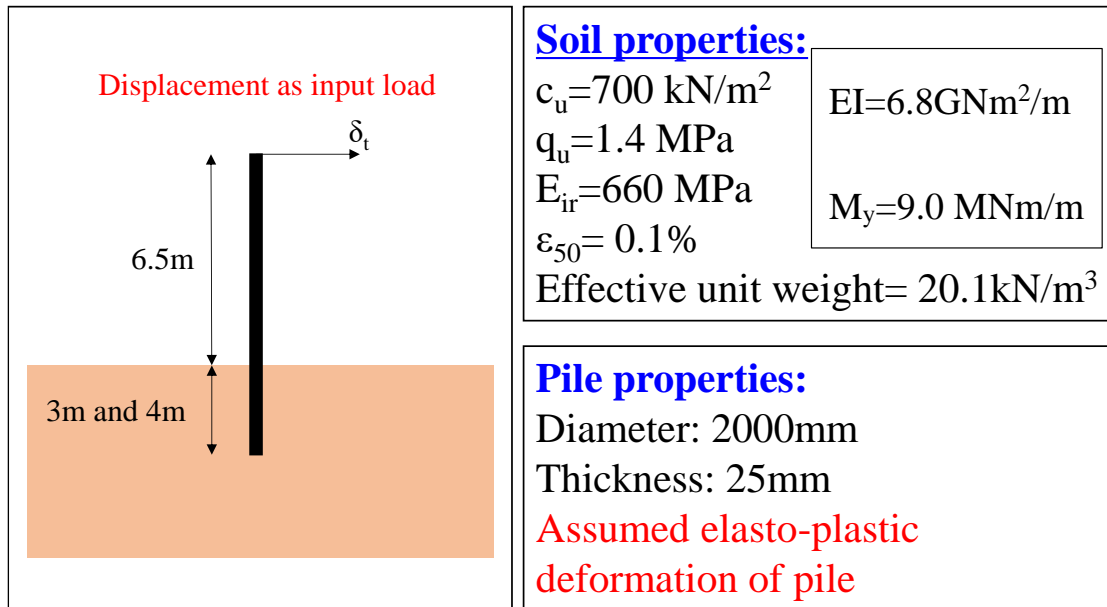


Figure 4.13: Lpile model condition.

Large diameter piles behave differently when the embedment length over diameter ratio is less than 3 ($d_t/\Phi < 3$). In those cases, the wall tends to rotate and translate instead of the conventional bending of a long, slender pile, as shown in Figure 4.14 (a). In this simulation, considering the combination of lateral and base shear springs (Figure 4.14b), four models were developed to conduct the p-y analysis.

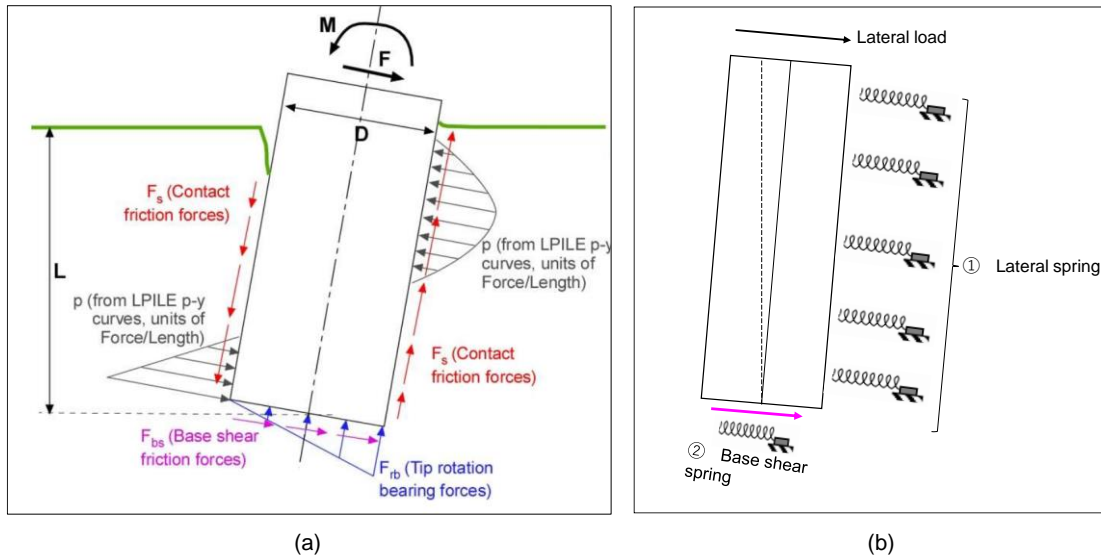


Figure 4.14: (a) effect of translation and rotation on the lateral response of large diameter pile (b) assumed condition in Lpile stimulation.

Figure 4.15 shows the Model 1 p-y curve, which was based on the JARA (2017), where a bi-linear p-y curve is used with the ultimate resistance equal to Rankine, the passive earth pressure. The stiffness of the lateral spring was calculated based on Chang's method (Equation 2.17). The mechanical properties used to calculate the spring stiffness (k_H) of the lateral spring are given in **Table 4.4**.

Table 4.4: Parameters used to calculate horizontal subgrade modulus

Parameters	Unit	Value
Pile diameter, Φ	m	2
Flexural rigidity, E.I.	kN-m ² /m	6.8x10 ⁶
α	-	4
Deformation modulus, E_o [kN/m ²]	kPa	220000
B_{ref}	m	0.3
B_H	m	6.03

Figure 4.16 shows the Model 2, which was based on two spring models, as shown in Figure 4.14(b). The lateral p-y curve (Figure 4.16a) was similar to Model 1. A bi-linear p-y curve was assumed to define the base shear p-y curve, where the ultimate resistance was defined as $p_{ult} = c_u$. Based on

JARA (2017), in the design of a deep foundation, the spring stiffness assumed for the skin friction is 30% of lateral spring stiffness. A similar assumption was made for the stiffness of the base shear spring. However, this assumption could overestimate the stiffness as the design guideline was given for concrete caisson foundations, where the base of the foundation was different from the model condition, as shown in Appendix 4.1.

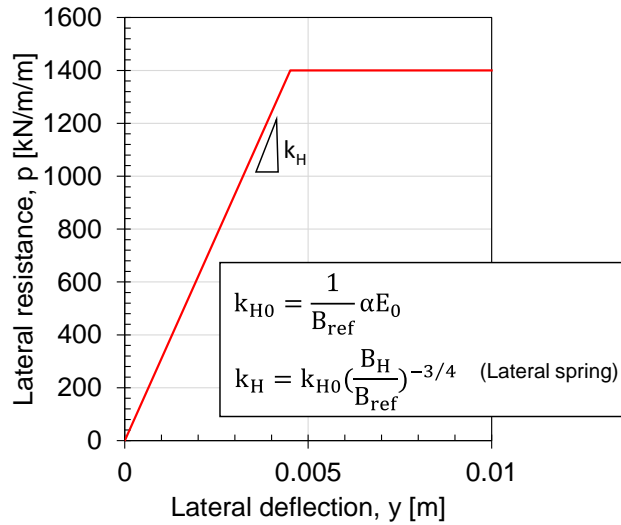


Figure 4.15: Model 1 p-y curve.

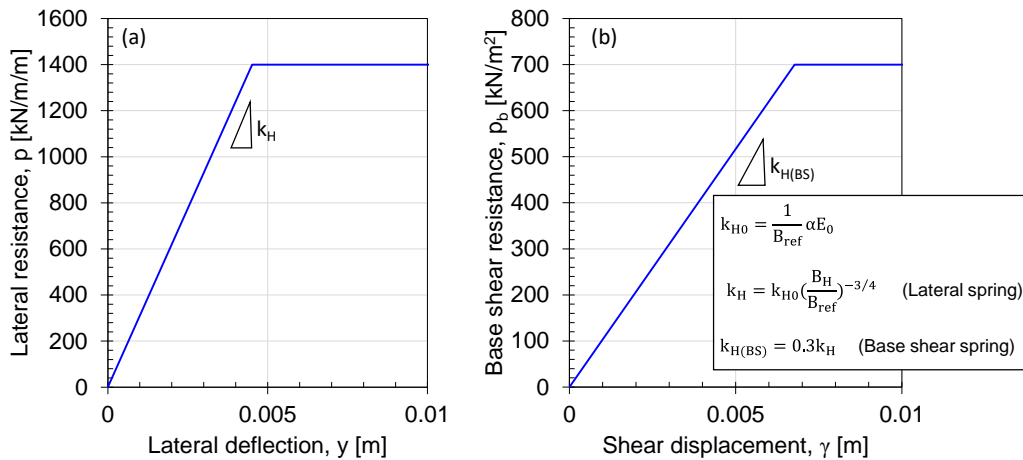


Figure 4.16: Model 2 p-y curve (a) lateral (b) base shear.

To predict this centrifuge model, two more p-y models were developed. Figure 4.17 shows the Model 3 p-y curve. Based on the laboratory direct shear testing and the numerical simulation, the peak shear displacement varies within 0.5-10mm depending on factors like confining pressure, normal stress, testing procedure etc. (Bardanis, 2024; Bahaaddini & Hebblewhite, 2013). Therefore, in Model 3 (Figure 4.14), the stiffness of the base shear p-y curve was assumed to be 1.5 times the lateral spring stiffness to obtain a shear displacement of about 1.5mm (Table 4.5).

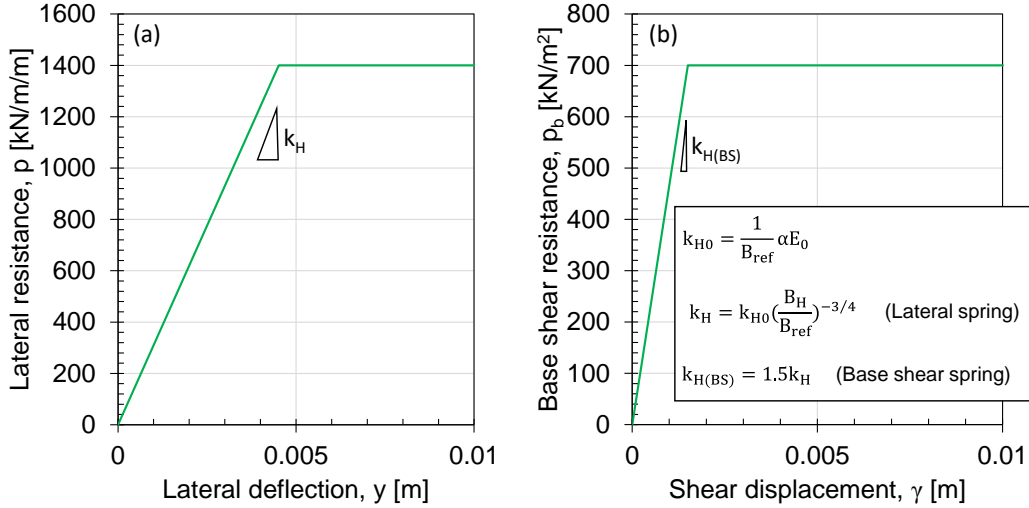


Figure 4.17: Model 3 p-y curve (a) lateral (b) base shear.

Figure 18 shows the Model 4 p-y curve. In Model 4, the slope of the lateral p-y curve was calculated based on the material properties. The ultimate lateral resistance was the same as JARA (2017) recommendation. The maximum deflection (y_c) required to reach the ultimate condition was assumed to be the same as y_{rm} given in Equation 2.41, where $y_{rm} = \epsilon_{rm} \cdot \Phi$. The ϵ_{rm} value was the same as $\epsilon_{s,50}$ reported by Kunasegaram and Takemura (2021). The slope of the p-y curve is then obtained by dividing the p_{ult}/y_{rm} . In the case of base shear (Figure 4.15b), the slope of the p-y curve was assumed to be similar to the slope of the lateral p-y curve. Finally, the calculated spring stiffness (k_H), ultimate resistance (p_{ult}) and maximum deflection (y_c) for all four models are reported in Table 4.5

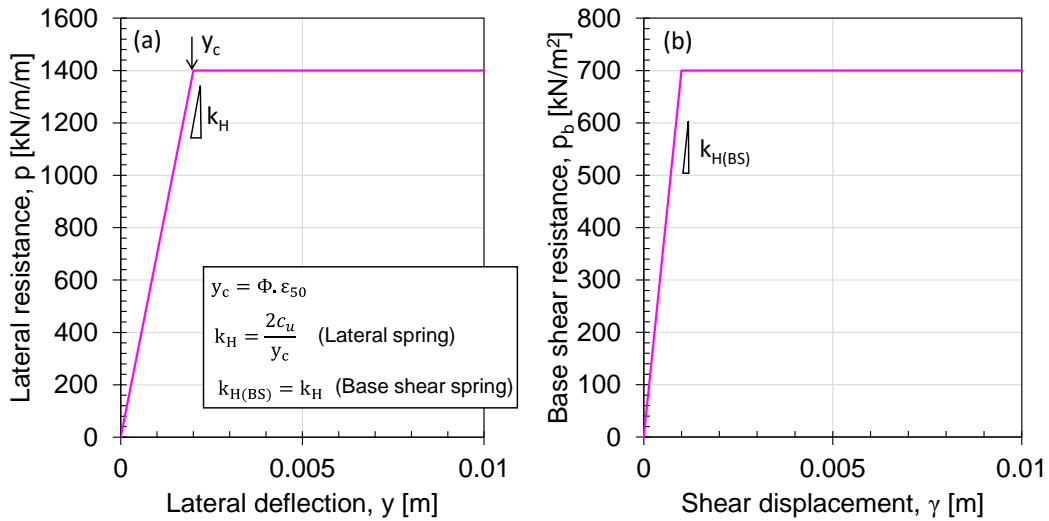


Figure 4.18: Model 4 p-y curve (a) lateral (b) base shear.

Table 4.5: List of spring stiffness (k_H), ultimate resistance (p_{ult}) and critical deflection (y_c) of model 1, 2, 3 and 4

Model no.	Lateral spring			Base shear spring		
	k_H (kN/m ³)	p_{ult} (kN/m ²)	y_c (m)	k_H (kN/m ³)	p_{ult} (kN/m ²)	y_c (m)
Model 1	310162	1400	0.00451	x	x	x
Model 2	310162	1400	0.00451	103387	700	0.00677
Model 3	310162	1400	0.00451	465243	700	0.00150
Model 4	700000	1400	0.002	700000	700	0.001

4.5.2 Results and Discussions:

The results (bending moment, shear force, wall deflection, soil reaction) from the p-y analysis at an imposed displacement of $1\%Φ$ are shown in Figure 4.19. The bending moment and shear force were larger for Model 4 than Model 3 than Model 2 than Model 1 (Figure 4.19a&b). For Model 1, there was no base shear. However, for models 2-4, the base shear increases with the increase of base shear p-y curve stiffness (Figure 4.19b, Table 4.5). On the other hand, the base shear displacement decreases with the increase of base shear p-y curve stiffness (Figure 4.19c Table 4.5). Furthermore, the base shear displacement is larger for smaller embedment depths than for larger embedment depths. Although the base shear displacement is smaller for Model 4 than Models 2 and 3, yielding of the shallow rock layer occurs earlier for Model 4 than for Models 2 and 3 (Figure 4.19d).

The observed load-displacement curve from the centrifuge test is compared with the p-y analysis in Figure 4.20. Also, a close view of the load-displacement curve at a small imposed displacement (20mm, i.e. $1\%Φ$) is shown in Figure 4.20b. In the centrifuge model test, a sudden drop in the load-displacement curve is observed around 300 mm of wall top displacement for $d_r=3.0m$ and $4.0m$, possibly due to the crack formation. After that, the load-displacement curve for $d_r=3.0m$ remains almost constant, but a gradual increase is observed for $d_r=4.0m$. This gradual increase for $d_r=4.0m$ could be due to the side wall effect, as the backward wedge reaches the container side wall (Figure 4.5). This effect of the side wall on the lateral displacement for $d_r=4.0m$ is also confirmed by the FEM analysis.

The lateral resistance of the wall increased with the embedment depth, which can also be confirmed by the p-y analysis. Also, the ultimate lateral resistance increased due to the base shear resistance. The ultimate lateral resistance predicted by the p-y analysis is smaller than the centrifuge model test, especially without base shear conditions (Model 1). Comparing Model 2 with Model 3, Model 3 reaches the ultimate condition at a smaller imposed displacement than Model 2. At small imposed displacement ($20mm=1.0\%Φ$), the slope of the load-displacement curve is underestimated by Model 1,2&3. A non-linear load-displacement relationship can be seen in the centrifuge model test

even at small imposed displacement, which the bilinear p-y curve failed to predict. Model 2 underestimates the load-displacement curve at an imposed displacement of about 80mm (4%Φ) but overestimates at an imposed displacement of 4-10%Φ. The overestimation could be considered as the limitation of the bilinear p-y curve. On the other hand, for $d_r=3.0\text{m}$, Model 2 underestimates the load-displacement curve compared to the centrifuge. Overall, it can be said that at small to large imposed displacement, Model 2 could predict the centrifuge load-displacement curve with a reasonable safety margin compared to other models. However, a non-linear p-y curve might be more suitable to predict the non-linear load-displacement relationship at small imposed displacement.

Model 4 can predict the load-displacement relation from the centrifuge with some accuracy. The secant stiffness (denoted as E_o) is back-calculated, about 2.25 times larger than the value presented in Table 4.4. The variation of β and $3/\beta$ with the pile diameter for wall and pile are shown in Figure 4.21. The β and $3/\beta$ are calculated based on Equations 2.20 and 2.19. Also, the β and $3/\beta$ calculated for Model 4 are shown in this figure. For Model 4, the β value increases more than the design condition, which reduces the required embedment depth ($3/\beta$) for $\Phi=2$ by about 30%. However, there are some uncertainties in the centrifuge load-displacement curve, especially at the small strain level, which could underestimate the initial stiffness of the load-displacement curve. Therefore, the initial stiffness could be even larger than Model 4, reducing the required embedment depth to less than 3m. This observation could explain the no embedment effect up to $\delta_t=1\%\Phi$, as shown in Figure 4.20b, as both walls behave as flexible walls.

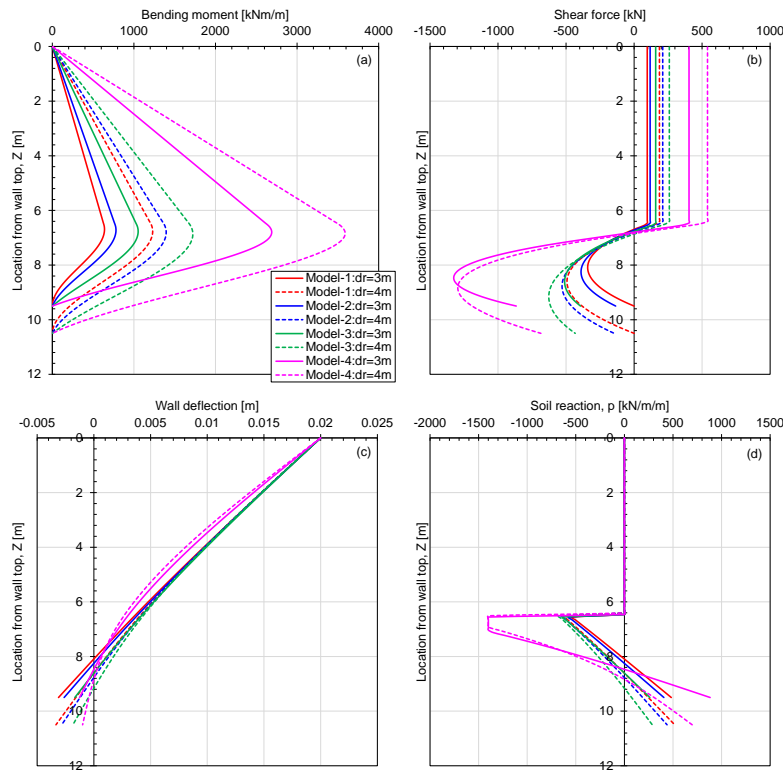


Figure 4.19: Observed results from p-y analysis at $\delta_t=1\%\Phi$ (a) bending moment (b) shear force (c) wall deflection (d) soil reaction.

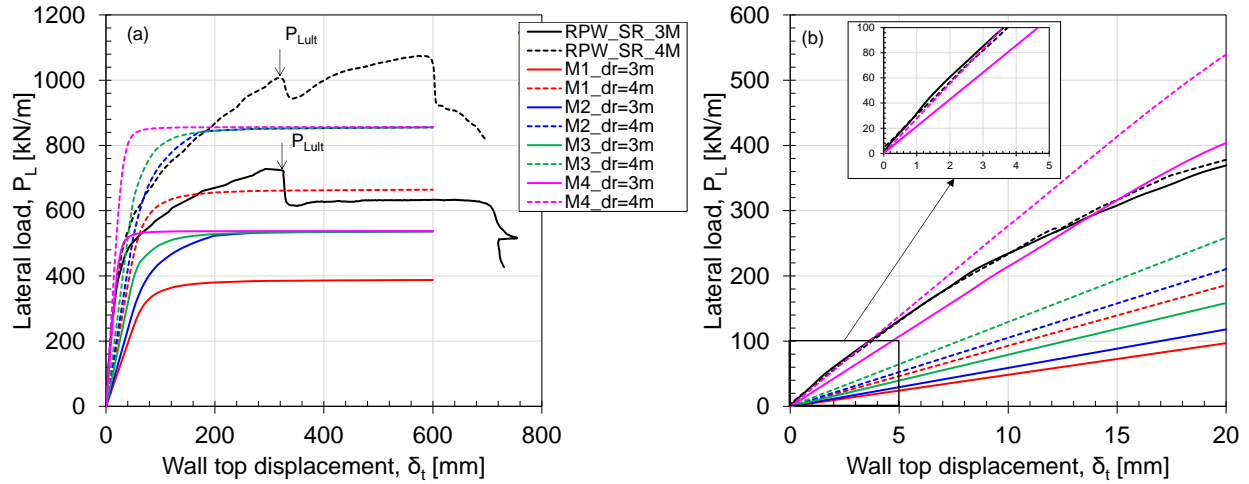


Figure 4.20: Variation of lateral load with wall top displacement from centrifuge test and p-y analysis.

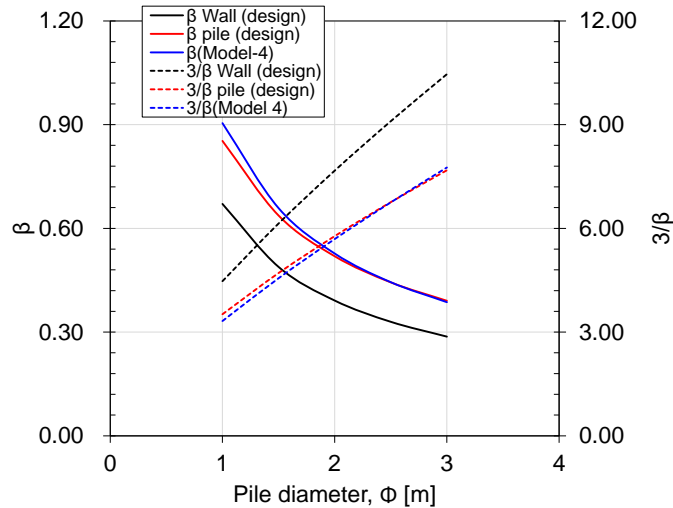


Figure 4.21: Variation of β and $3/\beta$ value with pile diameter.

To discuss the effect of base shear resistance to the lateral resistance of the wall, Model 2 is compared with Model 3. Both models have a p-y curve with similar lateral stiffness but different base shear stiffness. The ratio of lateral resistance of Model 2 and 3 to Model 1 is plotted to the wall top displacement in Figure 4.22. Larger lateral resistance is observed for Model 3 than Model 2, with a larger ratio obtained for $d_r=3\text{m}$ than 4m . Constant ratio is observed up to δ_t/H about 0.6% for both models. After this, a different trend is observed between Models 2 and 3, i.e., a decreasing trend in Model 3 but an increasing trend in Model 2. This behaviour could be due to less hardening in the load-displacement curve for Model 3 compared to Model 2 (Figure 4.20b). Although the ultimate lateral resistance is similar between Models 2 and 3, the p-y curve with a larger base shear stiffness (Model 3) will reach the ultimate condition at a very small imposed displacement compared to the p-y curve with a small base shear stiffness (Model 2).

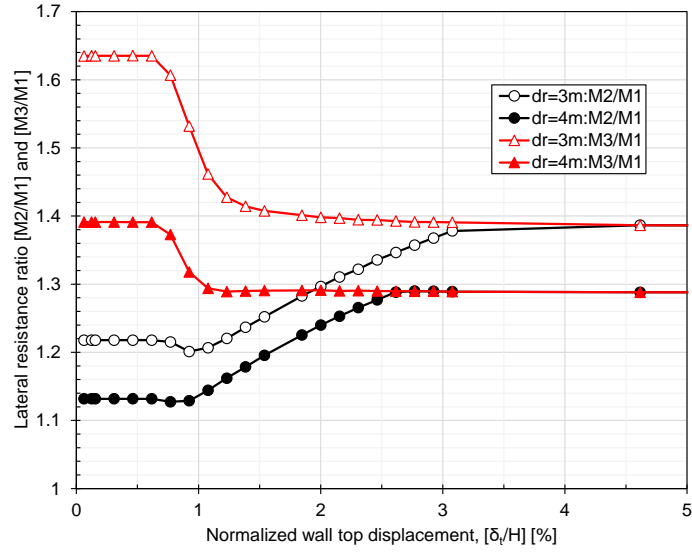


Figure 4.22: Effect of base shear stiffness on the lateral resistance of the wall.

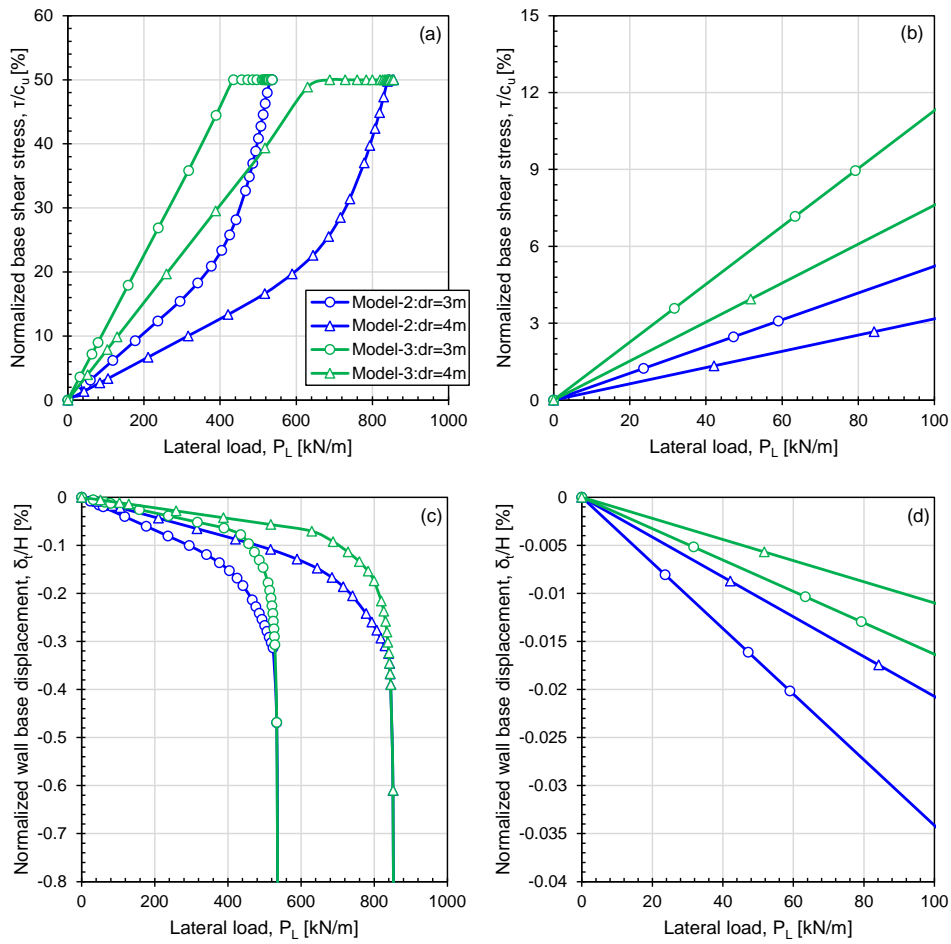


Figure 4.23: Variation of base shear and base displacement with lateral load (a,b) base shear (c,d) base displacement.

To discuss the effect of embedment depth on the base shear, the normalized base shear stress and base displacement are plotted against the lateral load in Figure 4.23. The shear stress is calculated by dividing the base shear by the pile area. In the ultimate condition, 50% of undrained cohesion (c_u) is mobilized at the base (Figure 4.23a). Different trends can be observed between Models 2 and 3. In the base shear stress-lateral load curve, more hardening can be observed for Model 2 than 3, with more nonlinearity for the larger embedment depth than the smaller embedment depth (Figure 4.23a). The contribution of the base shear in Model 3 is almost linear to the lateral load. At a certain lateral load, the mobilized base shear is larger for $d_r=3\text{m}$ than $d_r=4\text{m}$ (Figure 4.23b). As the embedment depth decreased, the base displacement increased because of translation and rotation of the wall, which caused a larger mobilization of the base shear (Figure 4.23c&d).

The following chapter will use the bi-linear p-y curve (Model 1) without the base shear recommended by the JARA (2017) to predict the residual wall displacement. Based on the p-y analysis, it can be said that two springs model (i.e., lateral spring recommended by the JARA (2017) and base shear spring with stiffness 1/3 of the lateral spring recommended for caisson type foundation by JARA (2017)) Model 2, could predict the centrifuge load-displacement relationship at small to large imposed displacement reasonably. Therefore, this p-y curve will also be used to predict the residual wall displacement.

4.6 Summary:

Based on the result and discussions from this chapter, the following conclusion could be derived:

- Based on the numerical analysis conducted for the centrifuge model test, no significant effect of the container wall was observed on the load-displacement behaviour by further increasing the container width, especially for $d_r/\Phi = 1.5$. The effect varies about 4-5% on the load-displacement behaviour. However, certain effects from the back wall could be expected for larger embedment depth $d_r/\Phi = 2.0$.
- The base shear positively contributes to the stability of the large-diameter CSTP wall. The contribution is larger for smaller embedment depth conditions than for larger embedment depth conditions.
- For the bi-linear p-y method, bi-linear P-y curve without base shear recommended by JARA (2017) could be more conservative for predicting the load-displacement relationship of large-diameter piles embedded in the stiff ground than the model with base shear spring. Two springs model, where the lateral spring is defined by the JARA (2017) and a base shear spring with stiffness 1/3 of the lateral spring recommended for caisson type foundation by JARA (2017), could predict the load-displacement curve at small to large imposed displacement ($<10.0\%\Phi$) reasonably in the conservative side, especially for the small loading level. However, a more sophisticated non-linear p-y curve might be suitable to predict the non-linear load-displacement relationship at small imposed displacement ($<1.0\%\Phi$).
- The contribution of base shear resistance to the lateral resistance of the pile depends on the base shear p-y curve stiffness. Larger base shear stiffness (Model 3) could provide larger

base shear resistance. However, the yielding might occur at a very small imposed displacement or lateral load.

- Different trends can be expected based on the base shear p-y curve stiffness. A non-linear relationship could be expected in the lateral load-base shear curve for the base shear p-y curve with smaller stiffness (Model 2) but almost linear for larger stiffness (Model 3). More hardening can be expected in the trend for smaller stiffness than larger stiffness based on the embedment depth (more hardening for larger embedment depth than the smaller embedment depth). Therefore, smaller stiffness could contribute less to the lateral resistance but prevent the quick occurrence of the ultimate condition.

References:

1. Bahaaddini, M., Sharrock, G. and Hebblewhite, B.K., 2013. Numerical direct shear tests to model the shear behaviour of rock joints. *Computers and Geotechnics*, 51, pp.101-115.
2. Bardanis, M., 2024. Direct Shear Testing of Various Hard Soils and Weak Rocks from Greece. *Geotechnical and Geological Engineering*, pp.1-20.
3. Brinkgreve, R.B.J., Engin, E. and Engin, H.K., 2010. Validation of empirical formulas to derive model parameters for sands. *Numerical methods in geotechnical engineering*, 1, pp.137-142.
4. Japan road Association (JARA). 2017. Specification of road bridges and explanations, IV: lower structures. (in Japanese).
5. Kunasegaram, V., Shafi, S.M., Takemura, J., Ishihama, Y., 2020. Centrifuge Model Study on Cantilever Steel Tubular Pile Wall Embedded in Soft Rock, in: Duc Long, P., Dung, N.T. (Eds.), *Geotechnics for Sustainable Infrastructure Development, Lecture Notes in Civil Engineering*. Springer Singapore, Singapore, pp. 1045–1052. https://doi.org/10.1007/978-981-15-2184-3_135
6. Kunasegaram, V., Takemura, J., 2022. Mechanical Behaviour of Laterally Loaded Large-Diameter Steel Tubular Piles Embedded in Soft Rock. *Geotech Geol Eng* 40, 2967–3005. <https://doi.org/10.1007/s10706-022-02075-z>
7. LPile, Version 2019. Program for the analysis of deep foundations under lateral loading, Ensoft, Inc, Texas. <http://www.ensoftinc.com>
8. Terzaghi, K., 1955. Evaluation of Conefficients of Subgrade Reaction. *Géotechnique* 5, 297–326. <https://doi.org/10.1680/geot.1955.5.4.297>

Chapter 5

Centrifuge modelling of large diameter Cantilever type Steel Tubular Pile wall wall embedded in soft rock subjected to sequential dynamic and static loadings

5.1 Introduction

In this chapter, the behaviour of a CSTP wall embedded in different ground conditions and subjected to various loadings is studied through centrifuge modelling. The preparation of the centrifuge model and the associated challenges are detailed in this chapter. Additionally, the p-y curves discussed in Chapter 4 are employed to predict the wall behaviour after complex loading is applied to the CSTP wall. Finally, this chapter concludes with some appraisal of potential enhancements to the current design method.

5.2 Modeling concept

The centrifuge model wall was designed to represent a permanent CSTP wall, as shown in Figure 1.3. This type of wall will be subjected to various loadings in its service period after construction, such as earthquakes and build-up water levels in the retained soil, which might cause excessive wall deformation, even catastrophic failure of the retaining structure (Day, 1997; D'Andrea and Day, 1998). In the centrifuge model of embedded CSTP wall in soft rock, a series of dynamic loadings were first applied in dry retained sand conditions. Then, a static loading was simulated by raising the groundwater height in the retained sand. Furthermore, dynamic loadings were applied in the wet sand conditions. Also, the loading sequence was changed where the water level was increased on the retained side without any prior dynamic loading, and then the dynamic loading was applied.

From the observation of the wall and retained sand behaviour, the interaction between the retained soil and the large diameter CSTP wall embedded in soft rock could be examined not only during loadings but also after loadings.

5.3 Model preparation and loading conditions

5.3.1 Model preparation:

The experiment was conducted using a TIT Mark III geotechnical centrifuge (Takemura et al., 1999) with a centrifugal acceleration of 50g. The setup of the centrifuge model is depicted in Figure 5.1. The model was prepared in a model container with internal dimensions of 600mm in length, 250mm in width, and 400mm in depth, as illustrated in Figure 5.2a&b. The container consisted of a removable rear-side aluminium wall and a front-side transparent acrylic wall, both bolted to the main container body to create a rigid box. To accommodate the model CSTP wall, a 33mm acrylic plate (shown in Figure 5.2c) was fixed to the back wall, reducing the container width, as depicted in Figure 5.3a.

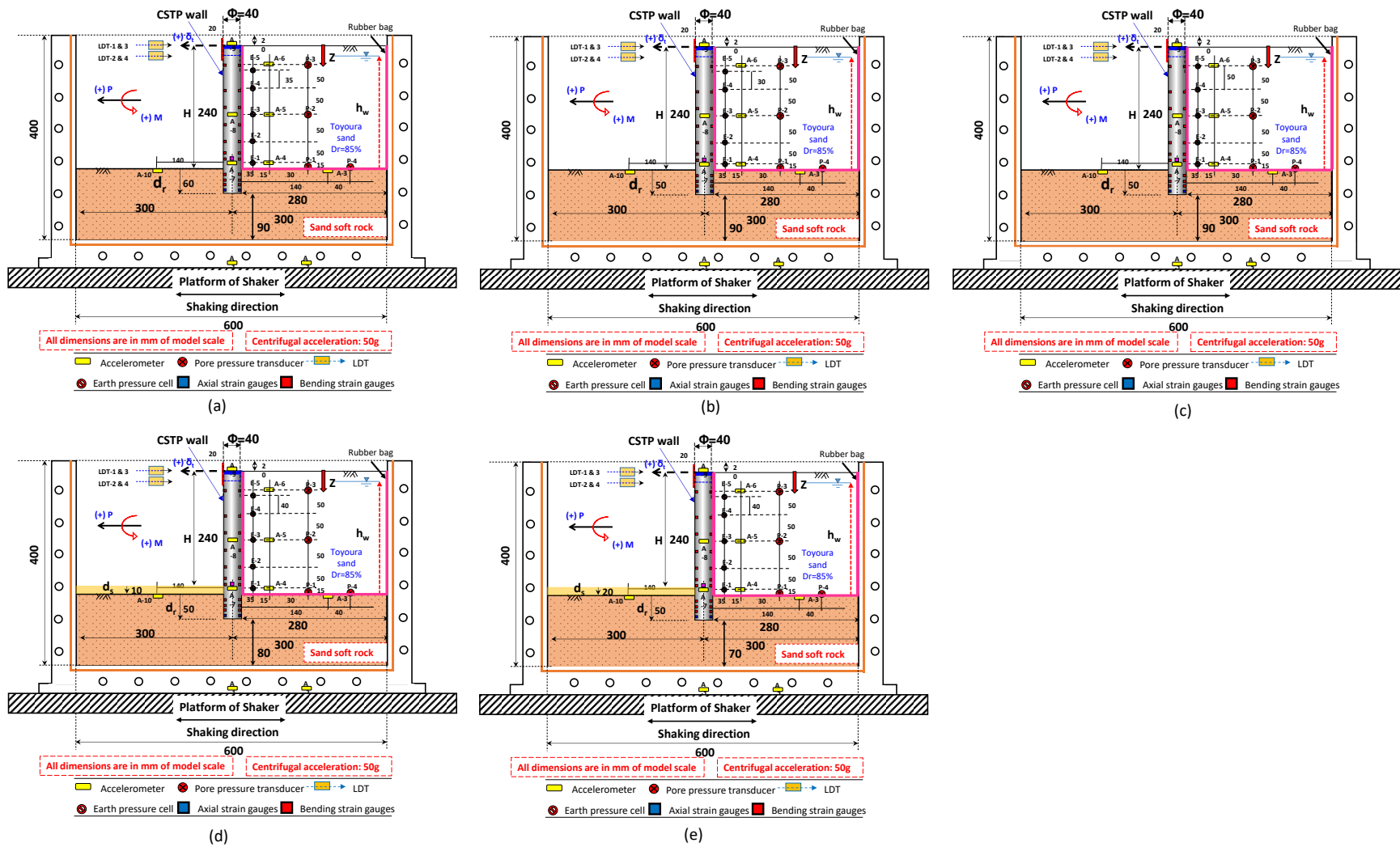


Figure 5.1: 2D view of the model setup (a) Case 1 (b) Case 3 (c) Case 6 (d) Case 4 (e) Case 5.

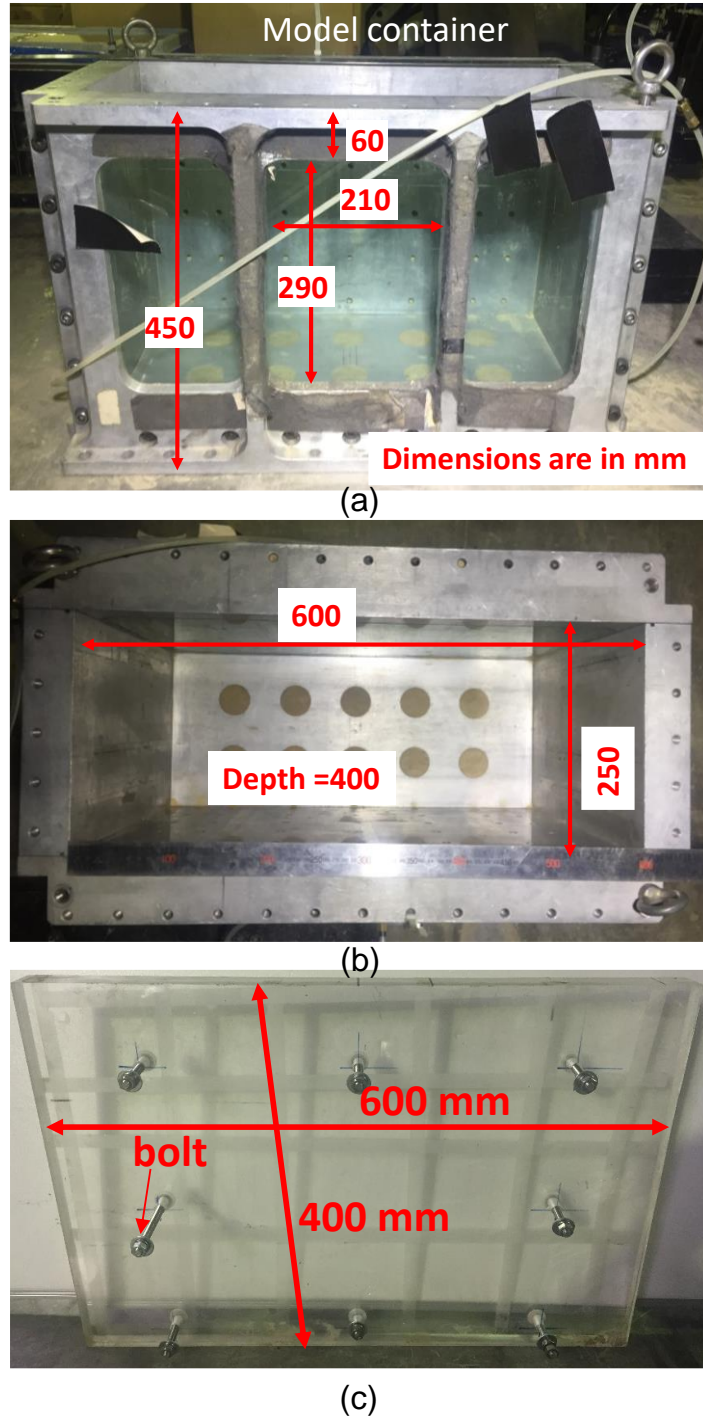


Figure 5.2: Model container used (a) front view (b) top view (c) acrylic plate attached to the container back wall to reduce the container width.

The model CSTP wall consisted of five stainless steel tubular piles with a pile holder, as shown in Figure 5.3a. Each individual pile had an outer diameter (Φ) of 40mm and a thickness (t) of 0.5mm.

A pile cap, made from a solid circular aluminium bar (refer to Figure 5.3b), was tightly attached to the pile head. The length of each pile, including the pile cap, was 300mm and 290mm for the single rock layer model. In the case of rock with an overlaying sand layer, the pile length was 300mm (for $d_s=10\text{mm}$) and 310mm (for $d_s=20\text{mm}$), including the pile cap. After fixing the pile cap, strain gauges were applied to the piles using epoxy resin coating at the specified locations shown in Figures 5.4 and 5.5 for the single rock layer model and the model with an overlaying sand layer, respectively. Once the resin coating solidified, the five piles were secured at the top using the pile holder, as depicted in Figure 5.3a.

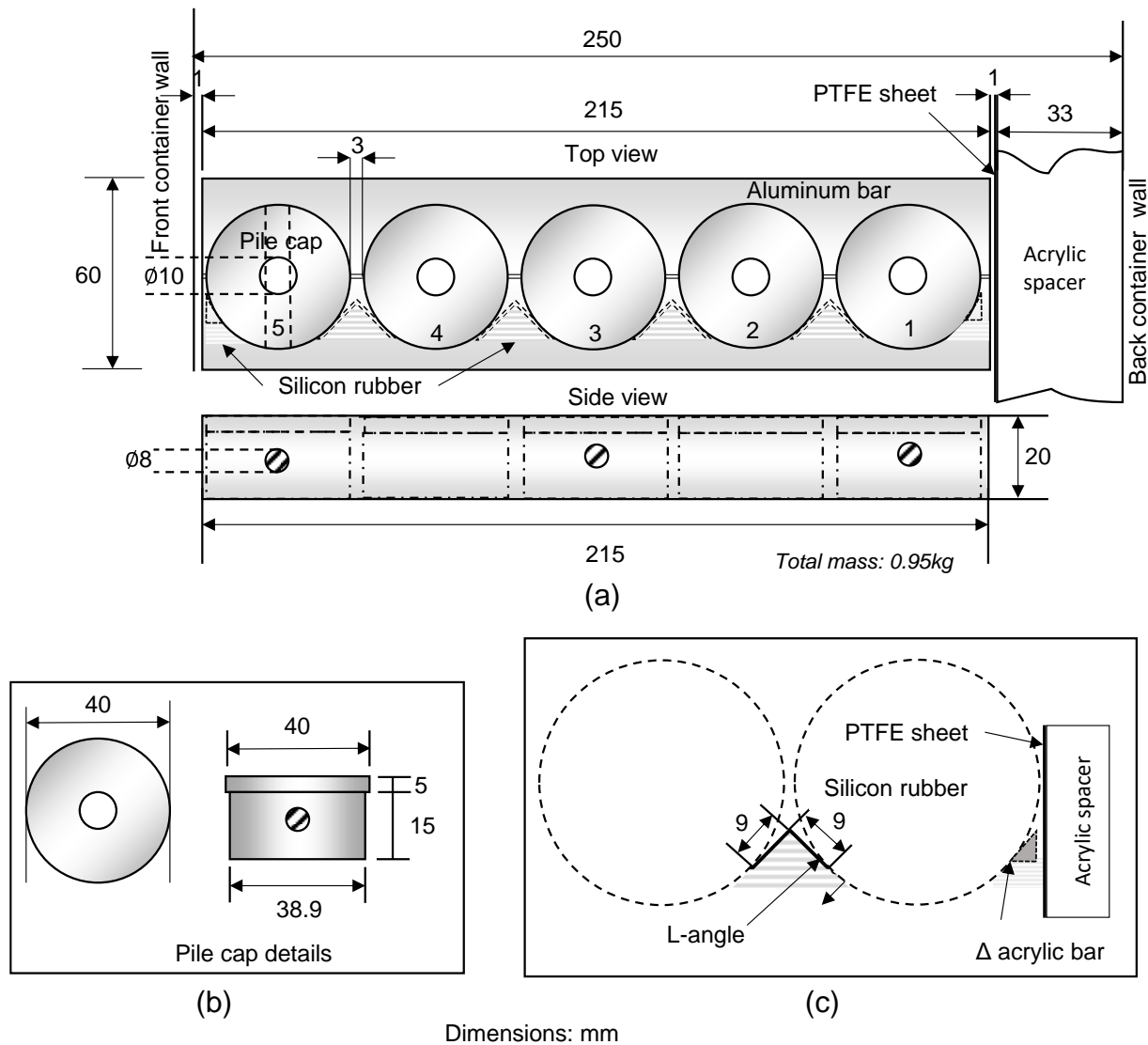


Figure 5.3: (a) Pile holder (b) pile cap used to attach at the top (c) location of L-angle and acrylic bar.

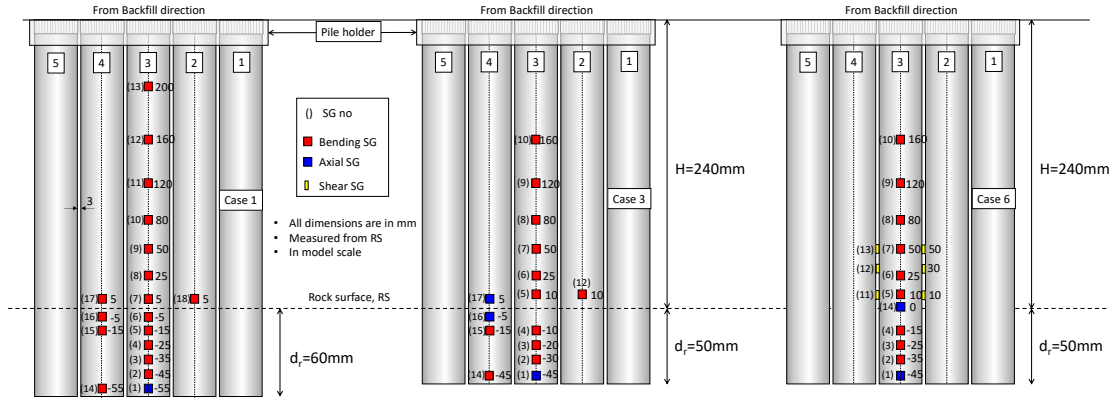


Figure 5.4: Strain gauges location in single rock layer model.

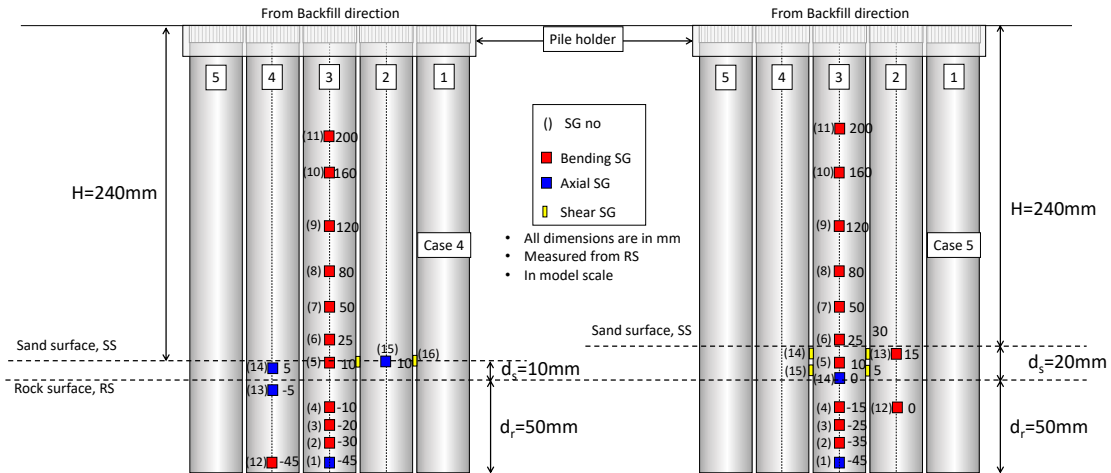


Figure 5.5: Strain gauges location in rock with overlaying sand layer model.

The CSTP wall was embedded in artificially created soft rock in the centrifuge model. The process of preparing the artificial soft rock is explained in section 3.3 of this paper. The artificial soft rock was formed by combining cement, sand, clay, and water according to the ratios specified in **Table 5.1**, following the methods described by Kunasegaram et al. (2015) and Kunasegaram and Takemura (2021).

Before casting, the unsolidified mixture was poured into the container, and 0.5 mm thick polytetrafluoroethylene (PTFE) sheets were pasted to the front and rear internal walls of the container. These sheets were lubricated with silicone grease to facilitate the detachment of the walls from the hardened soft rock ground. The rock ground was created by compacting the mixture layer by layer using a mechanical vibrator, with each layer having a thickness of 20mm. This compaction process ensured the desired density was achieved up to 140-150mm depth for the single rock layer, as depicted in Figure 5.1a-c. For the rock with an overlaying sand layer, the rock ground was compacted up to depths of 130mm ($d_s=10\text{mm}$) and 120mm ($d_s=20\text{mm}$), as shown in

Figure 5.1d-e. Additionally, ten mould samples with a diameter of 50mm and a height of 100mm were prepared from the same rock mixture for the unconfined compression test. The entire compaction process and mould sample preparation were completed within 1.5 hours before the cement solidified. Immediately after compaction, the model CSTP wall was vertically inserted into the unsolidified ground at the centre of the container, ensuring that the rock material fully surrounded the piles up to the rock surface. Once inserted, the wall was securely fixed in an upright position using a guide plate. The exposed surface of the unsolidified soft rock material was then covered with wet towels and kept at room temperature for curing.

Table 5.1: Physical properties of model soft rock

Property	Value
Water/Cement ratio	395 (%)
Clay: Sand ratio	30:70
Cement/Sand ratio	5.7 (%)
Water/solid ratio	21.5 (%)
Bulk density	2060 kg/m ³
Dry density	1715 kg/m ³

On the 10th day of the curing period, the rear wall of the container was removed, and a new PTFE sheet was greased and placed on the wall. The wall was then reattached to the container. Subsequently, the front wall of the container was also removed, and 5 mm square grids were drawn on the front surface of the rock to visualize ground deformation (Figure 5.6a). L-angle aluminium bars were affixed to the gaps between the piles and the front wall, while triangular-shaped acrylic bars were attached to the gaps between the piles and the rear wall (Figures 5.3a&c and 5.6b). These gaps were sealed using silicon rubber (Figure 5.6c). The PTFE sheet that was originally attached to the acrylic plate on the front wall of the container was removed to provide transparency in the front view of the model (Figure 5.6b). However, before reattaching the front wall, the acrylic plate was coated with grease.

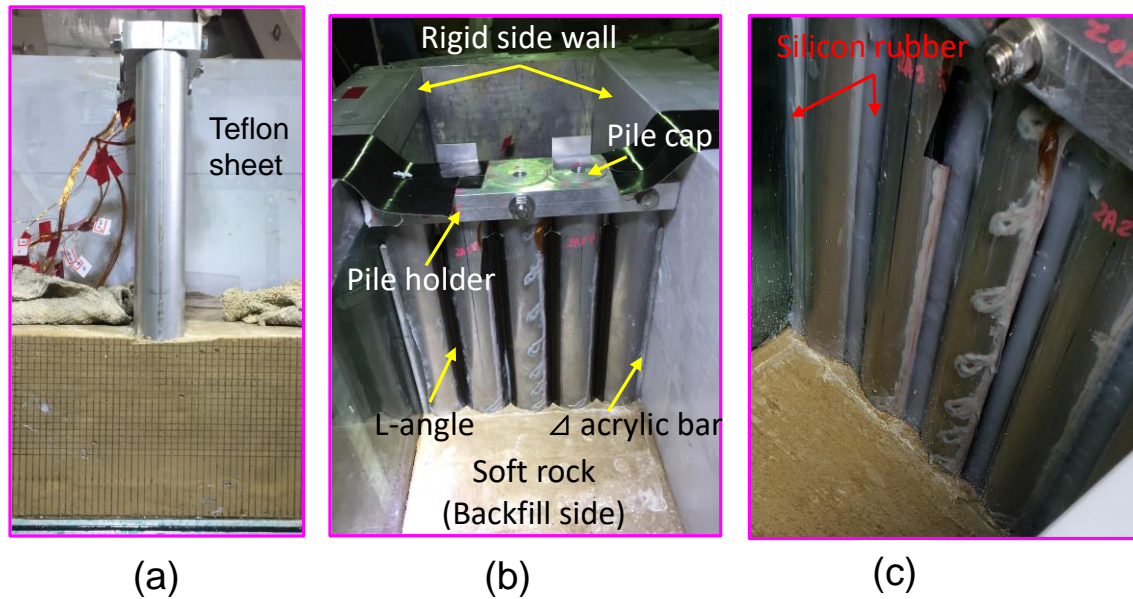


Figure 5.6: (a) 5x5 mm mesh drawn on rock surface for image analysis (b) Model CSTP wall in a rigid container and socketed into the artificial soft rock (c) Gap between the piles filled with silicon rubber.

On the 12th day of curing, the backfill soil behind the wall was prepared. A rubber box (see Figures 5.7a and 5.7d) was made using a 0.5mm thick latex membrane on the sides and a carbon fibre sheet on the bottom (see Figure 5.7b). The adhesive used for creating a watertight environment and attaching the sand to the carbon fibre is illustrated in Figure 5.7c. The rubber bag served to create a water-tight environment in the backfill and establish frictionless boundary conditions between the sand and the wall by applying grease to the outer surface of the rubber bag. To ensure better shear stress transmission during shaking, both sides of the carbon fibre sheet were roughened by adhering sand particles. After attaching the sand to the bottom of the rubber box, it was placed on the retaining side, and backfilling was carried out.

An open dry backfill sand with a height of 240mm was placed in a rubber bag (see Figure 5.1a). Toyoura sand (Fukushima and Tatsuoka, 1984; Tatsuoka et al., 1986) with a relative density (D_r) of 85% was prepared using the air pluviation method. In the case of rock with an overlaying sand layer, the sand layer in front of the wall was prepared to maintain the same relative density. The model was extensively instrumented to measure wall and ground accelerations, wall displacements, lateral and pore water pressure in the sand, and wall bending strains. Wall displacement was measured using a pair of Laser Displacement Transducers (LDTs) installed at the top of the wall. Lateral pressures were measured using small-sized Earth Pressure Cells (EP cells) placed at different depths in the backfill sand. It should be noted that there is uncertainty in assessing lateral forces using small earth pressure cells for several reasons, such as stress concentration on the cell, particularly near the CSTP wall with a concave/convex surface (Weiler and Kulhawy, 1982). Pile bending moments were calculated from the measured bending strains using the strain gauges (see

Figures 5.4 and 5.5). Euler-Bernoulli beam theory was employed in this study to convert bending strain to bending moment. The water pressures, measured by Pore Pressure Transducers (PPTs) installed at different depths, were used to estimate the water level in the backfill. All tests were conducted on the 14th day of curing. Figure 5.8 shows a photograph of the container mounted on the Tokyo Tech Mark III centrifuge just before starting the centrifuge spinning.

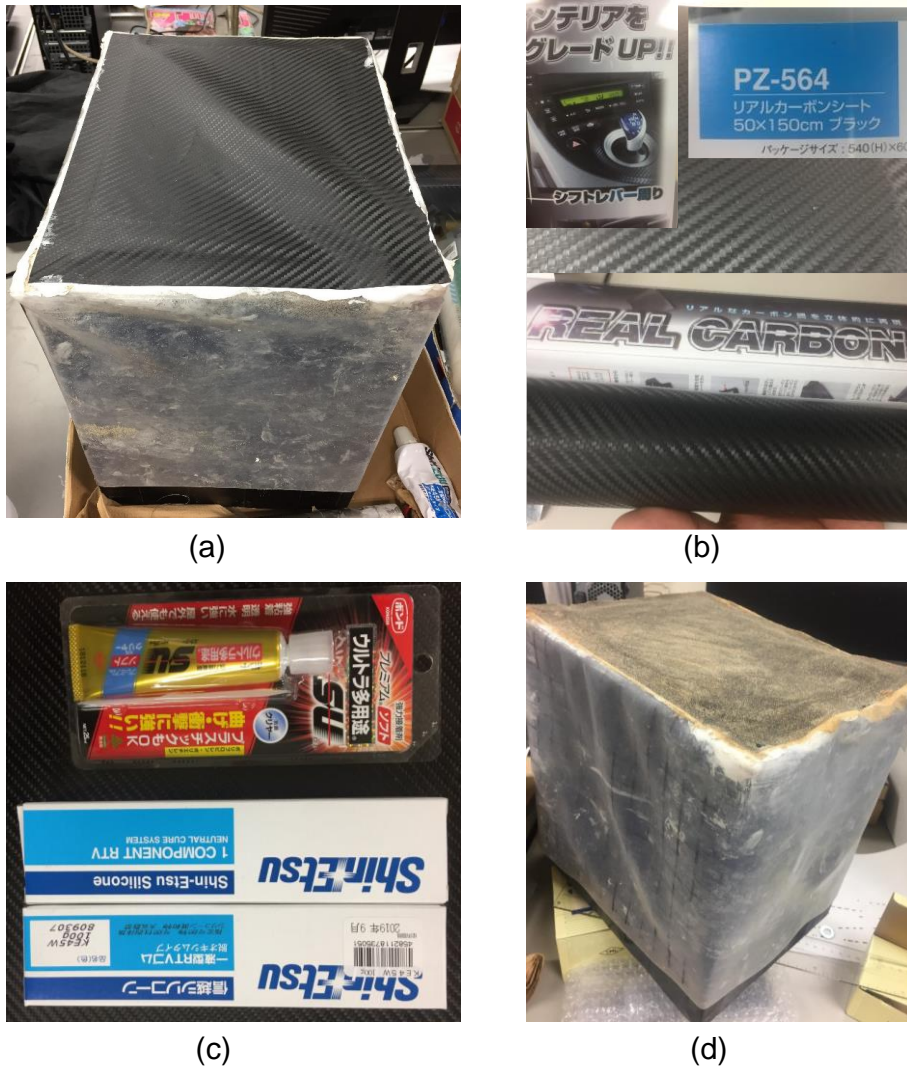


Figure 5.7 (a) rubber bag without bottom rough surface (b) carbon fibre used at the bottom of the rubber bag (c) adhesive used to prepare the rubber bag (d) rubber bag with sand attached at the bottom.

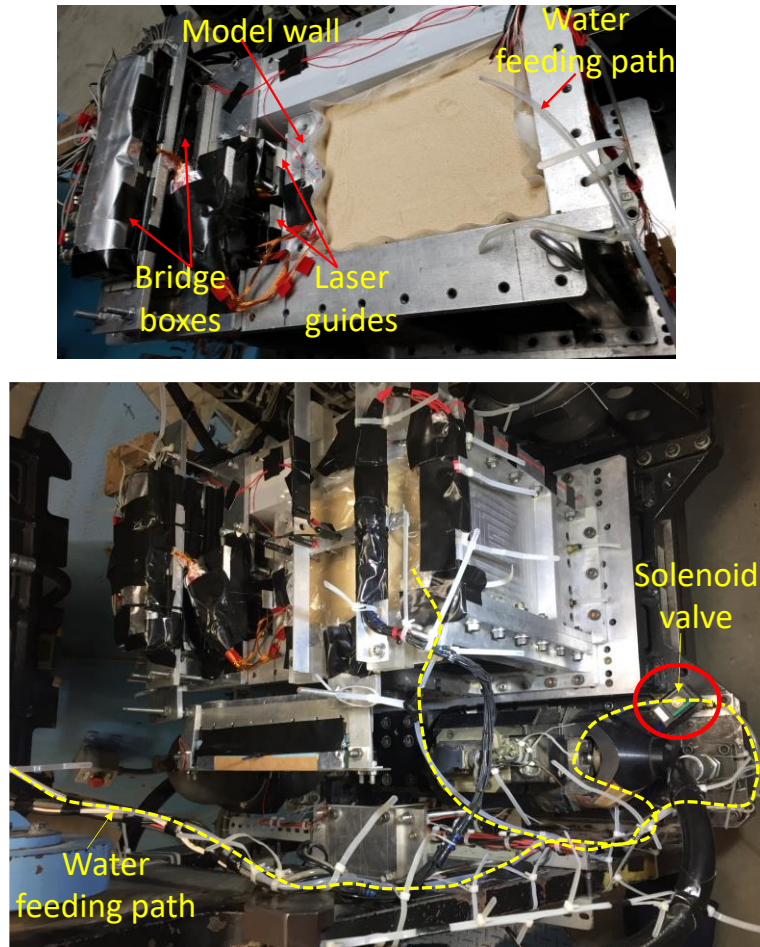


Figure 5.8: Model container mounted on the centrifuge platform just before the test.

5.4 Centrifuge test conditions

5.4.1 Single rock layer model test conditions

Three tests were conducted using the single rock layer model to investigate its behaviour. The test conditions and material properties employed in each test are summarized in Table 5.2. All test conditions were identical except for the embedment depth. In Case 1, the embedment depth was set to 3m, while in Case 3 and 6, it was reduced to 2.5m. Previous centrifuge tests conducted by Kunasegaram and Takemura (2021) utilized a 2D plate wall model (equivalent to CSTP wall with $\Phi = 2.5\text{m}$ and $H = 12\text{m}$) with an embedment depth of 3m, demonstrating a substantial factor of safety against catastrophic failure, even with a high water level ($h_w \sim 12\text{m}$) under 95g acceleration. An identical model of soft rock was employed in this study to maintain consistency. Therefore, Case 1 was conducted with an embedment depth of 3m ($\beta d_r = 1.2$). After analyzing the test results from Case 1, the embedment depth was further reduced to 2.5m ($\beta d_r = 1.0$) in Case 3. Similarly, Case 6 was conducted with an embedment depth of 2.5m ($\beta d_r = 1.0$) but with different loading sequences.

The mechanical properties of the model soft rock ground were determined through unconfined compressive strength tests (UCT), the results of which are presented in Figure 5.9. Two types of strain measurement were conducted: (1) using a dial gauge and (2) utilizing strain gauges. Prior to the test, two transverse and longitudinal strain gauges were affixed to the moulded sample. Figure 5.9a illustrates the unconfined compressive strength test results based on strain measurements obtained from both the dial gauge and longitudinal strain gauge. It was observed that the strain measured by the strain gauge was smaller than that obtained from the dial gauge. The unconfined compressive strength (q_u) and secant stiffness (E_{50}) of the model soft rock were calculated and compared with the results reported by Kunasegaram and Takemura in 2021, as depicted in Figure 5.9b. A wide variation was observed in the relationship between q_u and E_{50} . The measured q_u and E_{50} values of the model soft rock are provided in Table 5.2. Overall, the strength and stiffness measurements obtained through the strain gauges were found to be 2-3 times larger than those obtained through the dial gauges. Kunasegaram and Takemura proposed $q_u = 1.4$ MPa and $E_{50} = 660$ MPa as the mechanical properties of this artificial soft rock. These proposed values were subsequently utilized for conducting the stability analysis of the wall model.

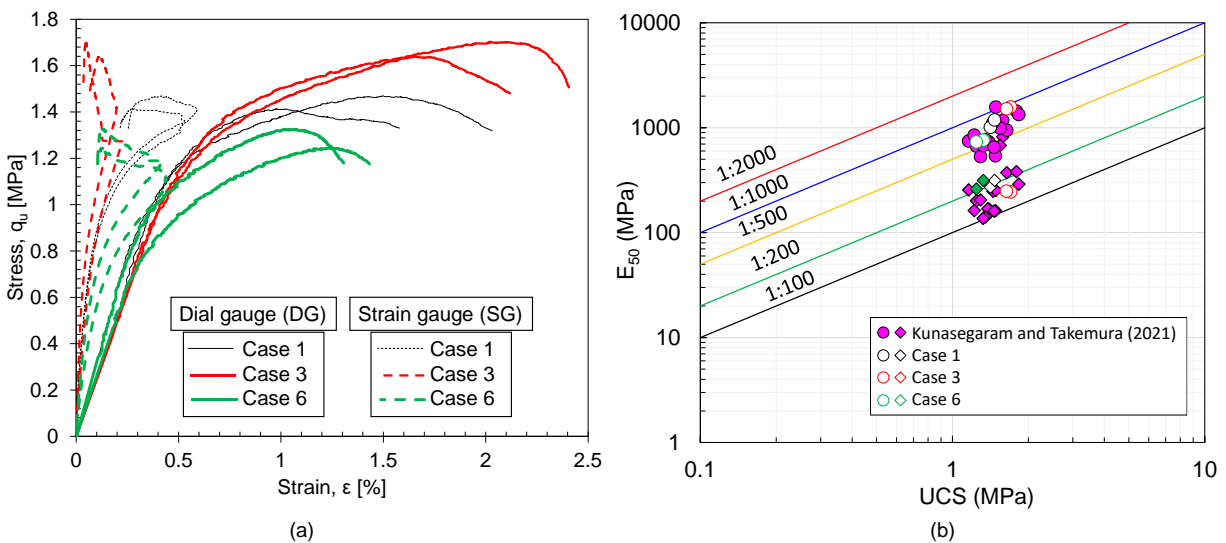


Figure 5.9 Mechanical properties of model soft rock (a) stress-strain relationship from UCT test (b) variation of E_{50} with the q_u .

The pressure diagram employed for the stability analysis is presented in Figure 5.10. The pressure distribution diagram was adapted from the pressure distribution provided for clay soil by Madabhushi and Chandrasekaran (2005). The following conditions were assumed for the modification of the pressure diagram: (i) the backfill material is cohesionless, (ii) the rock is treated as a cohesive material with zero friction angle ($\phi' = 0^\circ$), and (iii) due to the high undrained shear strength of the rock ($C_u = 700$ kN/m²), the tension zone beneath the rock surface was disregarded.

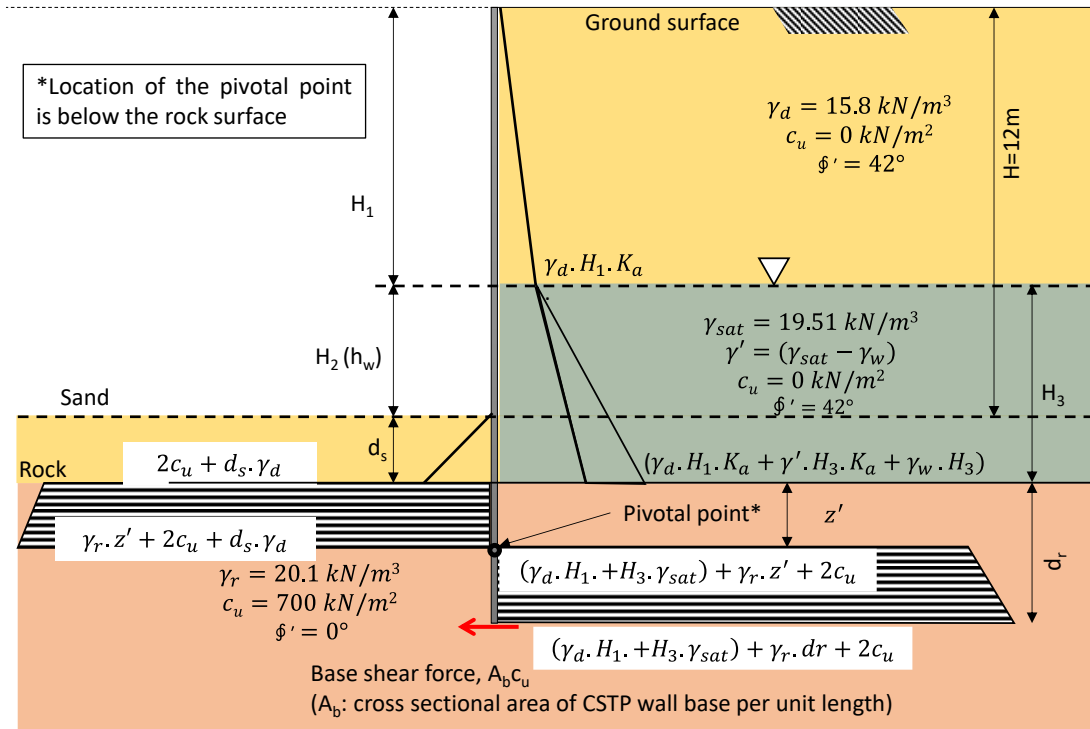


Figure 5.10: Assumed pressure distribution diagram for stability analysis.

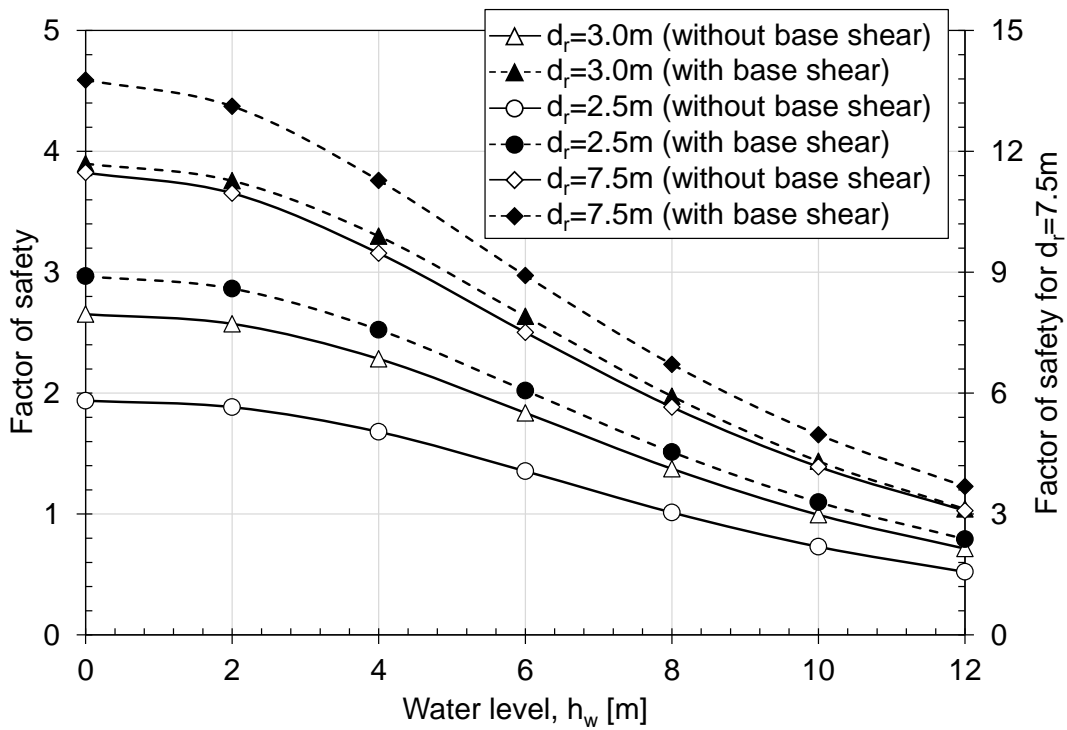


Figure 5.11: Variation of factor of safety with the water level.

The factor of safety is defined as the ratio of the resisting moment (M_r) to the disturbing moment (M_a). The resisting moment was computed based on the passive pressure, while the disturbing moment was determined using the active pressure diagram. Furthermore, the calculation of the factor of safety considered the presence or absence of base shear effects. By increasing the active pressure, which was achieved by raising the water level on the retained side, the factor of safety was evaluated, and the results are presented in Figure 4.11. It was observed that the factor of safety decreases with an increase in the water level. This figure also demonstrates the influence of the embedment depth on the CSTP wall's stability; a greater embedment depth corresponds to a higher factor of safety. Increasing the rock embedment depth by 0.5m resulted in an approximately 30% increase in the factor of safety. Additionally, it was noted that the factor of safety obtained for the design-recommended embedment depth yielded unrealistic values. Moreover, the inclusion of base shear effects contributed to an additional factor of safety (approximately 30% increase at $h_w=0m$) compared to the case without base shear effects.

Table 5.2. Test conditions and material properties of single rock layer Cases

Test code	Embedment soft rock and backfill sand	Rock socket depth: d_r () [§] , $[\beta d_r]$ { $h_w(m)$: WR1 ; h_w : WR2 } <FS: $h_w(m)$ = 0 ; WR1 ; WR2 >	Wall/Pile Properties Φ , t , EI , M_y () [§]
Case 1 C1	<u>Toyoura sand:</u> ($D_r=85\%$): $\gamma_d=15.8kN/m^3$	3.0m (60 mm) [1.2] { 9.6 ; 10.9 } < 2.6 ; 1.1 ; 0.86 >	$\Phi=2m$ (40 mm) $t= 25mm$ (0.5 mm) Spacing: 2.15m (43 mm)
Case 3 C3	$\phi'=42^\circ$ <u>Soft rock:</u> $\gamma_t=20.1kN/m^3$	2.5m (50 mm) [1.0] { 8.3 ; 10.3 } < 1.9 ; 0.95 ; 0.69 >	$EI= 6.8 GNm^2/m$ ($5.4 \times 10^{-5} GNm^2/m$) $M_y= 9.0 MNm/m$
Case 6 C6	$q_u=1.4MPa$ (C1) $q_u=1.6MPa$ (C3) $q_u=1.3MPa$ (C6) $E_s=1097MPa$ (C1) $E_s=1546MPa$ (C3) $E_s=746MPa$ (C6)	2.5m (50 mm) [1.0] { 7.7 } < 1.1 >	($3.6 \times 10^{-3} MNm/m$)

§:(model scale); βd_r : normalized depth of model CSTP wall;

The complete loading sequences and histories for Cases 1, 3, and 6 are summarized in Figure 5.12. The input motion considered for the analysis was obtained from the accelerometer A2, as depicted in Figure 5.1. This figure provides essential information such as the maximum amplitude of the input motion (a_i), the number of cycles (n_c) in each shaking, the incremental displacement ($\Delta\delta_i$) for each loading step, and the duration of white noise applied at the prototype scale. Initially, dynamic loadings were applied under dry conditions. In Case 1, five shakings were performed, gradually increasing the input motion amplitude. Conversely, in Case 3, a single shaking with a large input motion amplitude was applied. Subsequently, a static loading from the water pressure in the backfill was applied by supplying water to the retaining side. Following this, dynamic loadings were applied under wet conditions, following a procedure similar to the dry backfill loading sequence implemented in Cases 1 and 3, respectively. Afterwards, water was further supplied in the backfill. Lastly, one dynamic loading with the highest amplitude was applied under wet conditions for Case 1. In contrast, for Case 3, two dynamic loadings were performed. In Case 6, static loading was applied first, followed by dynamic loading with a large input amplitude.

Figure 5.13 illustrates a representative example of the input acceleration applied in the form of a sinusoidal wave with a predominant frequency of 1 Hz. The information about all the input motions from Cases 1, 3 and 6 is given in Appendix 5.1. The determination of the number of effective cycles (n_c) involves counting the cycles in the negative direction, as demonstrated in Figure 5.13a. The counting range is confined to nearly constant peak amplitude cycles in both positive and negative directions. The maximum amplitude (a_i) of the input motion is determined by averaging the maximum amplitudes in the positive and negative directions (Figure 5.13a). This maximum amplitude is approximately 15% larger than the average amplitude. As observed in Figures 5.12 and 5.13, the number of cycles varies among different cases. Therefore, the Arias intensity (A_i), defined in Figure 5.13b, was used as an index property for comparing results between different cases. Furthermore, Figure 5.13a presents examples of different time snaps used to collect data, like the beginning of residual after dynamic loading (t_1) or the end of the long-term residual of previous loading ($t=0$). The shape of the white noise and the corresponding transfer function of Cases 1 and 3 are shown in Appendix 5.2 -5.4. The transfer function was obtained by dividing the First Fourier Transfer (FFT) of the wall top or backfill top by FFT of input white noise. The frequency during the first maximum amplitude was defined as the frequency of wall and backfill after different loading conditions. The observed frequency at the wall top and backfill top after each loading event for Cases 1 and 3 is summarized in Tables 5.3 and 5.4, respectively.

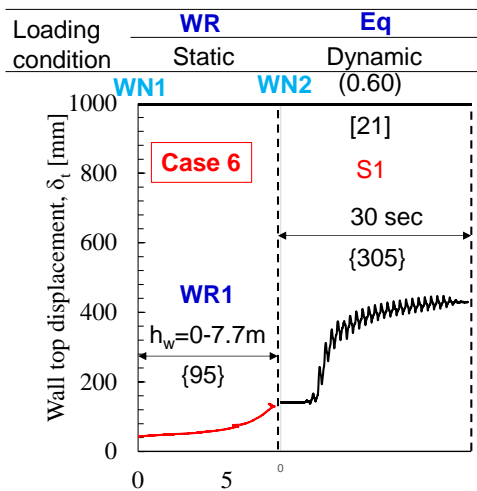
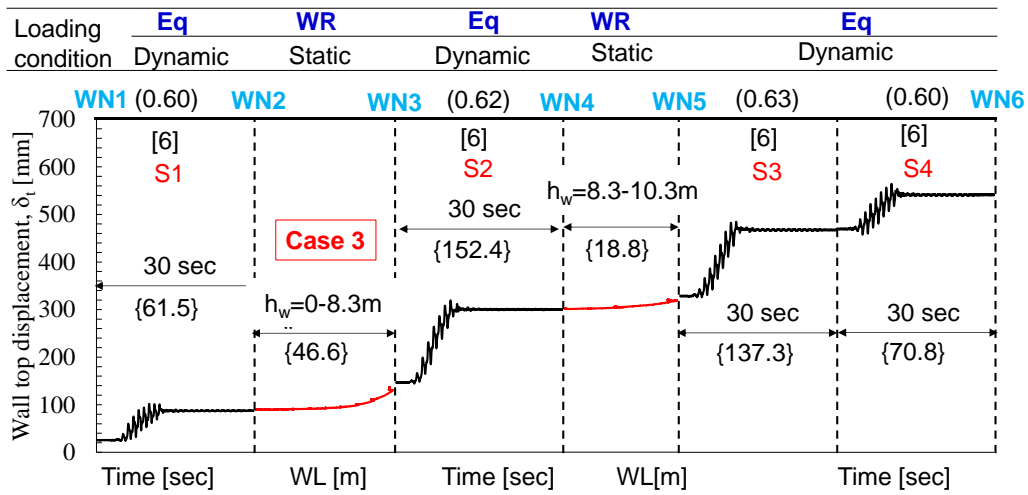
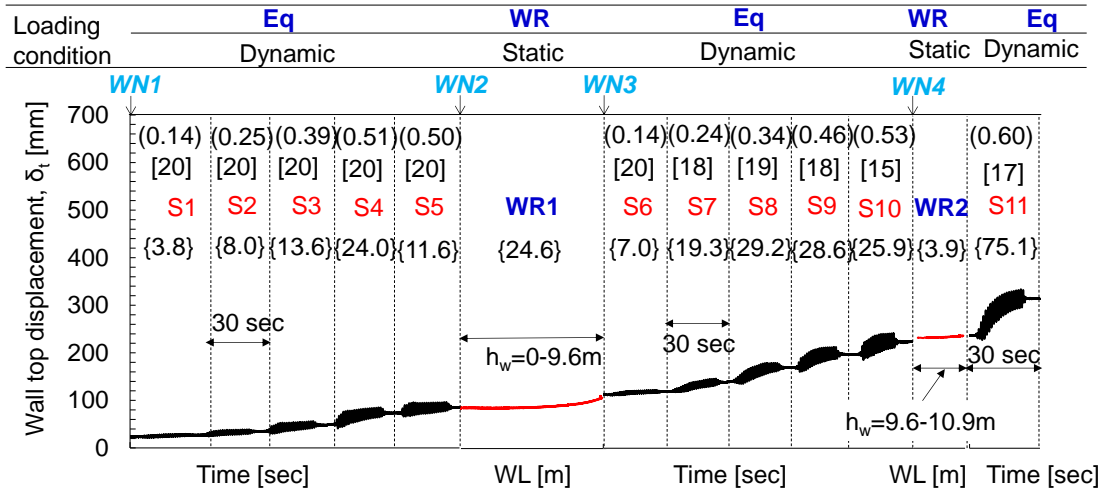


Figure 5.12: Loading sequence and histories followed in Cases 1, 3 and 6.

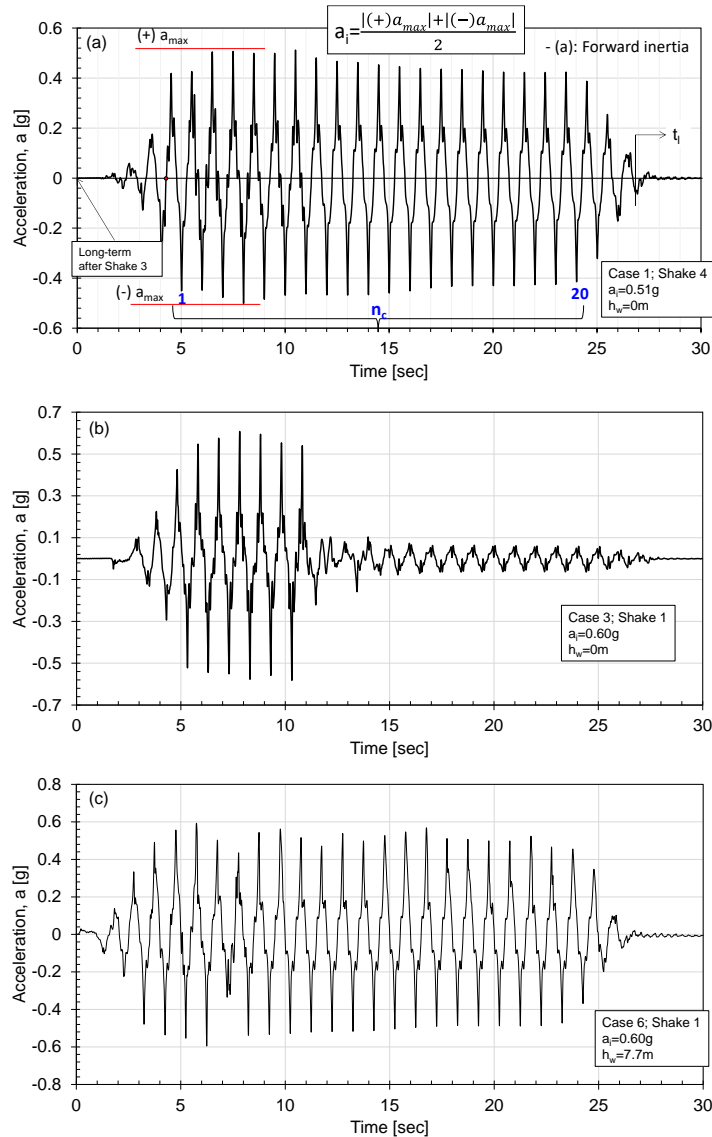


Figure 5.13: Typical shape of input motion in (a) Case 1 (shake 4) (b) Case 3 (shake 1), and (c) Case 6 (shake 1).

For static loading, high-pressure water was supplied from a water storage tank to the backfill (Figure 5.14c). The water pressure exerted on the wall was measured using the pore pressure transducer P1, as depicted in Figure 5.1. Based on the water pressure measurements, the corresponding water height was determined through back-calculation. Figure 5.14a&b displays the measured water levels during the WR1 and subsequent WR2 for Cases 1, 3, and 6. Once the maximum water level was reached during each static loading event, time was allowed to pass to achieve equilibrium conditions. During Case 6, a reduction of the water level (Figure 5.14a) occurred due to the leakage of the rubber bag. The maximum water levels attained during each water rise are reported in **Table 5.2**. As illustrated in Figure 5.11b, an increase in the water level

corresponds to a reduction in the factor of safety. Additionally, the calculated factor of safety at $h_w=0\text{m}$, WR1, and WR2, as obtained from Figure 5.11, is also presented in Table 5.2.

Table 5.3: Observed frequency of wall and backfill top by white noise from Case 1

WN no.	System condition	h_w (m)	Frequency (Hz) [Wall/Backfill]
1	After 'g' up	0	[5.4/5.4]
2	Before 1 st water supply	0	[5.8/5.8]
3	After 1 st water supply	9.6	[5.0/5.0]
4	Before 2 nd water supply	9.6	[5.7/5.6]

Table 5.4: Observed frequency of wall and backfill top by white noise from Case 3

WN no.	System condition	h_w (m)	Frequency (Hz) [Wall/Backfill]
1	After 'g' up	0	[5.3/5.3]
2	Before 1 st water supply	0	[5.6/5.6]
3	After 1 st water supply	8.3	[4.7/4.7]
4	Before 2 nd water supply	8.3	[5.3/5.4]
5	After 2 nd water supply	10.3	[4.5/4.6]
6	After final loading	10.3	[5.1/5.1]

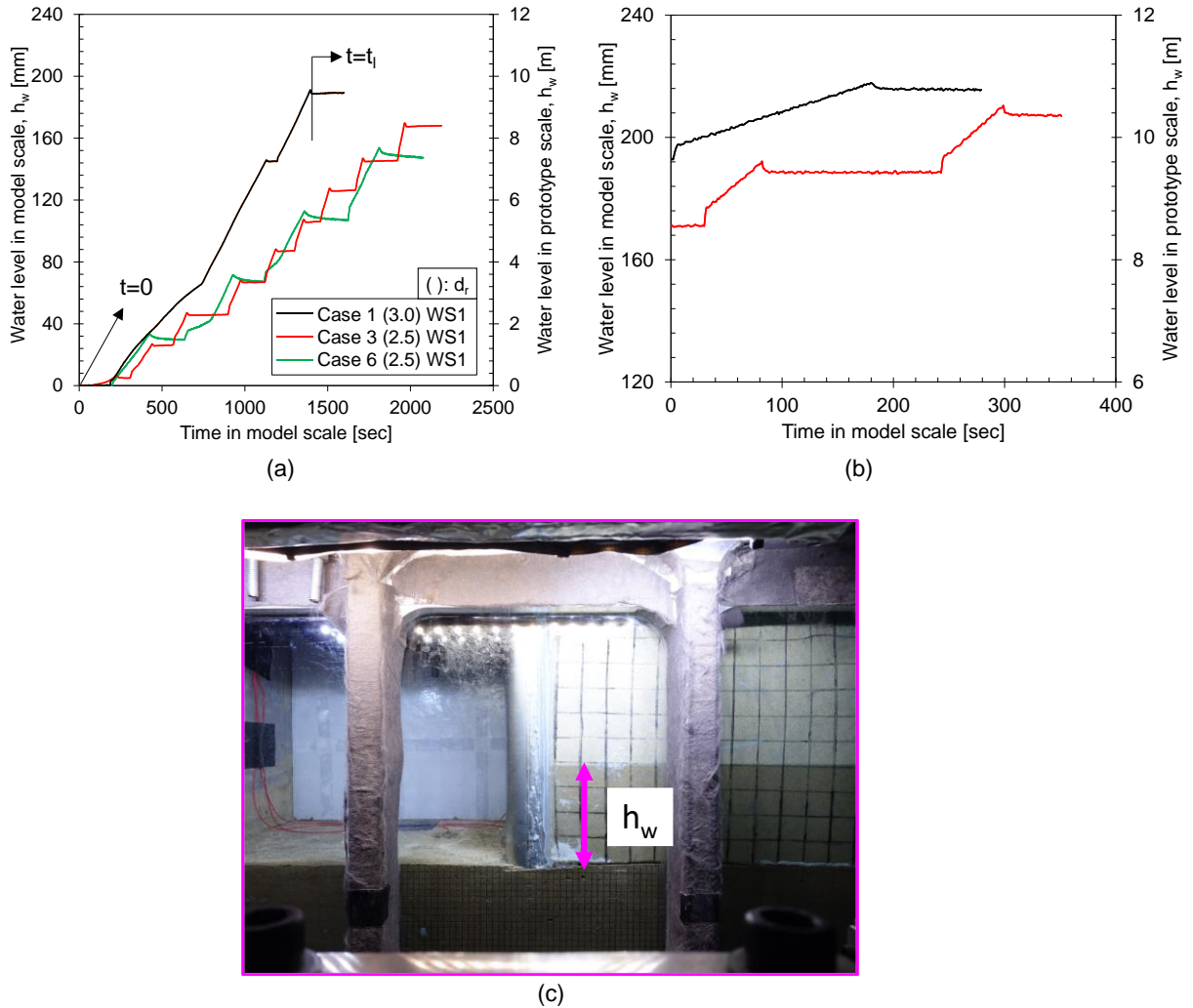


Figure 5.14: Applied static loading by water rise (a) WR1 (b) WR2 (c) photo showing the evidence of water level during Case 1 WR1.

5.4.2 Two layers model test conditions:

Two centrifuge tests were conducted on a rock ground with an overlaying sand layer. The test conditions are provided in Table 5.3, where Case 4 and Case 5 had overlaying sand layers of 10mm and 20mm (equivalent to 0.5m and 1m in prototype scale), respectively. The retaining wall had a height of 12m above the sand layer, as depicted in Figure 5.1d&e. The stress-strain relationship of the model soft rock ground, obtained from the unconfined compression test, is presented in Figure 5.15. The strength and stiffness parameters of the model soft rock ground from this test are reported in **Table 5.5**. To conduct stability analysis, the pressure diagram shown in Figure 5.10 was modified to account for the overlaying sand layer. The variation of the factor of safety with the water level is illustrated in Figure 5.16. It was observed that increasing the depth of the overlaying sand layer by 1m led to a decrease in the factor of safety. Specifically, introducing a 0.5m sand

layer resulted in a 7% decrease in the factor of safety compared to the condition without a sand layer. Further increasing the sand layer by 0.5m led to a 16% decrease in the factor of safety compared to the condition without a sand layer.

Table 5.5. Test conditions and material properties of rock with overlaying sand layer
Case s

Test code	Embedment soft rock and backfill sand	Rock socket depth: d_r ()[§], Sand layer: d_s {h_w(m): WR1; h_w:WR2} <FS:h_w(m)=0;WR1;WR2 >	Wall/Pile Properties Φ, t, EI, M_y ()[§]
Case 4 C4	<u>Toyoura sand:</u> (Dr=85%): $\gamma_d=15.8\text{kN/m}^3$ $\phi'=42^\circ$	2.5m (50 mm) 0.5 (10 mm) {8.9;9.5} <1.75;0.78;0.71>	$\Phi=2\text{m}$ (40 mm) t= 25mm (0.5 mm) Spacing: 2.15m (43 mm) EI= 6.8 GNm ² /m (5.4x10 ⁻⁵ GNm ² /m)
Case 5 C5	<u>Soft rock:</u> $\gamma_t=20.1\text{kN/m}^3$ $q_u=1.26\text{MPa}$ (C4) $q_u=1.3\text{MPa}$ (C5) $E_s=1204\text{MPa}$ (C4) $E_s=951\text{MPa}$ (C5)	2.5m (50 mm) 1.0 (20mm) {8.8;9.4} <1.6;0.6;0.55>	$M_y= 9.0 \text{ MNm/m}$ (3.6x10 ⁻³ MNm/m)

§:(model scale); βd_r : normalized depth of model CSTP wall;

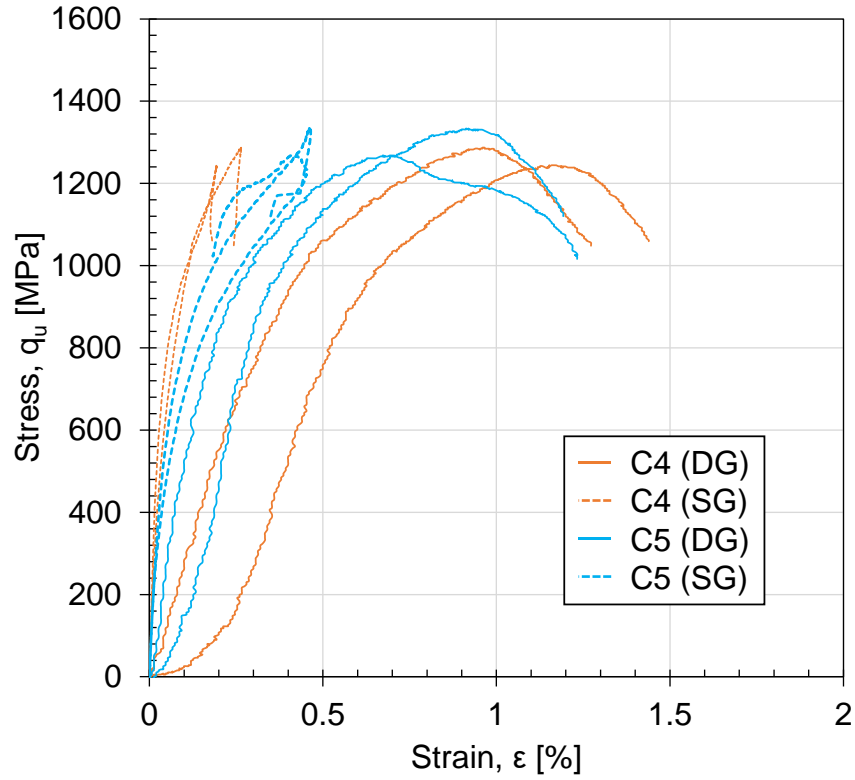


Figure 5.15: Variation of stress-strain obtained from the unconfined compression test for Cases 4 and 5.

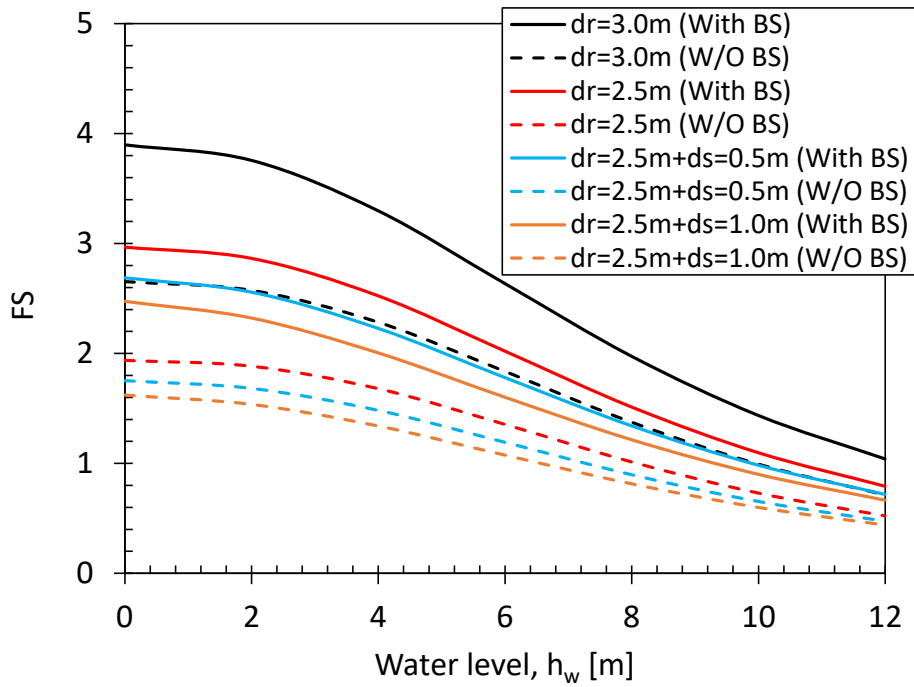






Figure 5.16: Variation of the factor of safety with water level for Cases 4 and 5.

Case 4: $d_r=2.5m+d_s=0.5m$	Sequence	Dynamic	Static	Dynamic		Static	Dynamic
	History						
	Shake no.	S1		S2	S3		S4
	a_i	0.61		0.36	0.58		0.57
	n_c	21		20	15		15
	$\Delta\delta_t$	84.4		153.5	159.9		152.6
	Water level	$h_w=0m$ 0.5m Sand layer	$h_w=8.9m$	$h_w=8.9m$	$h_w=8.9m$	$h_w=9.5m$	$h_w=9.5m$
	WN	1					2







Case 5: $d_r=2.5m+d_s=1.0m$	Sequence	Dynamic		Static	Dynamic		Static	Dynamic	
	History								
	Shake no.	S1	S2		S3	S4		S5	S6
	a_i	0.40	0.61		0.40	0.59		0.57	0.37
	n_c	21	21		21	21		21	20
	$\Delta\delta_t$	61.5	61.5		152.4			152.4	
	Water level	$h_w=0m$ 1m Sand layer		$h_w=9.6m$	$h_w=9.6m$		$h_w=10.3m$	$h_w=10.3m$	
	WN	1							

Figure 5.17: loading sequence followed in cases 4 and 5.

The loading sequence followed in both Case 4 and Case 5 is depicted in Figure 5.17. The loading sequences were identical, involving dynamic loading, followed by static loading, then dynamic loading, static loading, and another dynamic loading. In Case 4, one dynamic loading was applied in dry conditions, followed by raising the water level to 9.8m from the rock surface. Two more dynamic loadings were applied, followed by further raising the water level to 10.3m from the rock surface. Finally, one additional dynamic loading was applied. In Case 5, two dynamic loadings were applied in dry conditions, followed by raising the water level to 10.8m from the rock surface. Two more dynamic loadings were applied, and then the water level was further raised to 11.4m. Afterwards, two additional dynamic loadings were applied. As depicted in Figure 5.17, all the measurements of the water level were carried out from the rock surface. Therefore, to get the actual water level, the height of the overlaying sand layer is deducted and reported in Table 5.5. Also, this water level was used to calculate the effective earth pressure. During Case 4, the reduction of the water level (Figure 5.19; Appendix 5.8), the average water level after each loading is considered and reported in Table 5.5.

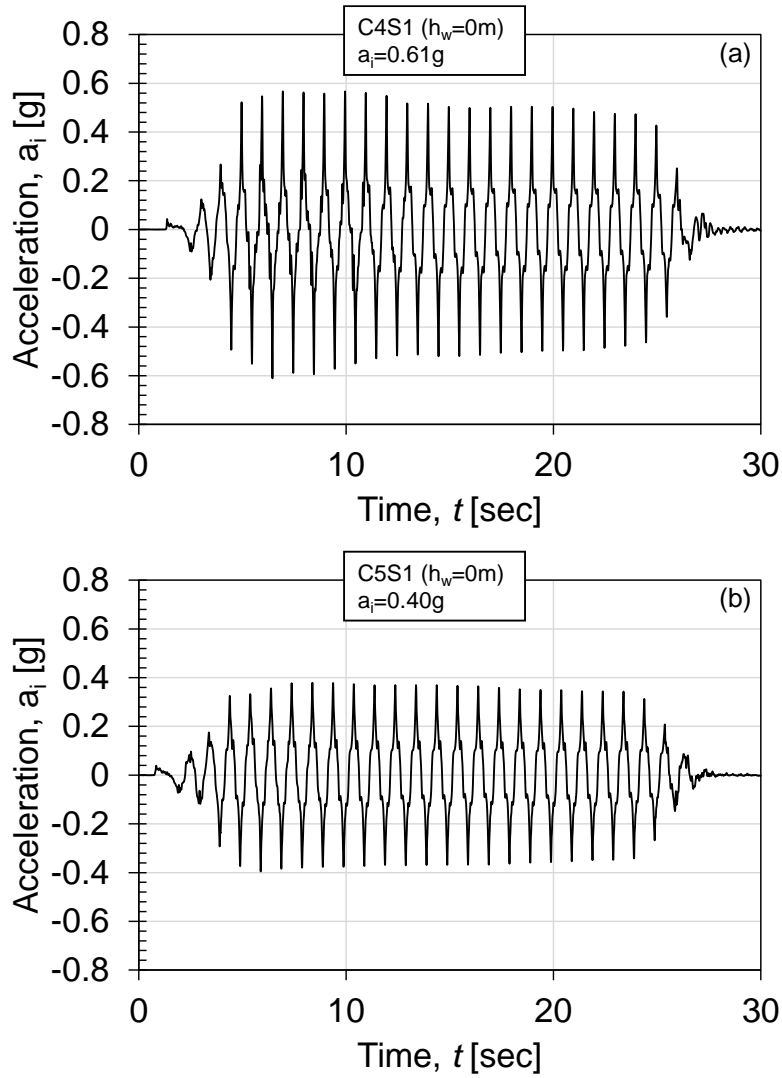


Figure 5.18: Typical shape of input motion in Cases 4 and 5.

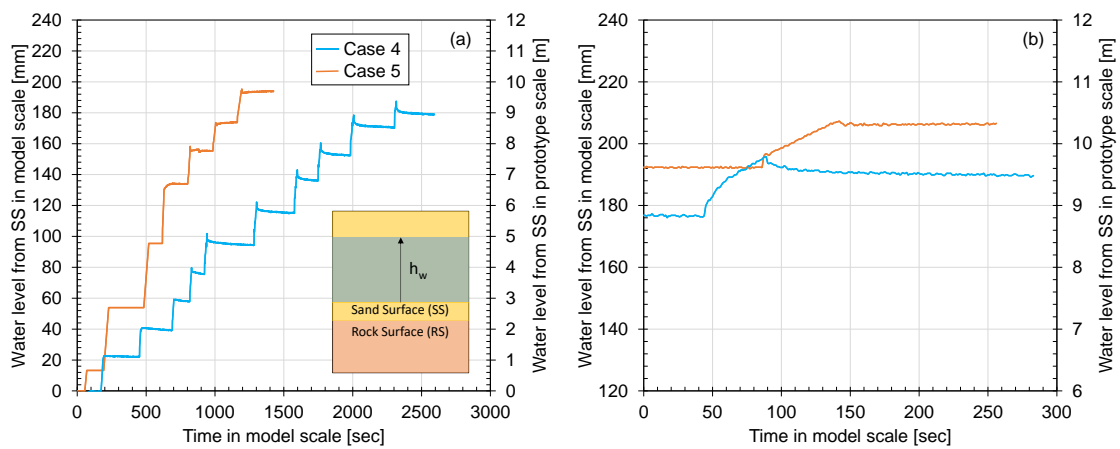


Figure 5.19: Measured water level during WR1 and WR2 for Cases 4 and 5.

The shape of the typical dynamic loadings for Case 4 and Case 5 is illustrated in Figure 5.18. A sinusoidal wave of a predominant frequency of 1Hz was used as dynamic loading. The number of cycles and the magnitude of the input motion were calculated based on the definition shown in Figure 5.13a and reported in Figure 5.17. The static loading applied in Case 4 and Case 5 is shown in Figure 5.19. Based on the water level measurements during the first and second water rise, the factor of safety was calculated and reported in **Table 5.5**.

Limitations of Centrifuge model tests:

- In Case 4, unintentionally, sand was poured outside the rubber bag, as shown in the Appendix. 5.5. Due to this, some friction might be generated between the model wall and the container wall. This effect might not be very significant during loading but could affect long-term behaviour. Also, the possible leakage could affect the wall long-term behavior. Therefore, the discussion about the long-term behaviour from Case 4 was avoided.
- In Case 4 and Case 5, many strain gauges did not work during the experiment. So, drawing the bending moment distribution was not possible. Therefore, all the discussions about the loading from Cases 4 and 5 are based on lateral pressure measurement.
- As the wall is displaced by loadings, the location of the earth pressure cell (especially at the shallower depth) could settle. Therefore, it is necessary to identify the exact location of the earth pressure cell, which can be done by checking the earth pressure measurement and pore water pressure measurement. In all the cases, the locations of the EP cell, especially at shallower depths, were adjusted accordingly (Figure 5.1).

The following section presents the results and discusses the centrifuge model test. Unless stated otherwise, all the results and discussions in this chapter are presented on a prototype scale.

5.5. Results and discussions:

5.5.1 Typical acceleration and phase angle response:

Figure 5.20 illustrates a representative example of the acceleration time history measured at various depths of the wall, backfill, and the base of the container (input) during Case 1, Shake 4 ($a_i=0.51g$). As shown in Figure 5.20 (d), the i^{th} peak of each negative cycle of input motion, wall, and backfill is defined by a_{ii} , a_{wi} , and a_{bi} , respectively, where the second 'i' stands for cycle number. To calculate the phase angle (for time period 1 sec, phase angle, $\theta_{PH} =$, time difference $\times 360^\circ$), the corresponding times of a_{ii} , a_{wi} , and a_{bi} are defined as t_{ii} , t_{wi} , and t_{bi} , respectively. The negative acceleration is chosen to account for the forward (positive) inertia force (defined as negative mass times acceleration) of the backfill soil and wall. Upon comparing Figure 5.20 (a) and (b), a well-synchronized acceleration response was observed between the input motion, wall, and backfill, with minor differences in amplitude. Figure 5.20c demonstrates an increase in amplitude at shallow depths in the backfill and wall. To gain a clearer understanding of the soil-wall behavior at shallow depths, a 2-second acceleration time history for the wall, backfill, and input is presented in Figure 5.20d. Based on Figure 5.20d, significant phase differences and amplification at shallow depths

can be observed. Furthermore, the observed amplification is more pronounced in the wall compared to the backfill.

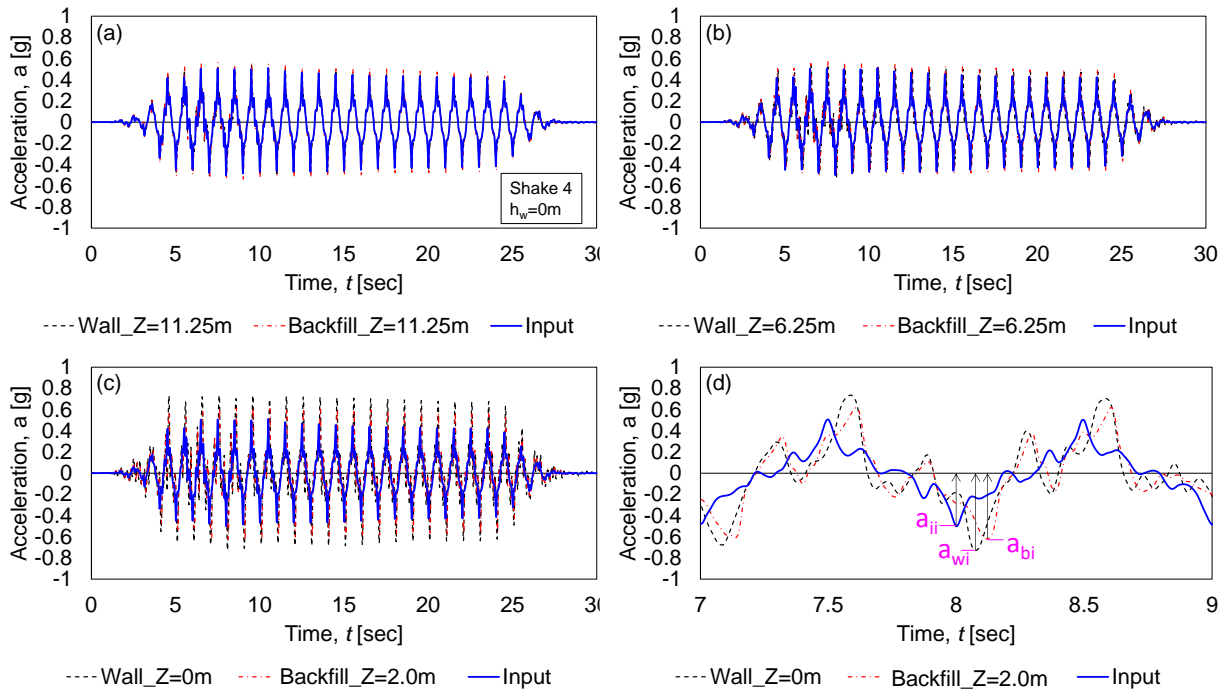


Figure 5.20: Typical example of acceleration time history measurement.

To discuss the amplification ratio, the negative peak of each cycle of wall/backfill is normalized by the negative peak of input, as shown in Figure 5.21a&b. The data from Case 1 is chosen as it has a large number of shaking, and the dynamic loading was applied by gradually increasing the amplitude of the input motion. From Case 1, Shake 4 and Shake 11 represent the final loading in dry and wet conditions with comparatively large input motion. From Figure 5.21a&b, amplification could be observed in both the wall and backfill. Overall, the amplification is higher for the wall than the backfill at shallow depths. The difference in the material stiffness and the sensors' relative location might cause a larger amplification in the wall than backfill at shallow depths. For backfill, the trends in amplification ratio observed by shakes 4 and 11 were almost constant. Shake 11, on the other hand, for wall, shows an increasing trend from $n_c = 5$. This increasing trend in amplification ratio for shake 11 could be due to a large increment in wall displacement and some deterioration of the rock-wall confinement caused by the loading history.

To discuss the soil-wall interaction, the phase angle for each cycle is calculated (defined in Figure 5.21c) and shown in Figure 5.21c&d. The observed difference in phase angle between the wall and backfill during shake 4 is almost constant but not during shake 11. Based on Figure 5.21c&d, the phase angle observed for shake 4 is smaller than for shake 11. Also, the phase angle observed in the wall is higher than in the backfill. As shown in Figure 5.20d, the input peak comes first,

followed by the wall and backfill. Therefore, the wall would try to push the soil when the system moves forward, increasing the lateral pressure. This behaviour is consistent in both shakes 4 and 11 during shaking. The effect of water can be confirmed by the difference in phase angle observed in Figure 5.21c&d. For the backfill soil, the phase angle observed by Shake 11 is larger than Shake 4. Due to the presence of water during shake 11, the wave propagation was delayed, causing a larger phase angle than shake 4.

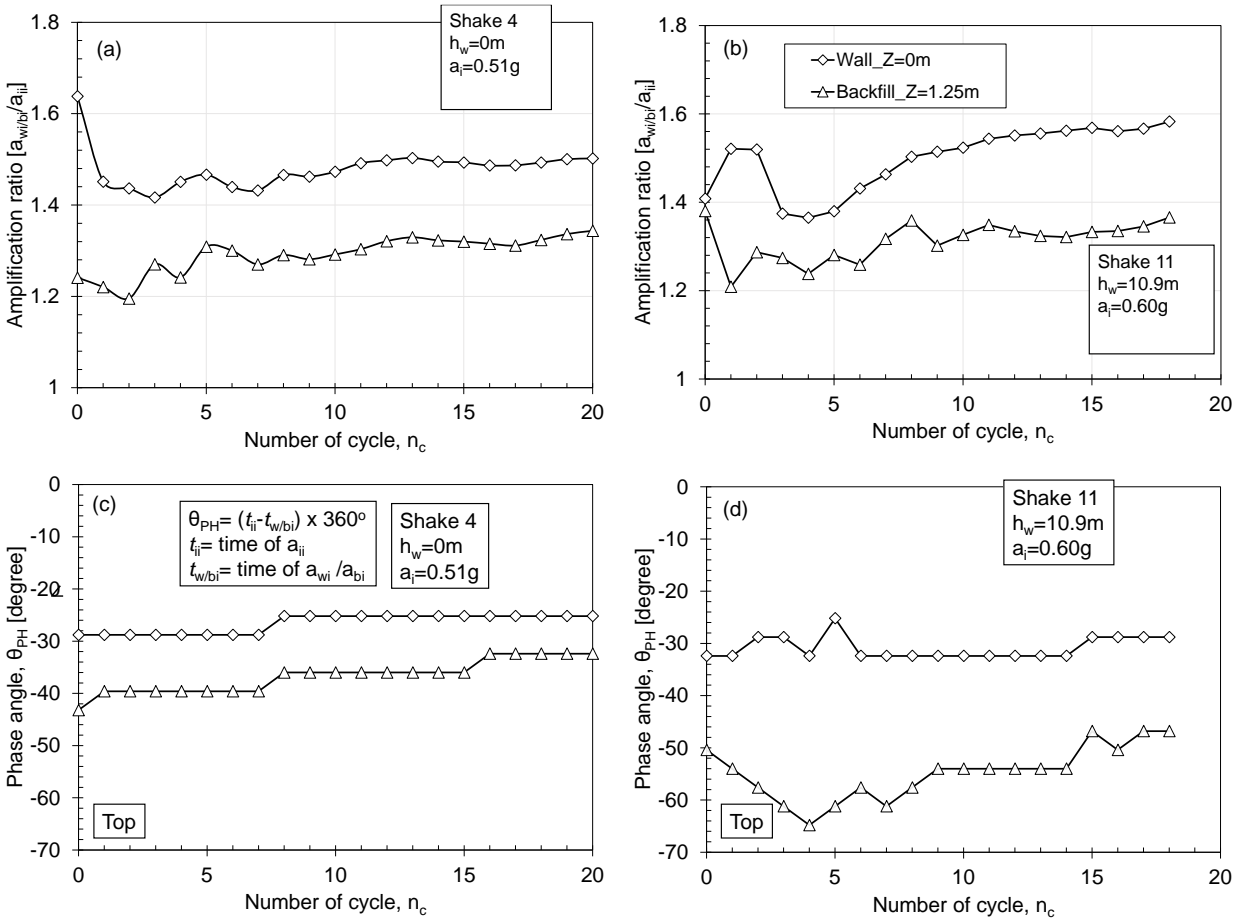


Figure 5.21: Variations of (a,b) amplification ratio; (c,d) phase angle; by cycles at the wall ($Z=0m$) and backfill ($Z=1.25m$): Shake 4 and Shake 11.

To summarize the amplification and phase angle, the average of cycles $n_c = 2-5$ and $13-16$ are plotted in Figure 5.22. The amplification was higher for the wall than for the backfill. In the dry backfill condition, the amplification ratio increased with the input acceleration, which can be confirmed for the wall and backfill. Meanwhile, the amplification behaviour in wet conditions was more complicated; for example, the largest ratio (much larger than in dry conditions) was at the second wet shake (Shake 7) and then gradually decreased with increasing shaking and amplitude. The a_i and loading cycle of the input motion affects the strain and excess pore water pressure of

retained soil, resulting in a change in the stiffness of retained soil and the predominant frequency (f_c) of the wall. Considering 1 Hz sinusoidal input motion and the f_c measured at the two locations in the white noise vibrations, more than 5.0 Hz (Table 5.3), the increase in amplification ratio with a_i in the dry condition is attributed to the stiffness reduction by larger strain at the soft rock. The larger amplification of the wet condition than the dry is for the reduction of effective stress in the sand by the water rise and the increase in excess pore pressure by dynamic loading. The gradual decrease of amplification after Shake 7 could be due to the densification of sand, which can be confirmed by the increased f_c by shakings after WR1 (Table 5.3). In the case of phase angle, the backfill shows a larger phase angle than the wall. The difference in phase angle between the wall and backfill becomes more significant in wet conditions than in dry conditions, confirming the effect of water. The backfill shows an increase in the increment of phase angle with the increase of input acceleration. This trend can be confirmed in both dry and wet conditions. However, the wall doesn't show this kind of behaviour.

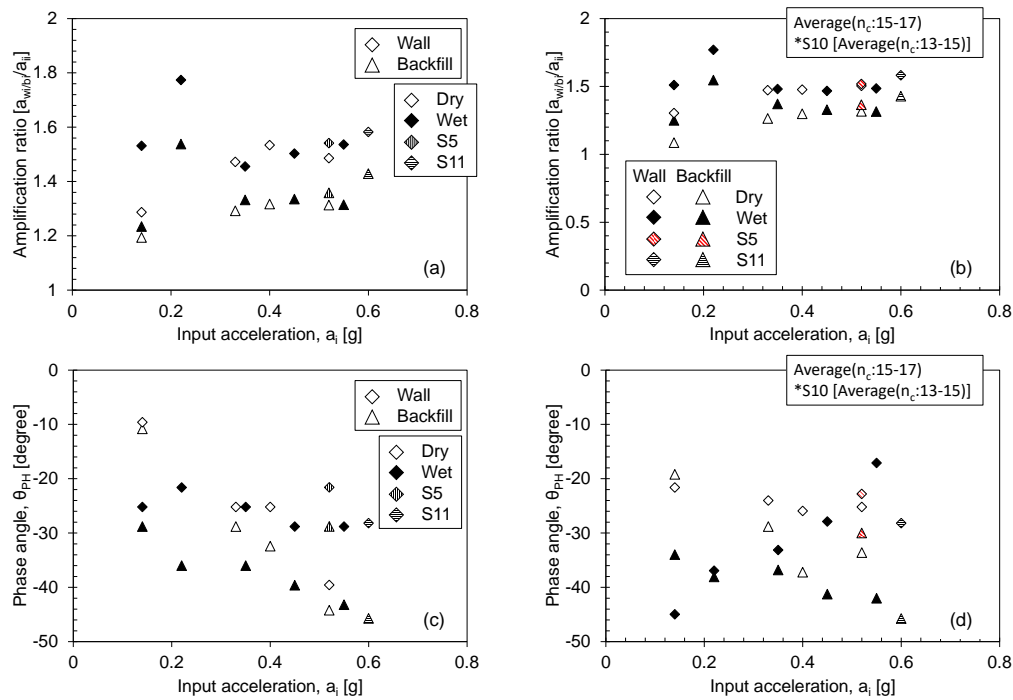


Figure 5.22: (a,b) Average amplification ratio; (c,d) average phase angle in early and late loading cycles at the wall ($Z=0m$) and backfill ($Z=1.25m$) plotted against input acceleration.

The variation of measured acceleration in the wall and backfill with respect to the input acceleration at different depths of Case 1&3 is illustrated in Figure 5.23. The acceleration is measured for the cycle in which the maximum acceleration was observed in the input acceleration. Three reference lines are plotted to indicate the amplification ratio. Larger amplification was observed at shallower depths as the shear modulus (G) approaches zero near the ground, which is typically expected in real conditions. This observation can be confirmed from both Case 1 and Case 3. Additionally, the amplification observed during wet shaking was greater than that during

dry shaking. This can be attributed to the increased mass of the retained soil due to the addition of water, resulting in a decrease in the predominant frequency. As the decreased predominant frequency approaches closer to the input frequency, the amplification ratio increases, which can be confirmed from both Cases 1 and 3. The amplification ratio of less than one was observed at $Z=6.25\text{m}$ for wall and backfill, especially for large-magnitude input motion. At $Z=11.25\text{m}$, the amplification ratio of backfill soil was larger than that of the wall.

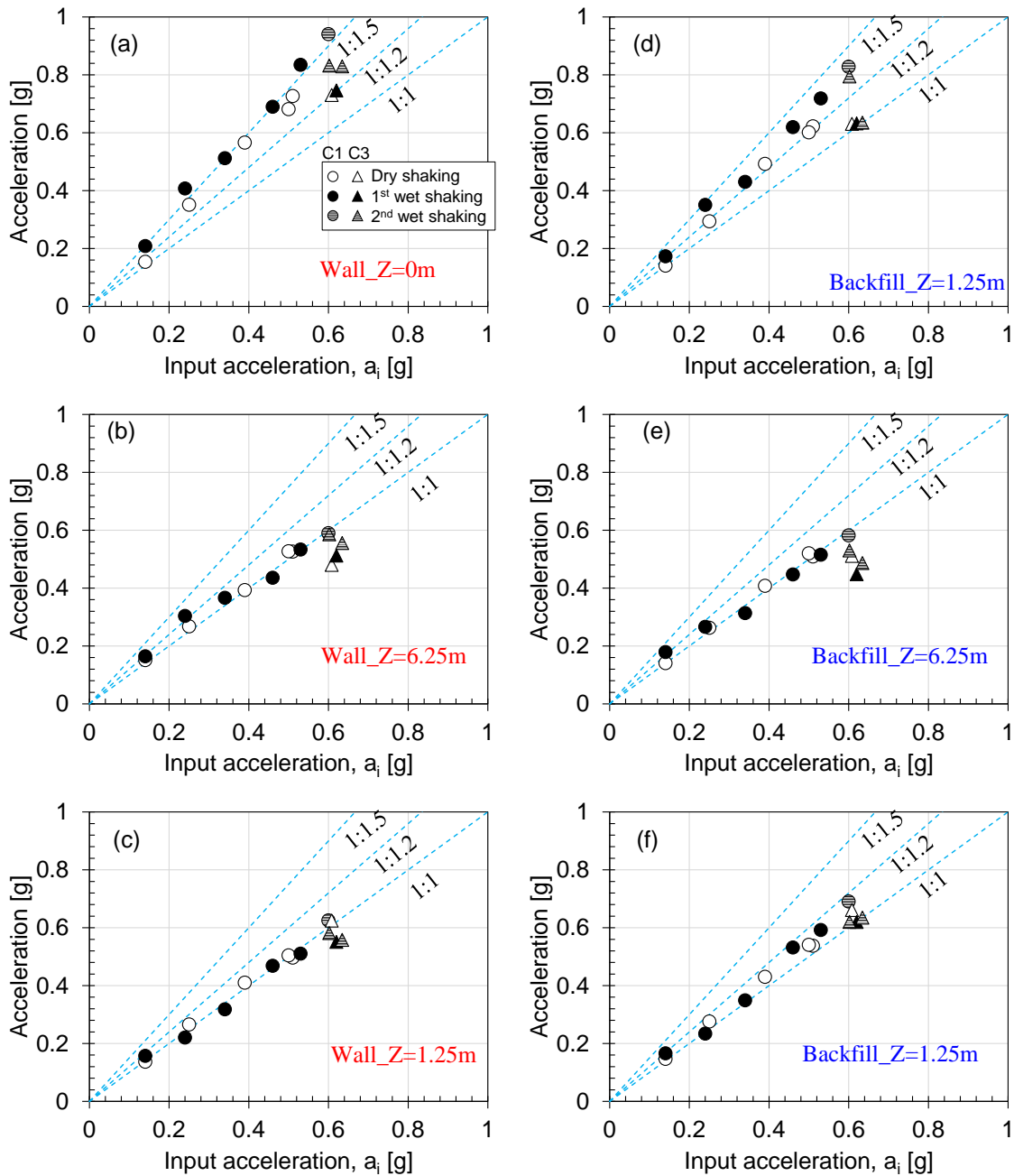


Figure 5.23: Amplification ratio observed at different depths of Cases 1 and 3.

5.5.2 Observed typical behaviour of CSTP wall under dynamic loading:

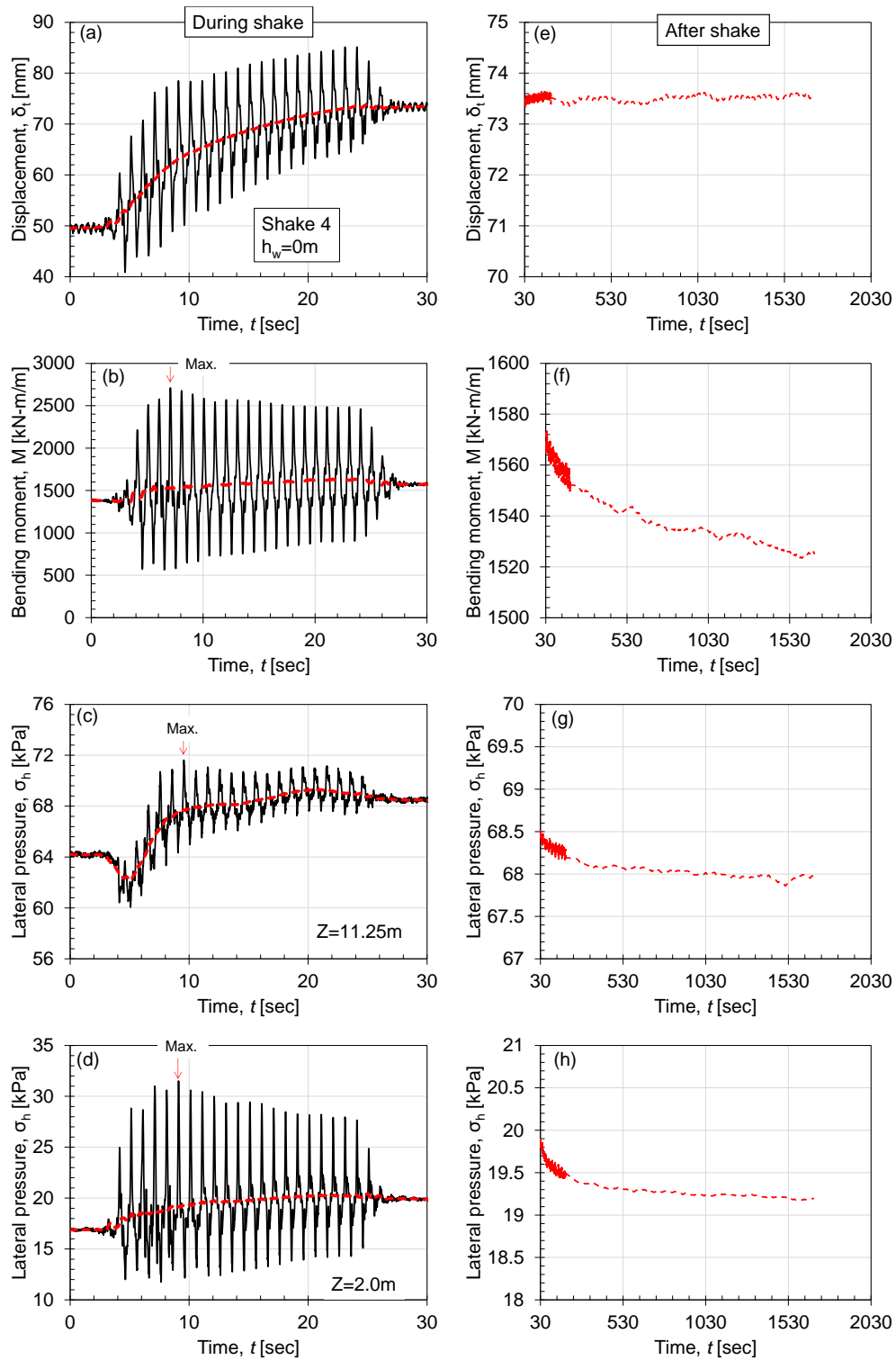


Figure 5.24: Example of measured (a,e) wall top displacement; (b,f) bending moment at $Z=10.75m$; (c,g) lateral pressures at $Z=11.25m$; (d,f) lateral pressure at $Z=2m$; with the kinematic components during shaking and the long-term variation after shake 4 Case 1.

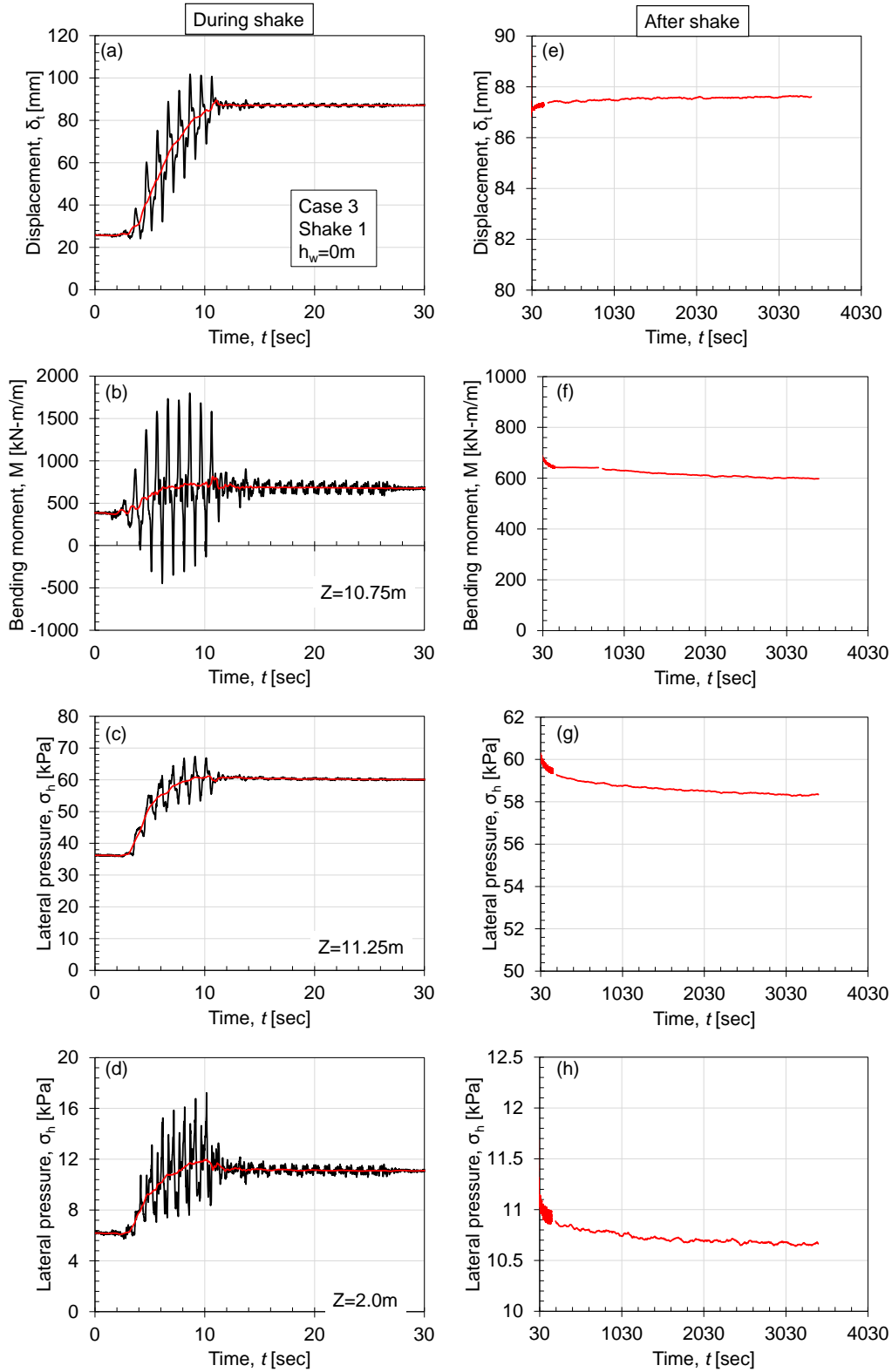


Figure 5.25: Example of measured (a,e) wall top displacement; (b,f) bending moment at $Z=10.75\text{m}$; (c,g) lateral pressures at $Z=11.25\text{m}$; (d,f) lateral pressure at $Z=2\text{m}$; with the kinematic components during shaking and the long-term variation after shake 1 Case 3.

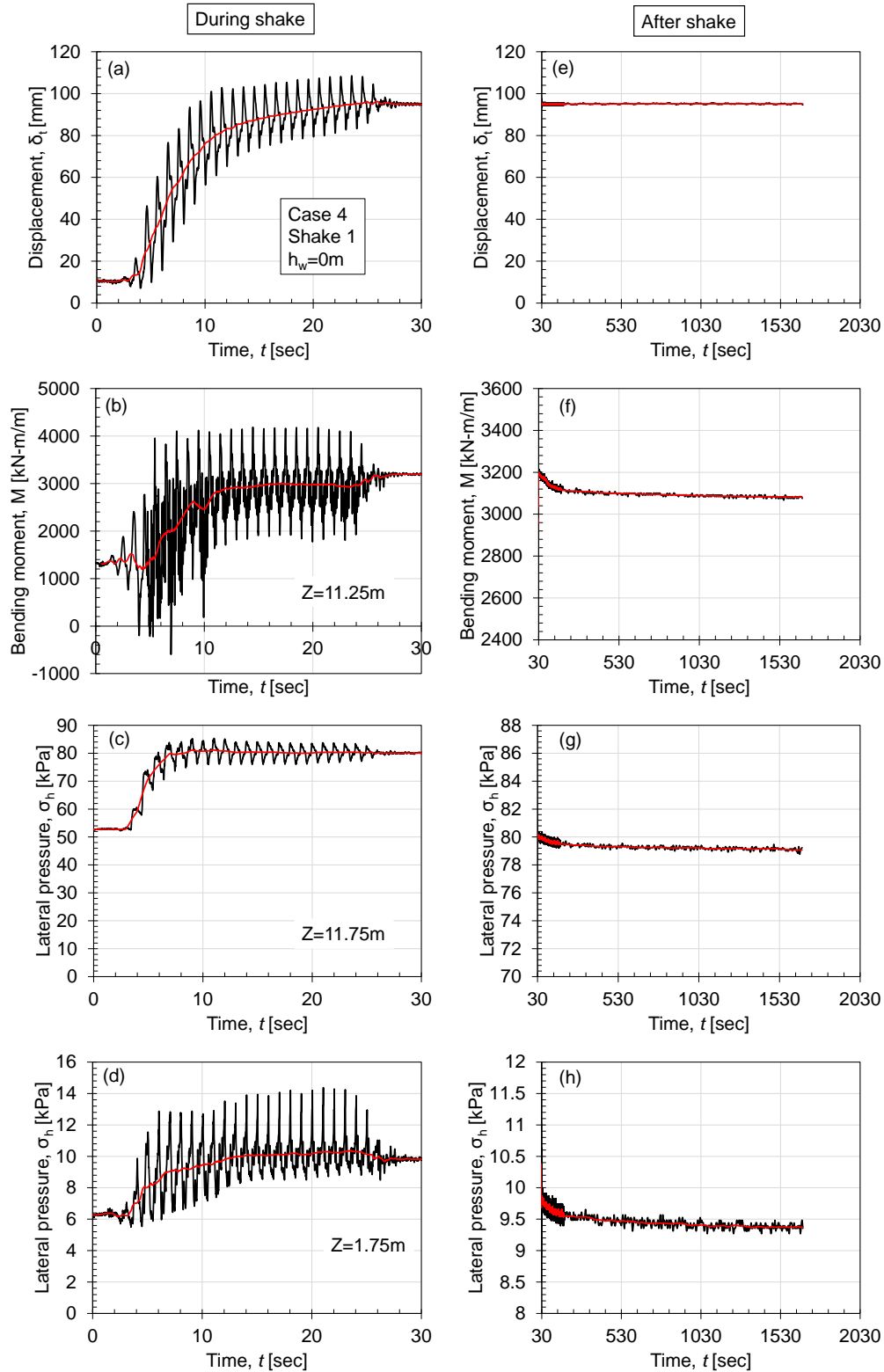


Figure 5.26: Example of measured (a,e) wall top displacement; (b,f) bending moment at $Z=11.25\text{m}$; (c,g) lateral pressures at $Z=11.75\text{m}$; (d,f) lateral pressure at $Z=1.75\text{m}$; with the kinematic components during shaking and the long-term variation after shake 1 Case 4.

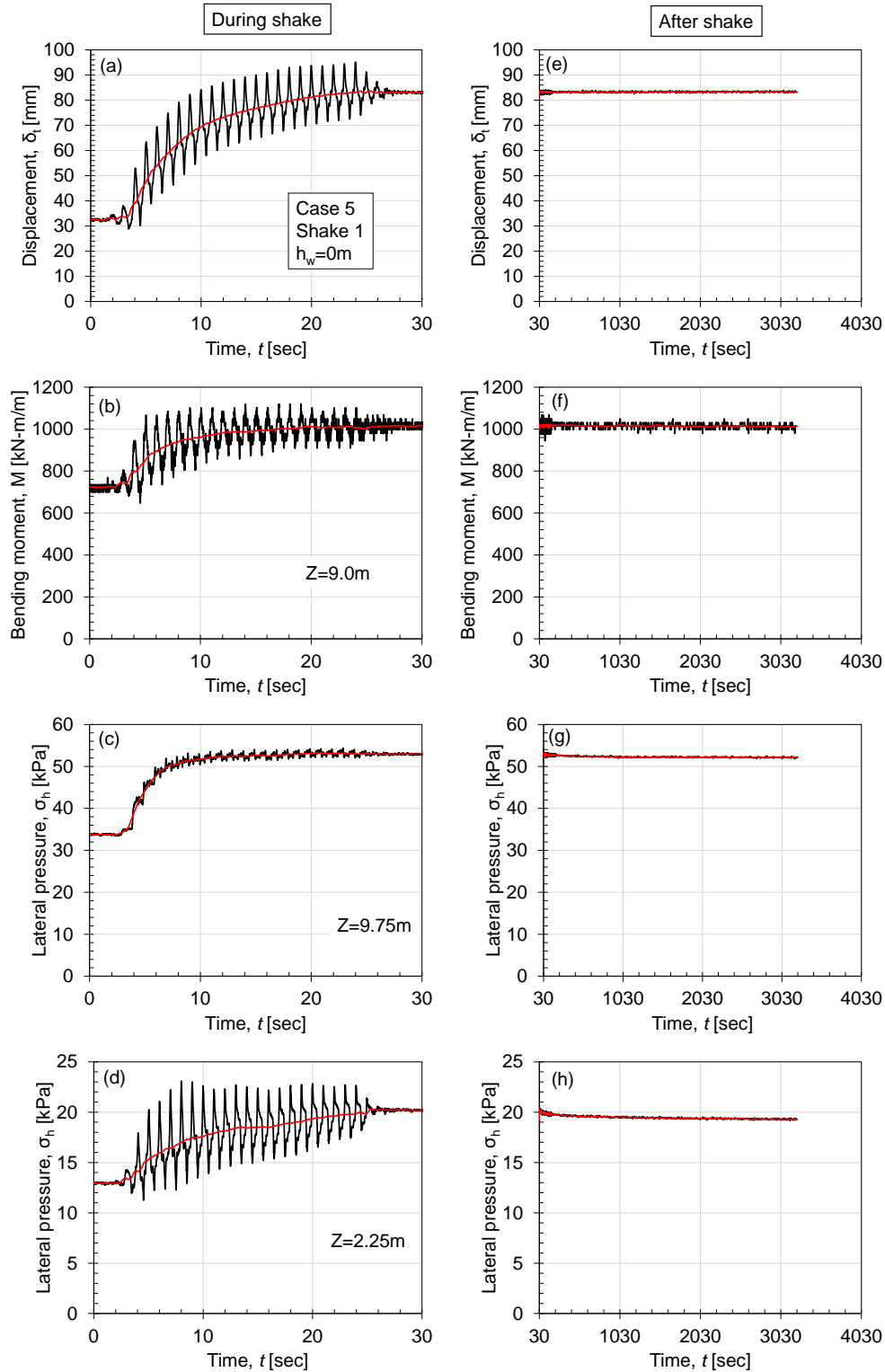


Figure 5.27: Example of measured (a,e) wall top displacement; (b,f) bending moment at $Z=9.0\text{m}$; (c,g) lateral pressures at $Z=9.75\text{m}$; (d,f) lateral pressure at $Z=2.25\text{m}$; with the kinematic components during shaking and the long-term variation after shake 1 Case 5.

Figure 5.24-27 presents an example of the total measured wall top displacement (δ_t), bending moment (M), and lateral pressure (σ_h) at both shallow and deeper depths during dynamic loading for Cases 1, 3, 4 and 5. As shown in Figure 5.24-27, the measured data can be separated into two parts: 'During shake' and 'After shake'. From time $t=0-30$ sec is defined as 'During shake' and later as 'After shake'. In all the measurements, the accumulation of kinematic components is shown by the red line. This kinematic component can also be represented as a static component. The residual component is referred to as the measurement after dynamic loading. In the 'after shake' part, a small displacement increase could be observed under constant gravity and water level. This slight movement of the wall reduced the residual lateral pressure and the bending moment, which can be confirmed in all cases.

In all cases, accumulation of the kinematic component of displacement occurred during dynamic loading. Similarly, an increase in the kinematic component of the bending moment during dynamic loading was observed, as shown in Figure 5.24-27. In all cases, the lateral pressure increased after dynamic loading at all measurement locations except some (at $Z=2.0$ m of Shake 7,8 from Case 1). Furthermore, a substantial dynamic component of the lateral pressure was observed at shallower depths compared to deeper depths, especially for all cases. The maximum bending moment and lateral pressure are indicated in Figure 5.24b-d and (d). The maximum bending moment and lateral pressure did not occur at the same time. Therefore, some phase differences could be expected between the measurements.

5.5.3 Typical dynamic soil wall interaction:

In this section the discussion about the typical Soil-Wall Interaction (SWI) between the CSTP wall and the retained soil is carried out by using the wall top displacement, total earth pressure and bending moment. The measured data from LDT, earth pressure cell and strain gauge are filtered by using a third-order Butterworth Low pass (LP) filter with prototype scale corner frequency of 10Hz to remove the noise. A third-order Butterworth High pass (HP) filter with a prototype scale corner frequency of 0.3Hz was applied twice to obtain the dynamic component. The kinematic component was obtained by subtracting the dynamic component from the Total.

To discuss the dynamic SWI, the dynamic displacement obtained by the LDT or the potentiometer is often avoided as the instrument rack to which displacement transducers were attached experienced vibration during spinning and shaking (Al Atik, 2008). This vibration resulted in large apparent deflections. However, in this research, the measured displacement by the LDT is used to discuss the SWI. Figure 5.28 shows the time history of the wall top displacement obtained from the LDT and back-calculated from the acceleration. The acceleration measured at the container bottom (input), rock surface (rock), the bottom of the wall (wall-bottom) and top of the wall is used to back calculate the displacement. A third-order Butterworth LP filter with a prototype scale corner frequency of 25 Hz was applied to reduce noise in the acceleration time series. Additionally, a third-order Butterworth HP filter with a prototype scale corner frequency of 0.3 Hz was applied to eliminate long-period drift that would show up in the records following integration to

displacement and velocity. The disadvantage of such filtering is that it removes any apparent permanent offset of the instrument.

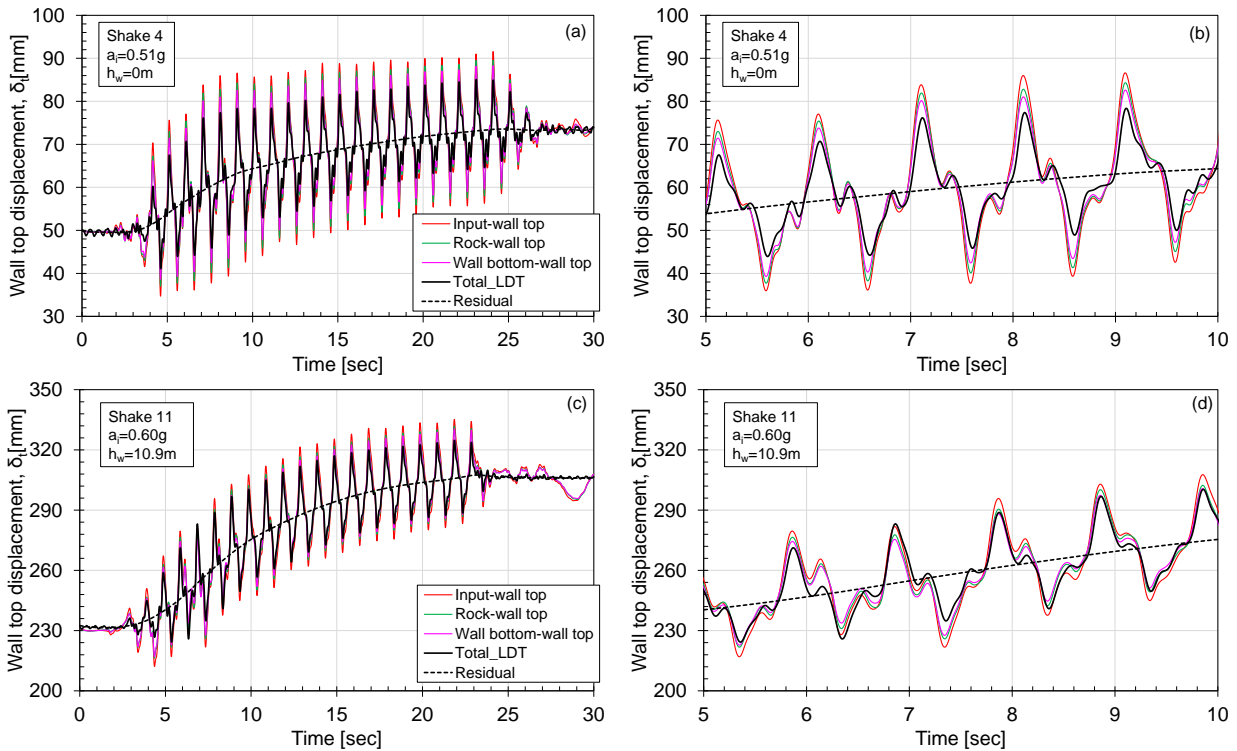


Figure 5.28: Time history of wall displacement measured by LDT and back-calculated from acceleration of Case 1 (a,b) Shake 4 (c,d) Shake 11.

Unlike LDT, the acceleration measurement contains the movement of the shaker. Therefore, the movement of the shaker is removed to obtain the actual displacement of the wall, which was obtained by subtracting the displacement by input, rock, and wall bottom from the wall top and termed as ‘input-wall top’, ‘rock-wall top’ and ‘wall bottom-wall top’, respectively. The displacement obtained from the accelerations is the dynamic displacement. Therefore, to obtain the total displacement from the acceleration, the kinematic component from the LDT is added to the displacement from acceleration. The three displacements obtained from the acceleration and the LDT along the kinematic component are shown in Figure 5.28. It is worth mentioning that a more accurate comparison between the LDT and acceleration could be possible if the acceleration of the instrument rack is measured directly (attaching an accelerometer to the LDT).

An almost synchronized relationship between the LDT and the displacement from the acceleration can be observed. However, the maximum displacement from the acceleration measurement in the forward and backward direction are about 5-12% larger than the LDT measurement. The dynamic displacement from the LDT and the acceleration are compared in Figure 5.29. The displacement during $nc=2$ is also highlighted in this figure. No significant phase difference between the

displacement from LDT and acceleration can be observed. However, the dynamic displacement measured by acceleration is larger than the LDT, with the maximum difference observed between LDT and input-wall top. This difference is larger in Shake 11 than in Shake 4, which could be attributed to the larger amplification ratio observed in Shake 11 than in Shake 4 (see Figure 5.22). Based on Figures 5.28 and 5.29, it can be said that the displacement measured by the LDT was not significantly affected by the vibration of the instrument rack. Therefore, the LDT measurement will be used to discuss the SWI.

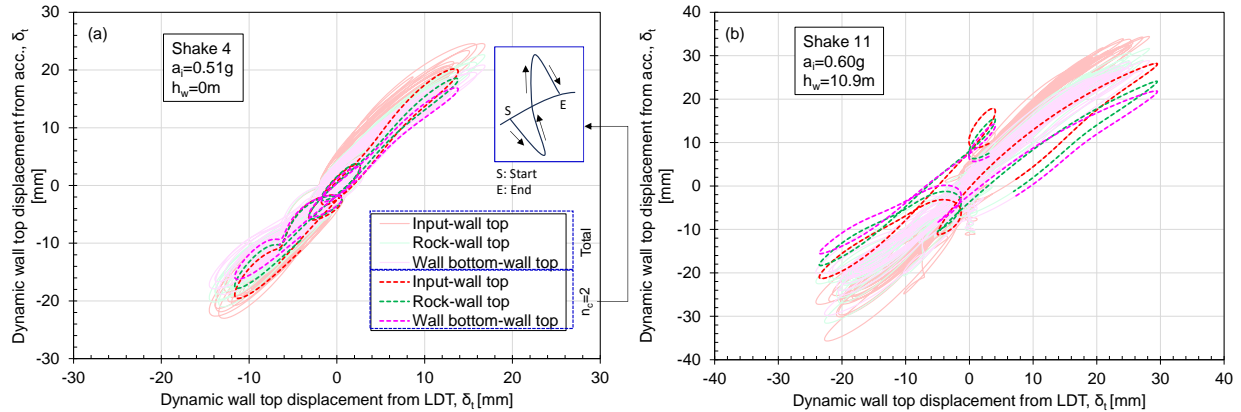


Figure 5.29: Comparison between dynamic wall displacement obtained from LDT and back-calculated from the acceleration of Case 1 (a) Shake 4 (b) Shake 11.

The variations of total earth pressure (σ_h) at $Z=11.25$ and 2.0 m and the bending moment (M) at $Z=10.75$ m with the wall top displacement (δ_t) during Shakes 4 and 11 are shown in Figures 5.30a-f. The solid red line shows the variation of the kinematic component, and two cycles (one from the initial part, $n_c=2$ and the other from the later part, $n_c=15$) are highlighted in the figures. Four points (A, B, C, D) are mentioned in this figure, where A and D represent the starting and end of the cycle, and B and C indicate the maximum displacement in the forward and backward direction.

Relatively complicated earth pressure variations were observed in the early cycle ($n_c=2$) compared to the later cycle ($n_c=15$), which could be attributed to soil structure interaction and spiky input motion (Figure 5.13a). Nonetheless, different trends were observed in the TEP behaviour at $Z=11.25$ m and 2.0 m (Figures 5.30a-d), i.e., negative relations between the increments of displacement and total earth pressure for the deep depth and positive relations for the shallower depth. However, the kinematic component of σ_h was increased by the cyclic loadings at the two depths in the two shakings, especially in the early cycles. The M and δ_t relations (Figures 5.30e&f) are similar to those of σ_h at $Z=2.0$ m, positive relation and the increase of residual M .

The variations of dynamic components of σ_h and δ_t are shown in Figure 5.30g&h, which were obtained by subtracting the kinematic component from the total. Magnitudes of the earth pressure

at $Z=2.0\text{m}$ are about 2-3 times larger than those at $Z=11.25\text{m}$. Regardless of the depths, the total earth pressure magnitudes were larger for $n_c=2$ than $n_c=15$.

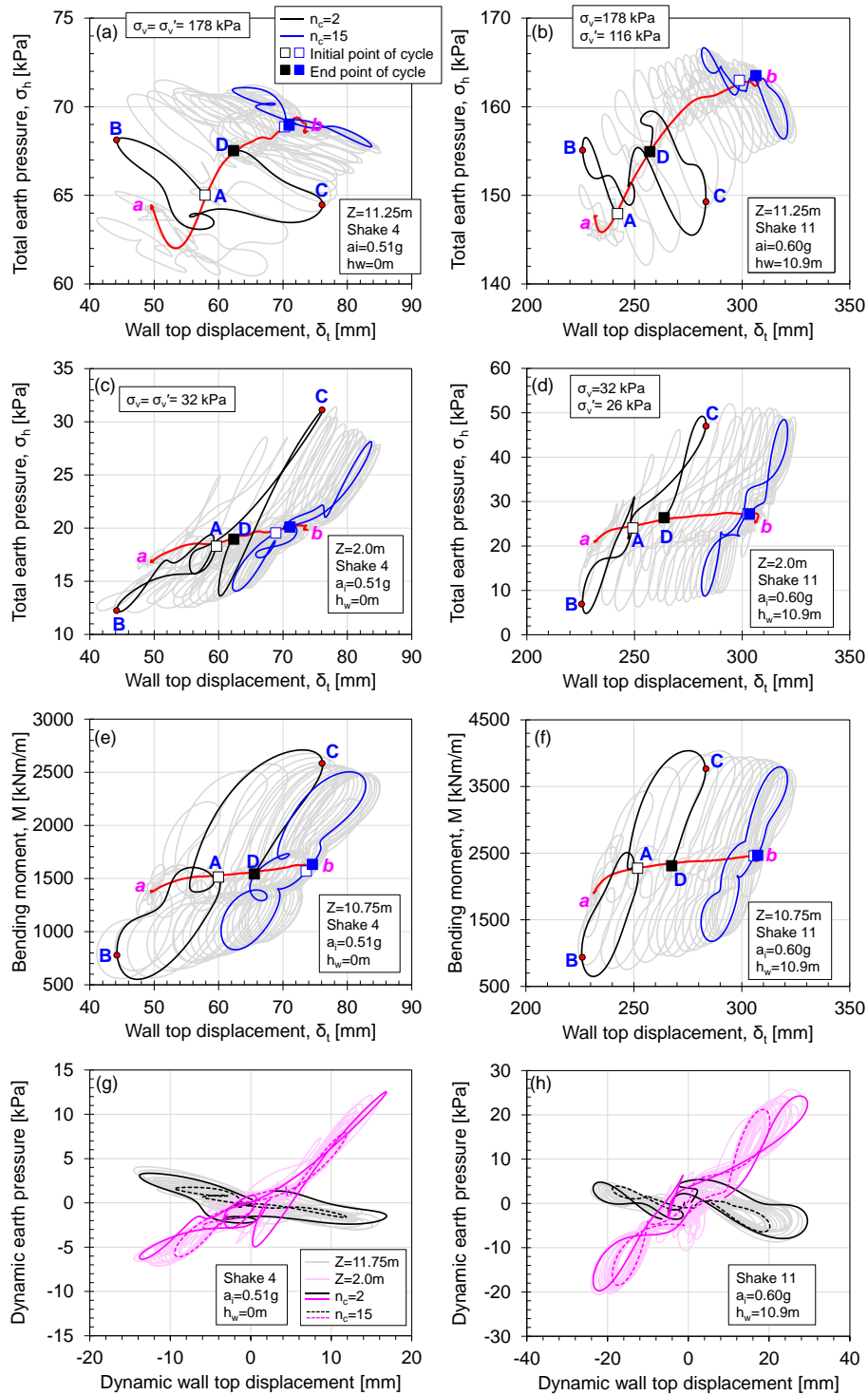


Figure 5.30: Relationships between the wall top displacement (a,b) total earth pressure at $Z=11.25\text{m}$; (c,d) total earth pressure at $Z=2.0\text{m}$; (e,f) bending moment at $Z=10.75\text{m}$ (g,h) dynamic component of earth pressure: Case 1 Shake 4 and Shake 11.

5.5.4 Lateral pressure acting on the CSTP wall:

The total lateral pressure distribution (σ_h) observed in Cases 1, 3, and 6 is presented in Figure 5.31. Two reference lines are drawn to represent the active pressure (σ_{ha}) and the at-rest pressure (σ_{ho}). The initial lateral pressure observed for $d_r=3\text{m}$ (CASE 1) was greater than for $d_r = 2.5\text{ m}$ (CASE 3). As depicted in Figure 5.31a&b, the lateral pressure increased after dynamic loading and exceeded the at-rest pressure. In this figure, "Max." represents the maximum lateral pressure measured at each location, which can be considered as the maximum lateral pressure experienced by the wall during shaking. "Max. BM" represents the lateral pressure at the time of maximum bending moment at $Z=10.75\text{m}$. The difference in lateral pressure distribution between "Max." and "Max. BM" was smaller for larger embedment depths than for smaller embedment depths. Additionally, the difference was smaller at shallower depths compared to deeper depths. Although there were some uncertainties in the measurement of earth pressure using the small sensor (Weiler and Kulhaway, 1982; Talesnick *et al.*, 2014), the measured pressures could provide helpful information on soil structure interaction during shaking (Figures 5.30) and after loadings (Figures 5.31-32).

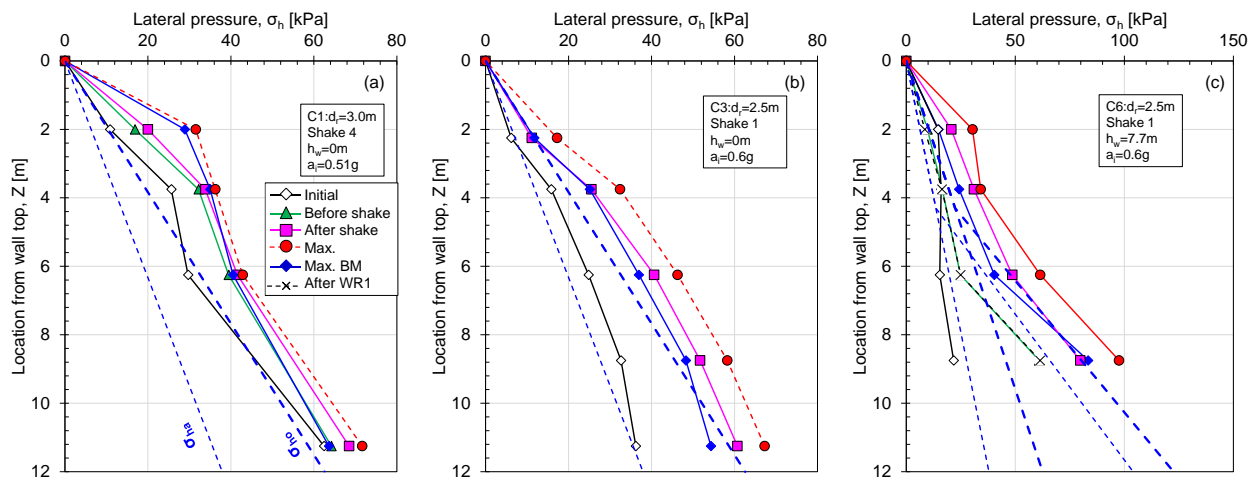


Figure 5.31: Total lateral pressure distribution with depths (a) CASE 1 shake 4 (b) CASE 3 shake 1 (c) CASE 6 shake 1.

The lateral pressure before the first water rises in Cases 3 and 6 can be represented by "After shake" for Case 3 and "Initial" for Case 6. It was observed that the initial condition before the first water rise in Case 3 exceeded the at-rest pressure, whereas in Case 6, it was lower than the active pressure. Furthermore, the effect of water feeding on the lateral pressure could be confirmed by comparing "Initial" and "After WR1" in Figure 5.31 (c), where the lateral pressure increased with the addition of water on the retained side.

The lateral pressure distribution with depth for Case 4 and Case 5 is presented in Figure 5.32. Four reference lines are included to indicate the active and at-rest pressure at two water level conditions.

The lateral pressure distribution is shown at various stages: initial (after ‘g’ up process), after dry shaking event (at t=30 sec of final dry shaking), before the first wet shaking event (end of WR1), after the first wet shaking event (at t=30 sec of final wet shaking), before the second wet shaking event (end of WR2), and after the second wet shaking event (at t=30 sec of final wet shaking).

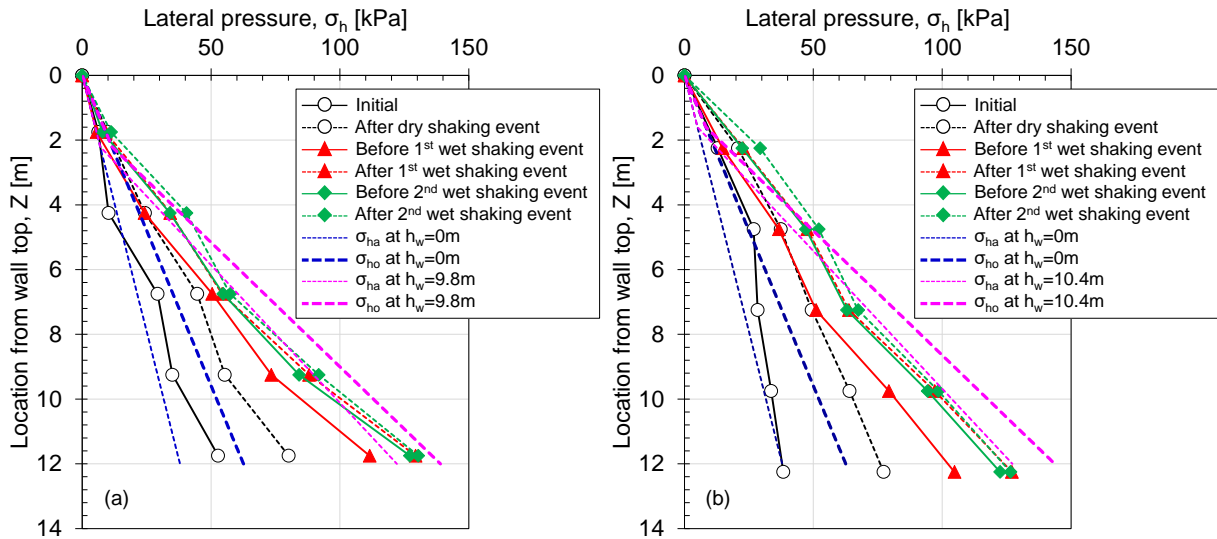
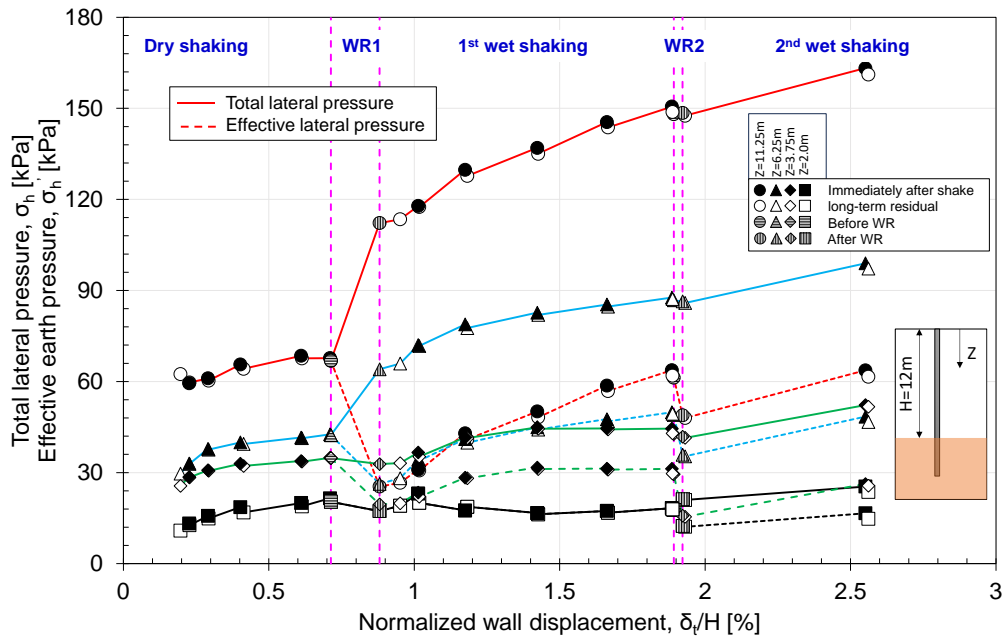


Figure 5.32: Lateral pressure distribution with depths (a) Case 4 (b) Case 5.



• First value indicates the measurement at t=0sec of shake 1

Figure 5.33: Variation of measured Lateral pressure and calculated effective earth pressures with the wall top displacements in the entire loading history from Case 1.

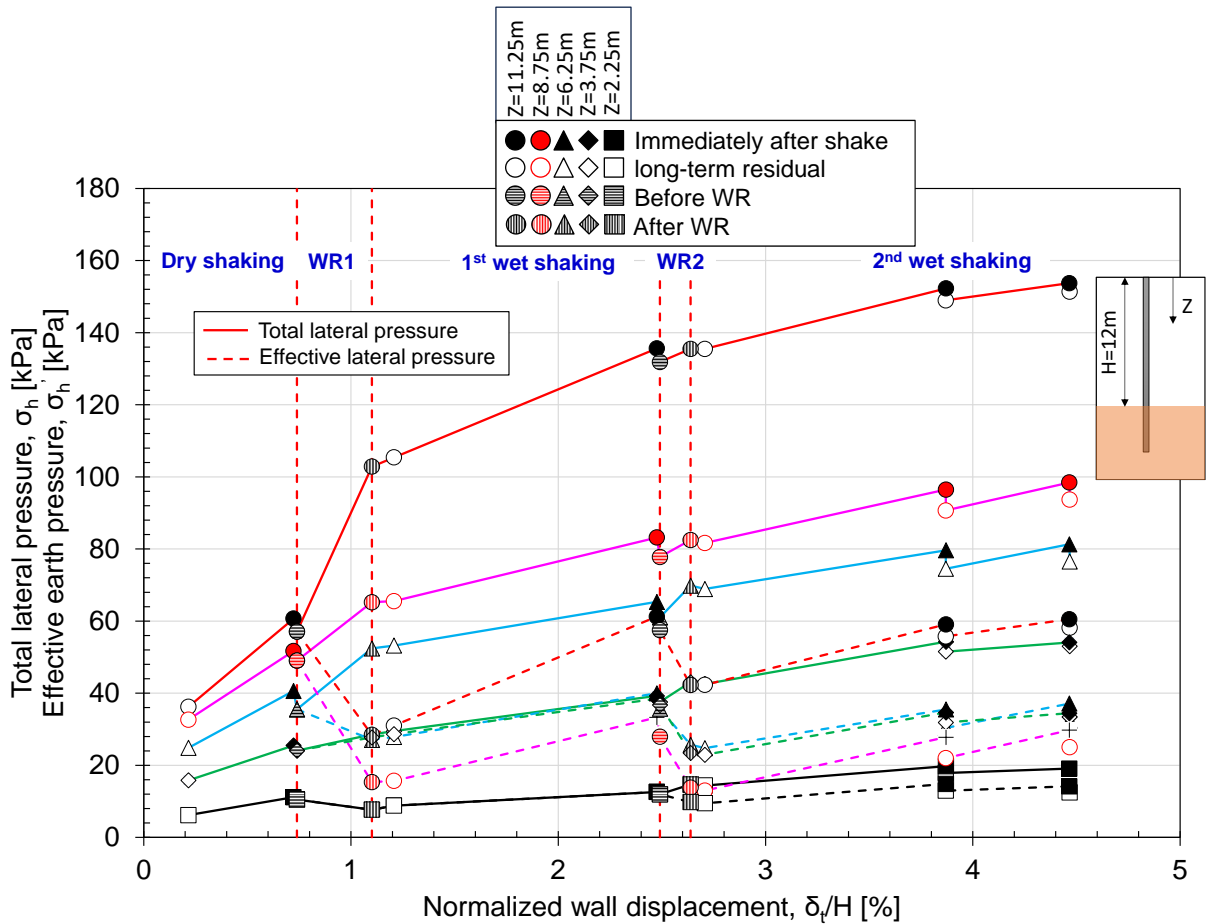


Figure 5.34: Variation of measured Lateral pressure and calculated effective earth pressures with the wall top displacements in the entire loading history from Case 3.

It is observed that after the dynamic shaking event, the lateral pressure increased beyond the at-rest pressure for both Case 4 and Case 5, confirming the presence of the resilience effect (section 5.5.9). Following the final loading (after the second wet shaking event), the lateral pressure exhibited a decrease that was less than the active pressure, especially at greater depths. In both models, no significant increase in lateral pressure was observed after the first wet shaking event, indicating a deterioration in the confinement condition of the rock wall.

The variation of measured lateral pressure and the effective earth pressure at different depths with displacement after loading from Cases 1 and 3 is depicted in Figure 5.33-34. The initial value represents the shake 1 measurement at $t = 0$ sec. Immediately after the shake, long-term residual data were collected based on the definition shown in Figure 5.14 (a).

Overall, the lateral pressure from before shake to after shake increases with the increase of displacement at $Z=11.25$, 6.25 m, and 3.75 m during dry shaking, 1st wet shaking, and 2nd wet shaking. A similar observation could be made for effective earth pressure as well. For $Z=2$ m, during dry shaking, the lateral pressure increases after shaking. However, after shaking for shakes

7 and 8 of Case 1, the lateral pressure decreases during the first wet shaking. Also, an abrupt increase in lateral pressure could be observed after shake 6 of Case 1. In the overall trends observed in Case 1, the total lateral pressure showed a convex variation with the wall top displacement during dry shaking and 1st wet shaking at Z=11.25m, 6.25m, and 3.75m. For Z=2m, a convex shape in the trends could be observed during dry shaking, but a concave shape during 1st wet shaking.

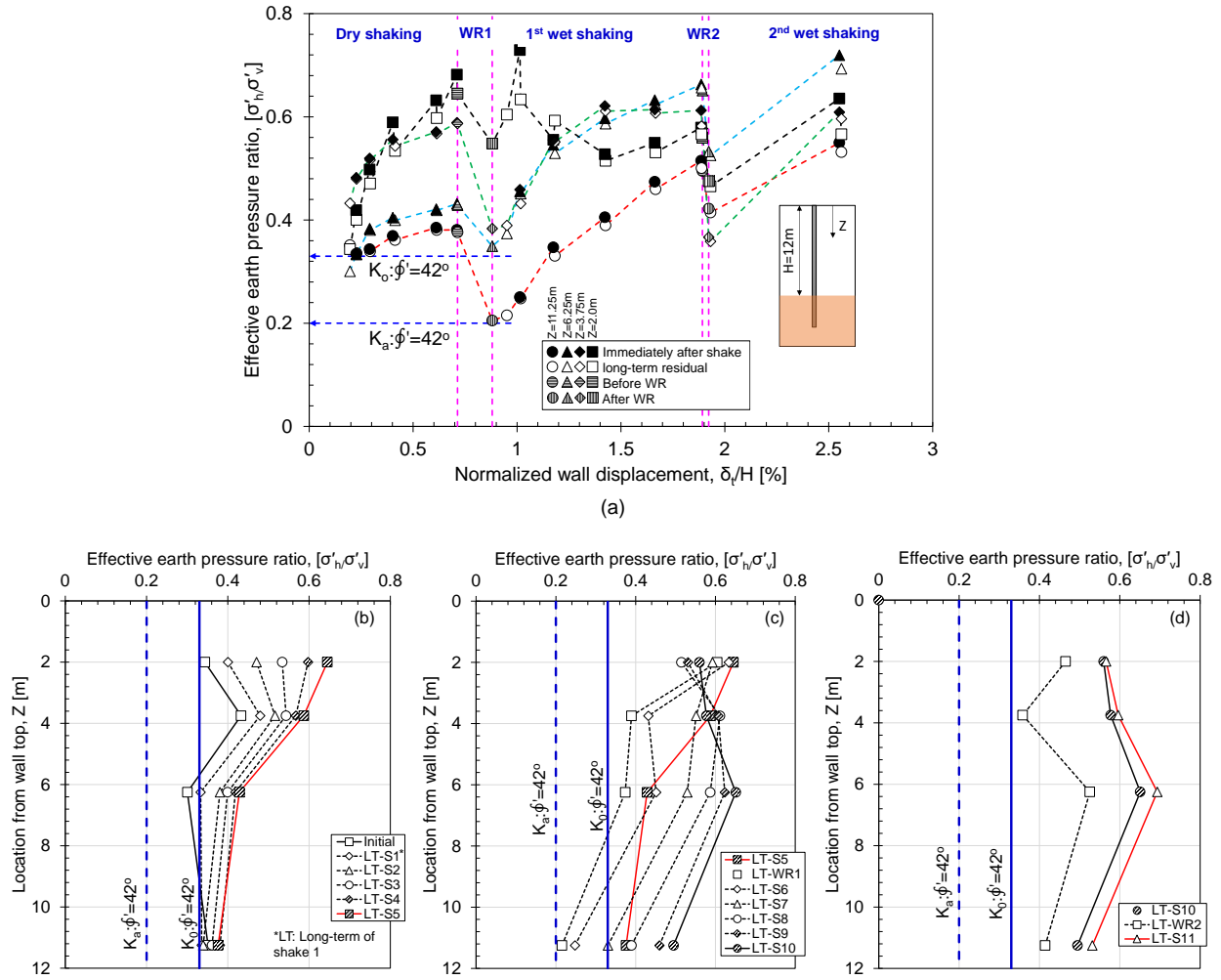


Figure 5.35: Effective earth pressure ratio of Case 1 (a) variation of effective earth pressures with wall displacements measured for the entire loading history of Case 1 (b-c) effective earth pressure ratios distribution with depth.

The measured effective earth pressure at different depths is normalized by the effective vertical stress in Figure 5.35-36 to understand the variation of the earth pressure from Cases 1 and 3. The earth pressure gradually increased with wall displacement for Cases 1 & 3 (Figure 5.35a-5.36a). This increase in earth pressure with the wall displacement can be attributed to the elastic resilience effect discussed in section 5.5.9. All the effective earth pressure gradually increased shake by shake

in dry conditions, especially at the shallower depth of Cases 1 & 3 (Figure 5.35a,b&5.36a,b). This behaviour implies that the densification of the backfill soil might occur in all depths, redistributing the earth pressure after each loading (Figure 5.35b&5.36b). The ratio significantly decreased by the static loading of WR1, especially at the deeper depth close to the active K_a condition (Figure 5.35c & 5.36b). In wet conditions, the ratio increased significantly for Case 1, especially at deeper depth, with some reduction at $Z=2.0\text{m}$ in Shakes 7&8, which could be attributed to partial saturation (Borghesi *et al.*, 2020) (Figure 5.35c). The large increase in earth pressure at deeper depth could increase the wall inclination, decreasing earth pressure at $Z=2.0\text{m}$ in Shake 7&8. However, Case 3 did not show such behaviour. For Case 1, the ratios become relatively constant with depth. A similar observation can be made from Case 3, except for a large decrease in earth pressure at $Z=8.75\text{m}$. Finally, after final loading, ratios about twice and three times the at-rest (K_0) and K_a values were seen for Cases 1 and 3.

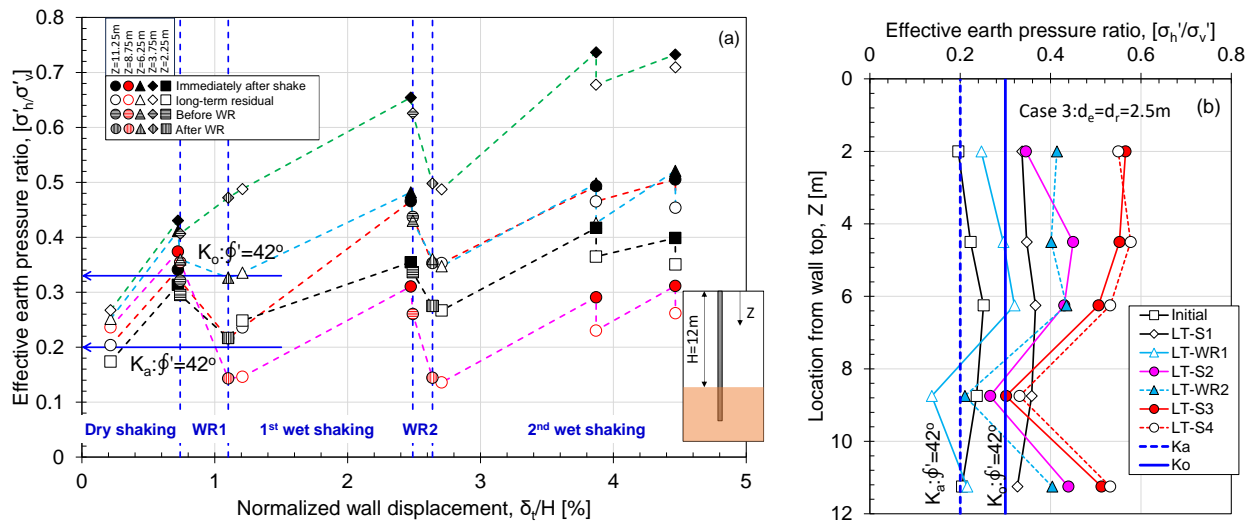


Figure 5.36: Effective earth pressure ratio of Case 3 (a) variation of effective earth pressures with wall displacements measured for the entire loading history of Case 3 (b) effective earth pressure ratios distribution with depth.

Finally, the lateral and effective earth pressure observed at $Z=2\text{m}$ and 11.25m for Cases 1 and 3 are compared in Figure 5.37. In both Cases 1 and 3, the effective earth pressure increases with the increase of wall top displacement. In Case 3, after the WR1, the maximum earth pressure ratio was observed at 11.25m rather than 2.25m . Overall, the observed earth pressure was larger for Case 1 ($d_r=3.0\text{m}$) than Case 3 ($d_r=2.5$), confirming the effect of the embedment depth. Also, effective earth pressure increased during the final loading (more than at-rest pressure), confirming the presence of the resilience effect (discussed in section 5.5.9). Therefore, it could be said that secured rock-wall confinement could be ensured even at δ_t over $2\%H$.

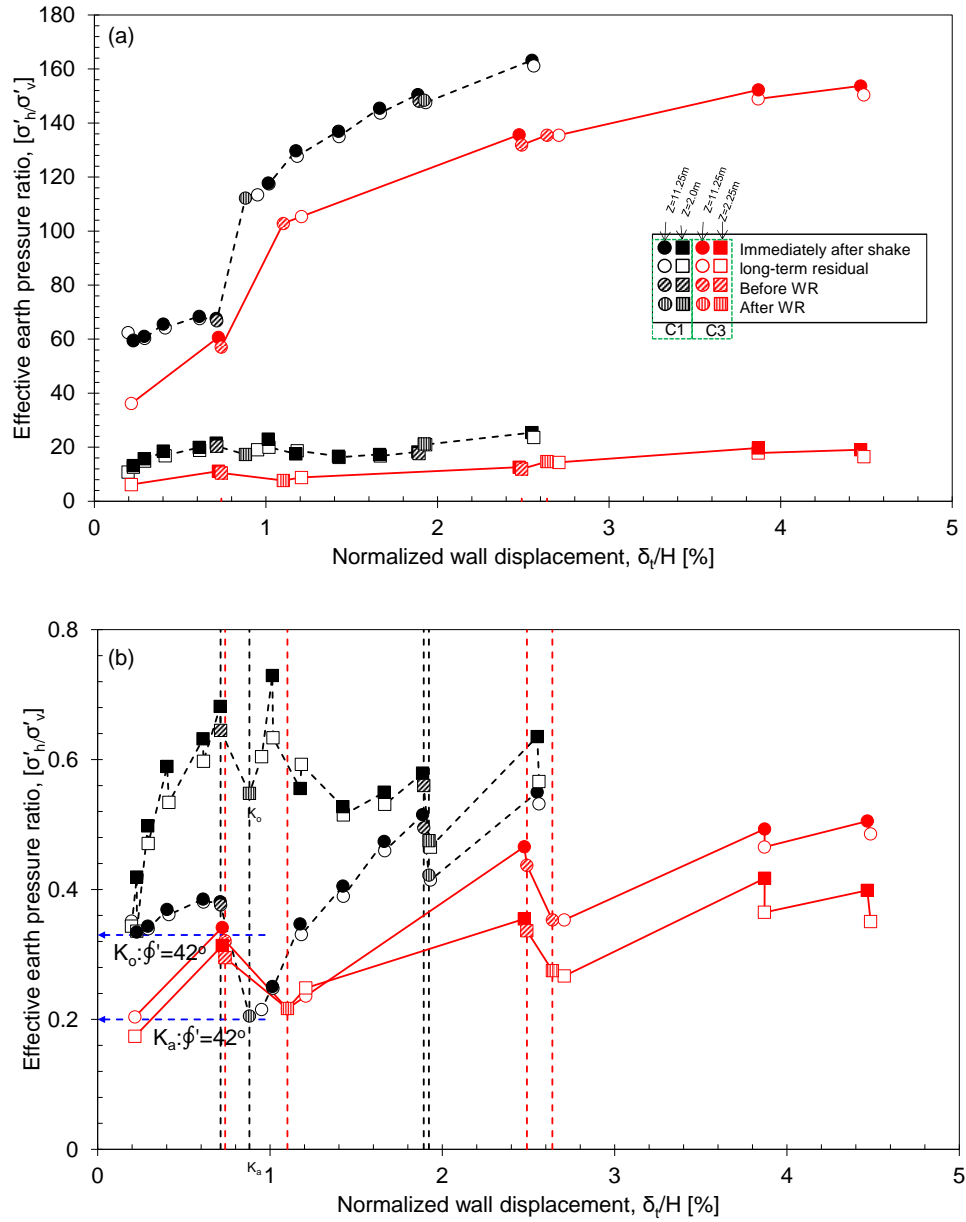


Figure 5.37: Comparison of lateral pressure and effective earth pressure at $Z=2m$ and $11.25m$ of Case 1 ($d_r=3.0m$) and Case 3 ($d_r=2.5m$).

5.5.4.1 Qualitative discussion on total thrust force and the location of the total thrust force:

The calculated effective thrust force (P_h') acting on the wall, the location of resultant thrust force (h_p) and the location of the effective thrust force (h_p') are plotted against the wall top displacement in Figures 5.38 and 5.39. Figure 5.38a depicts the method to calculate the resultant thrust force, the location of the resultant thrust force, and the vertical force. The resultant thrust force (P_h) and location of the resultant thrust force (h_p) are calculated from the total lateral pressure distribution.

The vertical force is calculated by integrating the vertical stress diagram with respect to depths for reference and termed as P_v' .

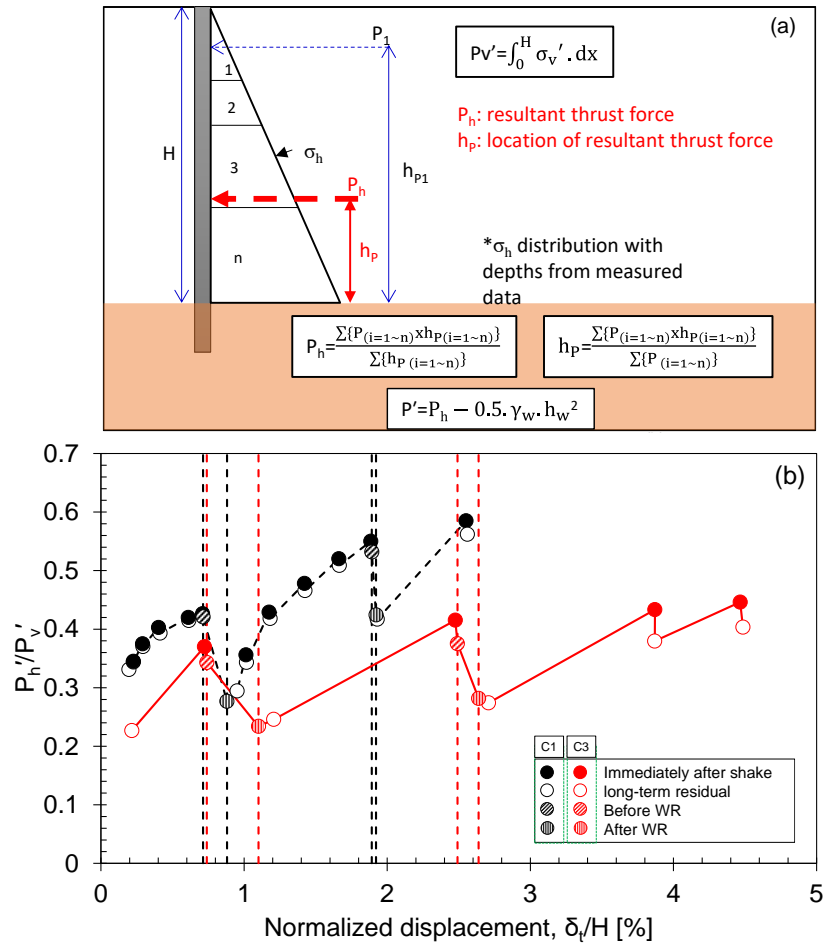


Figure 5.38: (a) method to calculate resultant thrust force and location of resultant thrust force from Case 1; (b) Variation of normalized resultant thrust force with the wall top displacement.

Based on Figure 5.38b, the effective thrust force was increased during dry shaking, 1st wet shaking, and 2nd wet shaking. However, after WR1, a reduction in the effective thrust force was observed in both Cases 1 and 3 due to the reduction in the effective earth pressure. During the first wet shaking event, the increase in the effective thrust force was confirmed in both Cases 1 and 3. Although the effective earth pressure at $Z=2.0\text{m}$ of Case 1 didn't follow a similar trend to other depths, as shown in Figure 5.35, the effective thrust force is showing an increasing trend. Finally, during shaking, the kinematic component always increased with displacement. However, in the case of the long-term residual component, it always decreased with the increase of the wall top displacement.

In the case of the location of resultant thrust force, during dry shaking, the location changed from about $0.35H$ to $0.37H$, as shown in Figure 5.39. After WR1, the location of the effective thrust force becomes larger than the total thrust force. In the case of the location of the total thrust force, the location remained constant (h_p/H about 3.3) in the later loadings. However, the location of the effective thrust force decreased from about $0.44H$ to $0.38H$ for Case 1 and $0.41H$ to $0.39H$ for Case 3. This trend for the location of the effective thrust force is mainly affected by the effective earth pressure at $Z=2m$, as shown in Figures 5.35 and 5.36. In Case 1, the observation can be justified by the increase in the location of the effective thrust force during WR1 and the decrease during WR2. During WR1, the water level did not reach $Z=2m$. Therefore, the water could not neutralize the resilience effect (section 5.5.9) at $Z=2m$, resulting in a larger effective earth pressure at $Z=2m$ than at other depths, as shown in Figure 5.35. Due to the large effective earth pressure at $Z=2m$, the location of the effective thrust force increased during WR1. On the other hand, the water level reached $Z=2m$ during WR2, resulting in a significant reduction of the effective earth pressure at $Z=2m$ compared to other depths, as shown in Figure 5.35. The reduction of the effective earth pressure at $Z=2m$ caused the reduction of the location of the effective thrust force.

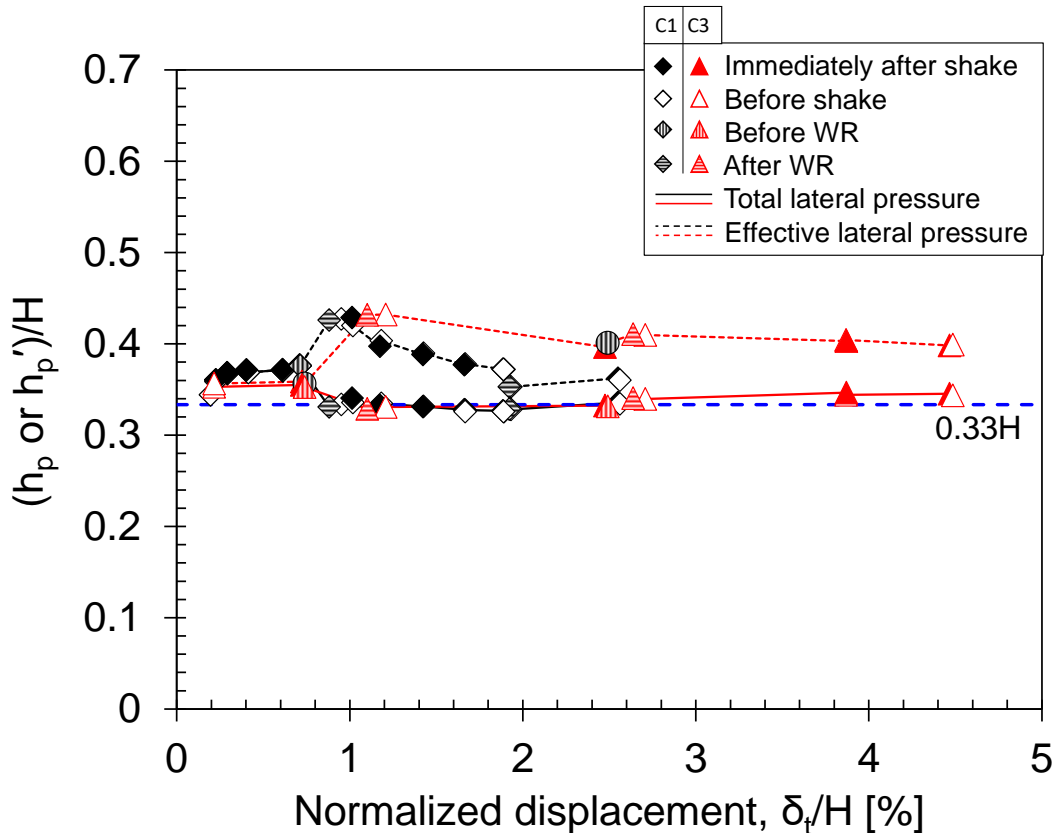


Figure 5.39: Variation of location of total and effective resultant thrust force with the wall top displacement.

Overall, in wet conditions, no significant change in the location of the resultant thrust force can be confirmed, as the hydrostatic pressure mainly governs it. Although different researchers concluded that the location of the resultant thrust force is at $0.3H$ (Al Atik and Sitar, 2010; Jo *et al.*, 2014,

2017), Overall, the observed location of the resultant thrust force and effective thrust force observed from this CSTP wall model condition is more than $0.34H$ and $0.4H$, respectively.

5.5.4.2 Dynamic lateral pressure:

The variation of the dynamic lateral pressure at two different depths ($Z=2\text{m}$ and 11.25m) from Cases 1 and 3 is plotted against the input motion in Figure 5.40. The measured maximum lateral pressure (Figure 5.31) was considered as the maximum dynamic lateral pressure at a particular location. The lateral pressure based on the Mononobe Okabe (M-O) method is also shown in this figure to compare the observation from the dry shaking. The lateral pressure was increased with the increase of input motion amplitude. It was observed that the lateral pressure during dry shaking at $Z=11.25\text{m}$ was smaller than the M-O lateral pressure. However, at $Z=2\text{m}$, the lateral pressure under dry conditions was larger than the M-O pressure, especially for large embedment depths. Therefore, further increasing the embedment depth might increase the lateral pressure during dynamic loading, especially at the shallow depth, which could lead to the failure of the retaining structure.

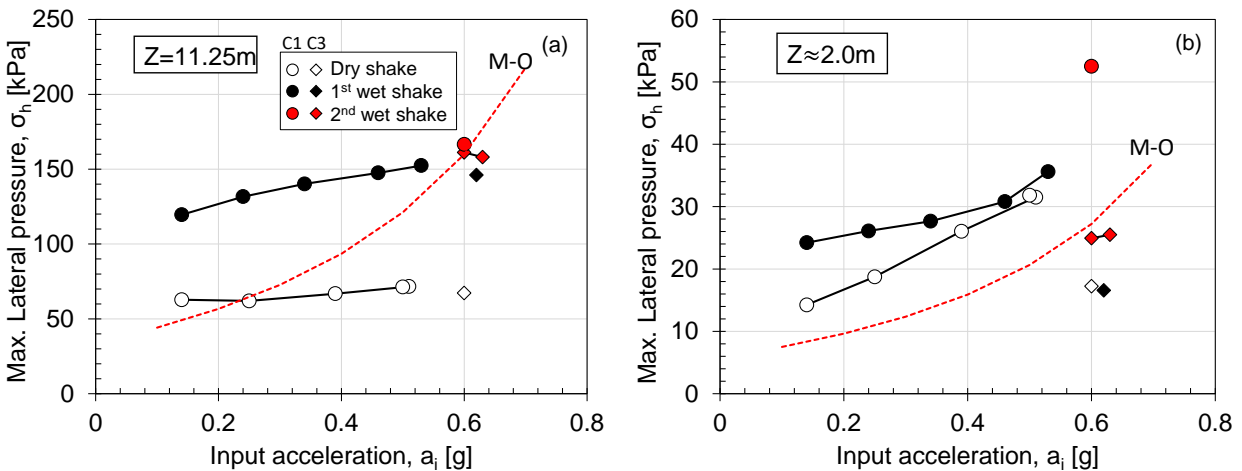


Figure 5.40: The variation of maximum lateral pressure with input acceleration.

5.5.5 Bending moment

Figure 5.41 illustrates a typical example of the bending moment distribution with depths for cases 1, 3, and 6. Some strain gauges did not respond during the test and were therefore excluded from the distribution diagram. The bending moment distribution is presented for four conditions: (1) Initial: after the 'g' up process, (2) Before shake, $t=0\text{sec}$, (3) After shake, $t=30\text{sec}$, and (4) Max.: the bending moment at the time of maximum value at $Z=10.75\text{m}$, which can be considered as the maximum dynamic bending moment. Two reference lines are included to represent the active

bending moment (M_a) and the at-rest bending moment (M_o), calculated based on the lateral pressure distribution given in Figure 5.31.

Based on Figure 5.41, it was observed that the maximum bending moment occurred above the rock surface, and there was an abrupt change in the bending moment below the rock surface. In a cantilever wall, a maximum M should be obtained at the rock surface. However, the maximum M was observed by the strain gauge measurement at $Z=10.75\text{m}$, not $Z=11.25\text{m}$ (Figure 5.41a), which could be attributed to a stress concentration or a propping action in the strain gauge measurement near the rock surface of the CSTP wall. The plugging condition and local deformation in the wall near the rock surface can cause this stress concentration (Ishihama et al., 2020). BM at the rock surface, equivalent to the moment load to the wall (M_L), was estimated by linear extrapolation using M_s at $Z=10.75$ and 9.5m , as shown in Figure 5.41a. This simplified approach might underestimate M_L , but it could be used as an approximate value. From the M distribution, M_s more than M_a were observed after Shakes 4 at the rock surface. Also, a large dynamic BM distribution (Max.) can be confirmed due to the combined effect of σ_h and inertia. The overall M distributions below the rock surface show a gradual decrease. However, discontinuous changes of M can be seen near the surface, which confirms the effect of the stress concentration and local deformation of the tubular pile below the rock surface (Carter and Kulhawy, 1988,1992). Less effect of stress concentration was observed for strain gauges placed approximately 25% of the pile diameter away from the rock surface, as shown in Figure 5.41b&c. Finally, the observed M was larger for $d_r=3.0\text{m}$ than 2.5m .

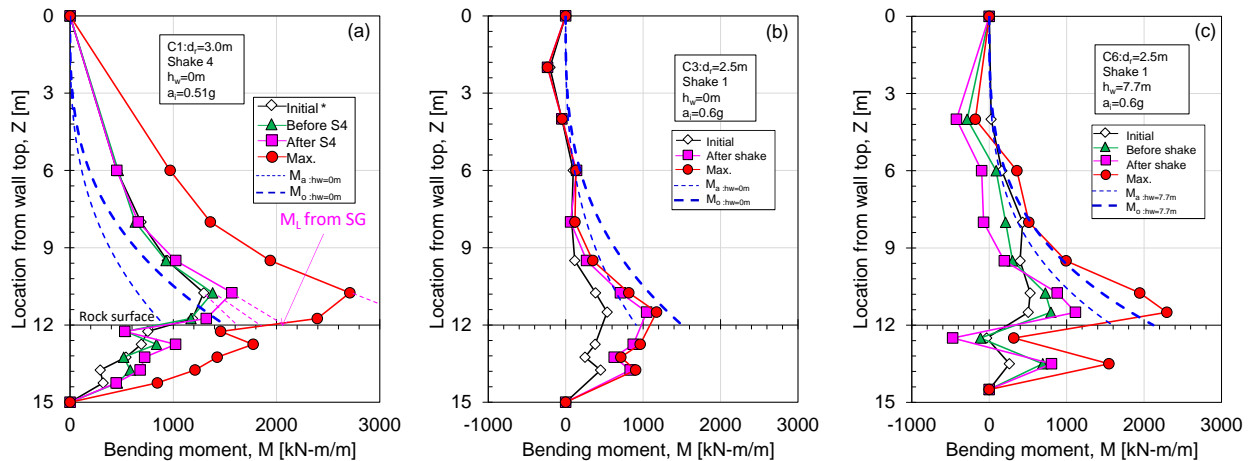


Figure 5.41: Bending moment distribution with depths (a) CASE 1 shake 4 (b) CASE 3 shake 1 (c) CASE 6 shake 1.

The bending moment measured at $Z=9.5\text{m}$, 10.75m , 11.75m , 12.25m , 12.75m , and 13.25m from the g-up process to the end of the final loading from Case 1 is plotted against the wall displacement in Figure 5.42. Similarly, the bending moment measured at $Z=10.75\text{m}$, 11.5m , 12.75m , and

13.25m from the g-up process to the end of final loading from Case 3 are plotted against the wall displacement in Figure 5.43.

An almost linear variation of the bending moment with the displacement can be confirmed during the g-up process, confirming the elastic condition of the wall and rock system for both Cases 1 and 3. At the end of the g-up process, the maximum bending moment was observed at $Z=10.75\text{m}$ instead of $Z=11.75\text{m}$ for Case 1. However, in Case 3, the maximum bending moment was observed at $Z=11.5\text{m}$. A significant difference between the bending moment below and above the rock surface was confirmed. This behaviour confirms the less stress dependency by the rock material but a large dependency on the confining stress (Carter and Kulhawy, 1987,1992).

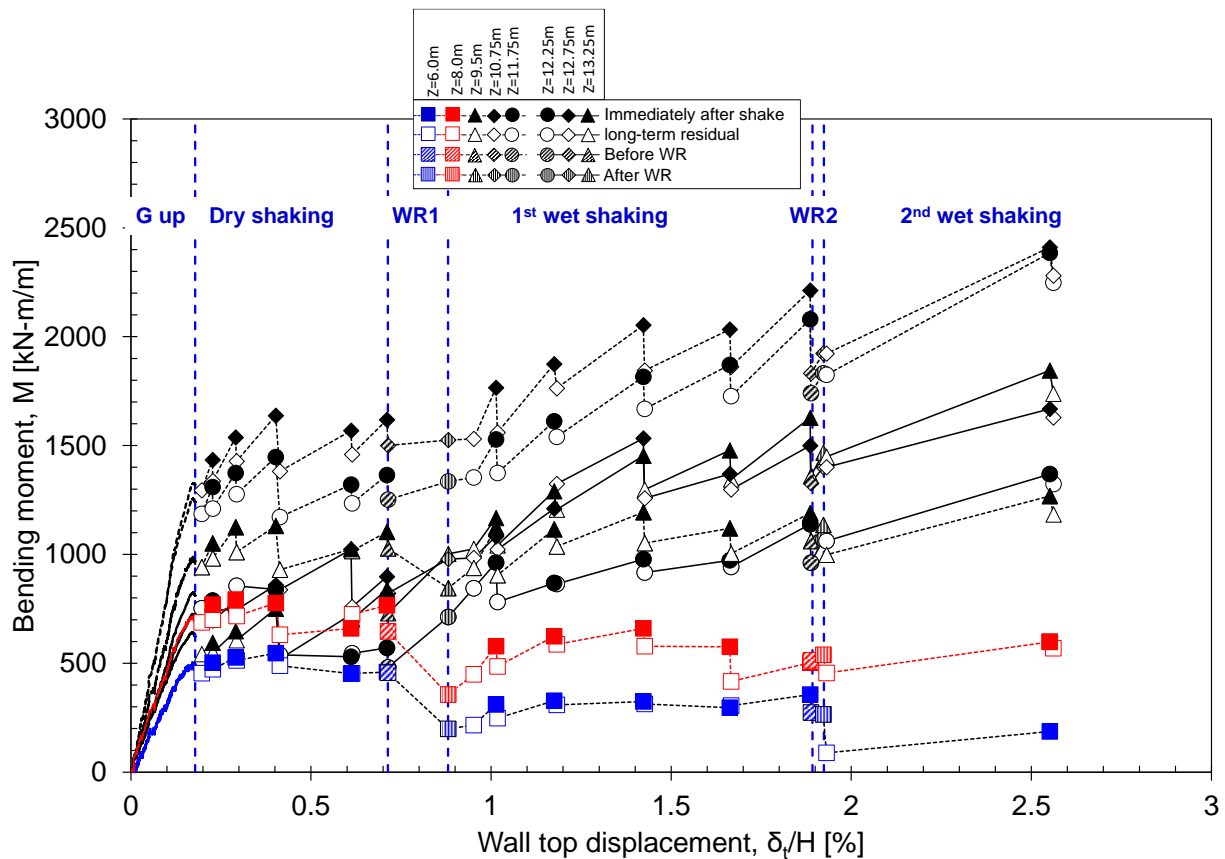


Figure 5.42: Variations of measured bending moment at different depths with the wall top displacement from Case 1.

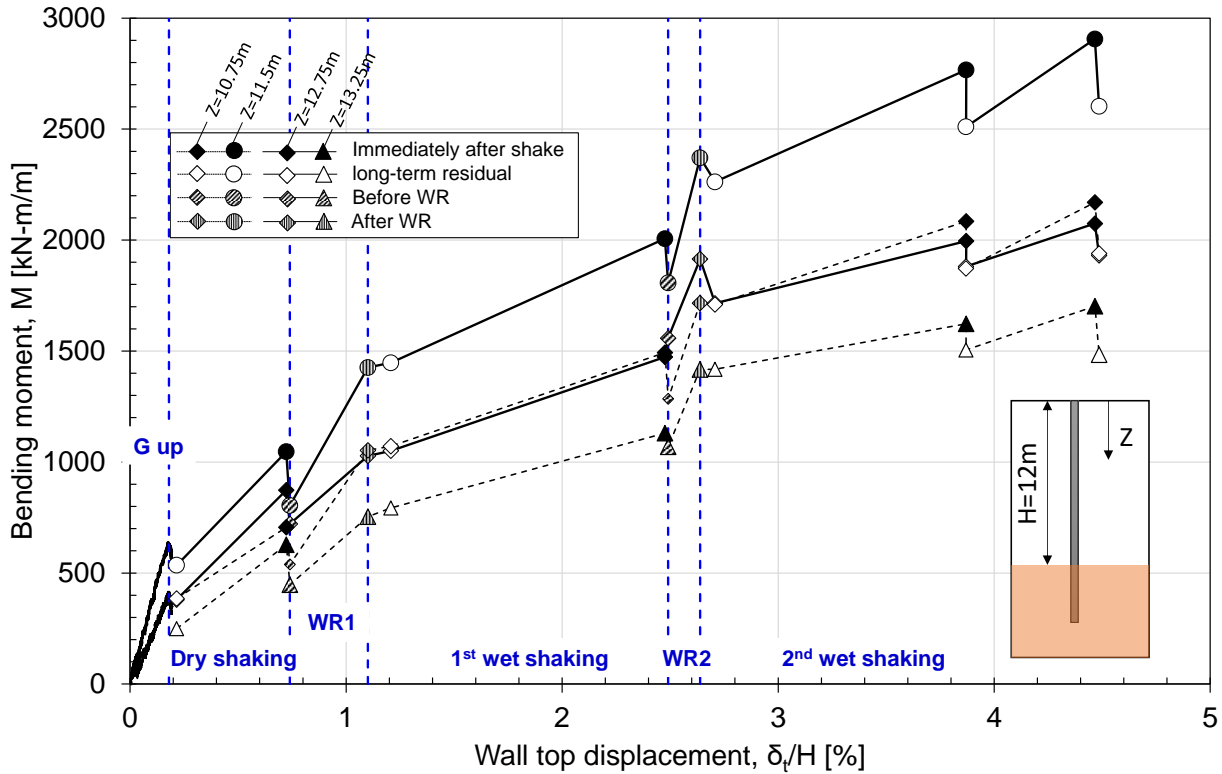


Figure 5.43: Variations of measured bending moment at different depths with the wall top displacement from Case 3.

At a wall top displacement of about $\delta_t=0.4\%H$, the location of the maximum bending moment below the rock surface changed from $Z=12.25\text{m}$ to 12.75m for Case 1. With further increase in the wall top displacement (from about $\delta_t=1.4\%H$), the location of the maximum bending moment changed from 12.75m to 13.25m for Case 1. This behaviour confirms the deterioration of the shallow rock layer, with the increase in wall top displacement. However, in Case 3, this behaviour could not be confirmed because of the location of the strain gauges, although the wall top displacement was more significant.

Figure 5.44(a) compared the variation of bending moment measured at $Z=10.75\text{m}$ with the wall top displacement for Case 1 and Case 3. Additionally, Figure 5.44(b) presents the variation of the extrapolated moment with the wall top displacement for Case 1 and Case 3. The figure also includes the calculated resisting and driving moments at $h_w=0\text{m}$, 9.6m , and 10.9m based on the pressure distribution shown in Figure 5.10. The effect of embedment depth can be observed through the larger bending moment and moment load in Case 1 ($d_r=3\text{m}$) compared to Case 3 ($d_r=2.5\text{m}$). The resilience effect (section 5.5.9) is evident in both cases during dynamic loading, as the bending moment and moment load increased following the dynamic loading and persisted even after the final loading. After the final loading, the observed moment load in Case 1 exceeded M_a at $h_w=10.9\text{m}$. Conversely, for Case 3, the observed moment load was smaller than M_a at $h_w=9.6\text{m}$ ($h_w=9.4\text{m}$ was the maximum water level after WR2 in Case 3). This confirms that a factor of safety

over 1 could be ensured for $d_r=3\text{m}$ (Case 1) but not for $d_r=2.5\text{m}$ (Case 3). Moreover, for Case 3, in final loading, the increase in moment load and bending moment was approximately 5%, while the increase in wall top displacement was about $0.6\%H$, indicating deterioration in rock wall confinement. However, it was not enough to cause catastrophic failure for $d_r=2.5\text{m}$.

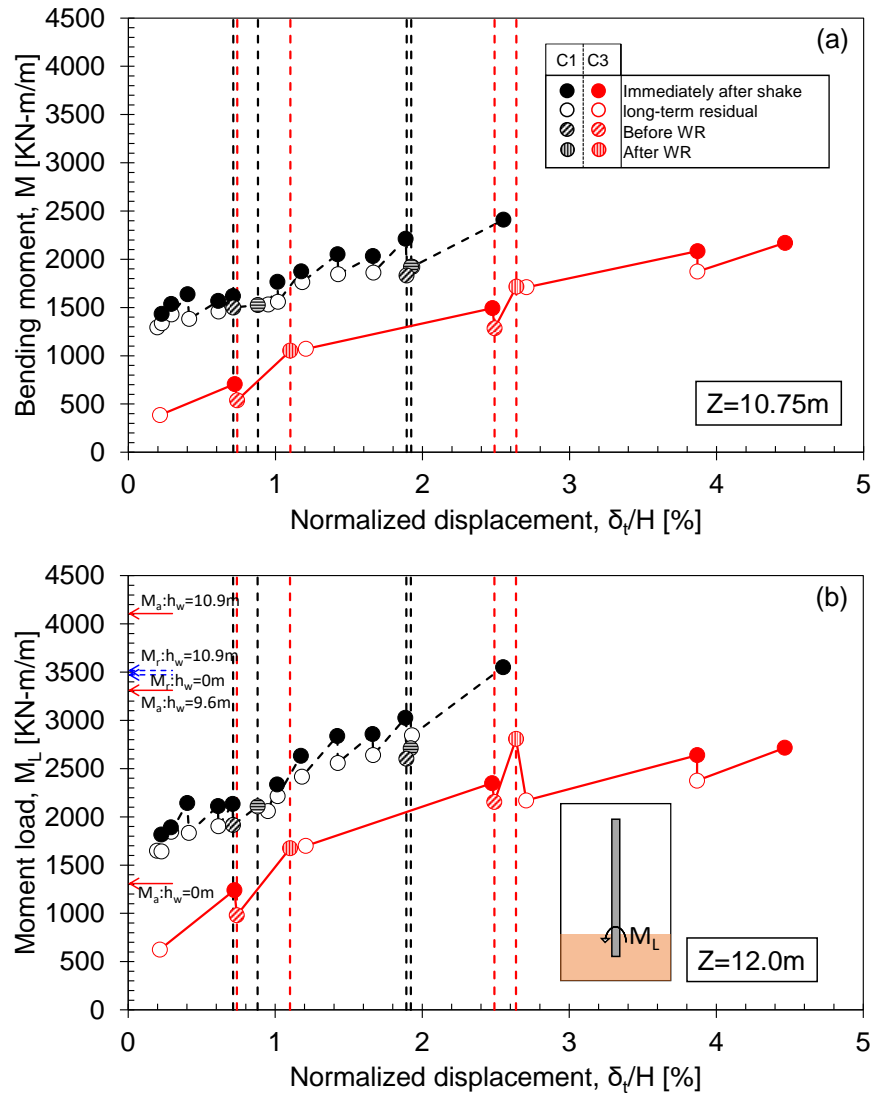


Figure 5.44: Variation of moment with wall top displacement from Case 1 and 3 (a) bending moment at $Z=10.75\text{m}$ (b) moment load.

5.5.5.1: Dynamic bending moment:

Variations of moment loads acting on the wall (M_L) are shown in Figure 5.45. The maximum dynamic M_L s obtained from the bending moment at the rock surface, and the σ_h distribution and the wall inertia at the time of the maximum bending moment are plotted to the input acceleration (a_i) in Figure 5.45a. The inertia moment was calculated similarly to Jo et al., (2017). In the figure,

the residual M_L s estimated from the bending moment and the σ_h distribution immediately after the shakings are also shown with linear regression lines, except for the M_L from the σ_h .

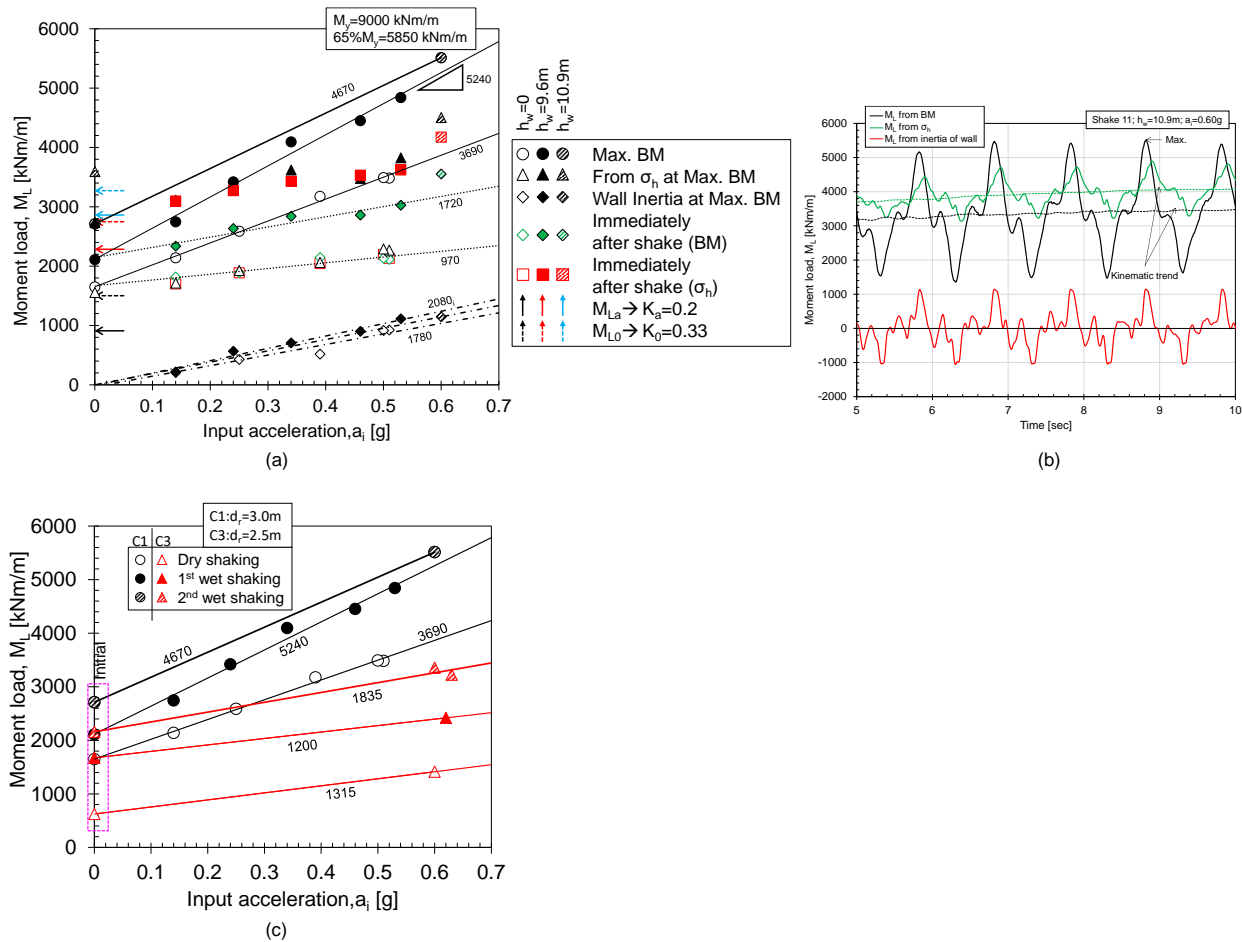


Figure 5.45: Variation of moment loads with series of loadings (a,b) Case 1 (c) Case 1&3 comparison.

The maximum M_L observed during Shake 11 was less than $65\%M_y$, confirming the elastic response of the wall structure for the entire loadings. Though there was uncertainty in pressure measurement by the small cell, the residual M_L s obtained from the bending moment and σ_h after dry loading show reasonable agreement, indicating the reliability of σ_h to some extent for accessing the total earth pressure on the wall. However, in wet conditions, the M_L s from σ_h tend to be larger than those from the bending moment, implying the inaccuracy of σ_h . Nonetheless, the dynamic maximum, residual M_L s and the inertia moment increase almost linearly with a_i , except for the M_L s from σ_h in the wet loadings. The residual M_L s after the loading are all larger than those calculated assuming K_a and K_0 pressures (M_{La} , M_{L0}), confirming the resilience effect (5.5.9). An example of time histories of M_L from bending moment, σ_h and the wall inertia is shown in Figure 5.45b. A well-synchronised relation is confirmed between M_L s from bending moment and the wall

inertia at their peaks, but some phase difference from σ_h due to the dynamic soil-wall interaction discussed in Figure 5.30. In Figure 5.45, the difference in the slopes of regression lines between M_L at the Max bending moment and after the shake can be considered as the dynamic component of the moment load. The slope differences and the slopes of the wall inertia are both slightly larger in the wet condition ($h_w=9.6\text{m}$) than in the dry condition due to the larger amplification ratio for the former than the latter (Figure 5.22a&b). Comparing these slopes, it can be said that the wall inertia wall contributed about 60% to the dynamic component of the moment load at its maximum in this particular series of dynamic loadings.

The effect of embedment depth can be confirmed in Figure 5.45c. For similar input acceleration, a larger moment load was observed for $d_r=3.0\text{m}$ (Case 1) compared to $d_r=2.5\text{m}$ (Case 3). Furthermore, the maximum moment load observed for the larger embedment depth was approximately 60% of the yielding moment (M_y), which is close to the actual yielding moment of $65\%M_y$ discussed in section 3.2. Therefore, it can be inferred that by further increasing the embedment depth, the concern will shift from wall displacement to structural failure.

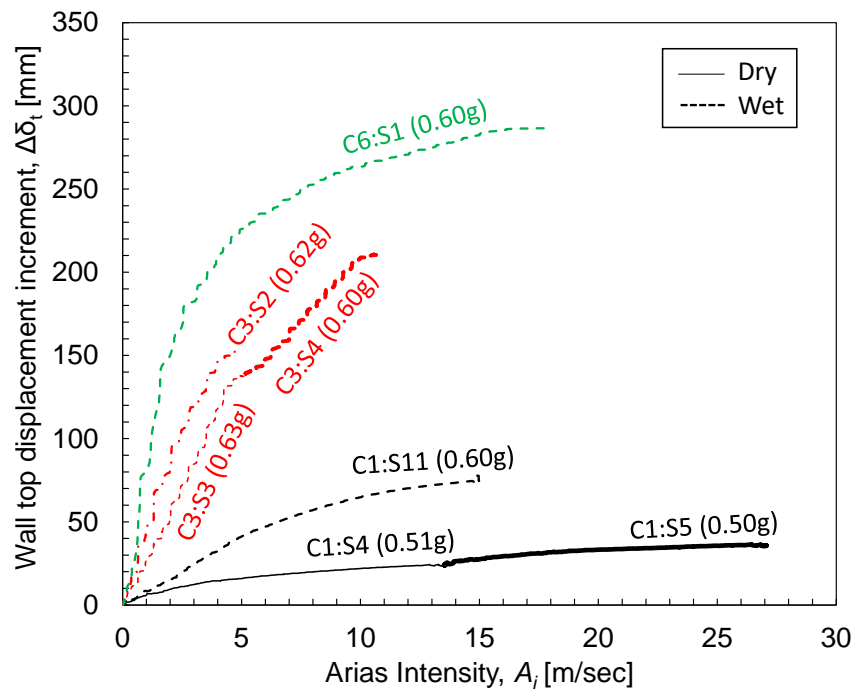


Figure 5.46: Variation of kinematic component of wall top displacement with arias intensity.

5.5.6 Typical CSTP wall displacement behaviour under dynamic loading

Figure 5.46 presents the variation of the kinematic component of wall top displacement with Arias intensity. Under similar water levels (Case 1 shake 4&3; Case 3 shake 3&4), the kinematic component of the wall displacement is plotted continuously to the arias intensity. The influence of embedment depth is evident in the kinematic component as well, with larger values observed for

$d_r=2.5\text{m}$ compared to $d_r=3.0\text{m}$. The observed displacement from Case 6 Shake 1 was larger than Case 3 Shakes 3 and 4. The difference in the loading sequence influences this behaviour. The initial loading of Case 6 was static loading by water rise. Therefore, no resilience effect was developed in Case 6. However, in Case 3, as the initial loading was dynamic, therefore, resilience effect caused an increase in the lateral pressure more than the at-rest pressure (Figure 5.36). The larger resilience effect in Case 3 caused a smaller displacement than in Case 6. Therefore, without pre-shaking, the wall displacement will be larger than the pre-shaking condition during dynamic loading.

Measured residuals δ_t s are plotted against the input acceleration, a_i , in Figure 5.47. The figures only include Case 1, as Case 1 had the input motion, which increased chronologically. The increment in displacement is taken from the initial values of dry shakings events, 1st wet shakings events, and 2nd wet shakings events to distinguish the trends more clearly. For the sinusoidal input motions with almost the same number of cycles ($n_c \sim 20$), a_i can be a common parameter of magnitude of dynamic loading. Nonlinear variations of δ_t s with a_i were observed for the dry ($h_w=0$) and wet ($h_w=9.6$) conditions. In other words, $\Delta\delta_t$ in each dynamic loading increased with a_i in the subsequent shake. The accumulated increments of δ_t for the wet condition was 110mm, about twice that for the dry conditions. These increases of $\Delta\delta_t$ are partially due to the increase of residual earth pressure by the resilience effect, as shown in Figure 5.35 and could be attributed to the deterioration of rock stiffness due to the cyclic deformation. Although the input accelerations of Shake 4 & 5 are almost the same, δ_t of Shake 4 was about twice that of Shake 5 (Figure 5.12), which also agrees with the smaller residual earth pressure increment by Shake 5 than Shake 4 (Figure 5.35&5.54). Conti et al. (2012) observed similar effects of the magnitude of input motion on the displacement of flexible cantilever walls in sand. In the long-term period after each loading, very small δ_t increases were observed, except for WR1, in which a visible increase was noticed.

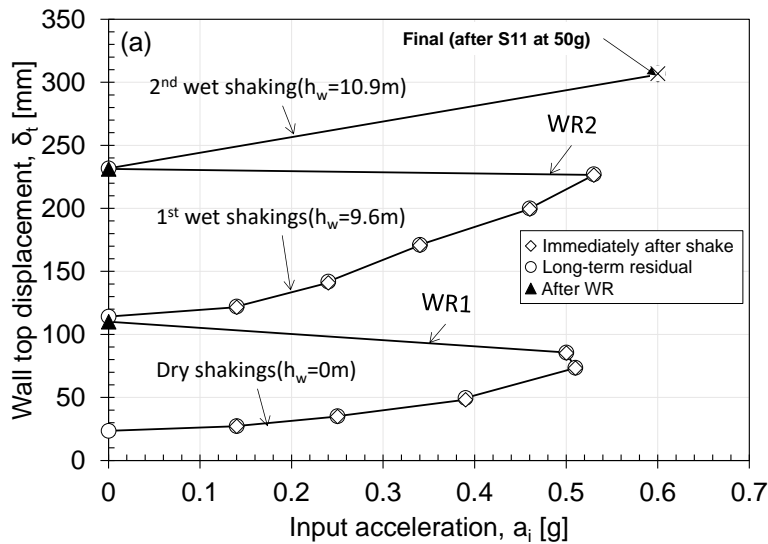


Figure 5.47: (a) Variation of wall displacement with input acceleration; (b) variation of wall displacement with cumulative arias intensity.

5.5.7 Effect of pre-shaking on the static loading behaviour of CSTP wall:

The behaviour of the CSTP wall during WR1 for Cases 1, 3, and 6 are compared with the 2D plate wall model reported by Kunasegaram and Takemura (2021) in Figure 5.48. The measured displacement is plotted against the water level in this figure. For identical water levels, the displacement is larger for the 2D plate wall model than for the CSTP wall. Additionally, in both wall models, smaller wall top displacement was observed for a larger embedment depth, confirming the effect of embedment depth on wall top displacement. In the CSTP wall, no significant increase in displacement was noticed at h_w around 4m. As shown in Figures 5.35, 5.36 and 5.54, the earth pressure for Cases 1 and 3 was larger than the at-rest pressure before the first water rises. This high earth pressure could prevent the immediate initiation of active conditions, resulting in small displacements at shallow water levels.

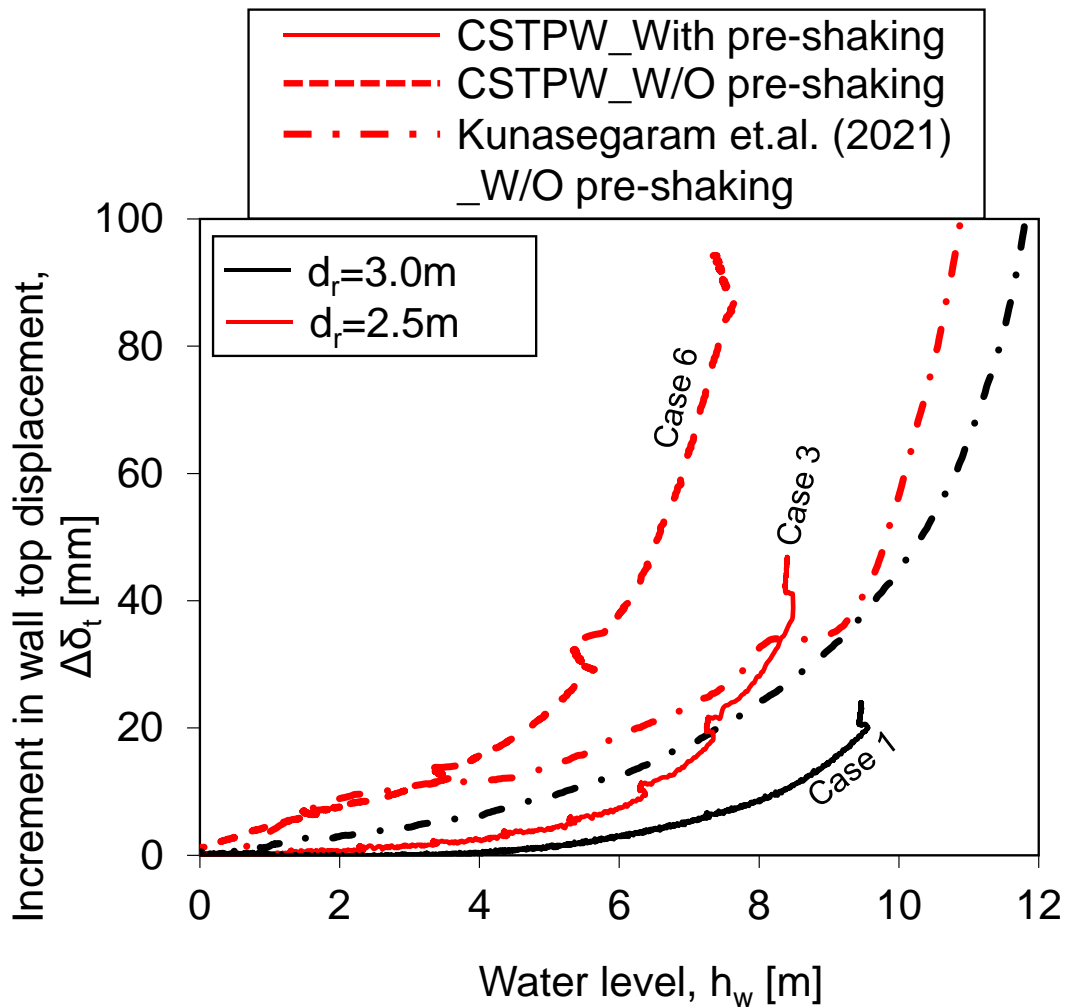


Figure 5.48: Variation of wall top displacement with water level.

Another effect of pre-shaking could be confirmed by the smaller increment in moment load caused by pre-shaking in the CSTP wall model (see Figure 5.44b). Moreover, the base shear of the 2D plate wall model is smaller than that of the CSTP wall model, which could also limit the displacement at higher water levels compared to the 2D plate wall model. However, for $d_r=2.5\text{m}$, both the 2D plate wall model and Case 6 exhibited larger displacements from the beginning. Almost identical wall top displacements were observed between Case 6 and the 2D plate wall model up to $h_w=4\text{m}$. Beyond that, the observed displacement in Case 6 exceeded that of the 2D plate wall model, which could be due to the smaller strength of the rock ground in Case 6 (**Table 5.2**). Subsequently, for Case 3, a significant increase in wall displacement was observed for $h_w\approx 8\text{m}$, which could be due to the previous dynamic loading, which caused the large rock strain.

5.5.8 Effect of embedment condition on the CSTP wall behaviour:

The variation of wall top displacement with cumulative Arias intensity is depicted in Figure 5.49, along with the wall and rock conditions after the single rock layer tests. Generally, a larger embedment depth ($d_r=3\text{m}$) resulted in smaller wall top displacement compared to a smaller embedment depth ($d_r=2.5\text{m}$). For Case 3 and Case 6, the wall top displacement reached approximately $5\%H$ at a cumulative Arias intensity of 25. However, for CASE 1, despite having a higher Arias intensity of over 100, the wall top displacement remained around $2.5\%H$. After the dry shaking event, the observed wall top displacement was nearly identical for Case 1 ($d_r=3\text{m}$) and Case 3 ($d_r=2.5\text{m}$), while the cumulative Arias intensity for Case 1 was approximately nine times higher than that of Case 3, confirming the influence of embedment depth. Comparing Case 6 with Case 3, the wall displacement during the first water rise was greater for the wall without pre-shaking (Case 6) than for the wall with pre-shaking (Case 3). Although significant wall top displacement was observed in Cases 3 and 6, exceeding the allowable displacement for level 2 seismic motion according to the IPA handbook (2016), no catastrophic failure was observed (Figure 5.49b). This confirms that stability against catastrophic failure can be ensured with an embedment depth smaller than the recommended design embedment depth. Overall, it can be said that the stability of the wall will significantly increase with the increase of 0.5m rock socketing depth.

During the construction process, the shallow rock layer could be significantly disturbed. Therefore, it is possible to have less or no resistance from this disturbed shallow layer. During the design, two conditions can be considered (i) assuming a smaller strength of the shallow rock layer and (ii) assuming no strength of the shallow rock layer (i.e., add the shallow rock layer to the wall height). To discuss the effect of the embedment depth condition, Cases 1, 3 and 4 are compared with one another. Figure 5.50 depicts the variation of wall top displacement with cumulative Arias intensity of Cases 1, 3, and 4. Due to the free sand layer present at the front of the wall, the large mobilization of side wall friction might be the reason for observing smaller wall top displacement after the ‘g’ up process of Case 4. Furthermore, the observed displacement for Case 1 ($d_r=3\text{m}$) was almost half of Case 4 ($d_r=2.5\text{m}+d_s=0.5\text{m}$). This observation confirms that although the embedment depth was similar, the presence of a 0.5m overlaying sand layer could significantly increase the wall top

displacement. This observation can further be justified by the stability analysis, where the factor of safety observed for a single rock layer was about 30% larger than the two layers.

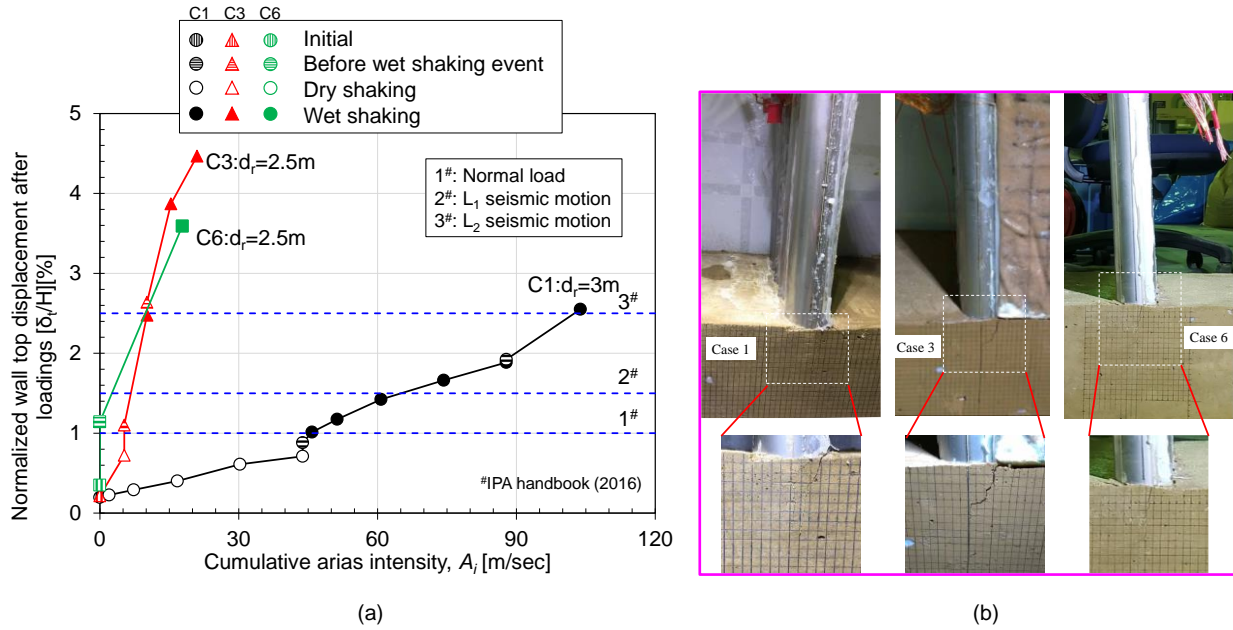


Figure 5.49: (a) variation of wall top displacement with cumulative arias intensity (b) wall and ground condition after tests.

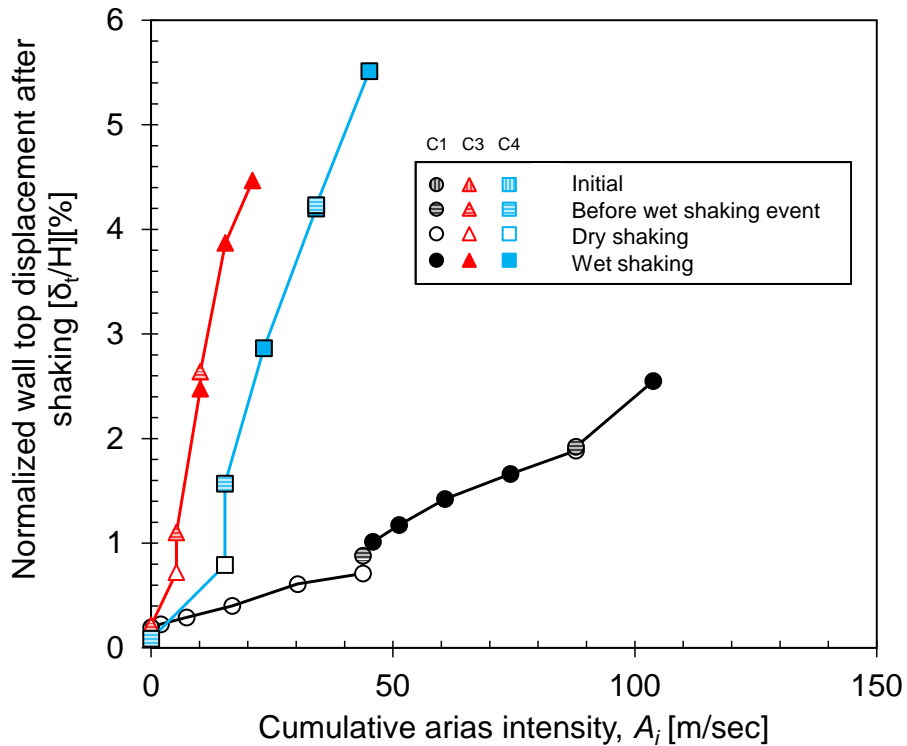


Figure 5.50: Variation of wall top displacement with the cumulative arias intensity.

The effect of the overlaying sand layer can be further observed during dynamic loading. Figure 5.51 shows the variation of the wall top displacement increment with the cumulative arias intensity. For similar embedment depth (Case 1 and 4), the wall with an overlaying sand layer produces a larger displacement than the wall without an overlaying sand layer. Comparing Cases 3 and 4, with a similar rock layer but Case 4 with 0.5m overlaying sand layer, no significant effect of 0.5m overlaying sand layer can be confirmed in dry conditions (Figure 5.51). A 10 % difference in the stability analysis could not significantly affect the wall displacement. During shake 1 of Case 4, a concave trend can be confirmed. However, during shakes 3 and 4 of Case 4, the almost linear trend can be confirmed between displacement and arias intensity.

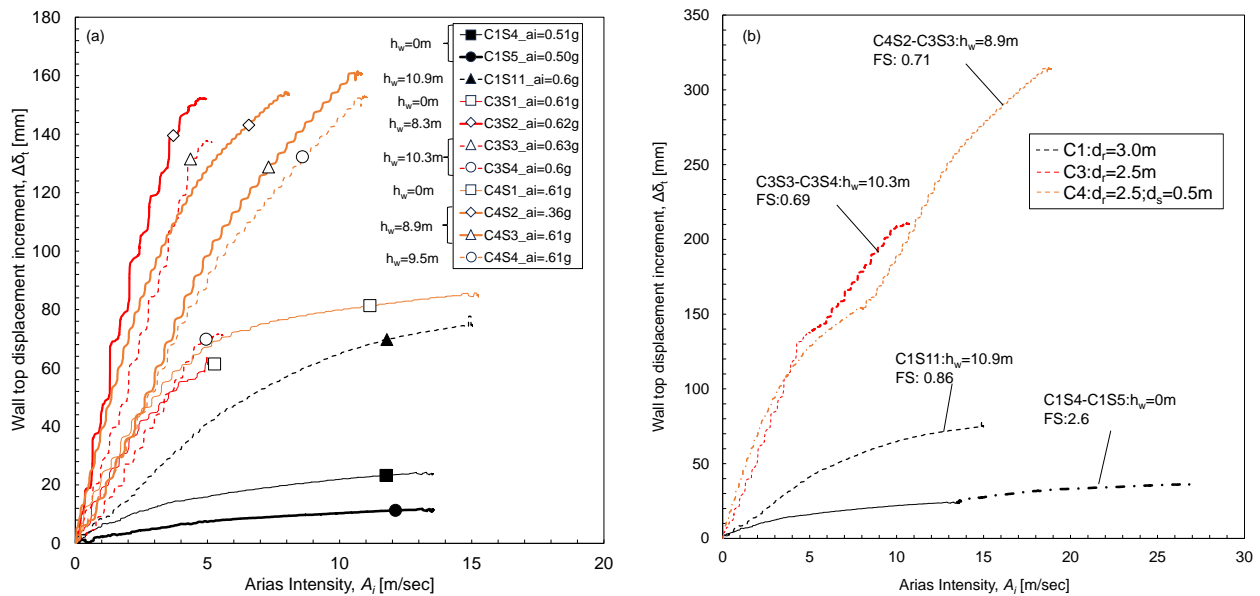


Figure 5.51: Variation of wall top displacement increment with the arias intensity during dynamic loading.

The variation of the amplification ratio of Cases 1, 3 and 4 is shown in Figure 5.52. the amplification ratio at the wall top is compared instead of backfill to avoid the effect of the sensor locations. Also, the average of the amplification ratio at cycles 2-5 is considered due to the small number of cycles in Case 3. At $h_w=0m$, the amplification ratio observed during the first shake of Cases 3 and 4 was almost similar. The amplification ratio observed during the final shakings of Case 3 was larger than that of Case 4, which could be due to the larger water level for Case 3 than Case 4. Also, during the final loading, the amplification ratio observed in Cases 1, 3 and 4 was almost similar. Compared to Case 1, the amplification ratio observed in Case 4 was smaller. However, the variation of the amplification ratio with the number of cycles is different. As shown in Appendix 5.15, during Case 4, the amplification ratio always showed increasing trends with the number of cycles. On the other hand, this kind of trend was only observed during shake 11 of Case 1 (Figure 5.21b). This observation confirms that Case 4 has smaller stability compared to Case 1.

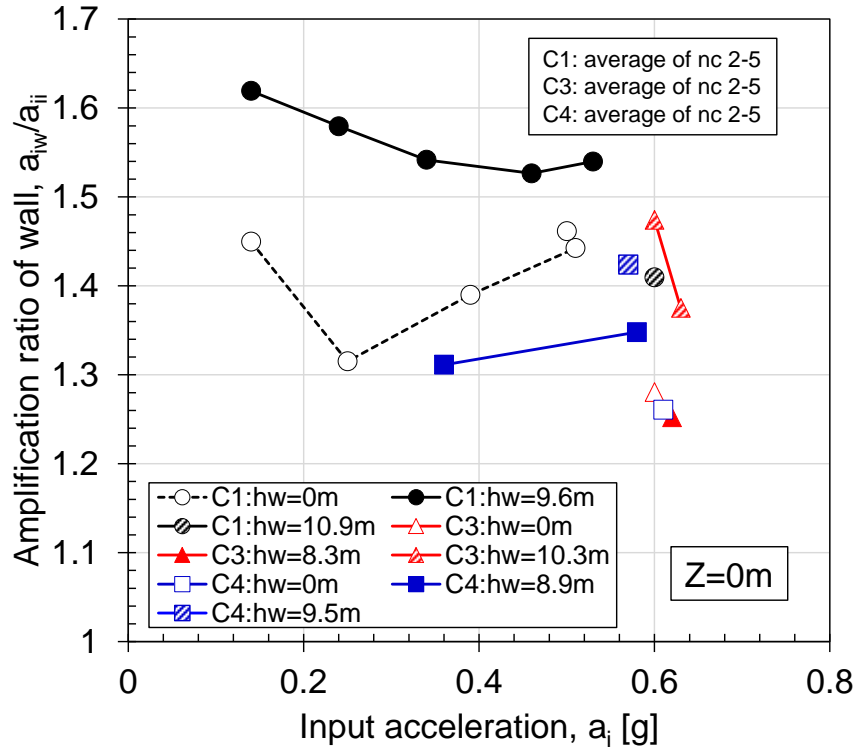


Figure 5.52: Variation of amplification ratio of Cases 1, 3 and 4.

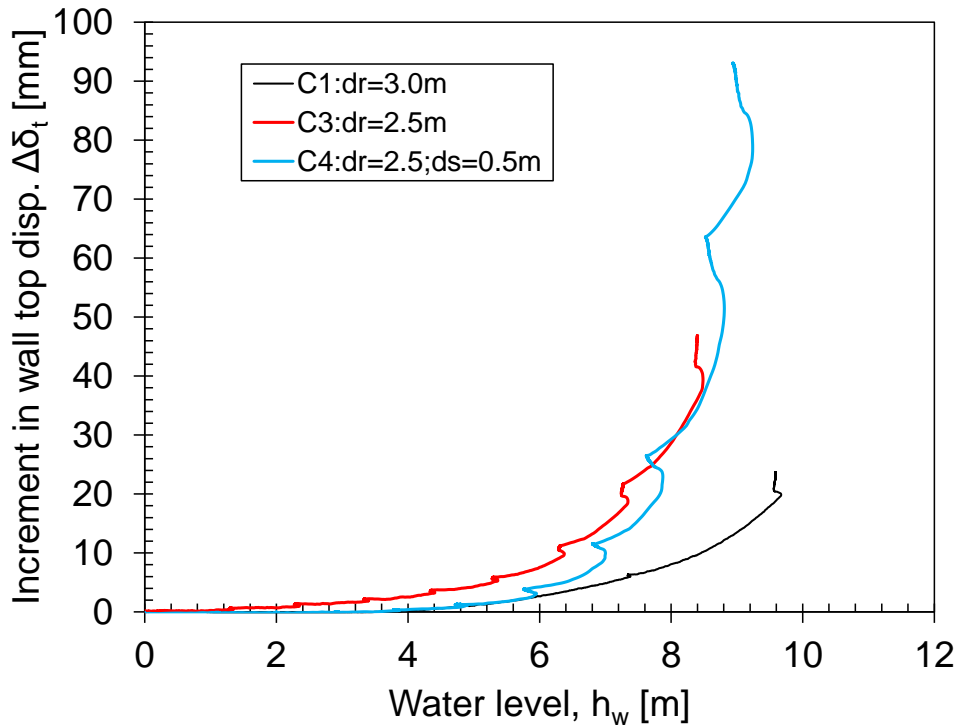


Figure 5.53: Variation of wall top displacement with water level of Cases 1, 3 and 4.

The variation of wall top displacement with the water level is shown in Figure 5.53. In Case 4, the height of the overlaying sand layer was subtracted for the comparison. It is seen that the wall top displacement in Case 4 is larger than in Case 1. However, the wall top displacement in Cases 3 and 4 is almost similar, possibly due to the similar effective earth pressure ratio observed in Figure 5.54. The smaller increment of wall top displacement during Case 4 at shallow water level could be due to the mobilization of side wall friction between the wall and free sand at the front. As the water level increases, this friction decreases, and a sharp increase in the wall top displacement can be confirmed after $h_w > 6\text{m}$. Also, it is to be noted that a small water leakage was observed during Case 4, which can be evident from Figure 5.53 and should be considered during the interpretation.

In the calculation of the effective earth pressure ratio for Case 4, the reduced water level was considered instead of the fixed water level. The variation of the effective earth pressure ratio with depth for Cases 1, 3 and 4 is shown in Figure 5.54. During Case 1, the increment in the effective earth pressure ratio at a shallower depth was more significant than the deeper depth during dry shakings. However, in wet conditions, the increase in the effective earth pressure ratio becomes larger at deeper depths than at shallower depths. After the final loading, the effective earth pressure ratio becomes almost constant. This behaviour can be interpreted as due to larger wall top displacement and the variation of the excess pore water pressure, the increment in the effective earth pressure ratio becomes smaller than the deeper depth and becomes almost constant throughout the depths. However, in Cases 3 and 4, this behaviour cannot be confirmed, but the location of the maximum effective earth pressure ratio was measured by the deeper depth than the shallower depth. At the final condition, these different trends between the Cases could be interpreted as for secured rock wall confinement (Case 1), the effective earth pressure ratio becomes almost constant along the depths, but for significant deterioration of the rock-wall confinement condition (Case 3 and 4) larger effective earth pressure ratio could be expected as the shallower depth than the deeper depth. Overall, the observed effective earth pressure ratio was larger than the at-rest pressure for Cases 1, 3 and 4. To understand the embedment depth condition more clearly, the variation of the effective earth pressure ratio calculated from the two earth pressure cells at the top and bottom with wall top displacement for Cases 1, 3 and 4 is shown in Figure 5.55. After final loading, at the shallower depth, the effective earth pressure ratio was larger for Case 1 than for Cases 3 and 4. However, Cases 3 and 4 had almost similar earth pressure ratios at the shallower depth. On the other hand, at the deeper depth, Case 1 had the larger ratio, followed by Case 3, then Case 4. The resilience effect defined in Section 5.5.9 can be confirmed for all the Cases, even during final loading in both depths. To further discuss the effect of the embedment depth condition, the back-calculated thrust force (Following the definition given in Figure 5.38a) is plotted against the wall top displacement in Figure 5.56. overall, the total thrust force observed in Case 1 was larger than in Case 3, followed by Case 4. A similar trend was confirmed for effective thrust force variation. During shake 1 of Cases 3 and 4, almost similar effective thrust force variation with wall top displacement was confirmed. However, after WR1, the effect of the embedment condition can be confirmed between Cases 3 and 4, which could be seen as the effect of mobilized friction by sand-wall getting reduced in Case 4. Finally, after the final loading, a larger effective thrust force can be confirmed for Case 3 than for Case 4.

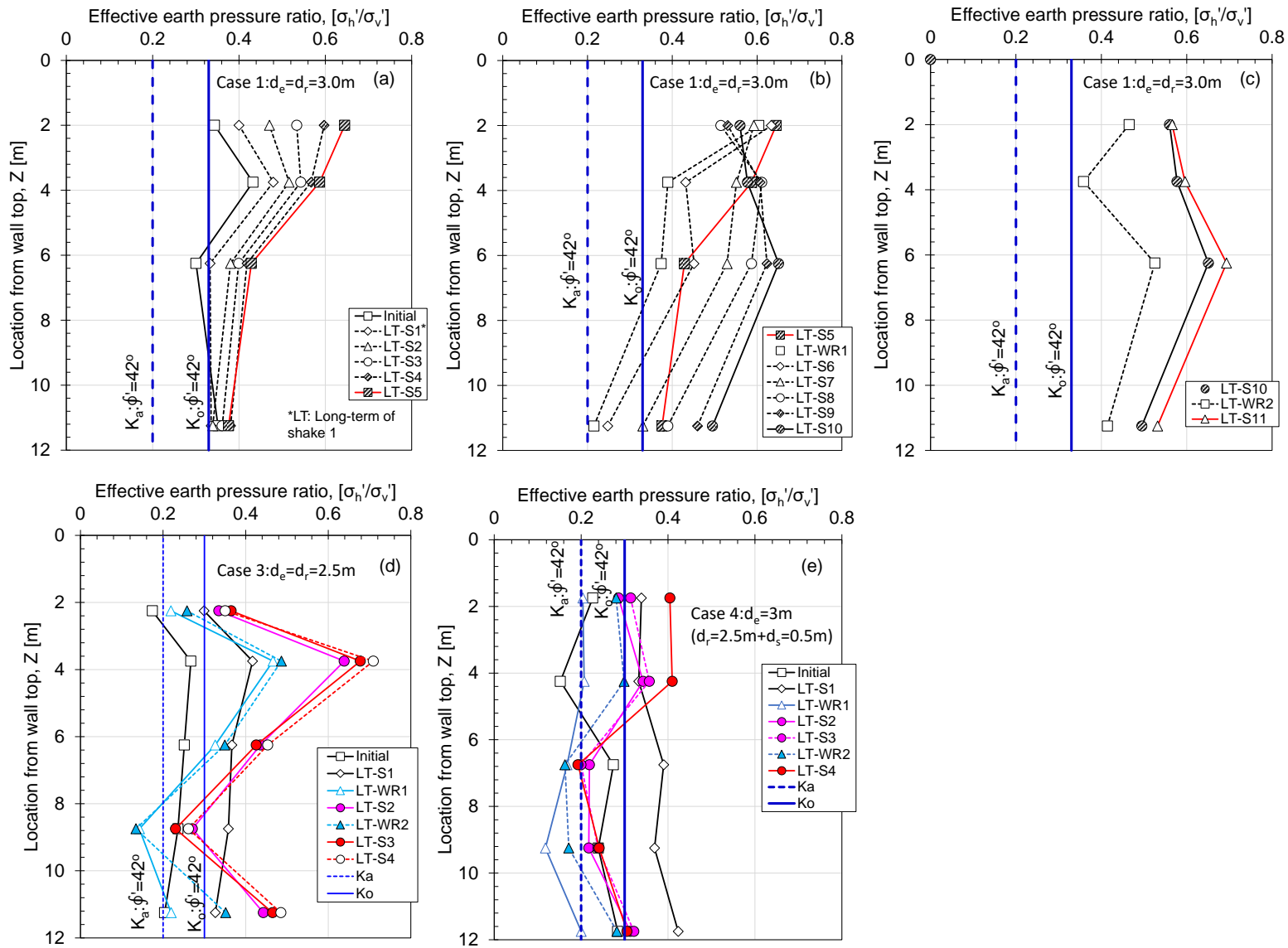


Figure 5.54: Variation of effective earth pressure ratio of Cases 1, 3 and 4.

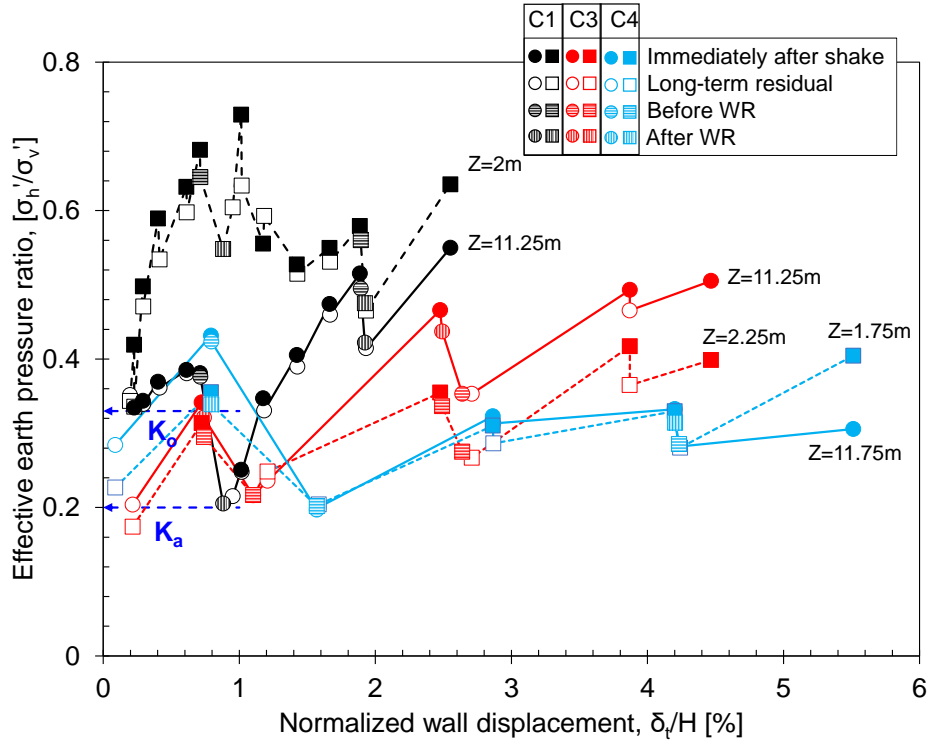


Figure 5.55: Variation of effective earth pressure with wall displacement of Cases 1, 3 and 4.

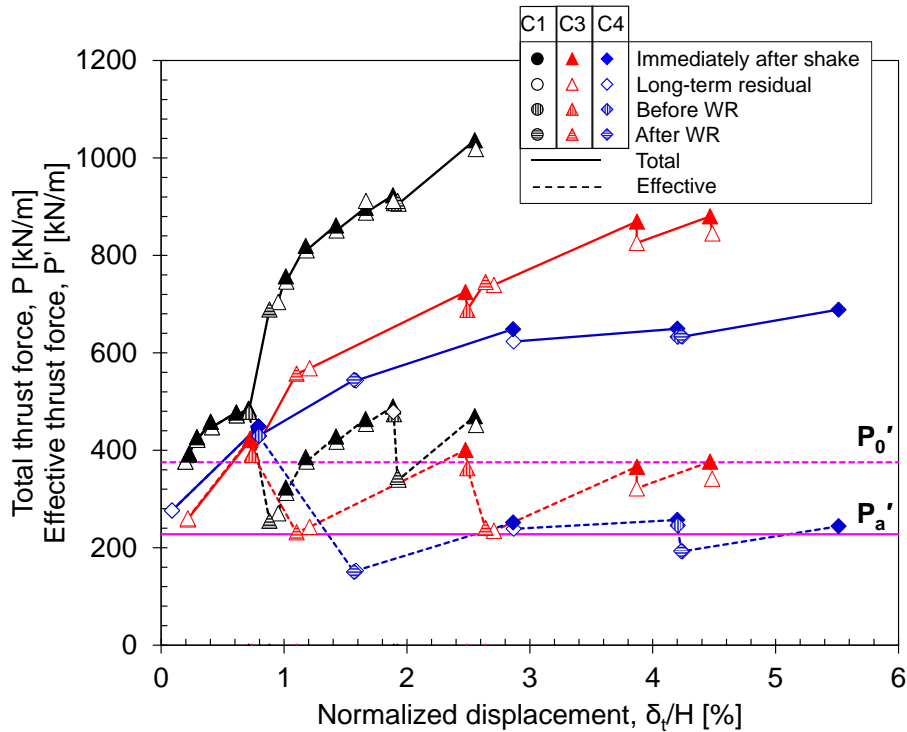


Figure 5.56: Variation of normalized effective thrust force with normalized wall top displacement.

Overall, the stability of the wall in Case 1 was larger than in Case 3, followed by Case 4, which supports the stability analysis (Figure 5.11&16, Appendix 5.13e).

5.5.9 Resilience effect:

The typical behaviour observed during dynamic loading is explained in Figure 5.30. Based on the relative position of the wall during dynamic loading (Figure 5.30), the corresponding distributions of the total and effective earth pressure are shown in the figure. Points B and C represent the minimum and maximum wall displacement during dynamic loading (See Figure 5.30). The wall displacement becomes minimum, when the dynamic load (inertia of wall and soil, water pressure) acting on the wall becomes minimum (Figure 5.57a). However, the maximum wall displacement occurs when the dynamic load become maximum. Some deviation from this behaviour could be observed at $Z=11.25\text{m}$ due to the phase difference as discussed in Figure 5.30.

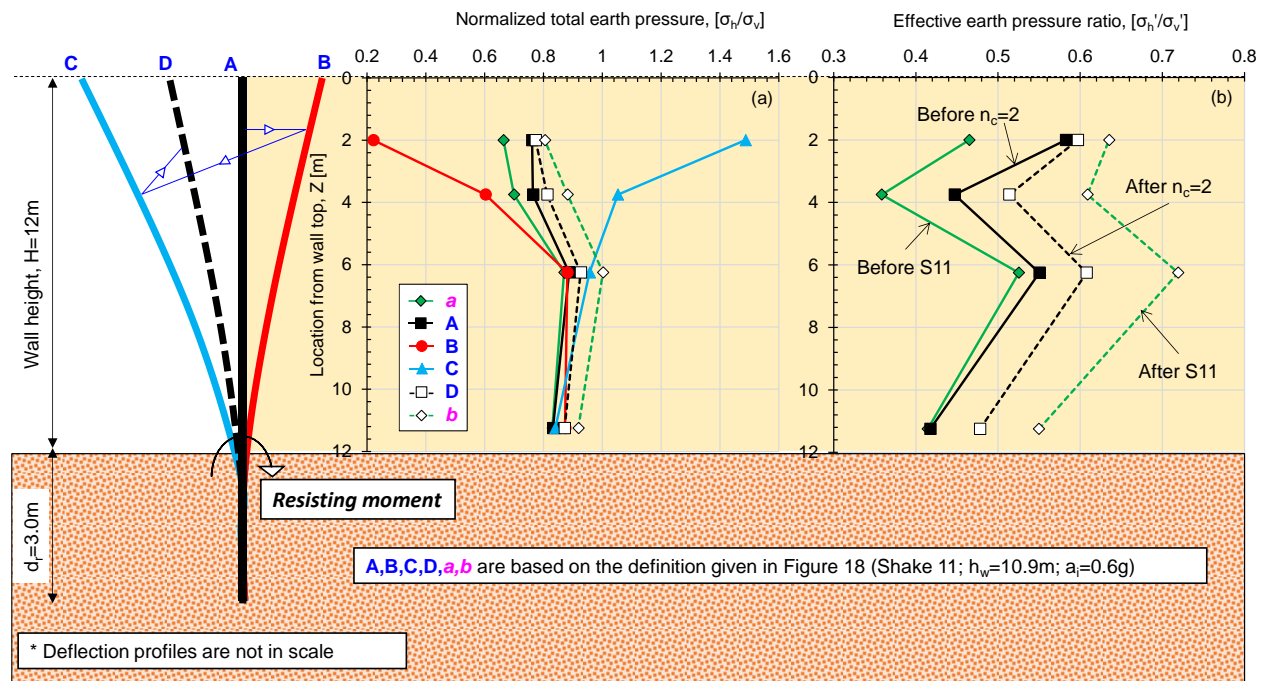


Figure 5.57. Schematic diagram to explain the mechanism of the resilience effect.

When the wall tends to move back to point A from C, due to the redistribution of the effective earth pressure (Figure 5.57b), the wall cannot move back. Instead, the wall remains in point D, thus creating a residual displacement. This increase in earth pressure from point A to D (Figure 5.57b) with the increase of residual displacement is often termed the 'ratcheting effect' (Hirakawa *et al.*, 2006; Tatsuoka *et al.*, 2003). However, the amount of ratcheting effect is influenced by the elastic resilience of the wall. Large elastic resilience can be expected for high-stiffness walls embedded into stiff ground, which could increase the earth pressure significantly with the increase of residual

displacement (points *a* and *b* in Figure 5.57b). Some exceptions to this behaviour can be observed during Shakes 7 and 8 at $Z=2.0\text{m}$, where no ratcheting effect occurs, which could be due to the significant resilience effect at the deeper depth (Figure 5.54). Based on the discussion above, in this study, the term ‘(elastic) resilience effect’ is used instead of ‘ratcheting effect’ to address the variation of the effective earth pressure with the wall displacement, which is caused by the embedded wall elastic resilience. Figures 5.54 & 55 show that the resilience effect can be confirmed even at wall displacement larger than $2\%H$, indicating the presence of secured rock-wall confinement conditions. Also, after the final loading, the $(\sigma'_h\sigma'_v)$ more than the design pressure (active pressure, K_a) can be confirmed due to the resilience effect. It suggests that designing the wall using active or K_0 earth pressure might lead to underestimating the force acting on the wall.

5.5.10 Use of active lateral pressure for the design of high-stiffness CSTP wall embedded into stiff ground.

In the design of an embedded retaining wall, active earth pressure is used for the structural design. Based on the sequential loading condition adopted in this research, the lateral pressure acting on the wall could be much larger than the active condition (Figure 5.54). Due to the resilience effect, the lateral earth pressure becomes much larger than the at-rest pressure, as shown in Figures 5.35, 5.36 and 5.54. For larger embedment depth, the observed earth pressure was larger than the smaller embedment depth. To investigate this point further, a p-y analysis was conducted by assuming the bi-linear p-y curve explained in section 4.2.3. In this analysis, design condition was assumed for the p-y curve, i.e., only using lateral spring (Model 1).

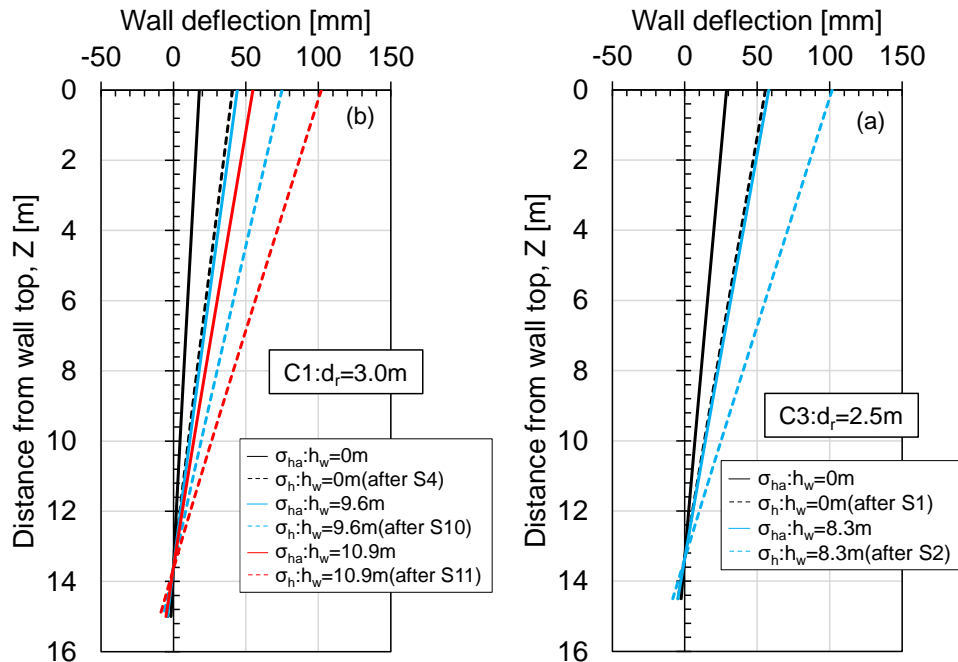


Figure 5.58: Wall deflection variation (a) Case 1 ($d_r=3.0\text{m}$) (b) Case 3 ($d_r=2.5\text{m}$).

The total active earth pressure was calculated for different water levels mentioned in **Table 5.2** for Cases 1 and 3. The measured total lateral pressure after shake 4, shake 10 and shake 11 from Case 1 and shake 1, shake 2 from Case 3 was used for comparison. The lateral pressures were used as the distributed load on the 12-meter-long pile with socketing depths of 3.0 and 2.5m. The observed deflection profile from the p-y analysis is shown in Figure 5.58.

It can be confirmed that using the active earth pressure will underestimate the wall displacement. In the case of larger embedment depth, the wall displacement could be underestimated by about 45% at larger water level. In the case of smaller embedment depth, the underestimation of the wall displacement could be about 40% at a water level of 8.4m. The resilience effect could be significant for high-stiffness walls embedded into stiff ground under sequential loading. Therefore, based on this particular loading sequence and testing condition, the retaining wall designed by assuming active conditions, might underestimate the wall deflection.

5.5.11 Qualitative discussion on CSTP wall deflection behaviour

A qualitative analysis of the wall deflection behaviour of the CSTP wall is presented in this section. Figure 5.59 illustrates that the wall top displacement of a cantilever retaining wall is influenced by three integral components: (1) wall displacement at the rock surface (translation, δ_T), (2) rotational displacement with respect to the rock surface (rotation, δ_R), and (3) bending deflection with respect to the rock surface (bending, δ_B).

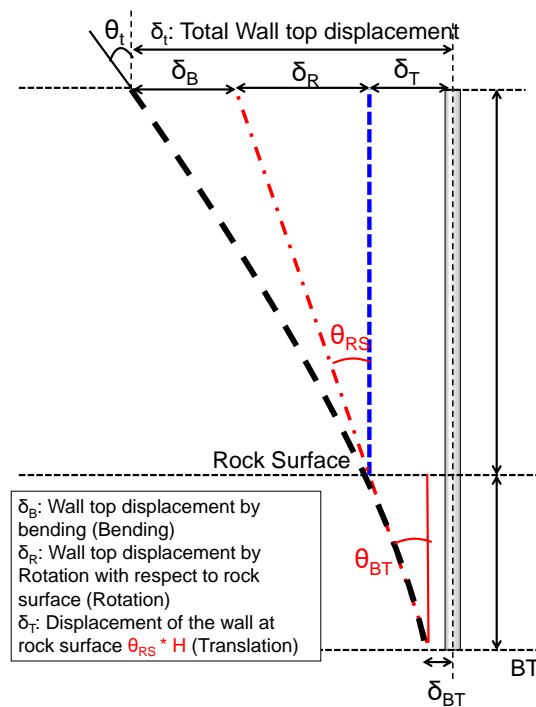


Figure 5.59: Different components contributing to the wall deflection.

The wall deflection was calculated by using the Euler-Bernoulli theory, i.e. by double integrating the bending moment and using the measurements from two top LDTs as boundary conditions. To obtain a uniform qualitative bending moment diagram, the measured bending moment diagram was modified due to its susceptibility to various influencing factors. Figure 5.60 displays the modified and actual bending moment distributions for Case 1 And Case 3. In Case 1, the bending moment at the modified locations was obtained through linear extrapolation, while for Case 3, a polynomial line was used to determine the bending moment distribution in the top half of the wall. In both Cases, the moment load remained consistent.

Based on the bending moment distribution shown in Figure 5.60, the calculated bending deflection is depicted in Figure 5.61. The deflection profile is presented on an absolute scale rather than as increments. It was observed that the wall deflection increased with the progression of the loading sequence. The wall deflection measured at the wall toe was approximately 47mm and 80mm for Case 1 and Case 3, corresponding to approximately 0.9mm and 1.6mm in the model scale.

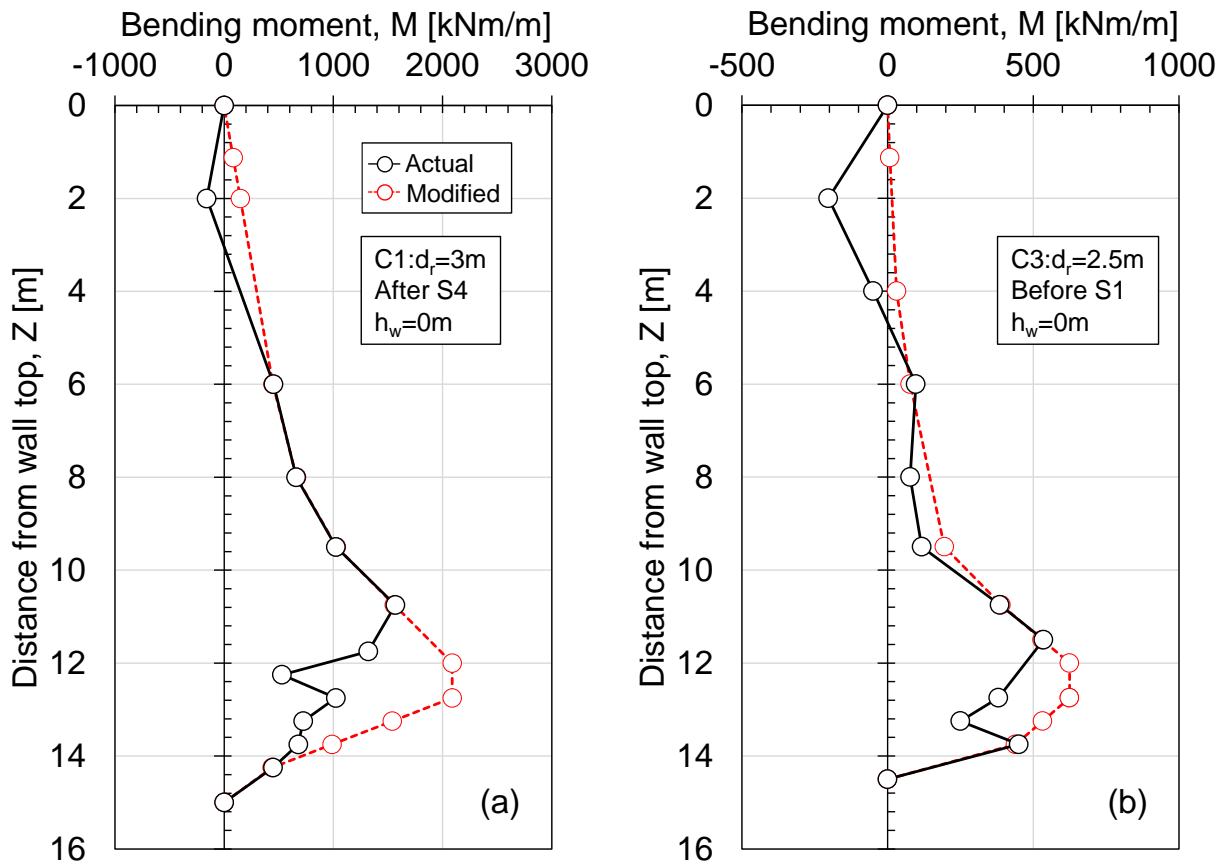


Figure 5.60: An example of qualitative bending moment distribution with depths (a) CASE 1 (d_r=3.0m) and (b) CASE 3 (d_r=2.5m).

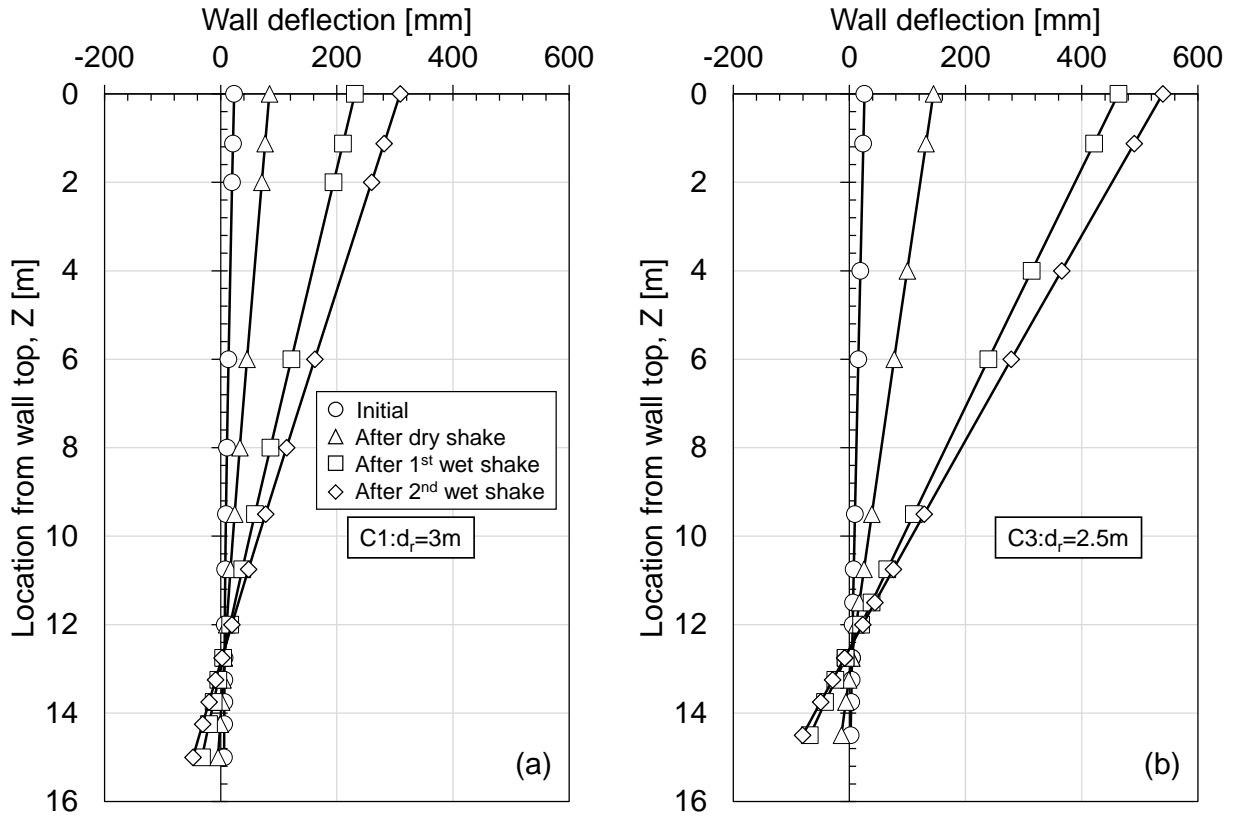


Figure 5.61: Wall deflection profile (a) Case 1 (d_r=3.0m) (b) Case 3 (d_r=2.5m).

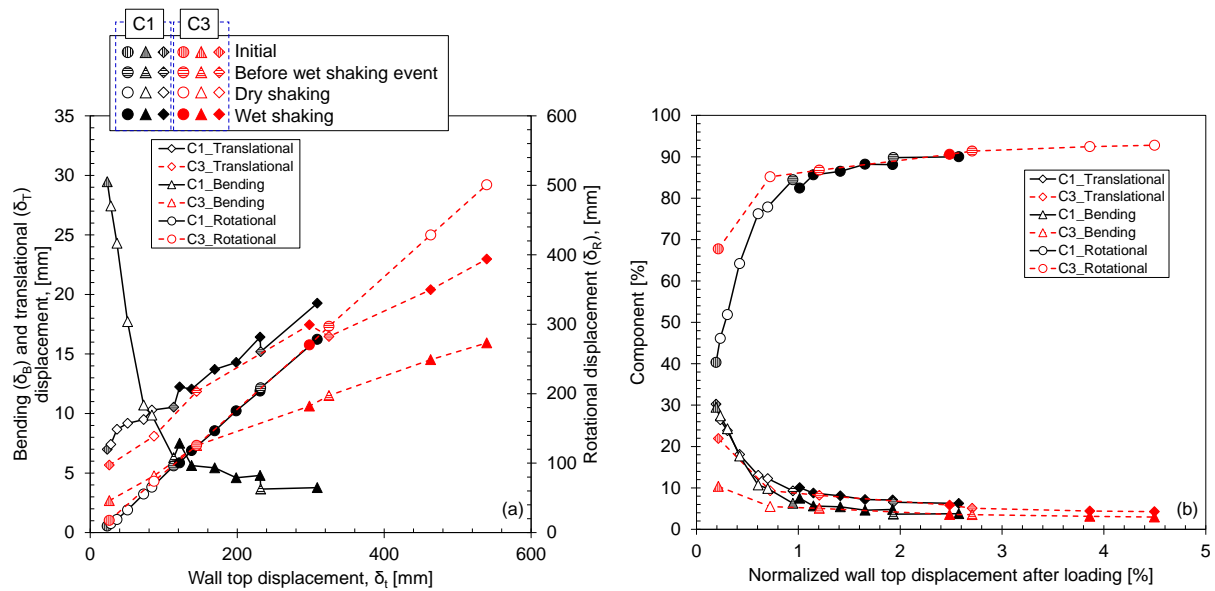


Figure 5.62: (a) Variation of different displacement components with wall top displacement (b) contribution of different components to the wall top displacement.

Figure 5.62(a) demonstrates the different components contributing to the wall top displacement based on the wall deflection profile. The percentage contribution of each component to the wall top displacement is depicted in Figure 5.62 (b). Initially, for Case 1, the wall top deflection was primarily influenced by rotation (40%), bending (30%), and translation (30%). In contrast, for Case 3, it was dominated by rotation (68%), followed by translation (22%) and bending (10%). Therefore, a change in embedment depth of 0.5m (25% Φ) could increase the rotational component by 1.5 times. In Case 1, a significant increase of approximately 40% was observed in the rotational component after dry shaking. Subsequently, the rotational component did not experience significant changes in the later loading. Similar observations were made in Case 3. However, in both Cases, the ultimate condition could be characterized by wall rotation with respect to the rock surface, followed by translation and bending. This behaviour suggests that reducing the embedment depth would cause the wall to exhibit more rigid behaviour rather than flexible.

5.5.12 Effect of backfill soil on the stability and the failure mechanism of the CSTP wall:

Comparing the simple pile wall model and the CSTP wall model, the simple pile wall model showed wedge-type failure, but in the case of the CSTP wall model, although the wall displacement was more than 4%H, especially for 2.5m embedment depth, no catastrophic failure was observed. The presence of overburden pressure might affect this observation. However, as shown in **Table 5.6**. Based on this model condition, the presence of overburden pressure from the retaining soil might not significantly affect the stability of this structure. It can be seen that the presence of overburden pressure can only increase the factor of safety by about 5% for different embedment conditions. On the other hand, this difference becomes even smaller if the contribution of the base shear is considered. Also, in the p-y analysis, the overburden pressure can only affect the ultimate condition. Therefore, it can be said that for this particular model condition, the effect of overburden pressure from the retained soil will be negligible.

Table 5.6 Variation of the factor of safety with and without backfill condition

		$h_w=0m$			$h_w=12m$		
		Without backfill	With backfill	%	Without backfill	With backfill	%
$d_r=3m$	Without Base shear	2.5	2.6	5.07	0.68	0.71	5.33
	With base shear	3.85	3.90	1.15	1.03	1.04	0.59

$d_r=2.5m$	Without Base shear	1.84	1.94	5.06	0.49	0.52	5.58
	With base shear	2.94	2.97	0.78	0.79	0.79	0.41

In the case of the development of the failure plane, the presence of overburden pressure could increase the normal stress acting on the failure plane. Thus, it could improve the shear strength along the failure plane. This might prevent the ultimate failure of the retaining structure.

A simple FEM analysis was carried out to investigate the effect of the backfill soil on the failure mechanism. The model condition mentioned in Figure 5.7 was used with the model dimension similar to the simple pile wall loading test. However, in the new model, backfill soil is considered. In the FEM analysis, the backfill soil was modelled as hardening soil with the parameters mentioned in **Table 5.7**. The parameter for the sand was determined from the empirical relationship given by Brinkgreve et al. (2010). A similar loading condition was used, as mentioned in section 4.2.2.1. The FEM analysis was carried out for the embedment depth of 3m.

Table 5.7: Parameters used to define sand layers

Parameters	Units	Value
Unsaturated unit weight, γ_{unsat}	kN/m ³	15.8
Saturated unit weight, γ_{sat}	kN/m ³	19.4
Initial stiffness, E_{50}	kN/m ²	48900
Relative density, D_r	%	81
Minimum void ratio, e_{min}	-	0.6
Maximum void ratio, e_{max}	-	0.966
Specific gravity, G_r	-	2.635
Power(m)	-	0.445
R_{inter}	-	1

The variation of the principal total stress at an imposed displacement of 1% Φ and 7.5% Φ for with and without backfill conditions is shown in Figure 5.63. No significant difference was confirmed in the principal total stress variation. This can also be confirmed by the only 5% difference in the

factor of safety mentioned in **Table 5.6**. So, in terms of total stress, the presence of backfill soil does not significantly affect it. However, in the CSTP wall model, no catastrophic failure was observed, although the wall top displacement was more than the allowable displacement given for level 2 seismic motion. However, in the simple pile wall loading test, wedge-type failure was observed in the ultimate condition. This observation could be explained by the variation of the shear strain, as shown in Figure 5.64. In the case of the wall without backfill soil, the shear strain accumulates near the rock surface at a small imposed displacement. However, at larger imposed displacement, the shear strain accumulates near the rock surface and the wall toe. The influence zone of shear strain at the wall base increased towards the backward direction, and the zone was also moving towards the surface. However, in the Case of the wall with backfill, a large shear strain was concentrated at the rock-sand interface. Also, the shear strain was larger in the backfill as the soil was deformed due to the wall movement. However, comparing Figure 5.64 (b) with 5.64 (d), at the wall, the shear zone did not move towards the backward direction for the wall with backfill. Based on Figure 5.64, it can be said that the presence of backfill soil or the overburden pressure could prevent the wedge-type failure, and the critical condition could be the sand rock interface.

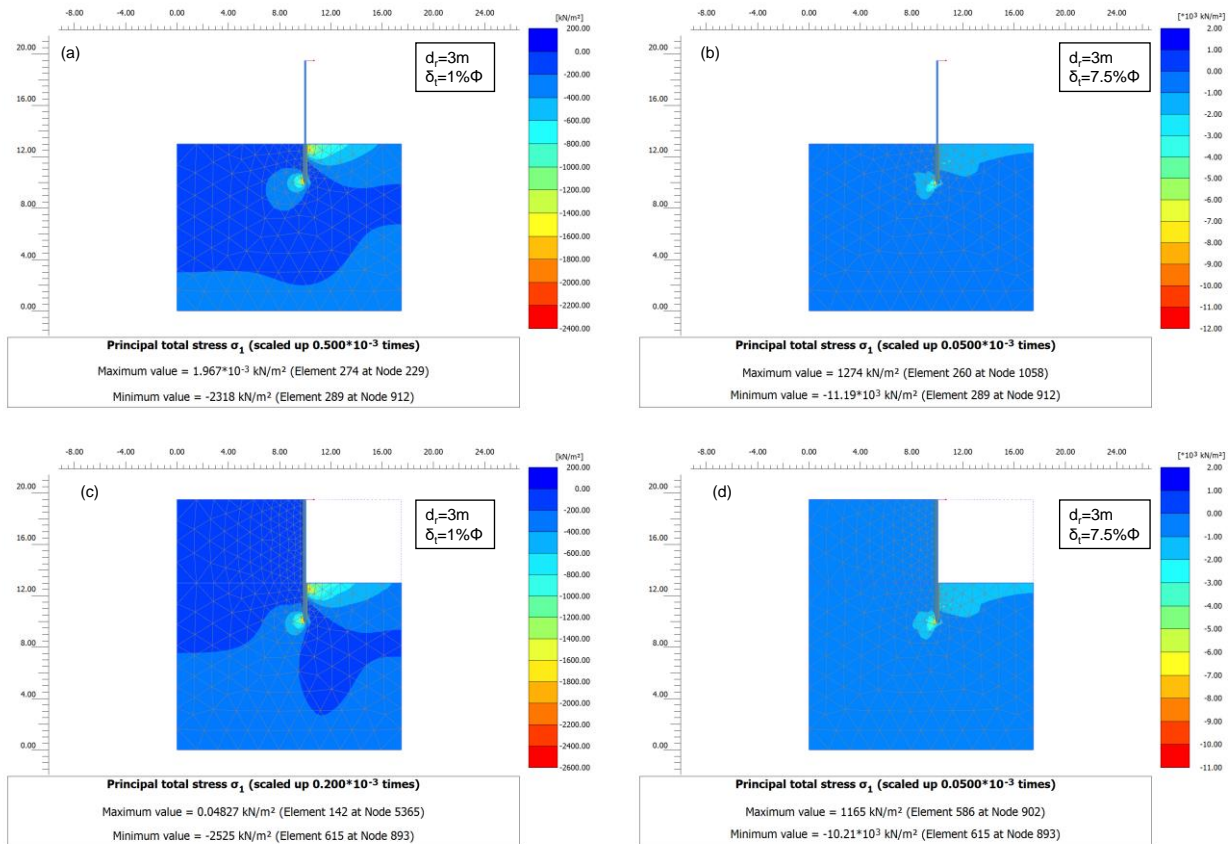


Figure 5.63: Variation of the principal total stress (a,b) without backfill (c,d) with backfill.

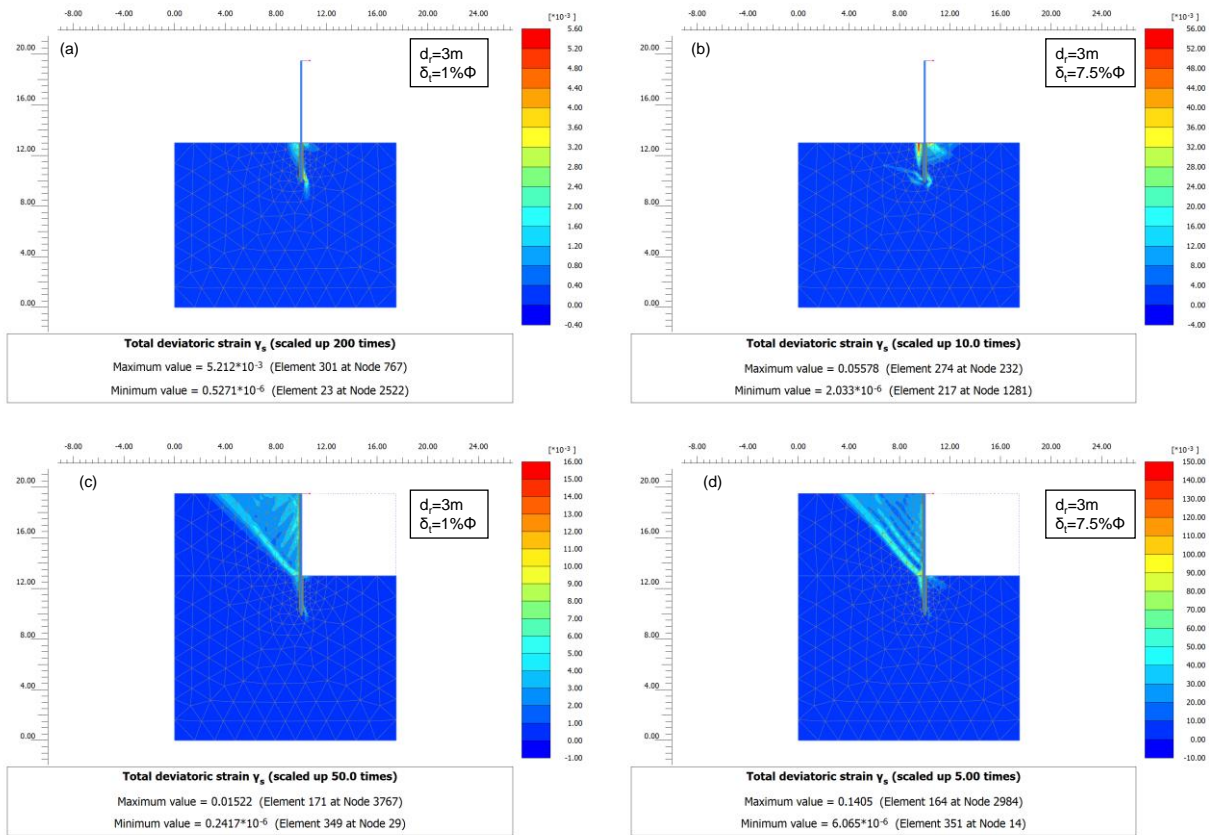


Figure 5.64: Variation of the shear strain (a,b) without backfill (c,d) with backfill.

5.5.13 Long-term behaviour of CSTP wall

For unpropped walls, the long-term behaviour of the wall can significantly affect the wall stability and displacement behaviour (Gaba et al., 2017). Due to the uncertainty about the long-term behaviour of the wall, cantilever-type retaining walls are often excluded as permanent structures by engineers. Based on Figures 5.24-25, the change of long-term residual component of wall top displacement, lateral pressure, and the bending moment can be confirmed. A typical variation of the long-term residual displacement, lateral pressure at $Z=2m$ and $11.25m$, and the bending moment at $Z=10.75m$ immediately after the shake and after the end of the water supply with time are shown in Figure 5.65-66 for Case 1 and Case 3, respectively. In the case of wet shaking, the variation of the pore water pressure is also shown in this figure. The increment of long-term time (t_l) is taken based on the definition shown in Figure 5.14 (a). In the case of dynamic loadings, on average, 5 minutes (± 2 minutes) were spent for each shaking. Typically, the increment in the displacement can be characterised as “creep”. This long-term creep effect could significantly affect the wall stability, which, in the worst-case scenario, leads to creep failure.

In Figures 5.65&66, the variations of δ_t , σ_h at $Z=2m$ and $11.25m$, and the bending moment at $Z=10.75m$ with time after loadings (t_l) are shown for the dynamic loadings (Shakes 4&11) and the

static loadings (WR1 and WR2) respectively. The increment of displacements by creep can be seen for all loadings. However, the magnitudes of creep displacement are very small, which are negligible compared to the displacements during the loading, except for WR1, as shown in Figure 5.65c&5.66c. In contrast, the σ_{hs} and bending moment decrease after loadings, as seen in Figures 5.24-27. The mechanism of creep after loading is explained in Figure 5.67. The earth pressure decreases with the forward movement of the wall until no further decrease occurs, which can be considered as creep failure. Due to the resilience effect, earth pressure more than at rest pressure can be observed (Figure 5.54). However, the forward displacement of the wall by the creep induces the reduction of earth pressure from the relatively large value caused by the resilience effect. However, the reduction of earth pressure can be expected until the wall reaches to the active condition. Also, as the earth pressure decreases, the load acting on the wall will also decrease. Then, this reduction of earth pressure prevents the creep displacement. However, in WR1, the resilience effect developed by the previous dry loadings was diminished significantly by the large water rise. The earth pressures close to active condition (Figure 5.54) do not cause further decrease, and a relatively large creep displacement takes place after the loading. However, in WR2, with the small h_w increment, the previously developed resilience effect remains, resulting in the decreases of σ_{hs} and the minor creep displacement. From the discussion above, it can be inferred that the effect of long-term creep displacement of the wall is less severe for the dynamic loading than the static loading due to the resilience effect, and no creep failure occurred. Also, no significant effect of the embedment depth can be confirmed from Figures 5.65 & 66.

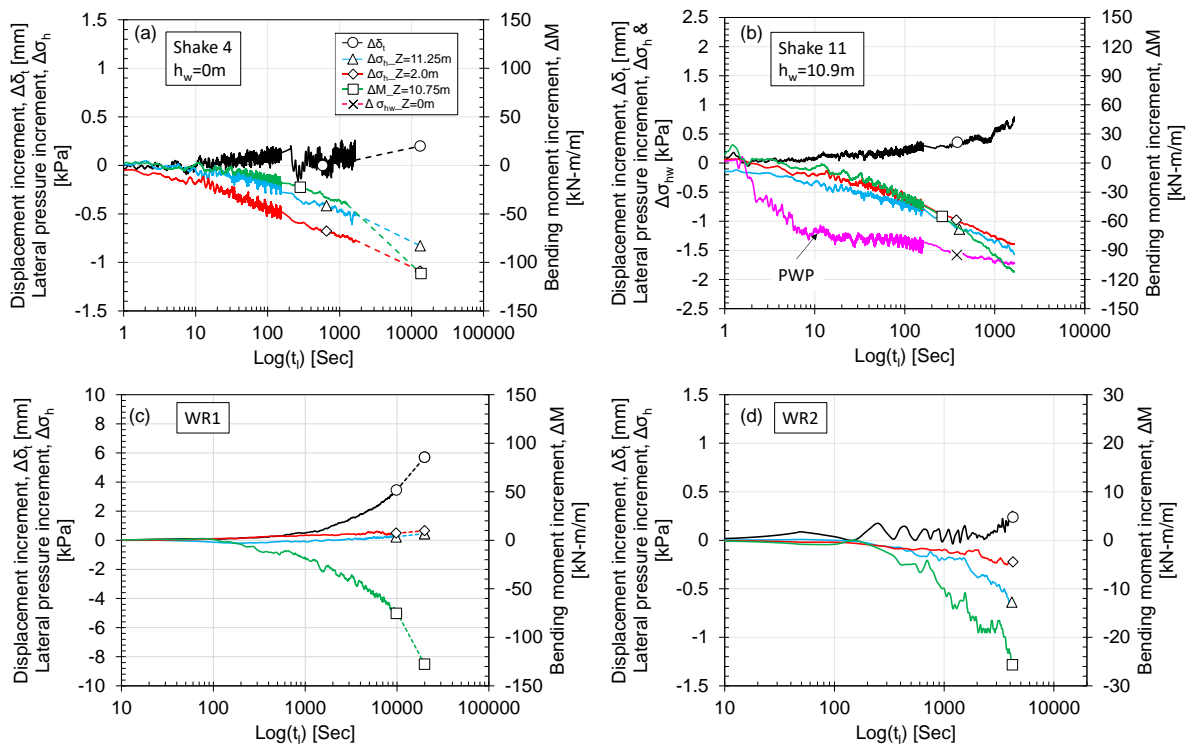


Figure 5.65: Variation of long-term residual component of wall top displacement, lateral pressures and bending moment with time for Case 1 (a) Shake 4; (b) Shake 11; (c) First water rise; (d) Second water rise.

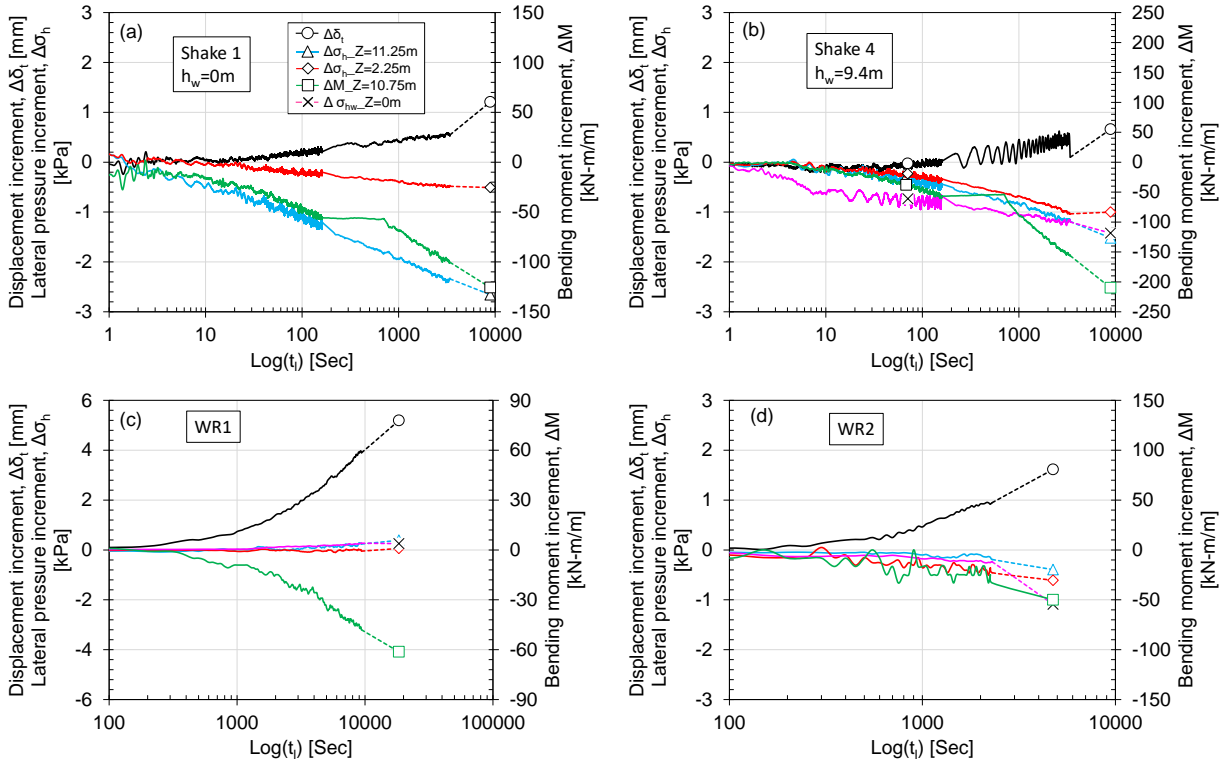


Figure 5.66: Variation of long-term residual component of wall top displacement, lateral pressures and bending moment with time for Case 3 (a) Shake 1; (b) Shake 4; (c) First water rise; (d) Second water rise.

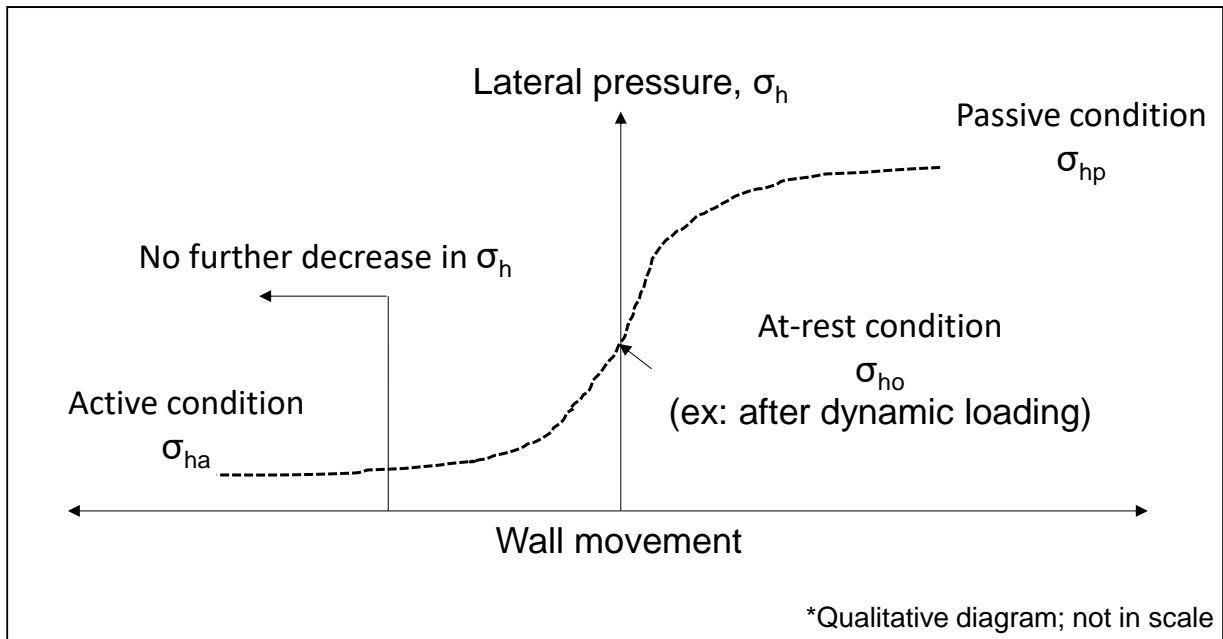


Figure 5.67: Schematic diagram for the mechanism behind the creep.

5.5.13.1 Long-term behaviour after dynamic loading:

Figures 5.68 and 5.66 summarise the increment or decrement of the kinematic (during shaking) and the long-term residual component of wall top displacement, the bending moment at $Z=10.75\text{m}$ and lateral pressure at $Z=11.25\text{m}$, 6.25m , 3.75m , 2m . White noise measurement is considered to determine the long-term increment or decrement more precisely. As shown in Figures 5.68 (a) and 5.69 (a), the increment during and long-term residual was always positive in the Case of wall top displacement. On the other hand, the increment of bending moment was positive during shaking but negative after shaking. In the case of lateral pressure at a deeper depth, a similar observation could be made. However, at shallower depths, the lateral pressure showed different trends, especially during Case 1, which can be confirmed by the effective earth pressure variation shown in Figures 5.35 and 5.54. After final loading, the decrement in bending moment was larger for smaller embedment depth than the larger embedment depth. A similar observation could be made for final loading in dry conditions. Based on Case 1, for sequential dynamic loading by a gradual increase of the amplitude of input motion, the long-term trends showed almost constant trends with the input motion. In Case 1, after dry shake 3, the long-term residual displacement was larger than the later dry shaking. In the case of bending moment, during dry shake 3 of Case 1, the long-term decrease in bending moment was larger than the bending moment during shaking.

To summarize the behaviour, the ratio of the long-term to during shaking is plotted against the input motion as a percentage in Figure 5.70. The positive ratio means the increment both during shaking and in the long term. However, a negative ratio means there may be a decrease during shaking or in the long term.

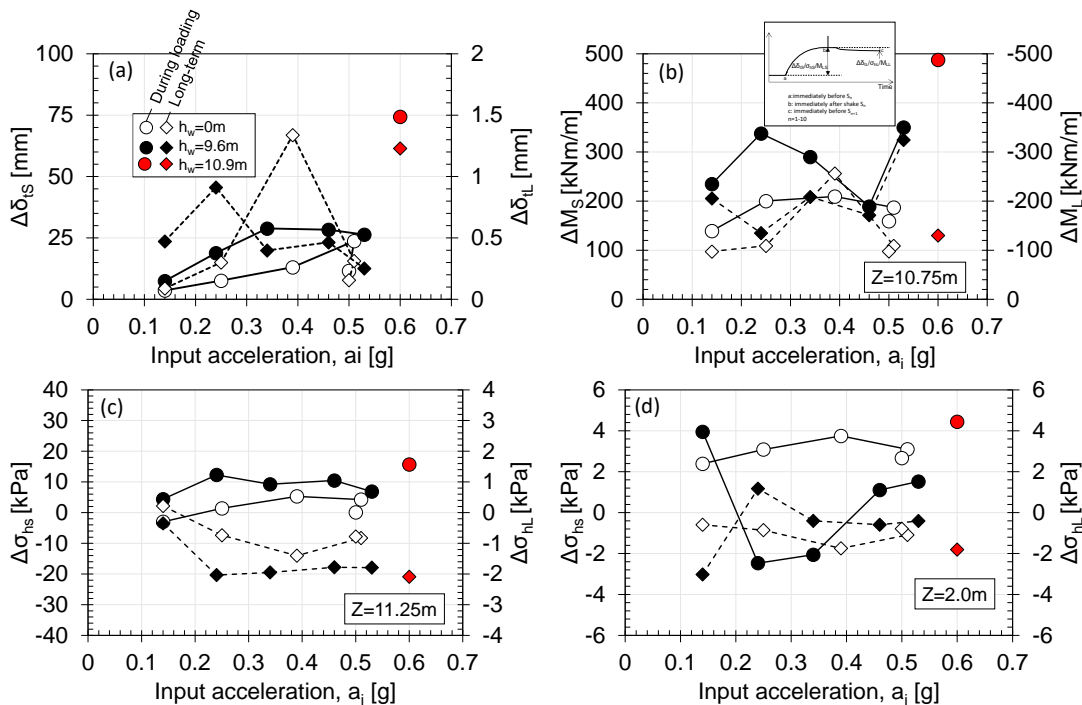


Figure 5.68: Increment during loading and long-term during dynamic loading from Case 1 (a) wall top displacement (b) bending moment at $Z=10.75\text{m}$ (c) lateral pressure at $Z=11.25\text{m}$ (d) lateral pressure at $Z=2.0\text{m}$

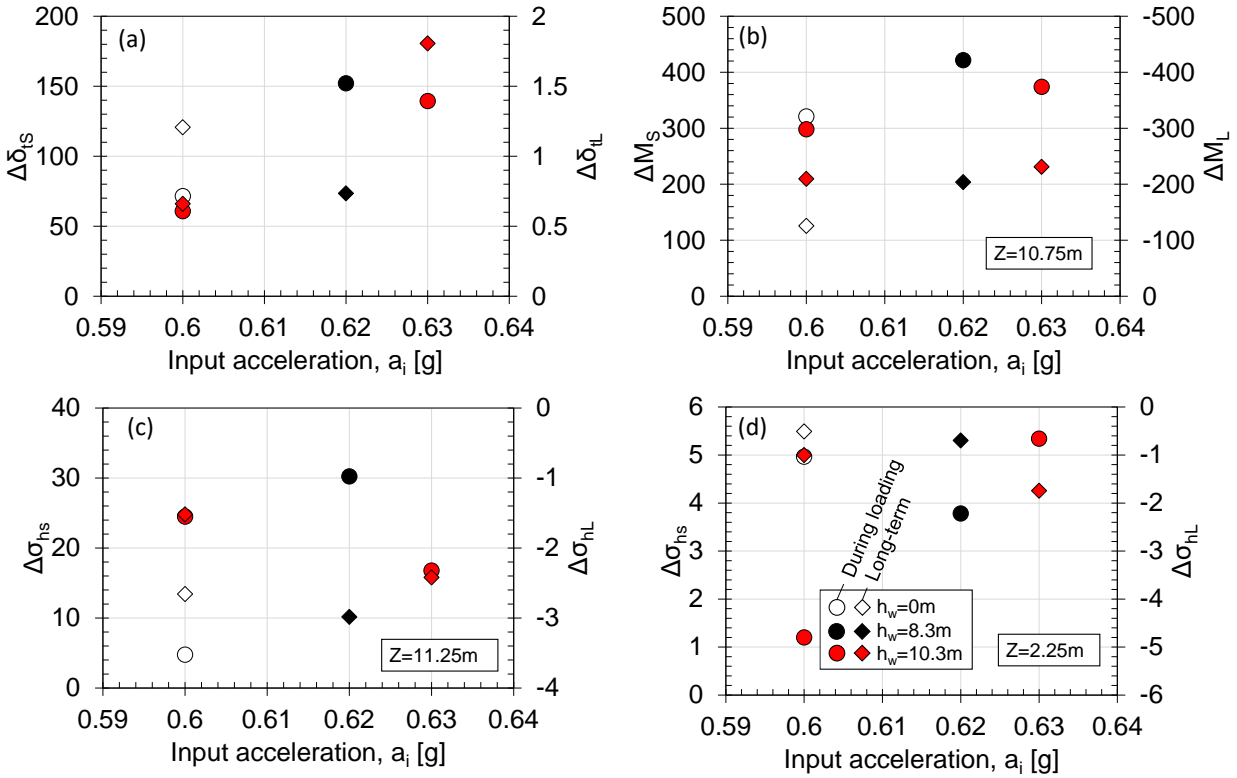


Figure 5.69: Increment during loading and long-term during dynamic loading from Case 3 (a) wall top displacement (b) bending moment at $Z=10.75\text{m}$ (c) lateral pressure at $Z=11.25\text{m}$ (d) lateral pressure at $Z=2.0\text{m}$.

As shown in Figure 5.70 (a), in the case of displacement, the ratio of displacement decreases with the increase in the amplitude of the input motion. The larger wall displacement during shaking by large amplitude motion caused the reduction of the ratio. Comparing the final shaking from CASE 1 (shake 11) with the shake from Case 3 (where large amplitude motion was applied), the ratio of displacement remains the same. During the dry shake 3 from Case 1, the sudden increase in the ratio was due to the large displacement increment in the long term. Also, as observed in Figure 5.70 (b), the ratio of the bending moment was more than 100%, which means the resilience effect was completely neutralized, which caused the larger long-term displacement. Comparing the final dry shake from Case 1 with Case 3 and the final shaking after the second water rise from Case 1 and Case 3, it was observed that the ratio of the bending moment was smaller in CASE 1 than in Case 3. Due to the smaller resilience effect by the smaller embedment depth, the reduction of the resilience effect was larger for the smaller embedment depth. In terms of lateral pressure, overall, the ratio is observed in Figure 5.70 (c) was smaller than the 5.70 (d). This observation indicates that the long-term effect on lateral pressure is more significant at shallower depths than at deeper depths.

Overall, due to the resilience effect, the long-term effect becomes less significant for this particular model and loading conditions.

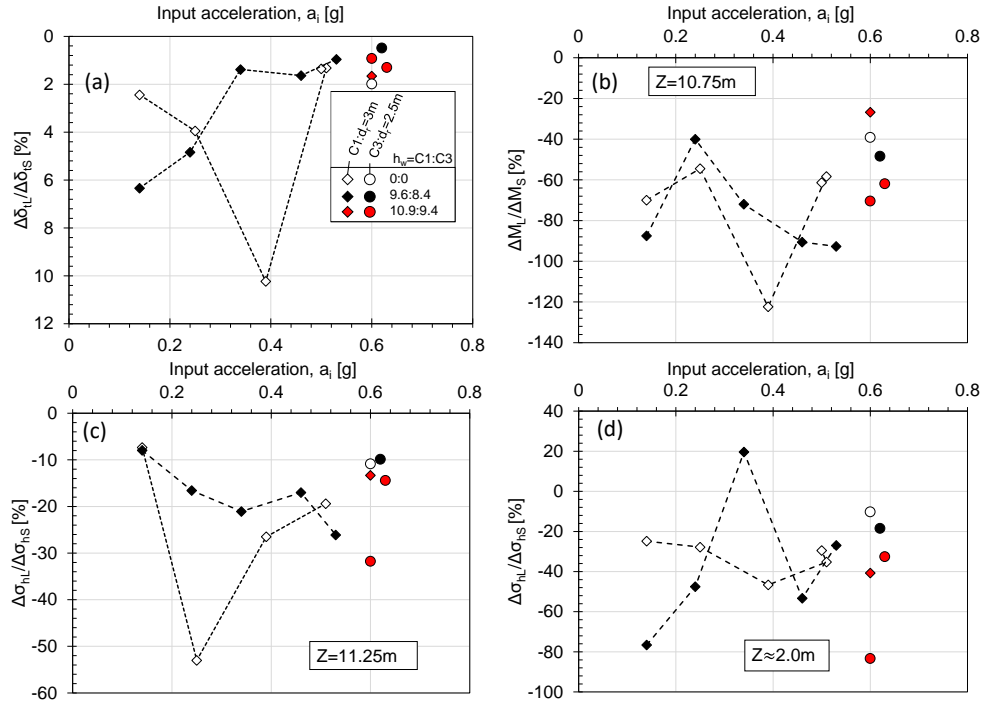


Figure 5.70: Ratio of long-term increment to the increment during shaking (a) wall top displacement (b) bending moment at $Z=10.75m$ (c) lateral pressure at $Z=11.25m$ (d) lateral pressure at $Z=2.0m$.

5.5.13.2 Long-term behaviour after static loading:

To discuss the long-term behavior after static loading, the increment of wall top displacement from Case 1 and Case 3 is plotted against the logarithmic time in Figure 5.71. Similarly, the variation of wall top displacement at constant water level from the 2D plate wall model reported by Kunasegaram and Takemura (2021) is plotted in this figure. It was observed that the long-term displacement from the 2D plate wall model was larger than that of the CSTP wall model. Also, the long-term displacement was larger for smaller embedment depth than for larger embedment depth, which was confirmed from both model tests. In the Case of the 2D plate wall model, the long-term displacement of the smaller embedment depth was about 65% larger than the larger embedment depth. On the other hand, in the CSTP wall model, the difference was about 20%. In the 2D plate wall model, a sharp increase in wall top displacement was observed in the later part but not for the CSTP wall model. This sharp increase in displacement indicated that the 2D plate wall model reached the creep rupture point for $d_r=2.5m$. For $d_r=3.0m$, a concave upward trend was confirmed at the beginning and then a linear trend.

The 2D plate wall model reached the active condition when a constant water level was maintained. Also, the water level was larger for the 2D plate wall model than for the CSTP wall model. On the other hand, as observed from Figures 5.36, 5.37 and 5.54, the CSTP wall did not reach the active condition after the end of the first water rise. The earth pressure, which was more than active

conditions at different depths for the CSTP wall model, caused a small wall top displacement increment after static loading. Also, no significant difference was observed for the CSTP wall with $d_r=2.5\text{m}$ and 3.0m , which could be due to the resilience effect.

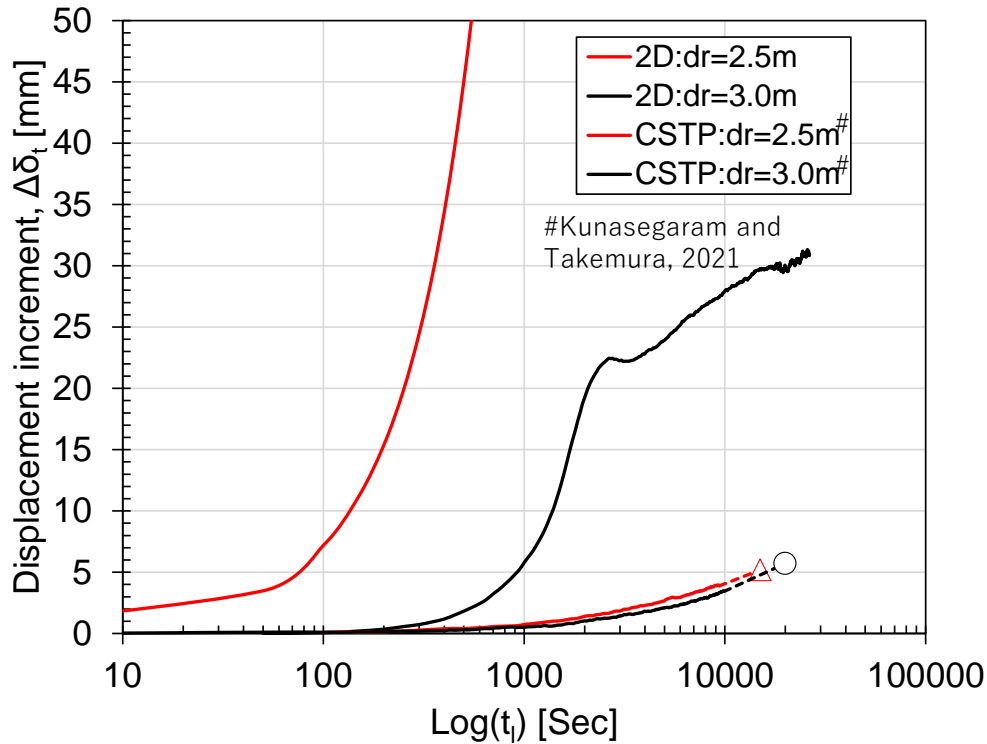


Figure 5.71: Long-term increment in wall top displacement after static loading.

5.5.14 Applicability of bi-linear p-y curve to predict the residual wall displacement after sequential loadings

In this section the applicability of the bi-linear p-y curve discussed in chapter 4 will be studied to predict the residual wall top displacement after dynamic loading. Two types of p-y models were considered similar to chapter 4 (Figure 4.15 & 4.16). In the first p-y analysis, only the lateral spring was used (Figure 4.15) and in the second p-y analysis both lateral and base shear spring was considered (Figure 4.16). The parameter used to calculate the slope of the p-y curve is given in Table 5.7.

In the Lpile model, the pile length above the ground was equal to the retained height of 12m, and below the ground, the height was 3m and 2.5 m, considering Case 1 and Case 3, respectively. The mechanical properties of the pile were the same as given in Table 5.7. The horizontal subgrade reaction (k_H) for Model 1 was calculated using the properties in Table 5.7. The measured earth pressures were considered as distributed load and applied as input load. The moment load from the p-y analysis and the back calculated moment load from the earth pressure was compared to

determine the applicability of the earth pressure as distributed load. Furthermore, the dynamic wall displacement was determined by using earth pressure measured at the time of max. bending moment at $Z=10.75\text{m}$ as input load. Also, the wall displacement was calculated against the commonly assumed active (K_a) and at-rest (K_0) condition at different water level from Case 1 and 3, given in Table 5.2.

Table 5.8: Parameters used to calculate horizontal subgrade modulus of Model-1

Parameters	Unit	Value
Pile diameter, Φ	m	2
Flexural rigidity, EI	kN-m ²	14559073.02
α	-	4
Deformation modulus, E_o [kN/m ²]	kPa	220000
B_{ref}	m	0.3
B_H	m	10

The measured wall deflection from the p-y analysis is shown in Figure 5.72 for embedment depths of 3m and 2.5m. The wall deflection is larger for without base shear condition than with base shear condition. Also, the wall deflection was larger for $d_r=2.5\text{m}$ than 3.0m.

The bending moment distribution obtained from the p-y analysis is shown in Figure 5.75. The bending moment distribution with and without base shear are similar as the input distributed load was similar. However, the bending moment distribution for $d_r=3.0\text{m}$ is larger than $d_r=2.5\text{m}$. Figure 5.74 shows the shear force distribution obtained for $d_r=3.0\text{m}$ and 2.5m under with and without base shear conditions. The mobilised base shear increases with the increase of the load. Also, the mobilised base shear is larger for $d_r=2.5\text{m}$ than $d_r=3.0\text{m}$. The soil reaction profile obtained from the p-y analysis is shown in Figure 5.75. In the soil reaction profile, the depth with constant soil reaction can be considered as yielding depth. The yielding depth is larger for without base shear case than the with base shear case.

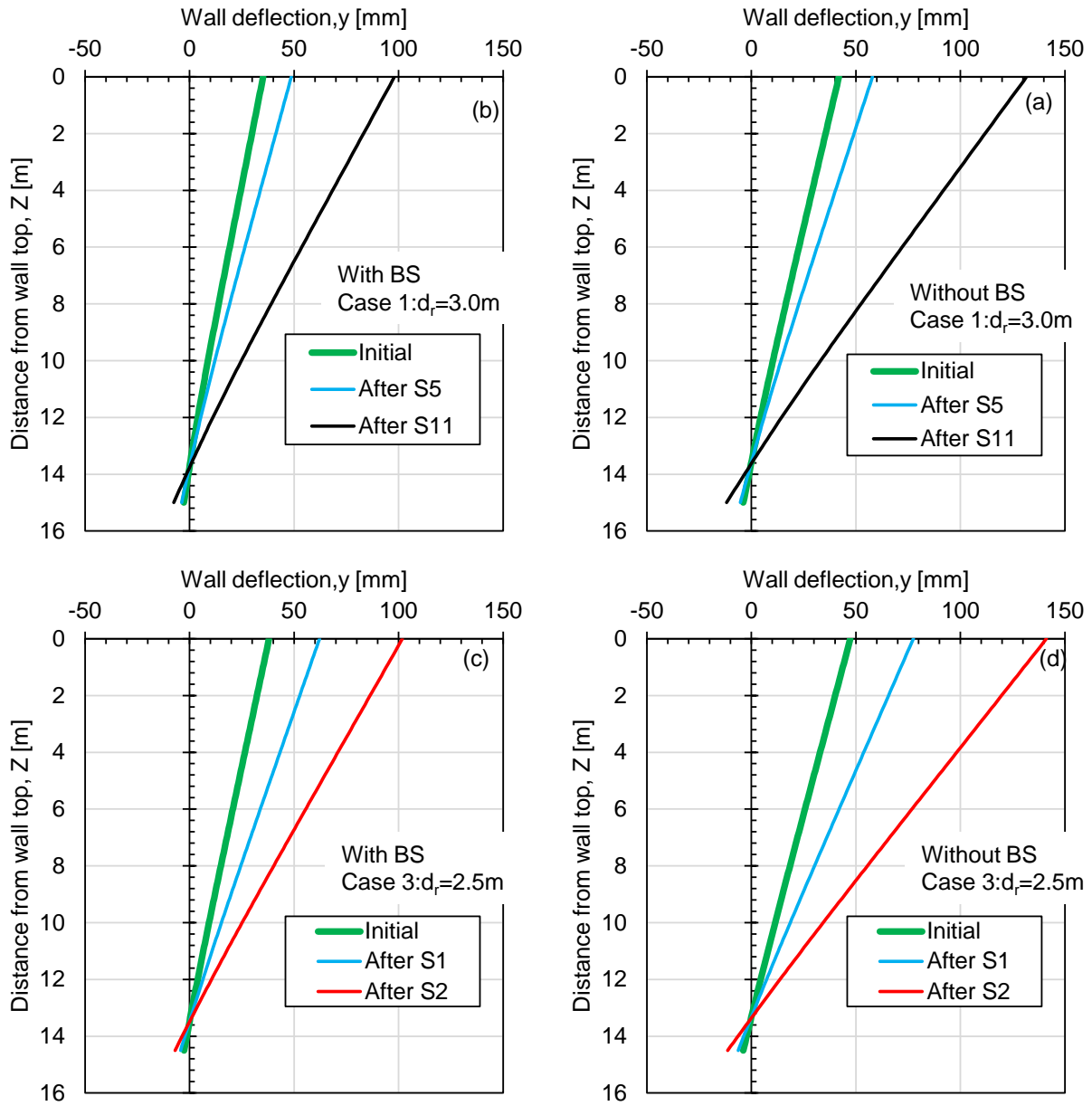


Figure 5.72: Wall deflection obtained from p-y analysis (a,b) Case 1: $d_r=3.0m$ (c,d) Case 3: $d_r=2.5m$.

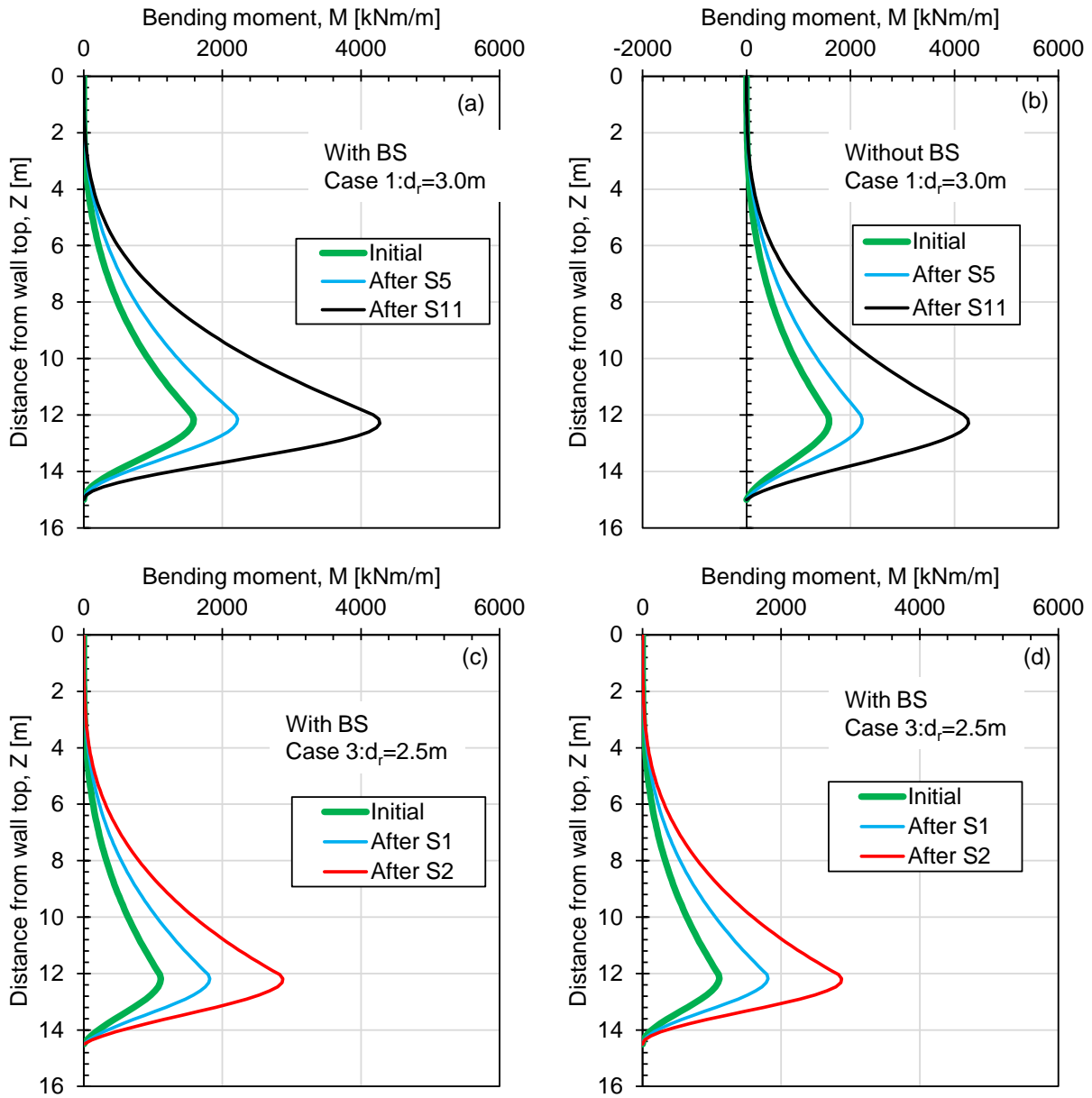


Figure 5.73: Wall bending moment distribution obtained from p-y analysis (a,b) Case 1: $d_r=3.0\text{m}$ (c,d) Case 3: $d_r=2.5\text{m}$.

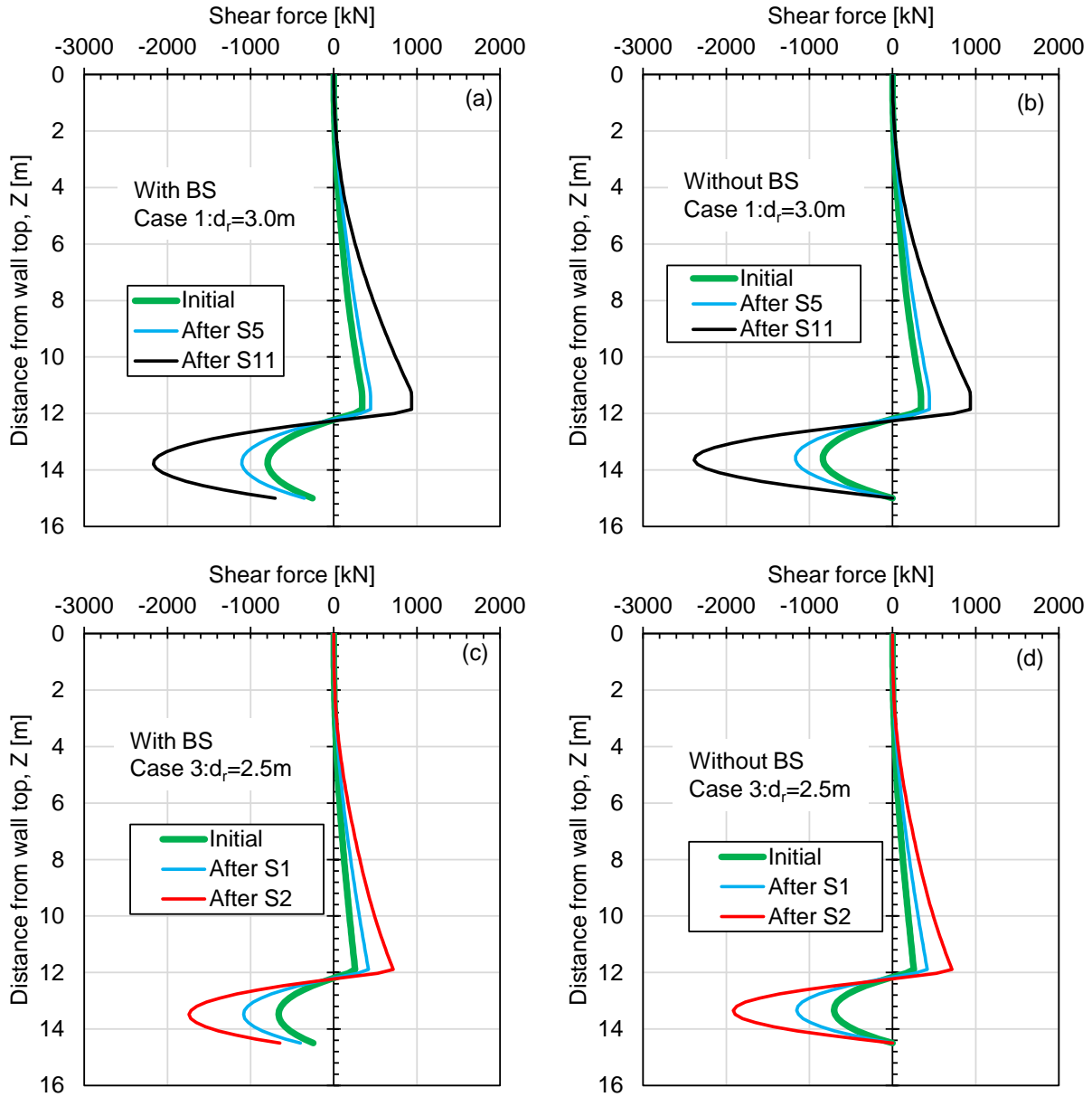


Figure 5.74: Wall shear force distribution obtained from p-y analysis (a,b) Case 1: $d_r=3.0\text{m}$ (c,d) Case 3: $d_r=2.5\text{m}$.

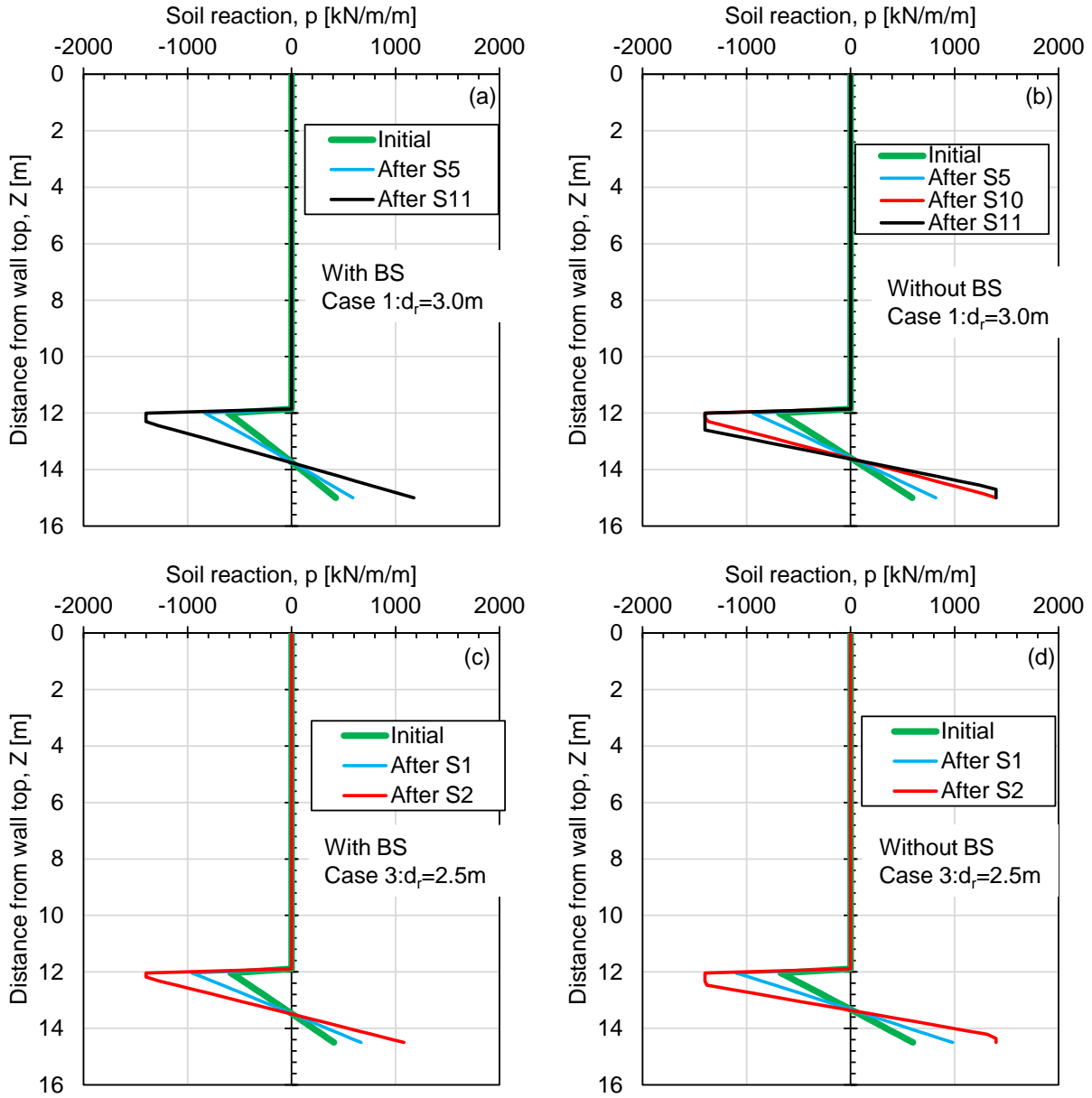


Figure 5.75: Soil reaction profile obtained from p-y analysis (a,b) Case 1: $d_r=3.0\text{m}$ (c,d) Case 3: $d_r=2.5\text{m}$.

Figure 5.76 shows the normalised residual wall top displacement variation with the moment load. For $d_r=3.0\text{m}$, the wall displacement predicted by the p-y analysis provides good agreement with the centrifuge test result, especially up to $M_L=2000\text{ MNm/m}$ or $\delta_t<0.5\%H$. However, for $M_L>2000\text{ kNm/m}$, the centrifuge test result provided a larger displacement than the p-y analysis. This observation suggests that the horizontal subgrade coefficient, K_H , from the centrifuge model gradually decreased by loading with the accumulation of residual displacement. On the other hand, the K_H from the p-y analysis remains constant, resulting in a larger wall top displacement from the centrifuge model than the p-y analysis. For $d_r=2.5\text{m}$, no such behaviour can be confirmed. Also, the p-y analysis fails to predict the wall displacement at a larger load without base shear condition, which could be due to insufficient mobilised resistance of the wall. After the final loading, the p-y analysis predicted a larger wall top displacement than the centrifuge model.

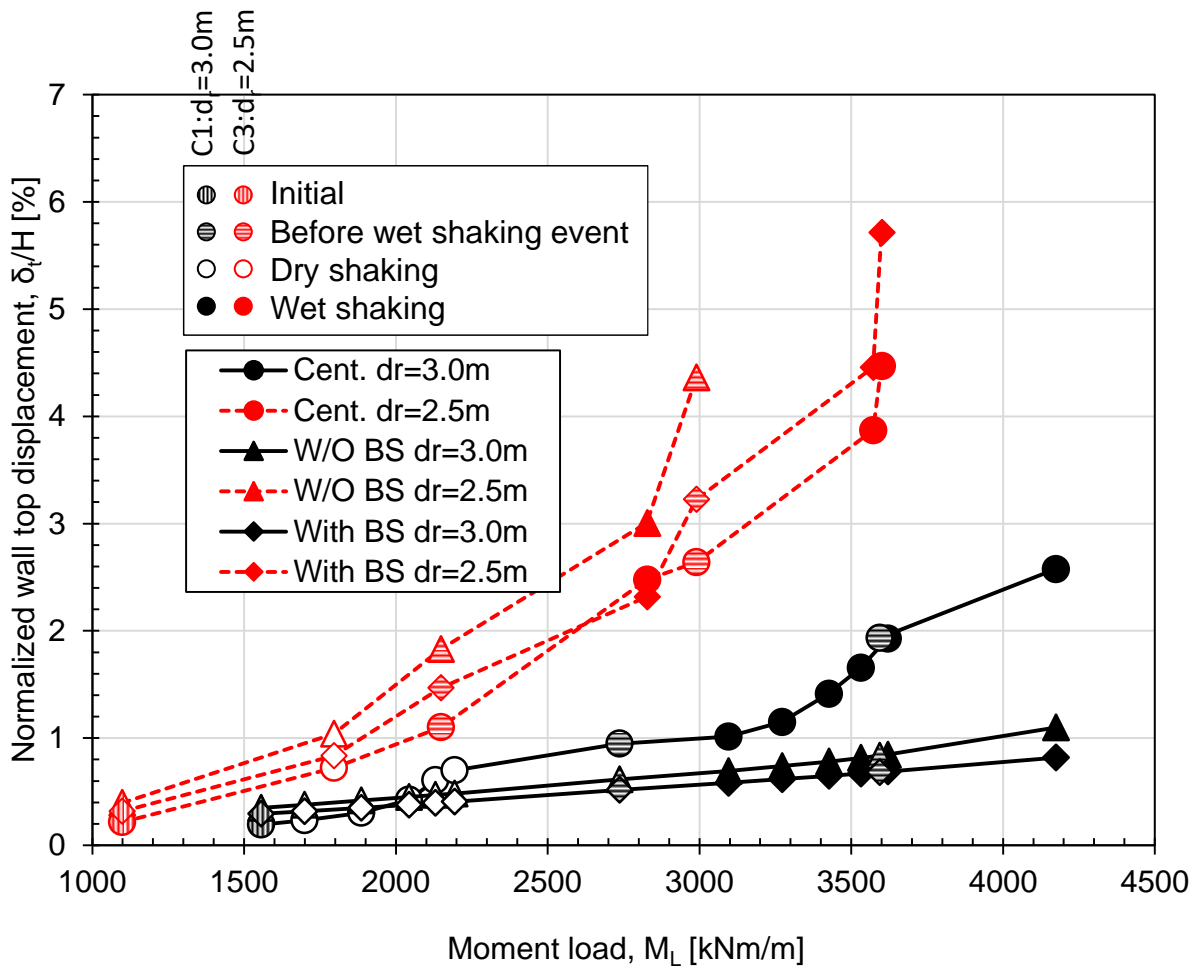


Figure 5.76: Predictability of residual wall displacement after dynamic loading by bi-linear p-y curve.

Dynamic wall top displacement variation is plotted against the input acceleration in Figure 5.77. Only Case 1 is used as it has the maximum loadings, and the dynamic loading was applied by

gradually increasing the amplitude of the input motion. The dynamic wall top displacement from the centrifuge model varied almost linearly with the input acceleration. However, in the p-y analysis, a nonlinear relationship between wall top displacement and input acceleration can be seen for the $h_w=9.6\text{m}$ condition. This observation could be attributed to the uncertainty in the earth pressure measurement, as discussed in 5.5.5.1. The bilinear p-y curve with base shear can predict the wall top displacement with reasonable accuracy up to shake 3 ($a_i=0.4\text{g}$) in dry conditions. However, with the increase of loading history, the centrifuge model showed larger wall top displacement than the p-y analysis due to the reduction of K_H .

Based on Figures 5.76 and 5.77, it can be said that the bi-linear p-y curve could reasonably predict the residual and dynamic wall displacement $\delta_t < 0.5\%H$. As the residual wall displacement increases, the plastic deformation of the rock could reduce the K_H , resulting in a large wall displacement. Therefore, a bi-linear p-y curve with variable K_H based on the plastic deformation could provide a more accurate prediction of the wall displacement. Also, it can be said that the bi-linear p-y curve cannot predict the resilience effect (see section 5.5.9), which occurs during the dynamic loading.

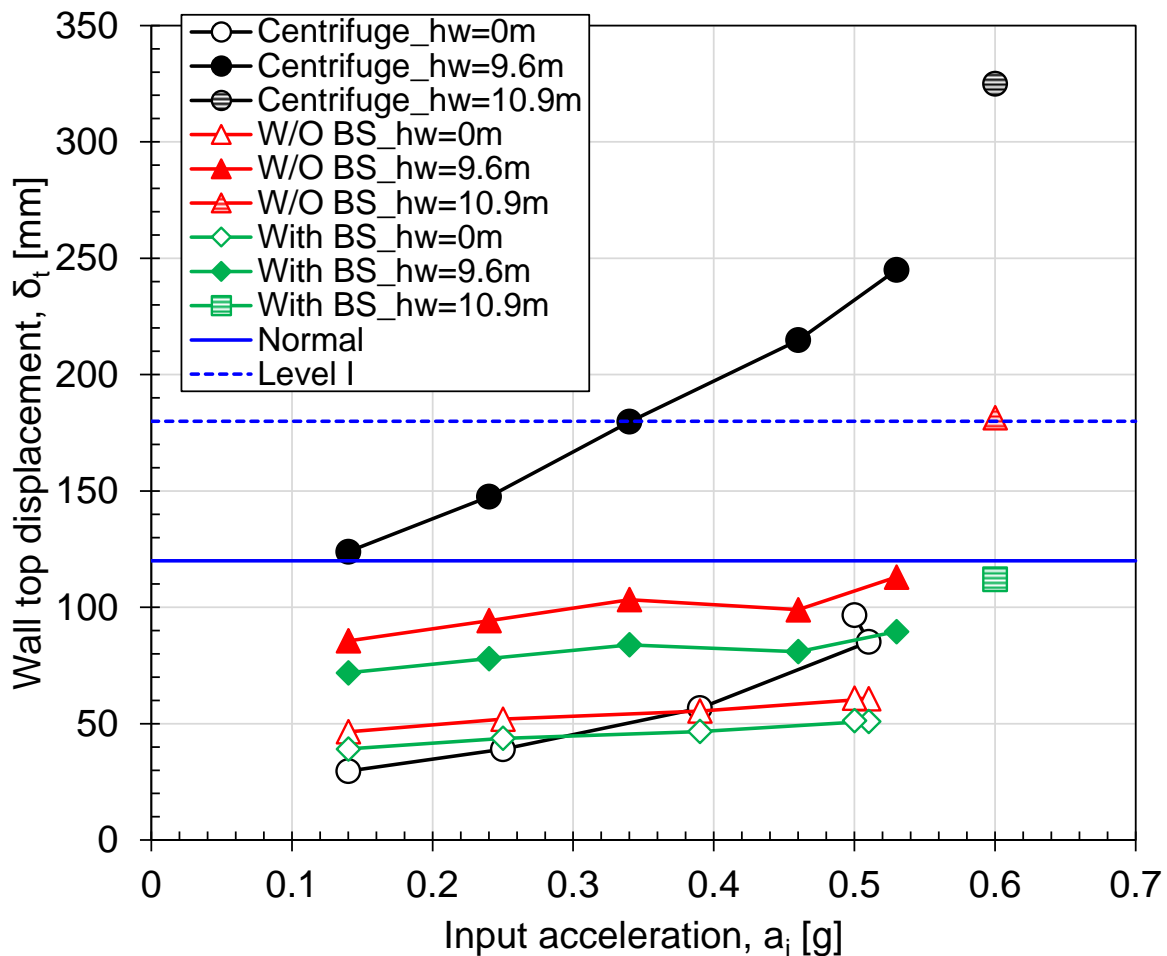


Figure 5.77: Predictability of dynamic wall displacement by bi-linear p-y curve.

From the p-y analysis, the level of plastic deformation or yielding below the rock surface is determined for with and without base shear conditions. Figure 5.78 shows the variation of the rock yielding with the moment load. Also, the variation of the normalised wall top displacement with moment load is shown in this figure. Larger yielding can be seen without base shear conditions than with base shear conditions for $d_r=2.5\text{m}$ and 3.0m . Without base shear condition, both $d_r=2.5\text{m}$ and 3.0m showed about 30% yielding, where the yielding for $d_r=2.5\text{m}$ occurred at a smaller moment load than $d_r=3.0\text{m}$. This observation can be interpreted as smaller the embedment depth, larger the residual displacement, which caused larger plastic deformation of rock. After the final loading, larger yielding can be seen for $d_r=2.5\text{m}$ than $d_r=3.0\text{m}$, with larger wall top displacement for the former than the latter.

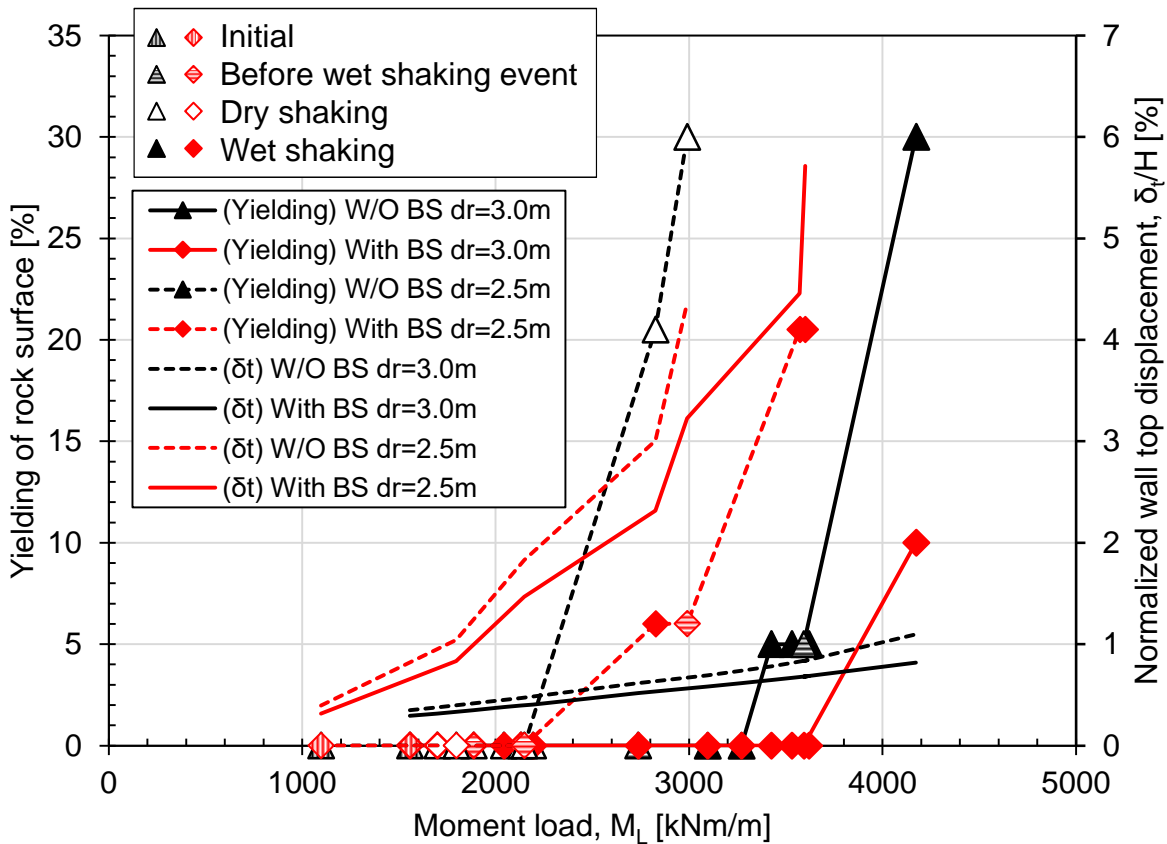


Figure 5.78: Variation of plastic deformation or yielding of rock with moment load.

To further discuss the effect of base shear, the base shear stress (τ) is normalised by the cohesion (c_u) and plotted against the moment load in Figure 5.79 for $d_r=2.5\text{m}$ and 3.0m . The shear force at the base of the wall (Figure 5.74) is divided by the area of the pile to get the τ . The shear stress is then normalised by the c_u . For an identical moment load, the mobilised base shear resistance is larger for $d_r=2.5\text{m}$ than $d_r=3.0\text{m}$. After the final loading, about 40% of c_u is mobilised for $d_r=2.5\text{m}$ and about 32% for $d_r=3.0\text{m}$. Based on the observation from Figure 5.79, it can be said that the

effect of base shear is more significant for smaller embedment depth than for larger embedment depth, which is also confirmed in Chapter 4.

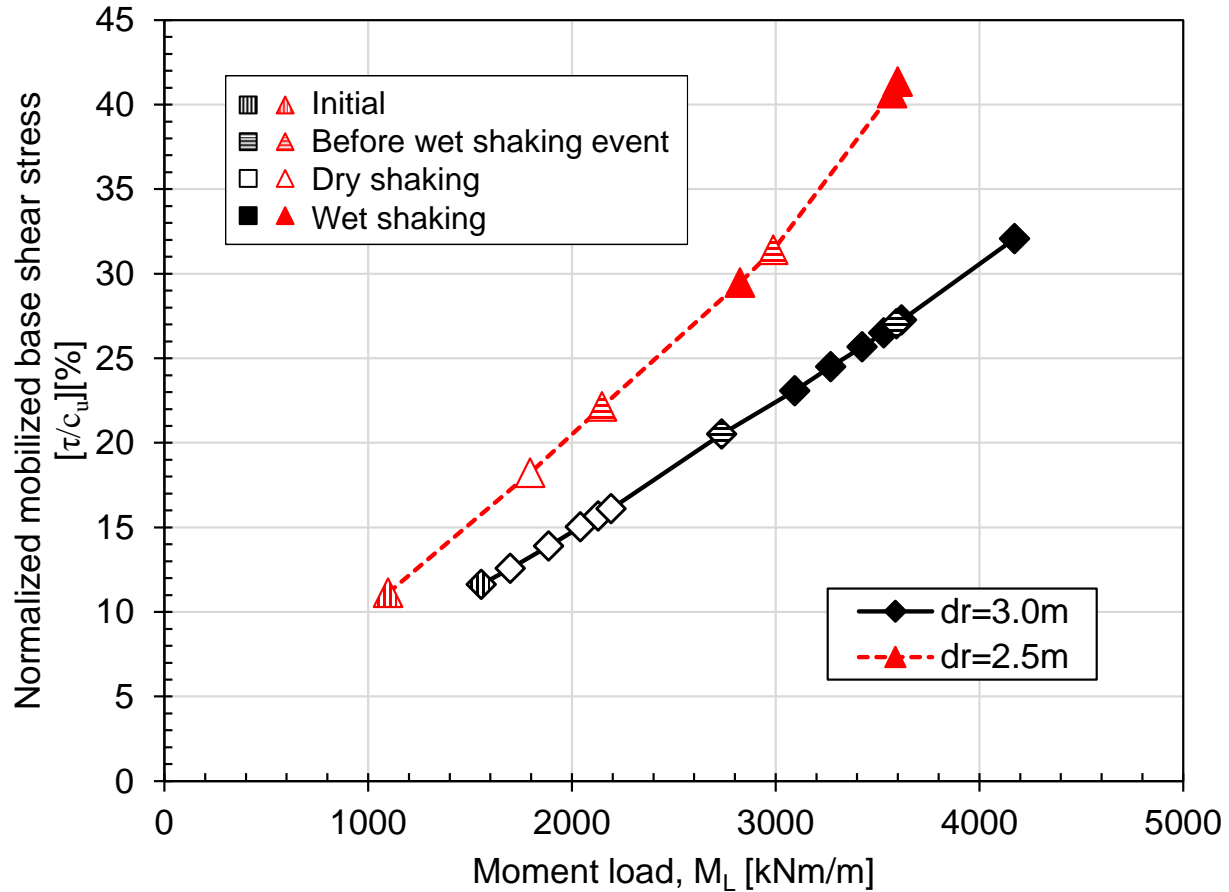


Figure 5.79: Variation of normalised base shear stress with moment load.

The wall top displacement obtained from the p-y analysis for with and without base shear conditions and commonly used active (K_a) and at-rest (K_0) conditions are plotted against the moment load in Figure 5.80. displacement for K_a and K_0 conditions is determined for different water levels mentioned in Table 5.2. Case 1 is used as it has the maximum number of loadings. The wall top displacement for with and without base shear conditions is larger than the commonly used K_a and K_0 . It can be seen that the wall displacement from with and without base shear conditions gradually increases from the K_a and K_0 conditions at $h_w=0m$ and $9.6m$. After the final loading, the wall displacement was about two times the K_0 condition. In the centrifuge test, due to the resilience effect, a constant earth pressure ratio of about 0.6 was observed after shake 11, which was about two times the K_0 (Figure 5.35d). It suggests that designing the wall using K_a or K_0 earth pressure might lead to underestimating the residual wall displacement for sequential loadings.

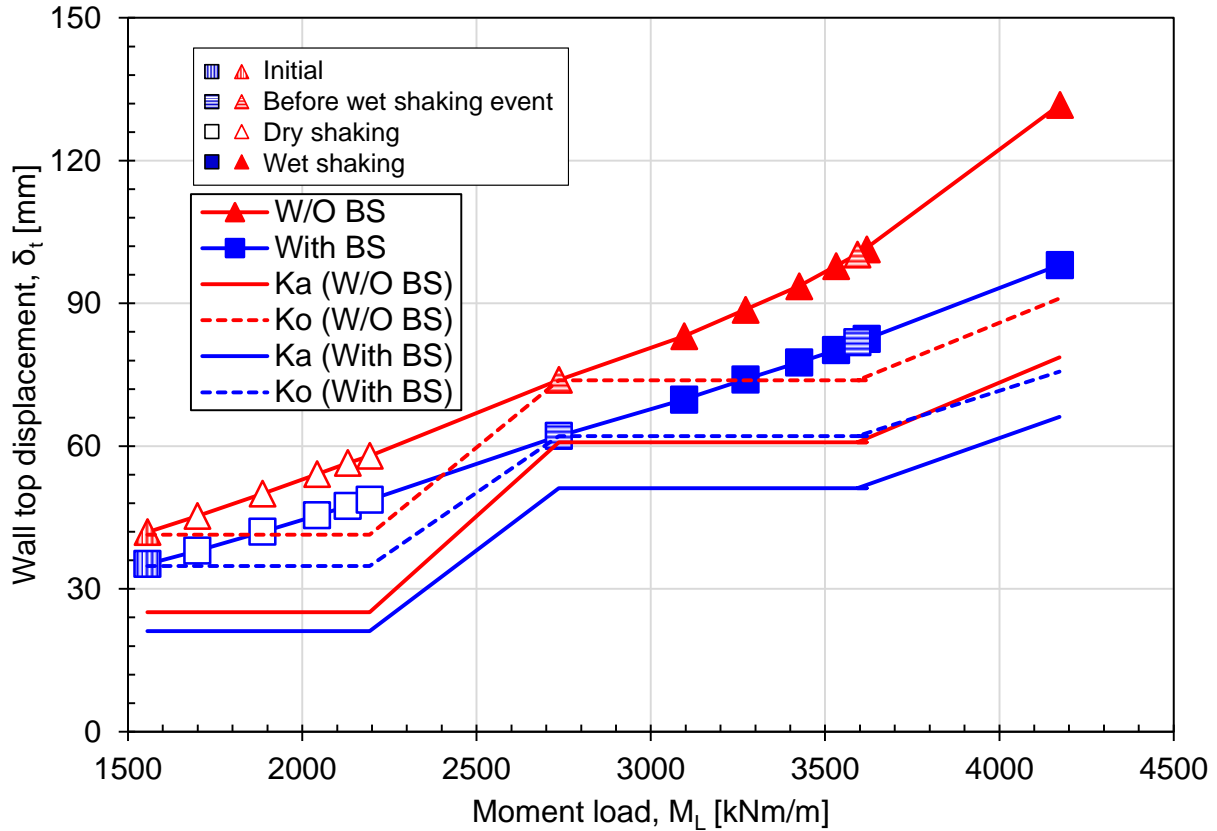


Figure 5.80: Applicability of using design active and at-rest pressure to predict wall displacement after dynamic loading.

5.6 Some appraisal against the concerns related to the design of CSTP wall embedded to the stiff ground:

[Appraisal 1] Required embedment depth:

Based on the test conditions presented in this chapter, the embedment depth was approximately 30-40% of the design embedment depth ($3/\beta$). Extreme loadings were applied to each model to assess the stability of the wall. Figures 5.49, 5.50 and 5.53 demonstrate that all models exhibited significant wall top displacement, exceeding the recommended displacement for level 2 seismic motion. However, no catastrophic failure was observed. Hence, it can be concluded that the CSTP wall embedded in the stiff ground can maintain stability under extreme loading conditions with an embedment depth smaller than the design embedment depth.

Considering the findings from previous research by Kunasegaram and Takemura (2021) and Kunasegaram et al. (2020), along with the results presented in this study, for high stiffness wall embedded into stiff ground like soft rock, an embedment depth of about 2-3 times smaller than the design embedment depth could provide sufficient extra margin of safety against the catastrophic failure.

[Appraisal 2] Effect of embedment condition on the stability of the CSTP wall:

In a construction site, the shallow rock layer could be disturbed during the construction process, leading to a smaller or no strength. Therefore, three scenarios could be expected: 1. Assuming the full embedment depth is equal to rock socketing depth (Case 1) 2. Assuming embedment depth in a combination of rock socketing depth and weak layer (sand) (Case 4) 3. Assuming the embedment depth with only reduced rock socketing depth (subtracting the weak layer) (Case 3). Based on the stability analysis given in Figures 5.11 and 5.16, at $h_w=0\text{m}$, the factor of safety for condition 1 is about 30% larger than that of condition 2. However, the factor of safety in condition 2 is about 10% smaller than in condition 3. A significant effect of the difference in the stability can be confirmed between conditions 1 and 2. However, between conditions 2 and 3, not much effect can be confirmed up to a certain level. However, in the ultimate condition, the effect of the stability becomes visible, and condition 2 provides more stability than condition 3. Therefore, when rationalising the design method, it is crucial to consider the influence of the heterogeneous ground conditions.

[Appraisal 3] Design of CSTP wall embedded into stiff ground subjected to dynamic loading by assuming the active condition:

The design of the CSTP wall, assuming an active condition in the stiff ground, may lead to an underestimation of the lateral pressure acting on the wall. Figures 5.35, 5.36, and 5.54 demonstrate the variation of the normalised effective earth pressure, which was larger than the at-rest pressure, especially at shallower depths. This increase in pressure can be attributed to the resilience effect discussed in this research, which is critical for high-stiffness walls embedded into stiff ground. Moreover, for larger embedment depths, the increase of the normalised effective earth pressure becomes more significant. Based on this large earth pressure, the wall deflection profile shown in Figure 5.58 confirms that if the wall is designed using active conditions, it will underestimate the wall deflection by about 40%. Furthermore, based on Figure 5.54, for $d_r=3.0\text{m}$, an almost constant earth pressure ratio distribution was observed. Therefore, residual earth pressure, which is more than the active or even at-rest pressure, should be considered for rational design, especially after the dynamic loading.

[Appraisal 4] Consideration of the ‘(elastic) resilience effect’ of high stiffness wall embedded into the stiff ground:

For high-stiffness walls embedded into the stiff ground with good confinement conditions, the residual effective earth pressure increases with the wall displacement by dynamic loadings, defined as the “elastic resilience effect” in this study (Figure 5.57). The resilience effect plays a critical role in CSTP wall behaviour under sequential loadings. By severe loading sequence of the dynamic and static conditions, the wall moved larger than $2\%H$ at the wall top. However, the effective earth pressures kept increasing trend, confirming the secured wall confinement by the rock until the end

of the final loading (Figure 5.35-36). The effective stress ratio (σ'_h/σ'_v) over at-rest (K_0) and active (K_a) pressure coefficient could be expected. It suggests that commonly assumed K_a or K_0 earth pressure in the design might lead to underestimating the wall bending moment.

[Appraisal 5] Long-term behaviour of the CSTP wall with large retain height without additional support:

Figures 5.68 and 5.69 illustrate that the wall displacement increases after loading while the lateral pressure and bending moment decrease. This phenomenon results from creep, causing the wall to gradually move forward and release accumulated lateral pressure by the resilience effect. However, as demonstrated in Figure 5.67, the reduction in lateral pressure only occurs until the wall reaches the active condition. Once the wall reaches the active condition, further movement does not decrease lateral pressure, which can be considered as creep failure. Figures 5.65 and 5.66 show that this condition may not be reached for this CSTP wall model with different embedment depths. In this particular model, the resilience effect plays a critical role in determining the long-term behaviour of the CSTP wall. The magnitudes of creep displacement are very small and negligible compared to the displacements during the dynamic loading. Noticeable creep displacement can be expected after the static loading by the rise of water. For the rational design of a less redundant CSTP wall, the long-term behaviour of such a structure needs to be considered.

[Appraisal 5] Use of simple bi-linear p-y curve for predicting the residual behaviour of the CSTP wall embedded into the stiff ground:

If the actual total earth pressure acting on the wall can be measured in the real site, using the two-spring model, where the lateral spring is defined by the JARA (2017) and a base shear spring with stiffness 1/3 of the lateral spring recommended for caisson type foundation by JARA (2017) and actual total earth pressure as imposed load, could reasonably predict the residual wall displacement up to $\delta_t < 0.5\%H$. However, assuming the commonly used active or at-rest earth pressure as imposed external load might underestimate the residual wall displacement due to the resilience effect, which is unique for the high stiffness wall embedded into stiff ground. There are several limitations of using the bi-linear p-y curve to predict the residual wall displacement. Firstly, in actual conditions, as the residual wall displacement increases, the plastic deformation of the rock could reduce the k_H , which cannot be predicted by the bi-linear p-y curve with constant k_H . Therefore, a bi-linear p-y curve with variable k_H based on the plastic deformation could provide a more accurate residual wall top displacement prediction. Secondly, the bi-linear p-y curve cannot predict the resilience effect, which occurs during the dynamic loadings.

5.7 Summary:

In this study, a large diameter ($\Phi=2\text{m}$) cantilever steel tubular piles (CSTP) wall embedded in a soft rock was modelled in a centrifuge with the wall height $H=12\text{m}$ and embedment depth to the

rock $d_r = 2.5\text{-}3.0\text{m}$ overlaying sand layer, $d_s=0\text{-}1\text{m}$, and dry, dense sand as the retained soil under $50g$ centrifugal acceleration. A series of dynamic and static loadings were applied to create an extreme loading condition. From these sequential loadings, the following conclusions were derived:

1. For the relatively small d_r , the resistance mobilised at the base of the tubular pile significantly contributes to the stability of the wall.
2. The CSTP wall demonstrated stability even with wall top displacement exceeding $2\%H$ for $d_r=2.5\text{m}$ ($\beta.d_r=1.0$). This suggests safety with an embedment depth below the recommended value ($\beta.d_r=3.0$). Increasing $\beta.d_r$ by 20% in a single rock layer notably reduces wall top displacement. However, weathering of the shallow rock layer could decrease wall stability.
3. The natural frequency of high-stiffness CSTP walls embedded in hard ground is relatively large ($>5\text{Hz}$). With the high natural frequency of the wall, the amplification of acceleration against the earthquake with a relatively lower dominant frequency could monotonically become larger with increasing input acceleration for dry retained soil conditions. While for the wall with a high water level, the amplifications are even larger than that of the dry condition, but the variation of amplification with the input acceleration is rather complicated and affected by several factors, such as excess porewater, densification and effective earth pressure.
4. For high-stiffness walls embedded into the stiff ground with good confinement conditions, the residual effective earth pressure increases with the wall displacement by dynamic loadings, defined as the “elastic resilience effect” in this study. The resilience effect is critical in CSTP wall behaviour under sequential loadings. By severe loading sequence of the dynamic and static conditions, the wall moved larger than $2\%H$ at the wall top. However, the effective earth pressures kept increasing trend, confirming the secured wall confinement by the rock until the end of the final loading. For $d_r=3.0\text{m}$, the effective stress ratio (σ'_h/σ'_v) close to 0.6 was observed at the end of final loading, which is about twice and three times at-rest (K_0) and active (K_a) pressure coefficient, respectively. It suggests that commonly assumed K_a or K_0 earth pressure in the design might lead to underestimating the wall bending moment.
5. The elastic resilience depends on the embedment conditions. A larger elastic resilience effect could be expected for a single rock layer for larger embedment depth. However, weathering of the shallow rock layer could reduce the resilience effect.
6. For the large diameter thin wall tubular pile, a stress concentration or a propping action might cause the local deformation of the pile near the rock surface, which affects the bending moment measurement using strain gauges.
7. The dynamic component of the total moment load acting on the wall could be estimated by the difference between the maximum and residual bending moments at the rock surface, which has two components: induced by the dynamic earth pressure and the inertia of wall mass. Due to the phase difference of the wall earth pressure at different heights, the maximum value of the earth pressure component does not occur at the same time as the maximum wall moment load. However, the inertia component is generated at the same time. As a result, although the mass of the tubular pile wall is relatively small, the

contribution of the wall inertia to the wall dynamic component became significant at about 60%.

8. The long-term creep displacement of the wall will be less of a concern for the dynamic loading than the static loading due to the reduction of earth pressure by the resilience effect developed by the dynamic loading.
9. If the actual total earth pressure acting on the wall can be measured in the real site, using the two-spring model, where the lateral spring is defined by the JARA (2017) and a base shear spring with stiffness 1/3 of the lateral spring recommended for caisson type foundation by JARA (2017) and actual total earth pressure as imposed load, could reasonably predict the residual wall displacement up to $\delta_t < 0.5\%H$. However, assuming the commonly used active or at-rest earth pressure as imposed external load might underestimate the residual wall displacement due to the resilience effect, which is unique for the high stiffness wall embedded into stiff ground. There are several limitations of using the bi-linear p-y curve to predict the residual wall displacement. Firstly, in actual conditions, as the residual wall displacement increases, the plastic deformation of the rock could reduce the k_H , which cannot be predicted by the bi-linear p-y curve with constant k_H . Therefore, a bi-linear p-y curve with variable k_H based on the plastic deformation could provide a more accurate residual wall top displacement prediction. Secondly, the bi-linear p-y curve cannot predict the resilience effect, which occurs during the dynamic loadings.
10. The mobilisation of base shear provides a positive effect on the stability of the wall. The smaller the embedment depth, the larger the effect of base shear.

References:

1. Brinkgreve, R.B.J., Engin, E. and Engin, H.K., 2010. Validation of empirical formulas to derive model parameters for sands. *Numerical methods in geotechnical engineering, 1*, pp.137-142.
2. Borghei, A, Ghayoomi, M, & Turner, M (2020) Effects of Groundwater Level on Seismic Response of Soil–Foundation Systems. *Journal of Geotechnical and Geoenvironmental Engineering*, 146(10), 04020110, [https://doi.org/10.1061/\(ASCE\)GT.1943-5606.0002359](https://doi.org/10.1061/(ASCE)GT.1943-5606.0002359)
3. Conti, R., Madabhushi, G.S.P., Viggiani, G.M.B., 2012. On the behaviour of flexible retaining walls under seismic actions. *Géotechnique* 62, 1081–1094. <https://doi.org/10.1680/geot.11.P.029>
4. Carter, JP, & Kulhawy, FH (1988) Analysis and design of drilled shaft foundations socketed into rock. Electric Power Research Inst., Palo Alto, CA (USA); Cornell Univ., Ithaca.
5. Carter, J. P., & Kulhawy, F. H. (1992). Analysis of Laterally Loaded Shafts in Rock. *Journal of Geotechnical Engineering*, 118(6), 839–855, [https://doi.org/10.1061/\(ASCE\)0733-9410\(1992\)118:6\(839\)](https://doi.org/10.1061/(ASCE)0733-9410(1992)118:6(839))
6. Day, R.W., 1997. Design and Construction of Cantilevered Retaining Walls. *Pract. Period. Struct. Des. Constr.* 2, 16–21. [https://doi.org/10.1061/\(ASCE\)1084-0680\(1997\)2:1\(16\)](https://doi.org/10.1061/(ASCE)1084-0680(1997)2:1(16))
7. D'Andrea, R. and Day, R.W., 1998. Discussion and closure: design and construction of cantilevered retaining walls. *Practice Periodical on Structural Design and Construction*, 3(2), pp.87-88.
8. Fukushima, S., Tatsuoka, F., 1984. Strength and Deformation Characteristics of Saturated Sand at Extremely Low Pressures. *Soils and Foundations* 24, 30–48. https://doi.org/10.3208/sandf1972.24.4_30

9. Gaba, AR, Hardy, S, Doughty, L, Selemetas, D and Powrie, W, 2016. Embedded retaining walls – guidance for design, Report C760, CIRIA, London.
10. Gopal Madabhushi, S.P., Chandrasekaran, V.S., 2005. Rotation of Cantilever Sheet Pile Walls. *J. Geotech. Geoenviron. Eng.* 131, 202–212. [https://doi.org/10.1061/\(ASCE\)1090-0241\(2005\)131:2\(202\)](https://doi.org/10.1061/(ASCE)1090-0241(2005)131:2(202))
11. Ishihama, Y., Takemura, J. and Kunasegaram, V., 2020. Analytical evaluation of deformation behavior of cantilever type retaining wall using large diameter steel tubular piles into stiff ground. In *Geotechnics for Sustainable Infrastructure Development* (pp. 91-98). Springer Singapore.
12. Japan road Association (JRA). 2017. Specification of road bridges and explanations, IV: lower structures. (in Japanese).
13. Joseph, M., Banerjee, S. and Pakrashi, V., 2021. Estimation of the dynamic amplification factor at backfill soil behind a gravity wall. *Geotechnical Research*, 8(4), pp.95-107.
14. Kunasegaram, V., Akazawa, S., Takemura, J., Seki, S., Fujiwara, K., Ishihama, Y. and Fujii, Y., 2015. Modeling of soft rock for a centrifuge study. *ProCase 12th GeoKanto*, pp.15-19.
15. Kunasegaram, V., Shafi, S.M., Takemura, J., Ishihama, Y., 2020. Centrifuge Model Study on Cantilever Steel Tubular Pile Wall Embedded in Soft Rock, in: Duc Long, P., Dung, N.T. (Eds.), *Geotechnics for Sustainable Infrastructure Development, Lecture Notes in Civil Engineering*. Springer Singapore, Singapore, pp. 1045–1052. https://doi.org/10.1007/978-981-15-2184-3_135
16. Kunasegaram, V., Takemura, J., 2021. Deflection and failure of high-stiffness cantilever retaining wall embedded in soft rock. *International Journal of Physical Modelling in Geotechnics* 21, 114–134. <https://doi.org/10.1680/jphmg.19.00008>
17. Takemura, J., Kondoh, M., Esaki, T., Kouda, M., Kusakabe, O., 1999. Centrifuge Model Tests on Double Propped Wall Excavation in Soft Clay. *Soils and Foundations* 39, 75–87. https://doi.org/10.3208/sandf.39.3_75
18. Tatsuoka, F., Sakamoto, M., Kawamura, T. and Fukushima, S., 1986. Strength and deformation characteristics of sand in plane strain compression at extremely low pressures. *Soils and Foundations*, 26(1), pp.65-84.
19. Weiler, WA, & Kulhawy, FH (1982) Factors Affecting Stress Cell Measurements in Soil. *Journal of the Geotechnical Engineering Division*, 108(12), 1529–1548, <https://doi.org/10.1061/AJGEB6.0001393>
20. Talesnick, ML, Ringel, M, & Avraham, R (2014). Measurement of contact soil pressure in physical modelling of soil–structure interaction. *International Journal of Physical Modelling in Geotechnics*, 14(1), 3–12, <https://doi.org/10.1680/ijpmg.13.00008>
21. Weiler, WA, & Kulhawy, FH (1982) Factors Affecting Stress Cell Measurements in Soil. *Journal of the Geotechnical Engineering Division*, 108(12), 1529–1548, 628 <https://doi.org/10.1061/AJGEB6.0001393>

Chapter 6

Conclusions and recommendations

6.1 Conclusions:

The stability of Cantilever type Steel Tubular Pile (CSTP) walls made of a steel tubular pile embedded into soft rock ground was investigated against various loading conditions. Tokyo tech Mark III centrifuge was used to conduct the tests under 50g centrifugal acceleration. Based on the model and test conditions provided in this research, the following conclusions can be drawn:

Based on model pile and soft rock:

- For the diameter over thickness ratio (Φ/t) equals 80, the actual yielding of the steel tubular pile occurs at around 65% of the theoretical yielding moment. In the ultimate condition, failure is characterized by the formation of elephant-footed buckling near the support, with the specific failure mechanism influenced by the socketing condition.
- The application of the Euler-Bernoulli theorem can be reasonably applied up to the point of nonlinear strain occurring at approximately 65% of the theoretical yielding moment for the diameter over thickness ratio (Φ/t) equals 80. Beyond this limit, the application of the theorem may lead to an overestimation of the bending moment.
- The lateral resistance of the pile increases with the increase of rock socketing depth, a behaviour that is effectively captured in both the 50g and 1g model tests. However, the 1g model underestimates the lateral resistance, particularly after the formation of tension cracks near the rock surface, indicating a limitation of the 1g model test.
- The failure mechanism significantly affects the load-displacement behaviour, particularly the post-peak behaviour, in both the 50g and 1g models. While both ground and structural failure were observed in the 50g model test, the 1g model consistently exhibited ground failure.
- No effect of confining pressure or rock socketing depth can be confirmed up to $\delta_t=1\%\Phi$ for $d_r/\Phi=1.5$ and 2 in the 50g model test. However, in the 1g model test, this behaviour is limited to $\delta_t=0.5\%\Phi$. For $d_r/\Phi=1$, due to the rigid nature of the pile, no effect of material weight or gravity can be expected.

Based on a simple pile wall model embedded into soft rock:

- Based on the numerical analysis conducted for the centrifuge model test, no significant effect of the container wall was observed on the load-displacement behaviour by further increasing the container width, especially for $d_r/\Phi=1.5$. The effect varies about 4-5% on the load-displacement behaviour. However, certain effects from the back wall could be expected for larger embedment depth $d_r/\Phi=2.0$.

- The base shear positively contributes to the stability of the large-diameter CSTP wall. The contribution is larger for smaller embedment depth conditions than for larger embedment depth conditions.
- For the bi-linear p-y method, bi-linear P-y curve without base shear recommended by JARA (2017) could be more conservative for predicting the load-displacement relationship of large-diameter piles embedded in the stiff ground than the model with base shear spring. Two springs model, where the lateral spring is defined by the JARA (2017) and a base shear spring with stiffness 1/3 of the lateral spring recommended for caisson type foundation by JARA (2017), could predict the load-displacement curve at small to large imposed displacement ($<10.0\% \Phi$) reasonably in the conservative side, especially for the small loading level. However, a more sophisticated non-linear p-y curve might be suitable to predict the non-linear load-displacement relationship at small imposed displacement ($<1.0\% \Phi$).
- The contribution of base shear resistance to the lateral resistance of the pile depends on the base shear p-y curve stiffness. Larger base shear stiffness (Model 3) could provide larger base shear resistance. However, the yielding might occur at a very small imposed displacement or lateral load.
- Different trends can be expected based on the base shear p-y curve stiffness. A non-linear relationship could be expected in the lateral load-base shear curve for the base shear p-y curve with smaller stiffness (Model 2) but almost linear for larger stiffness (Model 3). More hardening can be expected in the trend for smaller stiffness than larger stiffness based on the embedment depth (more hardening for larger embedment depth than the smaller embedment depth). Therefore, smaller stiffness could contribute less to the lateral resistance but prevent the quick occurrence of the ultimate condition.

Based on Cantilever Type Steel Tubular Pile (CSTP) wall embedded in soft rock subjected to sequential dynamic and static loadings:

- For the relatively small d_r , the resistance mobilised at the base of the tubular pile significantly contributes to the stability of the wall.
- The CSTP wall demonstrated stability even with wall top displacement exceeding $2\%H$ for $d_r=2.5\text{m}$ ($\beta.d_r=1.0$). This suggests safety with an embedment depth below the recommended value ($\beta.d_r=3.0$). Increasing $\beta.d_r$ by 20% in a single rock layer notably reduces wall top displacement. However, weathering of the shallow rock layer could decrease wall stability.
- The natural frequency of high-stiffness CSTP walls embedded in hard ground is relatively large ($>5\text{Hz}$). With the high natural frequency of the wall, the amplification of acceleration against the earthquake with a relatively lower dominant frequency could monotonically become larger with increasing input acceleration for dry retained soil conditions. While for the wall with a high water level, the amplifications are even larger than that of the dry condition, but the variation of amplification with the input acceleration is rather complicated and affected by several factors, such as excess porewater, densification and effective earth pressure.
- For high-stiffness walls embedded into the stiff ground with good confinement conditions,

the residual effective earth pressure increases with the wall displacement by dynamic loadings, defined as the “elastic resilience effect” in this study. The resilience effect is critical in CSTP wall behaviour under sequential loadings. By severe loading sequence of the dynamic and static conditions, the wall moved larger than 2%H at the wall top. However, the effective earth pressures kept increasing trend, confirming the secured wall confinement by the rock until the end of the final loading. For $d_r=3.0\text{m}$, the effective stress ratio (σ'_h/σ'_v) close to 0.6 was observed at the end of final loading, which is about twice and three times at-rest (K_0) and active (K_a) pressure coefficient, respectively. It suggests that commonly assumed K_a or K_0 earth pressure in the design might lead to underestimating the wall bending moment.

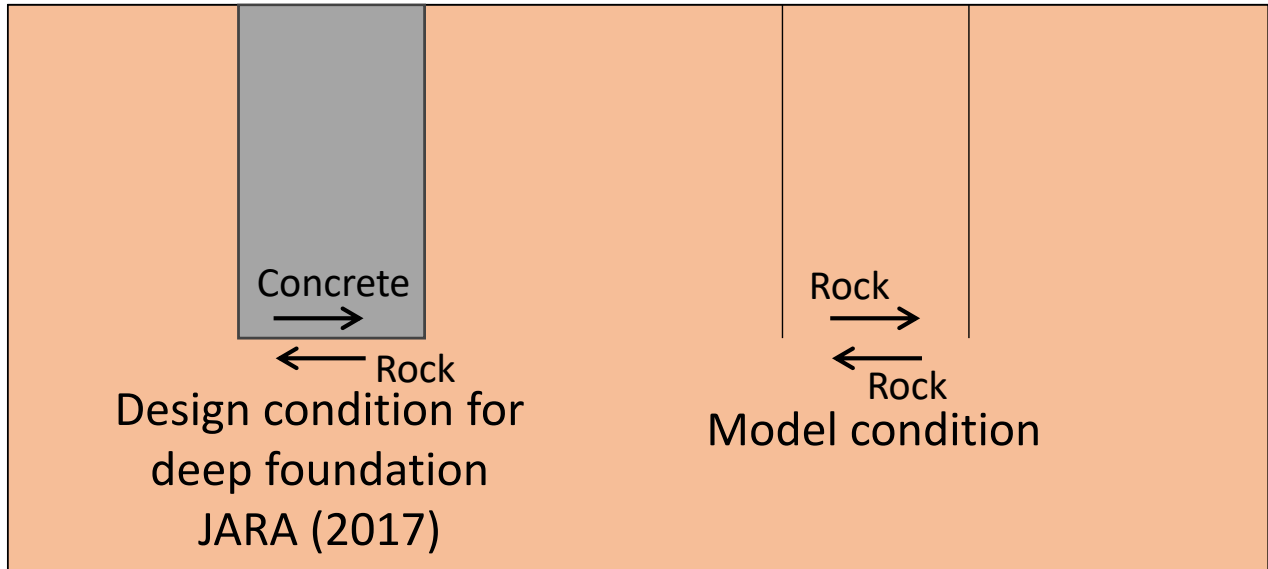
- The elastic resilience depends on the embedment conditions. A larger elastic resilience effect could be expected for a single rock layer for larger embedment depth. However, weathering of the shallow rock layer could reduce the resilience effect.
- For the large diameter thin wall tubular pile, a stress concentration or a propping action might cause the local deformation of the pile near the rock surface, which affects the bending moment measurement using strain gauges.
- The dynamic component of the total moment load acting on the wall could be estimated by the difference between the maximum and residual bending moments at the rock surface, which has two components: induced by the dynamic earth pressure and the inertia of wall mass. Due to the phase difference of the wall earth pressure at different heights, the maximum value of the earth pressure component does not occur at the same time as the maximum wall moment load. However, the inertia component is generated at the same time. As a result, although the mass of the tubular pile wall is relatively small, the contribution of the wall inertia to the wall dynamic component became significant at about 60%.
- The long-term creep displacement of the wall will be less of a concern for the dynamic loading than the static loading due to the reduction of earth pressure by the resilience effect developed by the dynamic loading.
- If the actual total earth pressure acting on the wall can be measured in the real site, using the two-spring model, where the lateral spring is defined by the JARA (2017) and a base shear spring with stiffness 1/3 of the lateral spring recommended for caisson type foundation by JARA (2017) and actual total earth pressure as imposed load, could reasonably predict the residual wall displacement up to $\delta t < 0.5\%H$. However, assuming the commonly used active or at-rest earth pressure as imposed external load might underestimate the residual wall displacement due to the resilience effect, which is unique for the high stiffness wall embedded into stiff ground. There are several limitations of using the bi-linear p-y curve to predict the residual wall displacement. Firstly, in actual conditions, as the residual wall displacement increases, the plastic deformation of the rock could reduce the k_H , which cannot be predicted by the bi-linear p-y curve with constant k_H . Therefore, a bi-linear p-y curve with variable k_H based on the plastic deformation could provide a more accurate residual wall top displacement prediction. Secondly, the bi-linear p-y curve cannot predict the resilience effect, which occurs during the dynamic loadings.
- The mobilisation of base shear provides a positive effect on the stability of the wall. The smaller the embedment depth, the larger the effect of base shear.

6.2 Further recommendation:

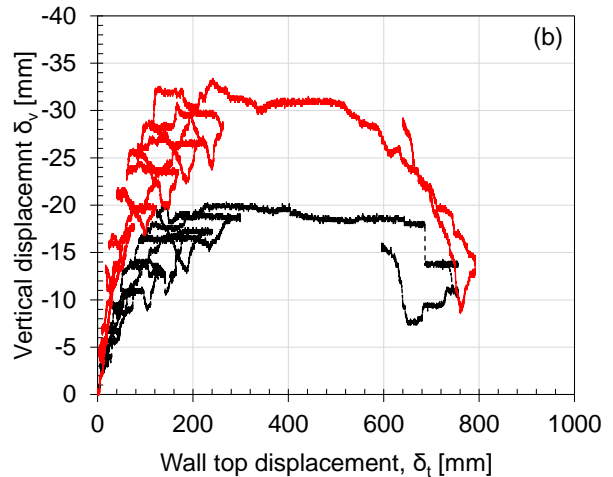
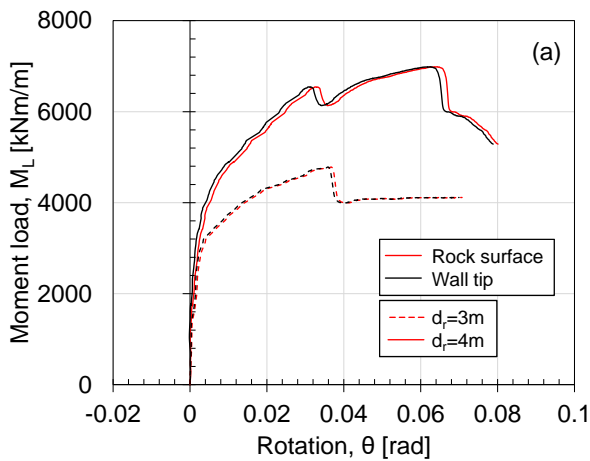
Numerical and analytical approaches could be used to investigate the CSTP wall behaviour subjected to various loadings. In predicting the residual wall displacement after the loading (especially after dynamic loading), a non-linear p-y curve with spring stiffness varies with the loading history could be used to predict the behaviour because the actual load-displacement curve is not bi-linear but shows post-peak softening behaviour. Also, a more sophisticated p-y curve should be considered to model the effect of base shear. A more detailed 3D FEM analysis is recommended.

Appendix:

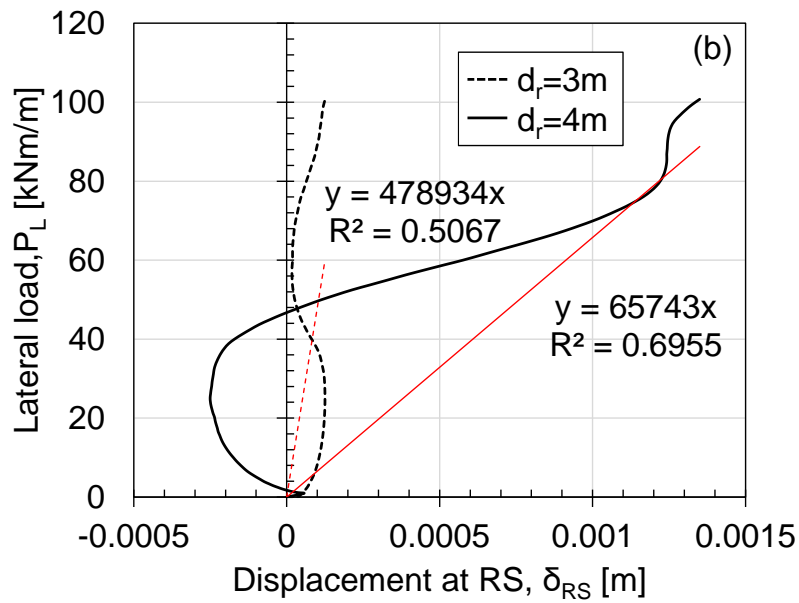
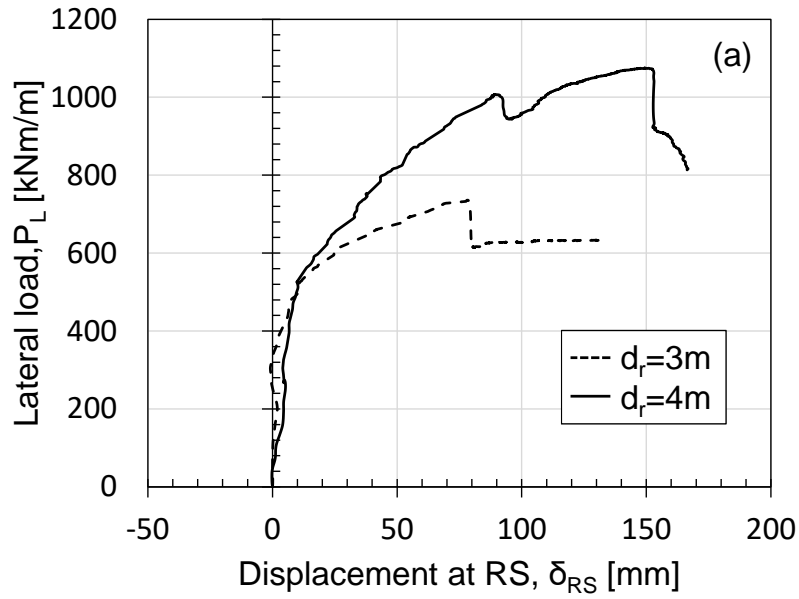
Appendix 4.1: Base condition observed in the design of deep foundation by JARA (2017) and the centrifuge model condition.



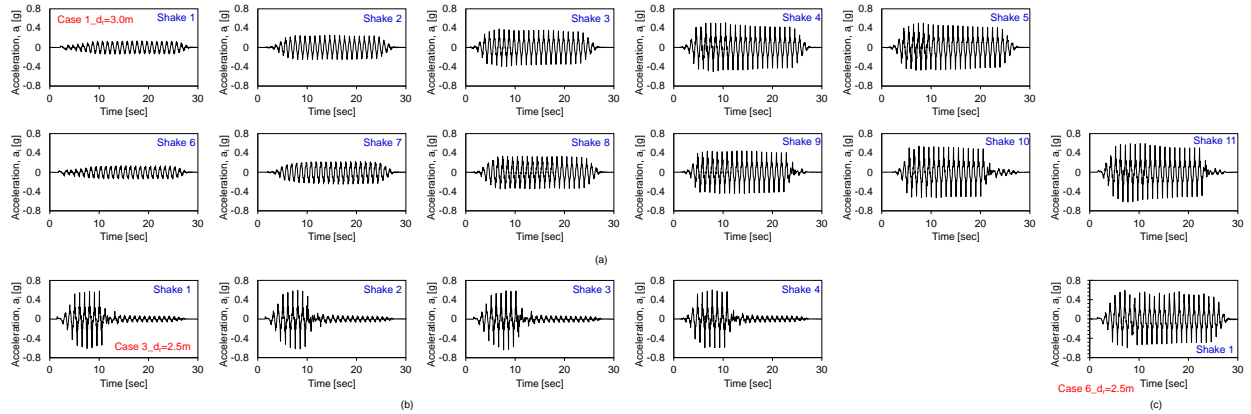
Appendix 4.2: Centrifuge test result from simple pile wall model (a) variation of moment load with wall toe rotation (b) variation of cyclic vertical displacement with the wall top displacement.



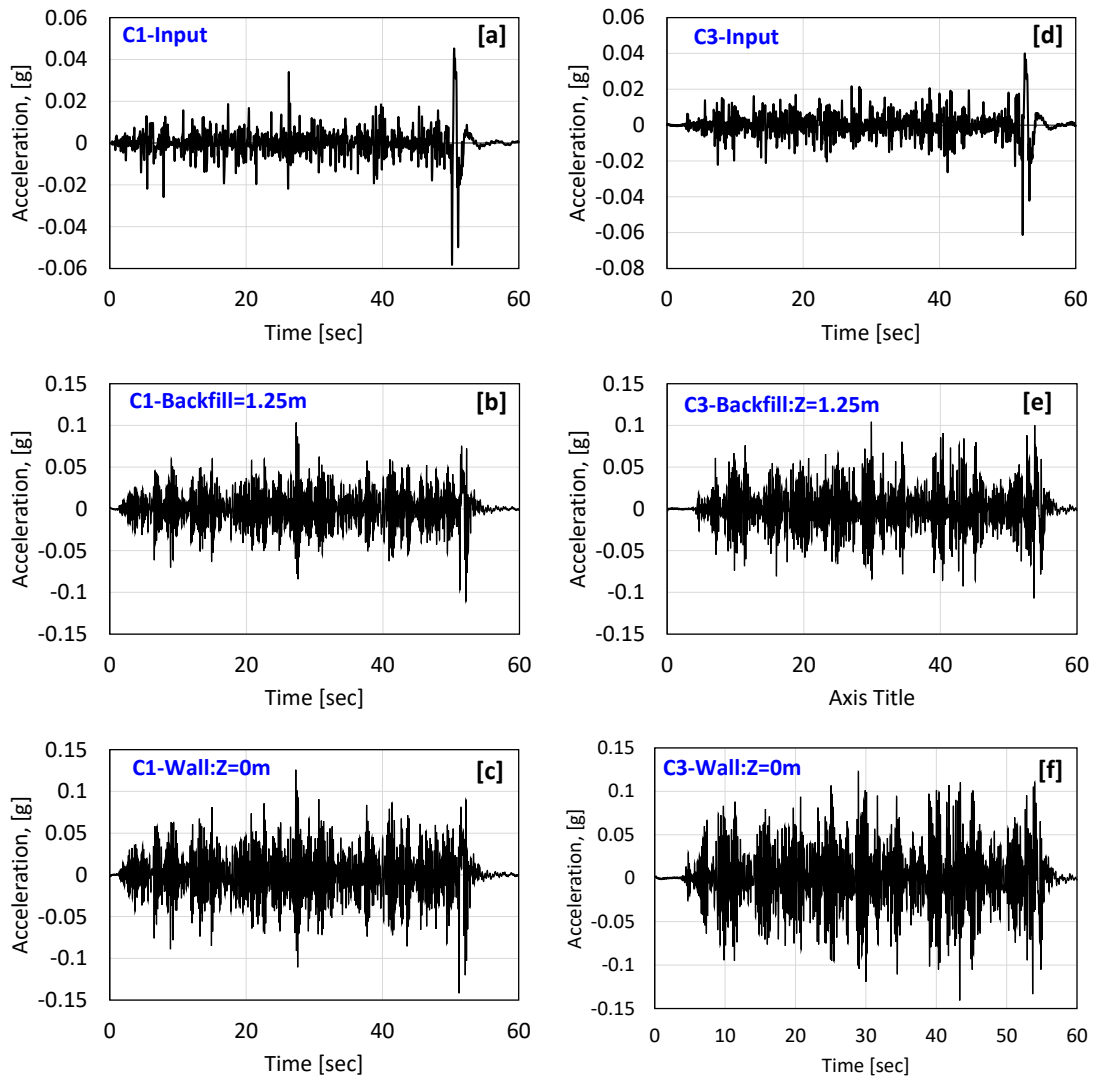
Appendix 4.3: (a) load displacement curve obtained at rock surface (b) load displacement curve at small imposed displacement.



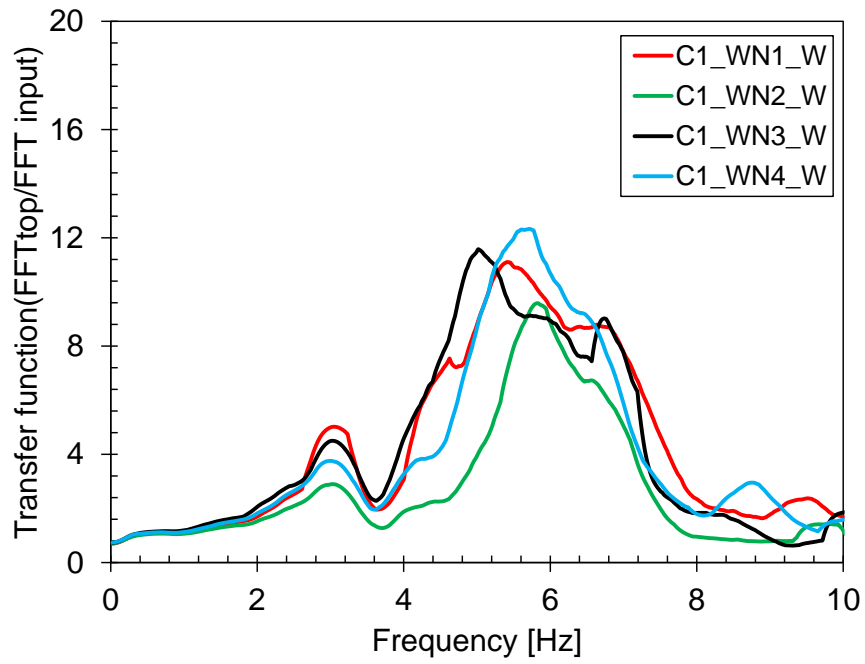
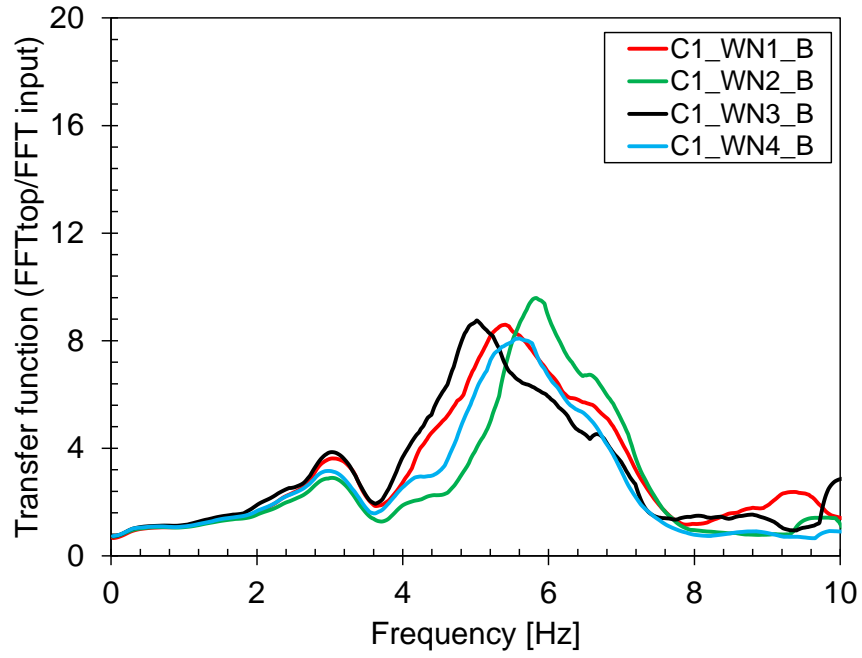
Appendix 5.1 Typical shape of the input motion applied in case 1, 3 and 6.



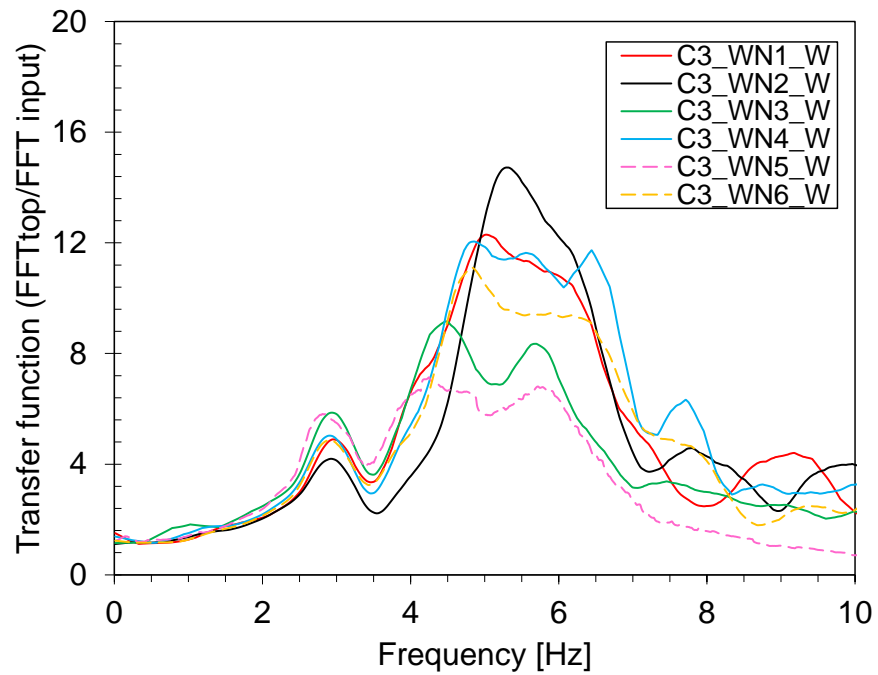
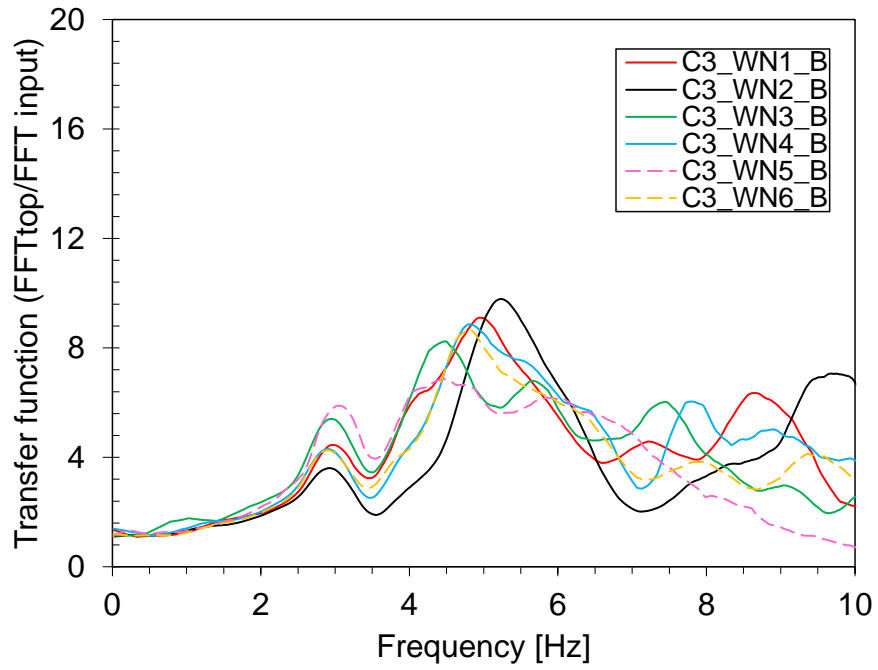
Appendix 5.2: Typical shape of white noise applied in case 1 and 3.



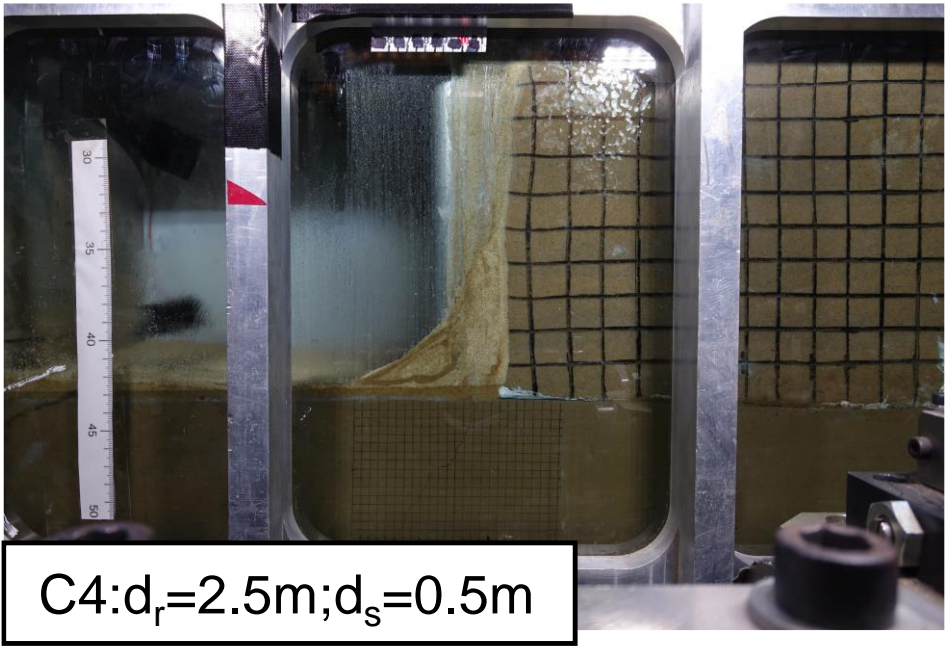
Appendix 5.3: Transfer function variation during different white noise in case 1.



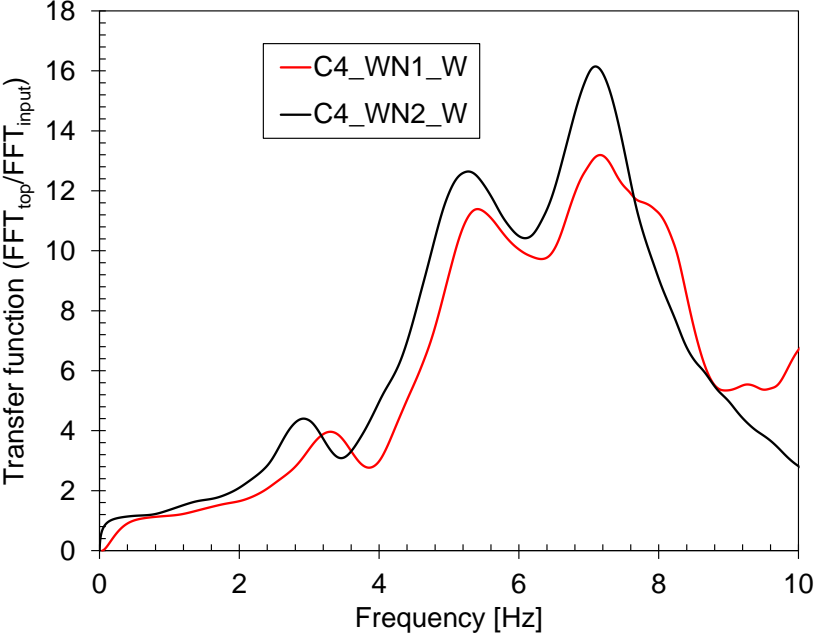
Appendix 5.4: Transfer function variation during different white noise in case 3.



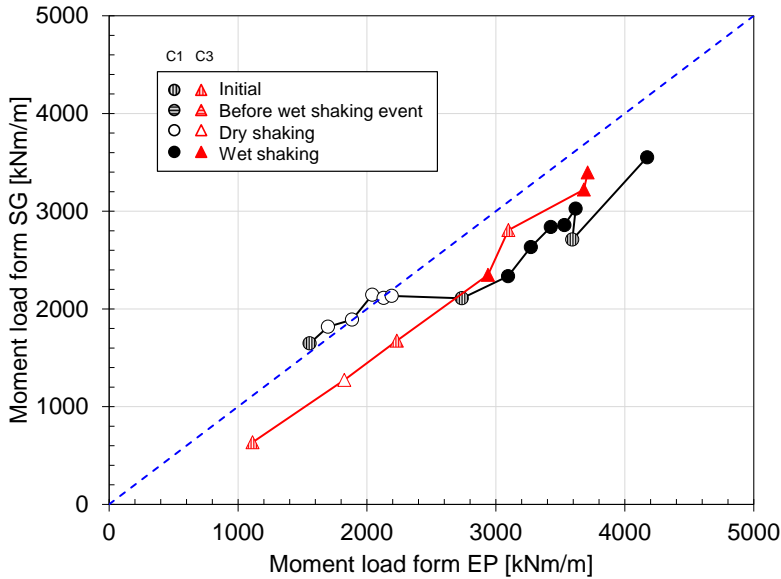
Appendix 5.5: Side view of the centrifuge model from case 4.



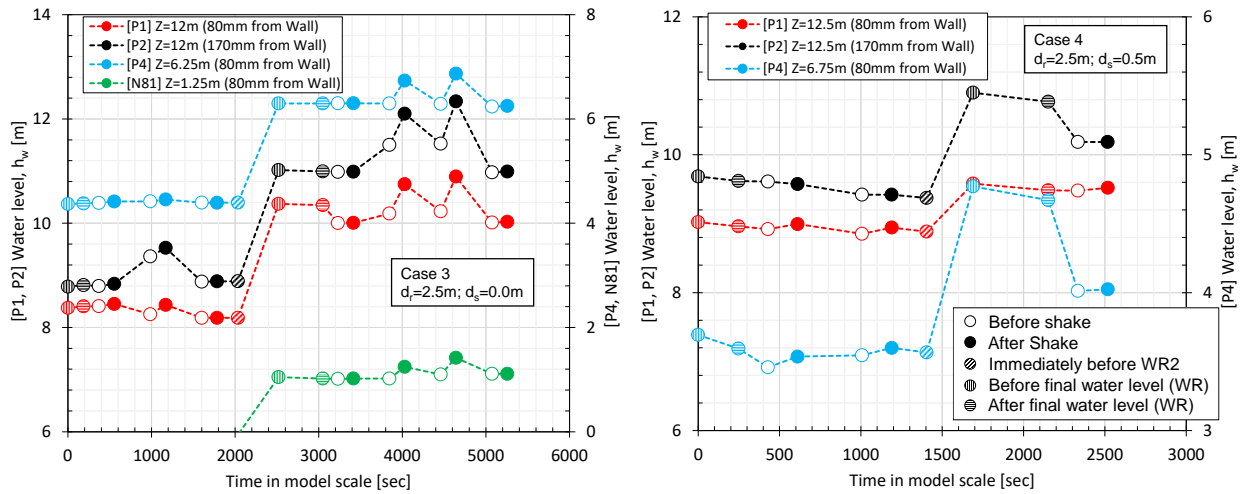
Appendix 5.6: Observed transfer function at wall top from case 4.



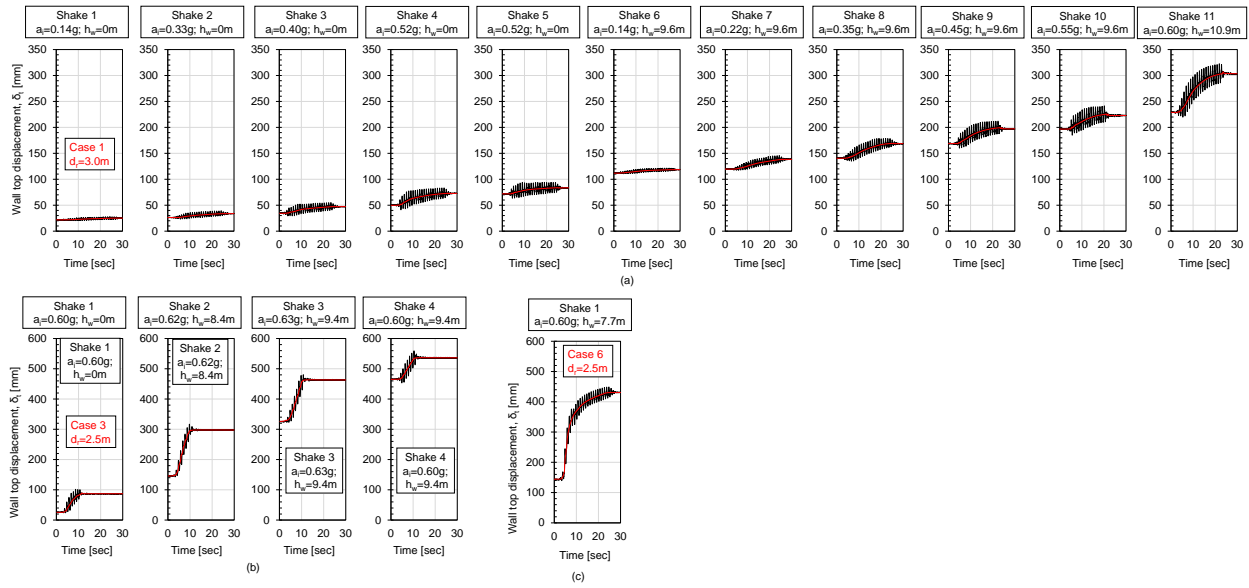
Appendix 5.7: Comparison of back calculated moment load from measured lateral pressure distribution with strain gauge moment load.



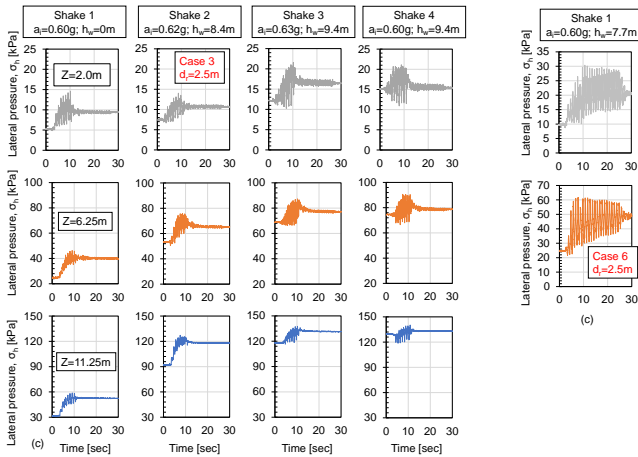
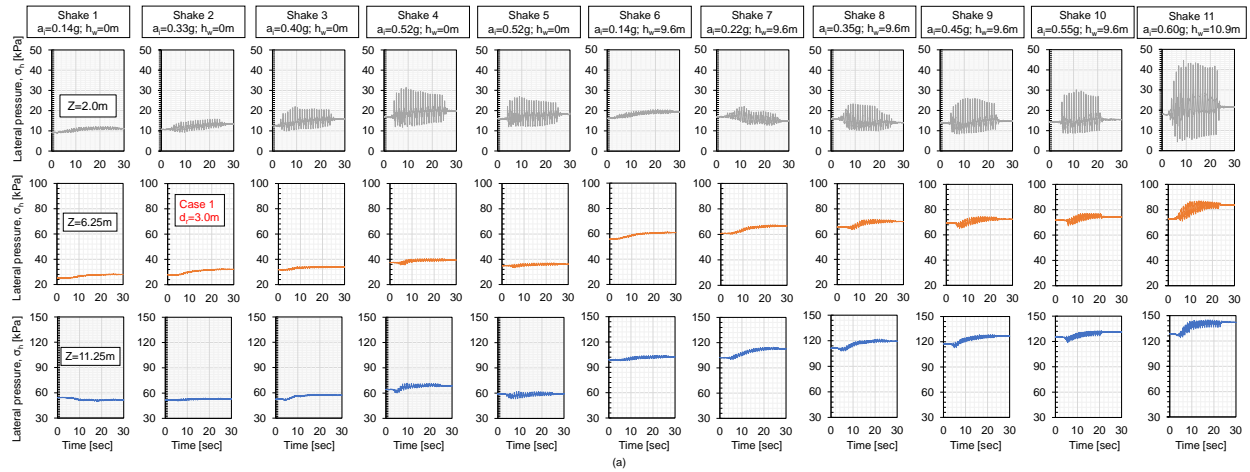
Appendix 5.8: Change of water level in case 3 and 4



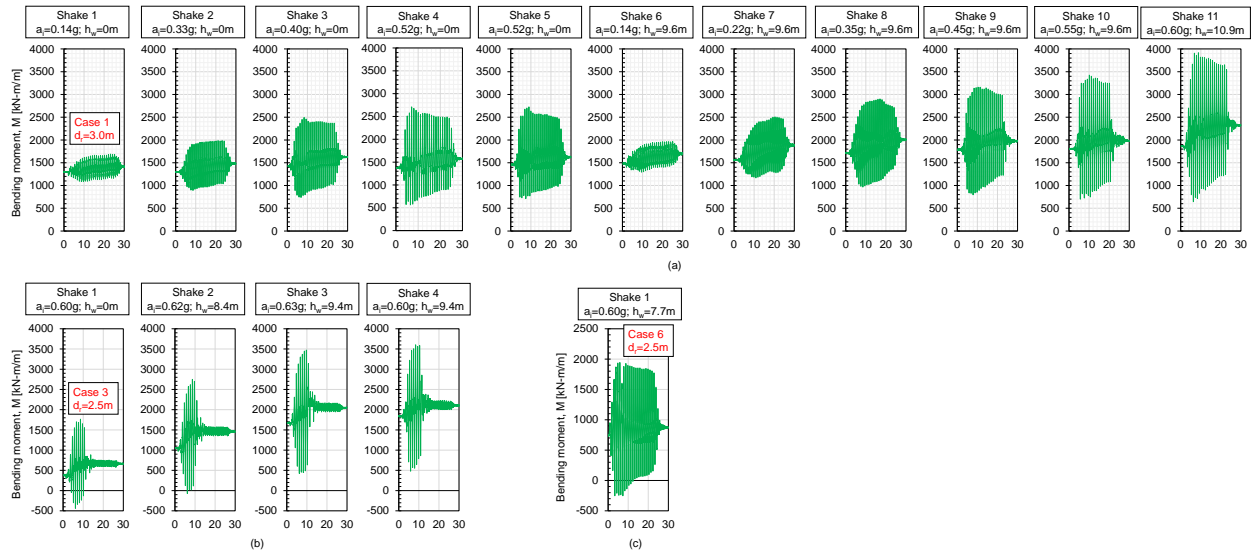
Appendix 5.9: Wall top displacement measured from case 1, 3 and 6.



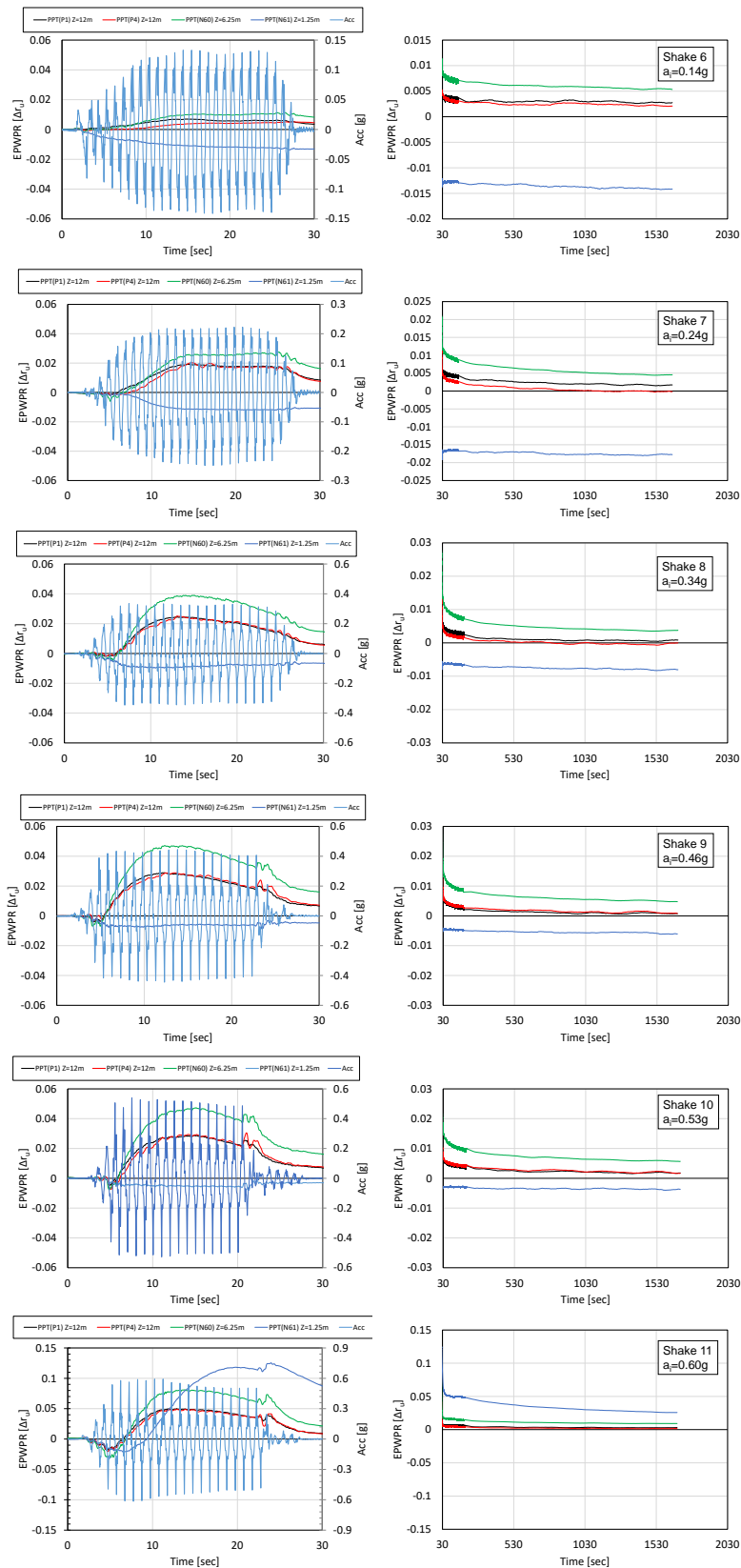
Appendix 5.10: Lateral pressure measured at Z=2.0m, 6.25m and 11.25m from case 1, 3 and 6.



Appendix 5. 11: Bending moment measured at Z=10.75m from case 1, 3 and 6.

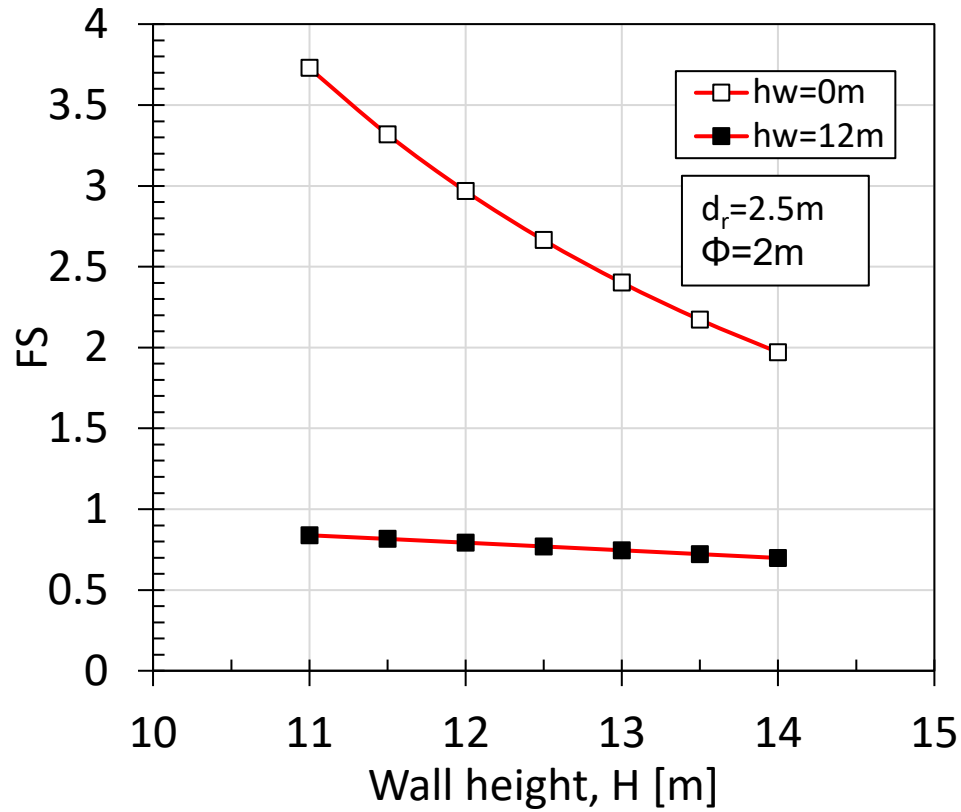


Appendix 5.12 Excess pore water pressure ratio obtained from case 1 for shake 6-11.

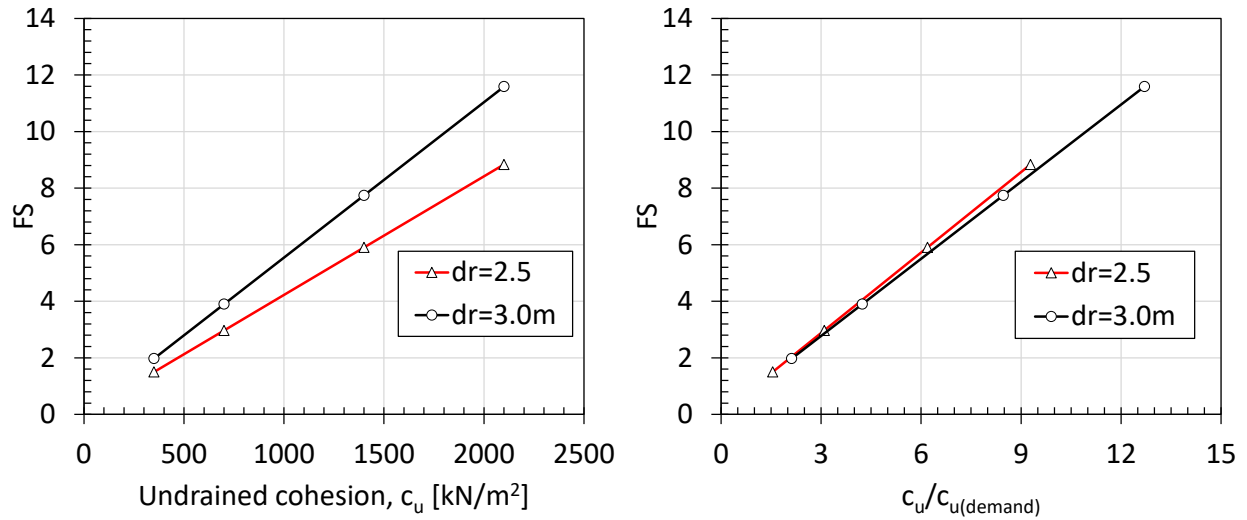


Appendix 5.13 Parametric study based on Figure 5.10

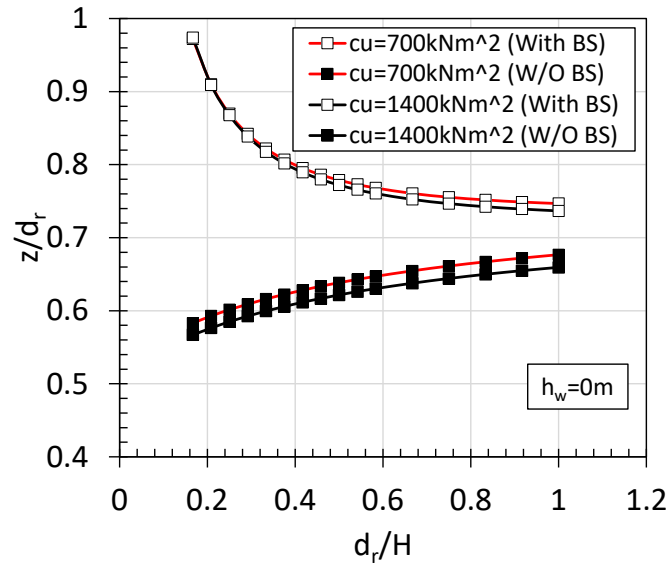
(a) Effect of wall height (H) on the factor of safety



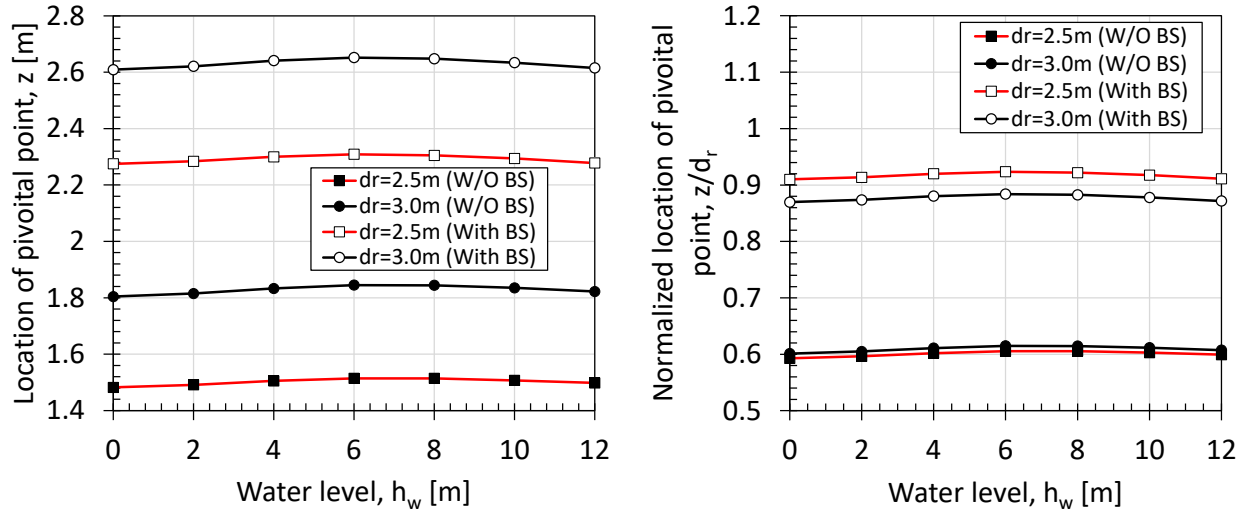
(b) Effect of material strength on factor of safety



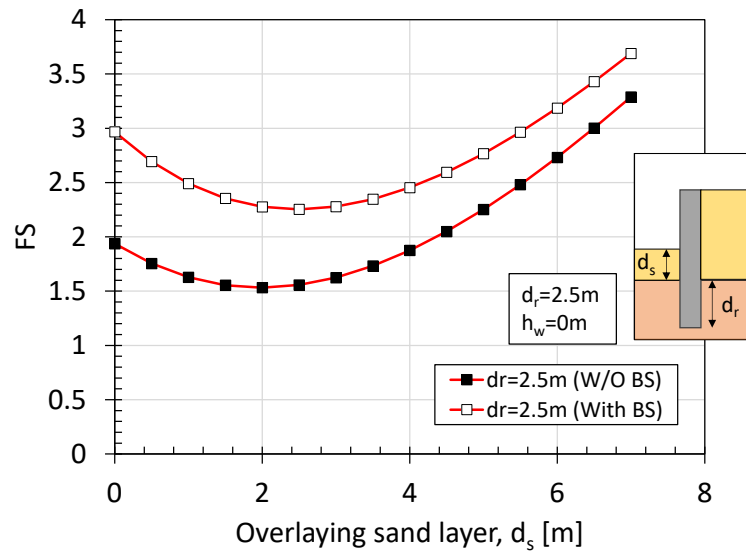
(c) Variation of pivotal point with embedment depth



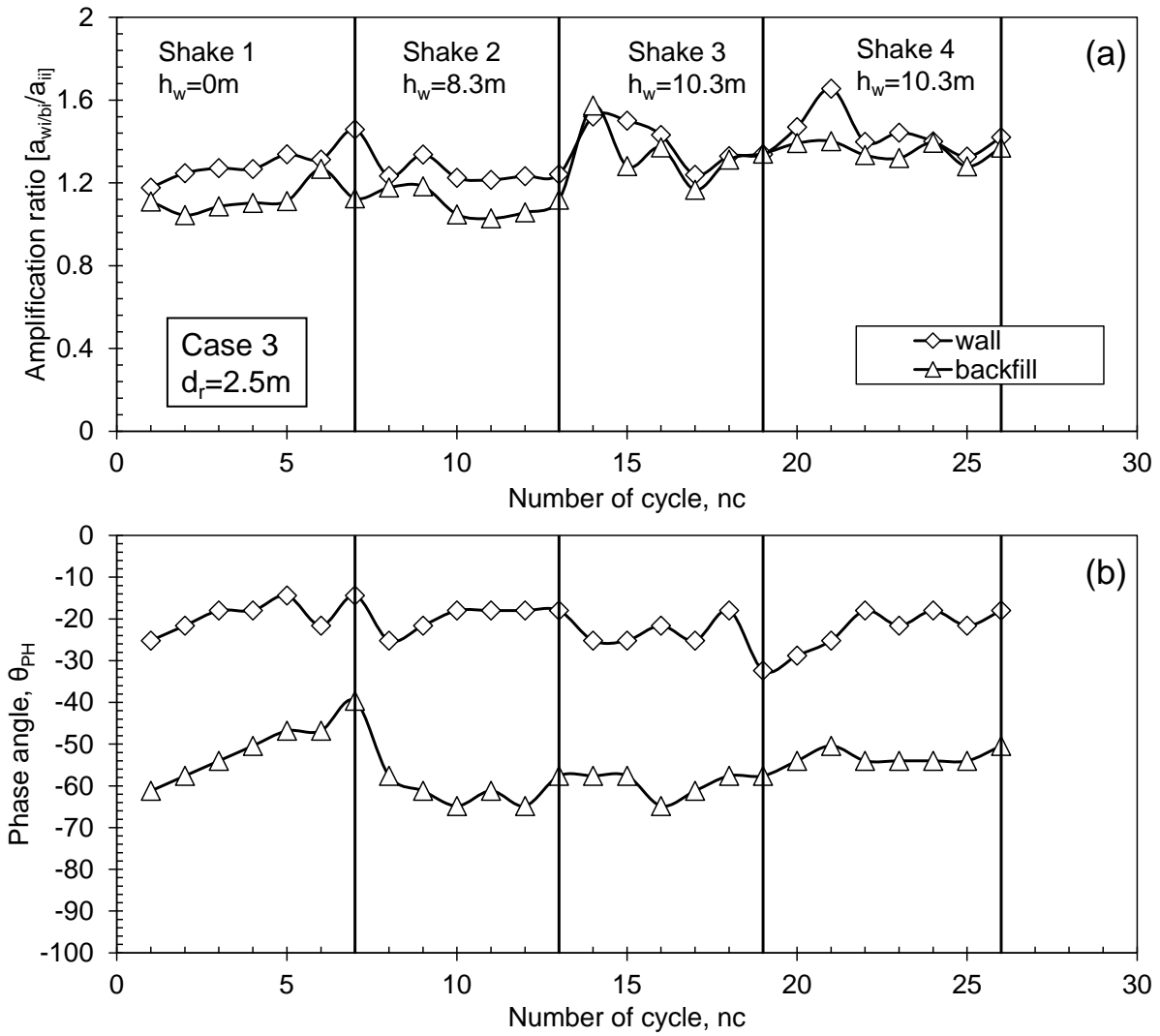
(d) Variation of pivotal point with water level (h_w)



(e) Variation of factor of safety with overlaying sand layer



Appendix 5.14: Variation of amplification ratio and phase angle with number of cycles for case 3 (shake 1-4)



Appendix 5.15: Variation of amplification ratio and phase angle with number of cycles for case 4 (shake 1-4)

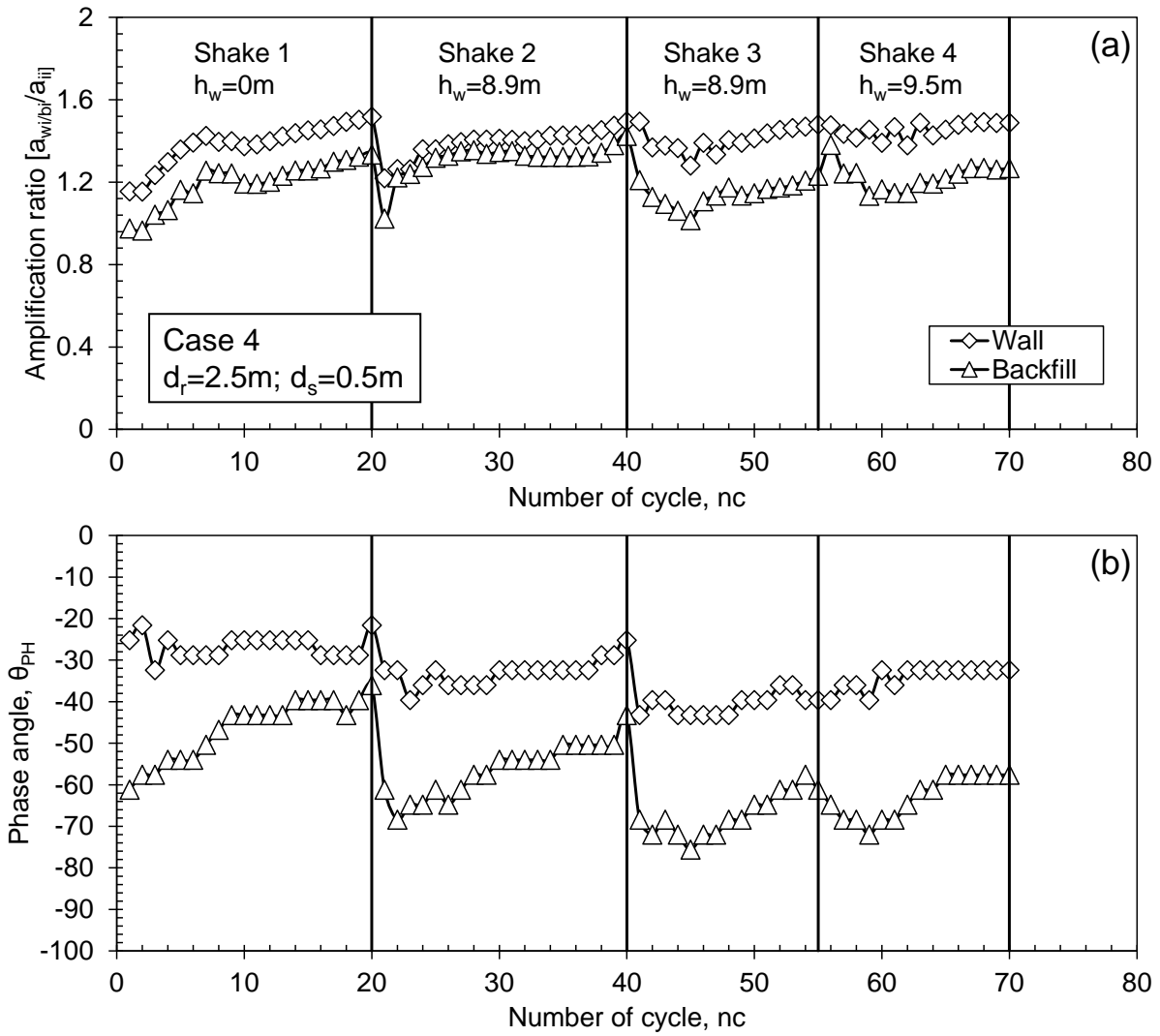


Figure 5.23: Variation of (a) amplification ratio (b) Phase angle with number of cycle of case 4 (shake 1-4).

Appendix 5.16: Comparison of residual moment load between the centrifuge and p-y analysis

